Sloping Convection: An Experimental Investigation in a Baroclinic Annulus With Topography

A Thesis Submitted for the Degree of Doctor of Philosophy

Samuel David Marshall

Lincoln College

Atmospheric, Oceanic and Planetary Physics,

Department of Physics,

University Of Oxford

March 2014

Abstract

This thesis documents a collection of experimental investigations in which a differentially-heated annulus was used to investigate the effects of topography on the atmospheric and oceanic circulation. To this end a number of experiments were devised, each using a different topographic base to study a different aspect of the impact of topography, motivated by the most notable outstanding questions found in a review of the literature, namely exploring the effects of topographic resonance, blocking via partial barriers, and azimuthally differential-heating via thermal topography.

First of all, whilst employing sinusoidal wavenumber-3 topography to extend the experimental parameter space of a similar study, namely Read and Risch (2011), a new regime within a region of structural vacillation was encountered. Denoted as the 'stationary-transition' regime, it featured periodic oscillations between a dominant stationary wavenumber-3 flow and axisymmetric or chaotic flow. An investigation into topographic resonance followed, keeping the wavenumber-3 base, but with a sloped lid to add a beta effect to the annulus. This acted to increase the occurrence of stationary waves, along with the 'stationary-transition' regime, which was discovered to be a near-resonant region where nonlinear topographic resonant instability led to a 23 to 42 'day' oscillatory structure. The base was then replaced with an isolated ridge, forming a partial barrier to study the difference between blocked and unblocked flow. The topography was found to impact the circulation at a level much higher than its own peak, causing a unique flow structure when the drifting flow and the topography interacted in the form of an 'interference' regime at low Taylor Numbers, as well as forming an erratic 'irregular' regime at higher Taylor Numbers. Lastly, this isolated ridge was replaced by flat heating elements covering the same azimuthal extent, in order to observe whether thermal topography could be comparable to mechanical topography. These azimuthally-varying heating experiments produced much the same results as the partial barriers study, despite the lack of a physical peak or bottom-trapped waves, suggesting that blocking is independent of these activities. Evidence of resonant wave-triads was noted in all experiments, though the component wavenumbers of the wave-triads and their impact on the flow was found to depend on the topography in question.

Table of Contents

Acknowledgements

This work was partially-funded by doctoral training awards from the UK National Environment Research Council and Science and Technology Facilities Council.

There are many people I have to thank for the completion of this thesis. Firstly, Professor Peter Read, for the Herculean task of keeping me and my work on track for half a decade. Also from GFD: Roland and James, for helping me with computers, theoretical concepts, and other such horrors; Alfonso and Tom, previous Kings of the Lab, for showing me both the right and the wrong way to wield my rig (respectively); and Yixiong, Judy and Joao for their total lack of complaining when I regaled them with stories about my latest problems. On that note, many thanks also go to Dane, for keeping me mostly sane during the bad times, and almost entirely sane during the good times.

I must also thank AOPP's brilliant network of support, namely Sarah and Monica, for "shielding me from numerous vast and terrifying bureaucracies" as Wordsworth (2008) put it, as well as Andy, Duncan and Bob for sharing their charity and sympathy from the beginning.

Finally, I would like to thank my parents, without whom I would not have had the opportunity to come to Oxford in the first place, and my long-suffering girlfriend, Shirlyn, who hardly ever moaned about the sentences: "it's resonantly vacillating, but is it period-doubling whilst it resonantly vacillates?", "alright, so the last experiment should be finished about midnight, if that's OK?" and "I have suspended a tank of water above a source of mains electricity – clearly nothing can go wrong.". Wo ai ni, Shirlyn.

Chapter 1

Introduction

Sloping convection – and the accurate comprehension of its implications – are arguably the most important aspects of atmospheric circulation, whether discussing the Earth, other planets within the Solar System, or even exoplanets still to be discovered. Also known as a form of baroclinic instability, sloping convection can occur when a thermally-forced zonal flow becomes sheared in association with a lateral density gradient, as in Figure 1.1.

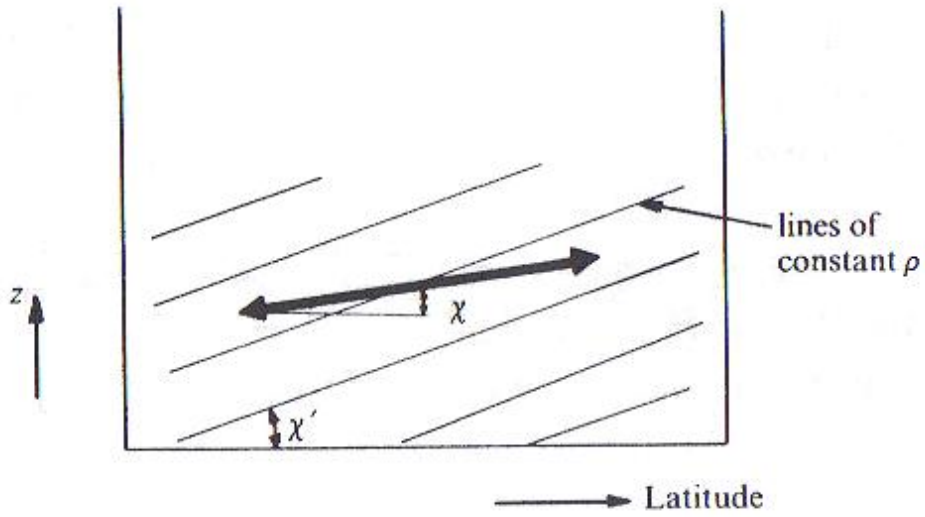

Figure 1.1: Illustration of sloping convection, where χ is the average slope between two "air parcels" in a hypothetical exchange during a disturbance and χ' is the slope of the density surfaces [adapted from Houghton (2002)].

If $\chi < \chi'$, (i.e. if the forcing causing the density surfaces to slope is large enough) this can lead to an decrease in potential energy, due to the interchange of the air parcels between surfaces of different densities. This in turn provides kinetic energy into the system and hence produces instabilities. A more detailed account of this process can be found in Andrews (2000).

The effects of sloping convection on the atmosphere are many and various. For example, Houghton (2002) notes that, outside of the Hadley Cell, sloping convection is the dominant method of heat transport in the atmosphere, and, according to Hide, Lewis and Read (1994), it is also a possible mechanism for the generation of such famous and long-lasting features as the Jovian Great Red Spot.

In the laboratory, sloping convection can be replicated using a piece of equipment known as a differentially-heated rotating annulus. As such, this thesis will utilise this apparatus to study the various impacts that sloping convection of the fluid has on the patterns governing atmospheric circulation, with special focus on the role of topography.

1.1 The Annulus

The rotating annulus is the standard for laboratory studies of the atmosphere, especially with topography. Differentially-heated annuli, such as those in Leach (1981), Li, Kung and Pfeffer (1986) and Risch (1999), are cylinders full of fluid on a rotating turntable that contain a second central cylinder which can be cooled, whilst the outer cylinder can be heated – this temperature difference is what drives the flow. In this way, the annulus becomes a simple simulation of the Earth's (or another planet's) atmosphere, as seen from directly above the poles, with the cool middle analogous to the pole and the heated outer edge analogous to the equator. More specific detail will be provided in a later section.

Annuli have their origin in the early ‘dishpan’ experiments of the 1800s, most notably that of Vettin (1857), who used a container of ice to cool the centre of the fluid. Unfortunately, only Vettin was able to see the importance of this model of the atmosphere at the time, and the development of the experiments stalled. The next time annuli with temperature gradients would occur in major literature would be almost one hundred years later, in Hide (1953). Interestingly, these annuli, despite essentially being in their modern form (with only minor differences in materials and structure), were

designed to study the thermal convection in the Earth's core. However, Hide did note the possible application to atmospheric circulation. By the time of Hide (1958), interest in atmospheric circulation had overtaken that of the Earth's core and the first modern investigation with an annulus led to the discovery of vacillation and the different flow regimes of the jet stream (including detailed images of wavenumber-2, wavenumber-3 and wavenumber-4 regimes, described in the next section). Several years later, Hide and Mason (1975) reviewed the state of work on annuli, and created the basis for most modern experiments. The authors charted the effects of increasing the rotation rate and thermal forcing on the flow, charting the transition from wavenumber-1, through wavenumber-2, wavenumber-3 and wavenumber-5, up to the chaotic/irregular regimes. As will be seen, the experimental arrangement of this thesis owes a lot to these studies.

1.2 Sloping Convection in the Annulus

The temperature difference of the differentially-heated annulus generates a radial flow (analogous to the atmosphere's meridional flow) that acts to create a baroclinic flow profile. This can be observed by taking temperature readings of the fluid, as illustrated in Figure 1.2, which shows a temperature stratification that represents the sloping density surfaces, with the corresponding zonal velocity shown for comparison. Hence, sloping convection can be replicated in the annulus, along with its dynamical effects on the flow.

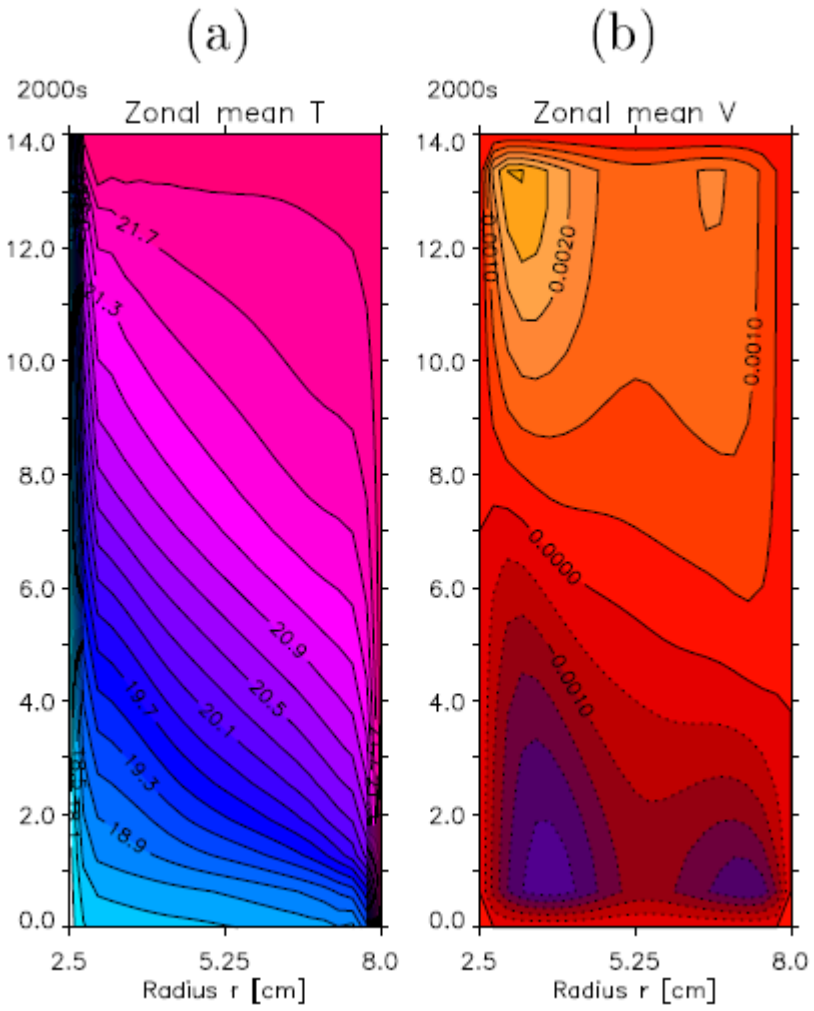

Figure 1.2: Cut-away of computational annulus showing temperature contours in °C (a) and zonal velocity in ms^{-1} (b) with respect to height/depth (y-axis) and radial distance (x-axis), heating occurs at the right-hand wall (r = 8cm) and cooling at the left-hand wall (r = 2.5cm) [from Risch (1999)].

1.2.1 Baroclinic Dynamics

The most important low-order effect of sloping convection in an annulus is the advent of baroclinic waves. At low thermal forcing and rotation rates, flow structure is uniform in the azimuthal direction[1]. Hide and Mason (1975) refer to this region as 'axisymmetric'. When the parameters are increased, however, the flow becomes 'non-axisymmetric' and azimuthal variation is introduced in the form of eddies. The number of eddies that occur depends on the location in parameter space, with distinct regions denoted as regimes, and with extremely large forcing leading to the structure becoming dominated by chaos. These eddies are baroclinic waves, and are illustrated in Figure 1.3.

[1] Williams (1967), amongst others, notes the similarity to the Hadley Cell circulation.

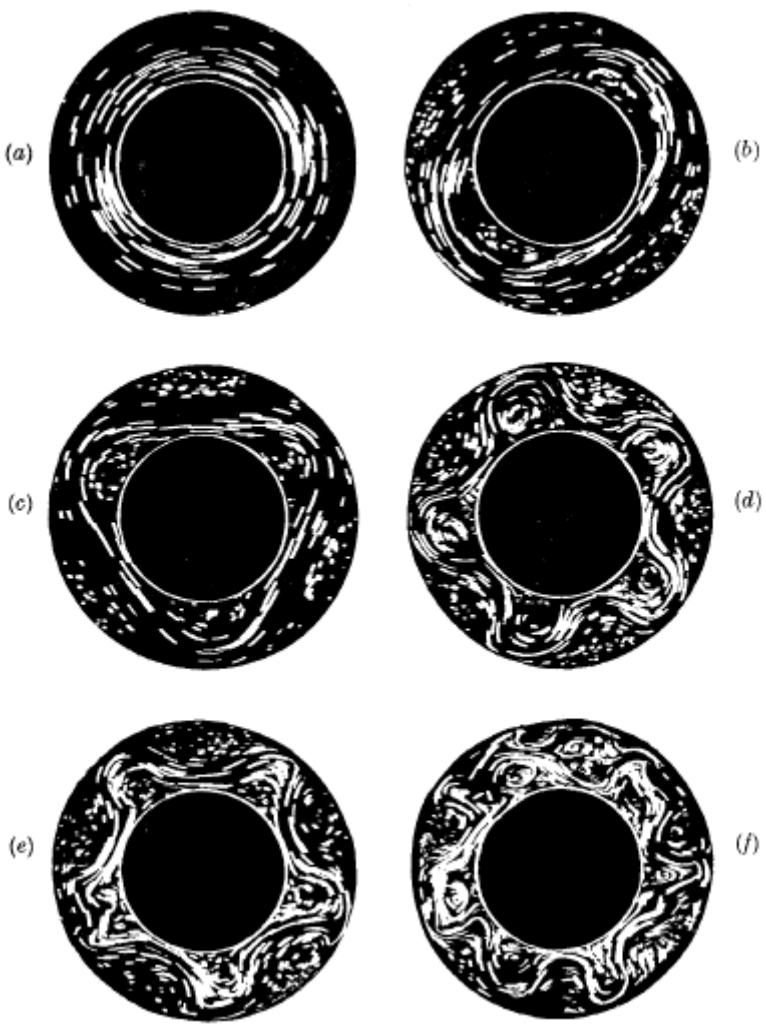

Figure 1.3: Streakline images illustrating how the flow structure develops as rotation rate increases in a particular annulus with a 4.64cm gap between cylinders, a 13.4cm depth and a 9K temperature gradient - a.) $\Omega = 0.41$ *rads*$^{-1}$*, b.)* $\Omega = 1.07$ *rads*$^{-1}$ *c.)* $\Omega = 1.21$ *rads*$^{-1}$ *d.)* $\Omega = 3.22$ *rads*$^{-1}$ *e.)* $\Omega = 3.91$ *rads*$^{-1}$ *f.)* $\Omega = 6.4$ *rads*$^{-1}$ *[from Hide and Mason (1975)].*

Each flow structure is named after the spatial 'period' of the cyclonic waves (i.e. rotating in the same direction as the flow), with Figure 1.3b referred to as wavenumber-2, (c) as wavenumber-3, (d) as wavenumber-5, and so-on. Furthermore, the waves can be either stationary or drifting, depending on whether they oscillate at the same rate as the annulus or not, and either vacillating or steady, depending on whether the eddies maintain a constant size and shape or not. Amplitude vacillation is where the eddies grow or shrink in the radial direction over time, and structural vacillation (which occurs with more intense forcing) is where the eddies change in appearance, for example becoming unevenly spaced around the annulus. These terms will become important in describing the results of this thesis' experiments.

1.2.2 Topographic Dynamics

Benzi et al (1986) stated that, if there was no topography, the long-term average atmospheric circulation would be zonally symmetric (although, short-term asymmetry can be caused by differential heating). Whilst this assertion neglects permanent asymmetries caused by land-sea heating contrasts (known as thermal topography, which will be discussed later), both mechanical and thermal topography must therefore have a spatial symmetry-breaking effect, which may take the form of stationary topographic waves superposed on the zonal flow. These waves[2] are defined as having peaks and troughs that do not move relative to the ground, occurring at locations determined by the shape of the planet's topography. According to Wallace (1983), topographic forcing dominates the interactions of the atmospheric circulation at high levels (most notably at the level of the jetstream), whereas, nearer sea level, thermal forcing takes over dominance. This is backed up by Held (1983); however he asserts that the effect of topography is still non-negligible at the surface.

Resonance, and in particular a flow's resonant interaction with topography, has a number of impacts on the atmospheric circulation. To facilitate understanding of topographic resonance, however, first the quasi-geostrophic potential vorticity must be derived, such as in Andrews (2000). Assuming an inviscid and undamped system, the quasi-geostrophic potential vorticity can be written in the form:

$$\left(\frac{\delta}{\delta t} + u_g \frac{\delta}{\delta x} + v_g \frac{\delta}{\delta y}\right)\left(f_0 + \beta \cdot y + \frac{\delta v_g}{\delta x} - \frac{\delta u_g}{\delta y}\right) = f_0 \frac{\delta w_a}{\delta z} \qquad (1.1)$$

where t is time, x, y and z are the zonal, meridional and vertical coordinates respectively, u_g and v_g are the geostrophic zonal and meridional velocities respectively, β and f_0 are from the beta-plane approximation to the Coriolis parameter, $f \approx f_0 + \beta \cdot y$, and w_a is the ageostrophic vertical velocity. As the flow crosses topography of height η, it is deflected vertically with a velocity of w at the lower boundary. Hence, it can be written that:

[2] Occasionally referred to as quasi-stationary waves, as in Cehelsky and Tung (1987), for example.

$$\frac{\delta w_a}{\delta z} \approx -\frac{w}{H} = -\frac{u_g \cdot \nabla \eta}{H} \tag{1.2}$$

where H is the mean atmospheric height. By substituting Equation 1.2 into Equation 1.1, the latter can be linearised about a steady, uniform, zonal flow $U(y)$, so that $u_g = (U + u)$ and $v_g = v$. Assuming a barotropic flow[3] and neglecting the products of u, v, η and their derivatives, this yields:

$$\frac{\delta \nabla^2 \psi}{\delta t} + U\frac{\delta \nabla^2 \psi}{\delta x} + v\left(\beta - \frac{\delta^2 U}{\delta y^2}\right) = -f_0 \frac{U}{H}\frac{\delta \eta}{\delta x} \tag{1.3}$$

where ψ is the streamfunction, defined as $u_g = -{\delta\psi}/{\delta y}$, $v_g = {\delta\psi}/{\delta x}$. If Equation 1.3 can be taken to have steady, stationary wave-like solutions (which therefore neglect time-dependence) with the form:

$$\psi = \psi_0 {}^{i(kx+ly)} \tag{1.4}$$

where k and l are the zonal and meridional wavenumbers, then it can stated that:

$$\nabla^2 \psi = -(k^2 + l^2)\psi = -K^2 \cdot \psi. \tag{1.5}$$

Similarly, topography can also be taken to be composed of a series of wave-like components, as follows:

$$\eta = \eta_0 {}^{i(kx+ly)}. \tag{1.6}$$

In this way, Equation 1.3 can now be solved for the amplitude of ψ for each wavenumber K, giving:

$$\psi_0 = \frac{f_0 \cdot \eta_0}{H\left(K^2 - \frac{\left(\beta - \frac{\delta^2 U}{\delta y^2}\right)}{U}\right)}. \tag{1.7}$$

Hence, the flow has a resonant response to the topography encountered when $K = \sqrt{\frac{\left(\beta - \frac{\delta^2 U}{\delta y^2}\right)}{U}}$ is satisfied. This is what is known as the linear resonance. Flows close to this value, referred to as near-

[3] The general case of Equation 1.1 can be transformed to the barotropic case by integrating over the vertical direction and dividing through by the depth of the system.

resonant, will experience amplification of the corresponding wavenumber, for example the wavenumber-3 component if the topography in question is a wavenumber-3 sinusoid. Much like in other resonant systems, such as a vibrating string, friction and damping remove the theoretical infinite response at the resonant peak.

Aside from the effects of amplification, near-resonant flows often also feature increased nonlinear interactions. These nonlinear effects can grow to dominate the resonant response, leading to a shift in the location of the resonant peak. This shift can in turn cause a folding of the response, as illustrated by Figure 1.4.

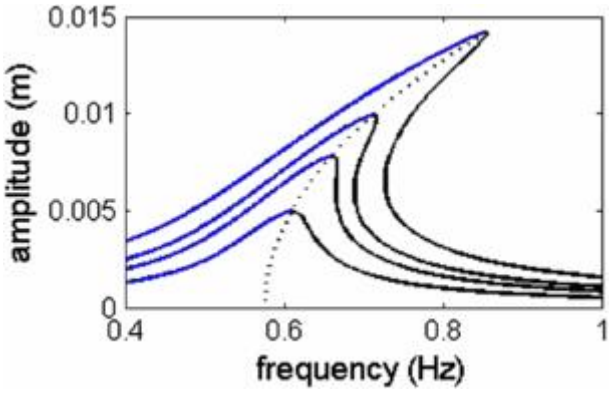

Figure 1.4: Electronic resonance response graph, showing folding of peak due to nonlinear effects as the amplitude is amplified by proximity to resonance. Note that frequency can be replaced by wavenumber for the atmospheric equivalent [from Donoso and Ladera (2012)].

As can be seen in Figure 1.4, the nonlinear folding leads to multiple solutions (in this example, for instance, at 0.8 Hz). Two of these solutions are stable, being the cases at the high and low amplitude response, and one solution is unstable, being the case between the two. This unstable solution will attempt to become stable by becoming one of the other solutions, giving rise to pitchfork or saddle-node bifurcations. Furthermore, the high-amplitude solution, despite being stable, may also experience period-doubling as a route to chaos.

Another influence of these two stable solutions on the atmosphere is the formation of distinct, stable circulation regimes, as explained by Charney and DeVore (1979), hereafter CDV. In simple, truncated models, topographical forcing can lead to the development of either a 'low index' flow or a 'high index' flow as alternative states, depending upon initial conditions. However, the existence of these states in fully continuous flows is still in question. The former state (also known as blocked flow) is defined by CDV as having "a strong wave component and a weaker zonal component locked close to linear resonance"; this locking is caused by the nonlinear interactions of the topography with the zonal flow. The latter state (also known as zonal flow) has "a weak wave component and a stronger zonal component much further from linear resonance". Both of these states are stable at the same location (sometimes also referred to as metastable or quasi-stable), giving rise to the concept of multiple equilibria. Transitions between the two states are forced by baroclinic instabilities of the topographic waves. The importance of blocking to the atmospheric circulation has been noted as early as Berggren, Bolin and Rossby (1949), who describe the synoptic-scale disturbances that affect both the local weather and the climate. Topography and blocking are inherently linked; for example Luo (2005) states that large-scale topography can act to lock a blocking flow to a single geographical position, hence creating a stationary wave. The extent to which this interaction occurs, and the conditions for it to do so, are amongst the main motivations for the study of blocking in the annulus. Li, Kung and Pfeffer (1992) also discuss the relationship between topographic resonance and blocking in the baroclinic annulus, as well as the relationship between annulus experiments and the atmosphere in general.

Topographic resonance has other major impacts on the atmosphere as well. One such impact concerns the origin of Low-Frequency Variability (alternatively Low-Frequency Vacillation, hereafter shortened to LFV). LFV is defined by Koo and Ghil (2002) as the variability of the atmosphere with a time scale longer than major weather phenomena (5-6 days) but shorter than seasonal variability (about 100 days). Naturally, this means that this intraseasonal variability is extremely important for weather predictions and forecasting. Koo and Ghil state that LFV is dominated by atmospheric zonal

flow vacillation, and that it is often caused by nonlinear interactions and transitions between multiple equilibria regimes, but the precise mechanism for its formation is still unresolved.

One example of LFV lies in the Northern Hemisphere extratropics – an intraseasonal (30-60 day) oscillation with an uncertain cause[4]. However, nonlinear barotropic vorticity models, both low-order (shown by CDV, amongst others) and high-order (Legras and Ghil (1985), hereafter LG, and Tribbia and Ghil (1990), for example), seem to suggest that the oscillation is due to an oscillating topographic instability associated with a resonance between a linear wave and the topography, as described by Pedlosky (1981). In their numerical channel model Jin and Ghil (1990) note that, from this resonance, Hopf bifurcations occur (a type of bifurcation wherein a limit cycle is formed from a stable focus in a continuous nonlinear system becoming unstable), causing stationary solutions in nonlinear systems to become asymptotically stable finite-amplitude oscillations. In other words, nonlinear behaviour near the resonance location, which should cause a slow drift for the stationary resonance wave due to a frequency shift, shows a nearly stationary wave undergoing slow amplitude vacillation. If the wave is strong and close to resonance, the period of the Hopf bifurcation is found to be 30-60 days, and thus is assumed to be the cause of this particular LFV. In addition, as forcing increases, such as in the studies of Feigenbaum (1979) and Lin, Busse and Ghil (1989), the wave amplitude grows larger and larger until a critical value where a period-doubling cascade is set up, which becomes a route to chaos. The importance of topography for periodic oscillations (rather than steady state solutions) is backed up by atmospheric angular momentum (AAM) data analysed by Dickey, Ghil and Marcus (1990) which shows that the 40-day oscillation in the Northern Hemisphere is strongest in the 26°N-44°N belt, where root-mean-square topography (associated with the wavenumber-2 structure of the Rockies and the Himalayas) is largest.

These previous studies are all based on numerical models, however, and so many of the conclusions given involving the mechanism of LFV's generation and its link to resonance are still unproven in more general contexts. Hence, this thesis' experiments with a topographic annulus will be

[4] Hoskins and Karoly (1981), amongst others, believed the oscillation to be due to Rossby wave propagation, whilst Simmons, Wallace and Branstator (1983) claimed it was created by unstable low frequency modes, and Ghil (1987) suggested that nonlinear interactions with topography were the origin.

conducted as to shed some light on what can occur in a real fluid flow. A deeper analysis of resonance and LFV will be explored in Chapter 2, along with a further examination into what aspects of the topic are still considered as open problems in the literature. Once again, finding solutions to these problems dictated the goals of the investigation into resonance, as well as the form of the experiments employed.

Another type of topography much less frequently discussed in the literature is that of 'thermal topography' – the concept of employing differential heating in the azimuthal direction, in addition to laterally-varying heating, as before. As mentioned by Risch (1999), it is an interesting question as to whether the azimuthally-varying heating can be thought of as a parallel to mechanical (i.e. non-thermal) topography, and whether there is a direct comparison to be found between the two. In this way, it remains to be determined which type of forcing has a greater impact on the general circulation, under given conditions[5]. In the annulus, thermal topography can be employed to emulate the differential heating caused by the thermal differences between land and sea. This effect is felt most strongly in the tropics, where the large-scale flow generated is known as the Walker Circulation. Due to its comparative weakness throughout most of the year, the Walker Circulation is not as well understood as more major atmospheric processes like the Hadley Cell, but Boubnov, Golitsyn and Senatorsky (1991) note that, during the winter, "the temperature contrast between continents and oceans is of the same order as the temperature difference between tropical and polar regions." The azimuthally-varying heating is also important for recreating the atmospheric circulations of other planets as well, such as Mars. Away from the poles and when global dust storms are not in effect, the Martian diabatic heating is dominated by radiative processes, with very little sensible and latent heating compared to Earth, as noted in Nayvelt, Gierasch and Cook (1997). Similarly, on Earth, topographic peaks do not extend outside of the atmosphere's background thermal structure, so the surface temperature of these peaks is the same as the temperature of the atmosphere at that height. On

[5] For a brief discussion of thermal versus topographic forcing on Eastern continental boundaries, see Kaspi and Schneider (2011).

the other hand, Webster (1977) states that Martian topography, due to having short radiative timescales, has uniform surface temperature, regardless of height. In this way the Martian surface topography can act as atmospheric heat sources at peaks and heat sinks at troughs, as well as functioning as mechanical topography.

As topography is so important to atmospheric circulation (with the above paragraphs only giving a few consequences of its impact), this thesis will take the form of an experimental investigation of topography with regards to the annulus. More impacts of topography will be discussed in Chapter 2, along with unresolved questions found from a review of the literature on the topic. It is the answers to these questions that determined the course of the topographic study, as well as the precise nature of the experiments to be carried out.

1.3 Thesis Aims and Objectives

In order to study topographic resonance, a differentially-heated annulus with topography gives a good opportunity to explore the robustness of the results found using numerical models, in a physical analogue of atmospheric circulation systems. To achieve this, the flow fields created over a range of parameters will be searched for evidence of linear resonance and nonlinear secondary effects such as Hopf bifurcations, period-doubling as a route to chaos, and oscillations with a similar timescale to LFV. Once discovered, the mechanism for generation of these effects, and thus the corresponding atmospheric phenomena, can then be explored.

Hence, part of the experimental investigation of this thesis will be a topographic study into resonant effects on the flow, especially with regards to a comparison between near-resonant flow structures and the non-resonant flow structures found elsewhere in parameter space. In addition, the results of experiments under topographic resonant conditions may also go some way to answering the open questions of the topic, such as the role topographic resonance plays in the atmospheric

circulation, the existence of multiple equilibria in the annulus and the mechanism of generation for LFV.

There are many ways to study blocking, especially when using numerical models, but within the annulus one of the best methods of investigation, in terms of both simplicity and versatility, is via partial barriers experiments. Partial barriers serve to block part of the flow (either radially or vertically), and allow comparison between blocked and unblocked flow. Partial barriers experiments should be quick and easy to set up, require only a minimum amount of topography, and offer straight-forward combination with other experiments. The physical structure of a partial barrier most resembles that of the margins of a continental shelf on the ocean basin - this will permit a comparison with oceanic topography.

As such, another set of this thesis' experiments will explore partial barriers in the annulus and will be employed to study both blocking and the effects of continental shelves on the ocean basin. In addition, a better characterisation of the blocking regime will also help with unresolved questions about multiple equilibria, as described previously, as well as possibly providing more information on topographic resonance in the annulus.

The concept of thermal topography is, as noted earlier, fairly uncommon in studies of the annulus. It is therefore hoped that this thesis' investigation may improve knowledge of this topic, by, for example, conducting experiments with azimuthally-varying heating in the same parameter space and layout as the non-thermal experiments discussed above. As well as a parallel to mechanical topography, azimuthally-varying heating also helps to create a "less-idealised" annulus, which takes account of the temperature differences both between the Equator and the poles and between the continental landmass and the ocean. Adaptations to the study of tidally-locked exoplanets are also possible, but are mostly outside the scope of this investigation, due to the numerous alterations that would have to be made to the annulus.

Thus, the remainder of the experiments of this thesis will investigate thermal topography, especially with regard to examining an analogue of the Walker Circulation and comparing results with the mechanical topography studies. The latter should allow context for those results, in turn permitting superior characterisation of topographically forced oscillations and perturbations.

In brief summary, the motivating questions that this thesis sets out to attempt to answer are as follows:

- Can topographic resonance and associated Hopf bifurcations be found in a differentially-heated annulus and, if so, under what conditions?
- If topographic resonance is found, what is its mechanism for generation?
- If topographic resonance is found under fully sinusoidal conditions, does it still occur with partially sinusoidal (i.e. isolated ridge) topography?
- Does blocking from partial barriers lead to the occurrence of multiple equilibria in the annulus?
- Does bottom-located azimuthally-varying heating have the same effect on the large-scale flow as mechanical topography?
- If so, how similar are mechanical and thermal topography, over the same parameter space?

1.4 Summary

The format that this report will take is as follows. Firstly, Chapter 2 will form a theory section and literature review of existing topographic studies, describing what unresolved questions about the effects of topography on the atmospheric circulation remain to be investigated, what laboratory work has already been carried out on the subject and how the current apparatus can be altered to investigate these effects. After that, Chapter 3 will be a detailed account of the experimental apparatus that this

project utilised, including the methodology that was employed and explanations of the experiments that were conducted. The chapter will also contain a short explanation of some of the key dimensionless numbers needed to describe the parameter space. Next, Chapters 4, 5, 6 and 7 will provide the results of the Extended-Regime experiments, the Resonance experiments, the Partial Barriers experiments and the Thermal Topography experiments, respectively. Each chapter will contain observations made, analysis of the results gathered, and a discussion of what is discovered. This will be followed by a summary of conclusions, Chapter 8, which will examine how successful the thesis has been at achieving the aims and objectives set out in the previous section, discuss the physical implications of the results gathered, and consolidate all the outstanding issues and possible further work from these studies for future investigation. Lastly, a list of the various references used to assemble this report will be given.

Chapter 2

Theory and Topographic Review

As described in Chapter 1, a major aspect of sloping convection and atmospheric circulation in general is that of topography. That being the case, this thesis will investigate several different impacts of topography on the atmospheric circulation, using a differentially heated annulus that will be described in Chapter 3. These impacts are resonance, blocking, and thermal topography, as discussed in the previous chapter. This chapter will therefore give a brief review of the topic, with an assessment of the various unresolved questions regarding these impacts of topography, found within a study of the relevant literature. Of these problems, the most interesting (and most applicable to the annulus) will be looked at in greater detail, forming an initial outline of the experiments to be carried out in this investigation.

2.1 Topographic Problems

Within the literature on the topic of topography there are several open questions that have yet to be resolved. In this section, several of the most pressing of these for each of the planned investigations will be studied, looking at the original papers that raised them, any further development in subsequent works, and how the questions could possibly be addressed through a series of experiments in a thermally-driven annulus.

2.1.1 Resonance

Whilst nearly any type of periodic forcing (thermal, topographic, etc) can cause resonance, this thesis will focus upon flows resonating with zonally-periodic topography. Topographic resonant effects, as found by CDV, may also be characterised by nonlinear interactions between the

topography itself and the main flow, often leading to oscillations and period-doubling. Wang and Redekopp (2001) also note the formation of long waves that propagate upstream from the topography.

In the last chapter it was mentioned how the folding of the resonant response caused by dominance of nonlinear interactions can lead to the high level amplitude solution experiencing period doubling via bifurcations. Another nonlinear interaction that can also arise from instability of the high level amplitude solution is for the forced wave component to lose energy to other modes, often via the creation of wave-triads - three distinct wave modes with a robust spatial phase relationship, as discussed by Früh and Read (1997). This relationship is such that, in the presence of quadratic nonlinearity, a fixed phase relation between forcing and response in space and time is maintained, conserving both total energy and potential vorticity within the triad. Bretherton (1964) defined the resonant wave-triad as occurring under two conditions: firstly, the summation or difference of the vectors of the three wave modes, i.e. their wavenumbers (zonal, radial and vertical), must be zero; secondly, the drifting frequencies of the three wave modes must also be self-interacting and have a summation or difference that equals zero, as below:

$$k_m = k_{m'} + k_{m''} \tag{2.1}$$

and

$$\omega_m = \omega_{m'} + \omega_{m''} \tag{2.2}$$

where m, m', and m'' are the three wave modes that make up the triad, k is the wavenumber of each mode and ω is the modal drift frequency of each mode determined by the Rossby wave dispersion relation. These are weakly nonlinear conditions, as it is assumed that the nonlinear forcing is a small perturbation to the linear system. Früh (1996) noted that Equation 2.2 implies that the nonlinear interaction timescale must therefore also be much smaller than the dispersion timescale of the flow. Früh and Read (1997) expanded the analysis, using a technique originated in Plumb (1977), to finite-amplitude flows, stating that, due to the wave amplitude altering the drift frequencies of the modes,

Equation 2.2 may only be satisfied irregularly by these time-dependent flows. In addition, integrating Equation 2.2 with respect to time[6] gives the following:

$$\varphi_m + \varphi_{m'} + \varphi_{m''} = const. \tag{2.3}$$

where φ is the phase of each mode. As such, the relative importance of a wave-triad to the dynamic evolution of the flow can be measured by how constant the summation or difference of the phases of the component wave modes remains over time. Important resonant wave-triads are often found to lead to the occurrence of oscillations and period-doubling, and have also been noted as one of the causes of the onset of turbulence, according to Rhines (1975) and Wordsworth (2008).

Recently, with climate change so significant an issue, Petoukhov et al (2012), amongst others, have blamed topographic resonant interactions for the severe weather events over the last few years, especially in North America. These weather events were tied to near-resonant flows in the midlatitude causing stationary waves, which had the effect of increasing the persistence and frequency of atmospheric blocked states. Relationships such as these have increased academic interest in the topic of resonance, especially in regards to its impact on the long-term atmospheric circulation and its relationship to persistent blocking events. In a similar way, the formation of quasi-stationary waves on Mars has also been linked, by Hollingworth and Barnes (1996), to near-resonant flows, which in turn leads to the triggering of global dust storms. Once again, the resonance of planetary waves and topography has been found to have a drastic effect on the global weather, regardless of the planet in question, further motivating studies of these linear and nonlinear resonance phenomena.

Low Frequency Variability

Amongst the pioneers of research into LFV were Madden and Julian (1971), who discovered a 41–53 day oscillation within long-term atmospheric velocity measurements. This Madden-Julian Oscillation, as it is now known, is a very robust phenomenon, and is centred in the mid-Pacific. Since

[6] Note that this also applies if Equation 2.1 is integrated with respect to the zonal coordinate x. This is the essence of why the triad of waves is known as 'resonant' in this case.

that work, several other intraseasonal oscillations have been discovered - some tropical, like that of Lau and Chan (1985), and others extratropical, such as in LG, which was mentioned in the last chapter. Keppenne et al (2000) suggest that the latter type of oscillations are the most important in terms of determining the overall intraseasonal variability of the Northern Hemisphere, both due to their own effects and via interactions with the other major oscillations, such as the Madden-Julian Oscillation. Keppenne et al characterise LG's 36-40 day extratropical oscillation as a topographically-locked zonal wavenumber-2 flow, which is strongest in the winter, and undergoes what is known as 'tilted-trough vacillation'. This type of vacillation was described in Pfeffer and Chiang (1967) as a periodic transformation whereby the baroclinic waves generated start out with a standard, commonly-found structure, like in the non-chaotic parts of Figure 1.3, but then tilt in one direction (prograde or retrograde), return to the original standard state, and then tilt in the other direction before repeating the sequence. An example of a drifting wavenumber-5 flow undergoing 'tilted-trough vacillation' is shown in Figure 2.1.

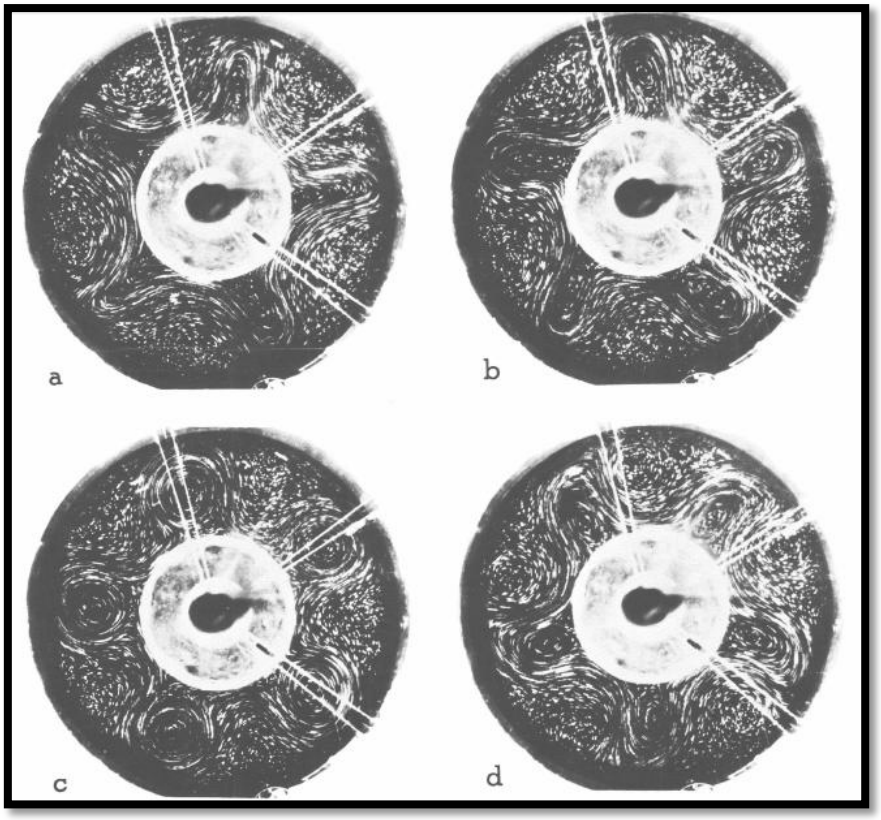

Figure 2.1: 'Tilted-trough' vacillation sequence in a counter-clockwise flow, with untilted waves (a) and (c), prograde tilted waves (b) and retrograde tilted waves (d) [from Pfeffer and Chiang (1967)].

Tian et al (2001), amongst others, demonstrated that oscillations with LFV periods are possible in the annulus, finding examples with dominant periods of 6-25 rotations, the annuli equivalent to days. Li, Kung and Pfeffer (1992) also found evidence of a topographically resonant oscillation under baroclinic forcing, which they claimed to be a parallel to atmospheric intraseasonal oscillations. In addition, numerical models have found multiple instances of resonant wave-triads, many tied to LFV. Luo (1994) found both a triad of Rossby waves for zonal wavenumbers 1-3, and a four-wave interaction between Rossby waves for zonal wavenumbers 1-4, both with oscillation periods of 30-60 days. Furthermore, Ghil et al (2003) reviewed in detail the link between intraseasonal oscillations and resonant topographic instability, leading to a bifurcation sequence, as mentioned in the last chapter. Ghil et al describe what is currently known about the relationship, and also what still remains to be uncovered. This resonant topographic instability will be discussed in the next section.

Mechanism for Impact upon the Circulation

Whilst searching for the mechanism of generation for persistent blocked states, CDV were amongst the first to discover evidence for topographic instability. This instability was associated with resonance between the topography and a zonal flow, which in turn led to nonlinear interactions that kept the flow locked to a near-resonant state. Later, LG described another area of topographic resonance at a much lower zonal flow, with similar impacts on the circulation. In numerical models, Hopf bifurcations can occur from both resonances, as described in the last chapter. Jin and Ghil (1990) set out to analyse this behaviour, using a numerical barotropic beta-plane channel with a simple topography, as shown in Figure 2.2. First of all, the authors determined that CDV resonance would require an unreasonably high atmospheric flow rate for Earth: for an example with a channel of 5000 km in width and with a zonal wavenumber of 2, it was calculated that CDV resonance would require a zonal flow speed of 100 ms^{-1}, whilst LG resonance would only need 23 ms^{-1}. This is due to the Rossby wave dispersion relation, wherein the phase speed of the wave decreases with larger total

wavenumber. Hence, since CDV resonance has a meridional wavenumber of $l = 1$ and LG resonance has a meridional wavenumber of $l = 2$, the latter has a more attainable flow velocity. It was also discovered that nonlinear wave-wave interactions are much stronger for LG resonance than CDV, once again suggesting that the former is a more realistic cause for atmospheric oscillations, and explaining why LG resonant bifurcation is much more complex than for CDV. Under LG resonance, blocking in the flow is stronger, more localised and with a meridional shift upstream of topography, and weaker downstream. Finally, third order analysis notes that the time-scale of the evolution of the previously mentioned amplitude vacillation contains terms in wave-wave, wave-zonal flow and topographic interactions.

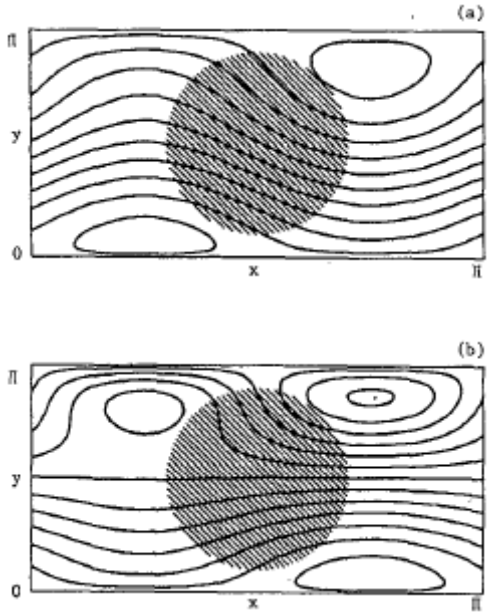

Figure 2.2: Plan view of periodic channel model with boundaries at $y = 0$ and $y = \pi$, showing the central topographic peak (shaded) and streamlines of flow at (a) CDV resonance conditions and (b) LG resonant conditions [from Jin and Ghil (1990)].

Furthermore, if wave-zonal flow effects are ignored, Jin and Ghil (1990) found that form-drag alone leads only to stable equilibria, and that wave-wave interactions must also be present to create a finite-amplitude periodic solution, via a supercritical Hopf bifurcation. This is in contradiction to CDV and Pedlosky (1981), as neither took into account wave-wave effects in their studies. It was found that, if the wave is strong and close to resonance, the period of the Hopf bifurcation will be 30-

60 days. If wave-zonal flow interactions are not ignored, then this leads to a second Hopf bifurcation of 30-60 days independent of wave-wave interactions (but not independent of form-drag, unless it is replaced by other forcing). Due to the fact that the meridional momentum transport of the forced wave often results in the zonal jet shifting its location, this second Hopf bifurcation is known as a jet-shifting bifurcation. This is known to also occur in the real atmosphere, during the Northern Hemisphere Winter, according to Namias (1950). If both wave-wave and wave-zonal flow interactions are present, then the location of the bifurcations in phase space will alter and higher-order resonances may arise, but the basic features of the oscillation will remain the same. Both types of bifurcation give rise to a low frequency oscillation that is determined by the amplitude of the topographic-forced wave and by the zonal flow structure.

If topography is replaced by a different zonally asymmetric vorticity forcing, such as due to differential heating (azimuthally-varying heating in the annulus), the lack of form-drag causes the wave-wave Hopf bifurcation not to appear, though the wave-zonal flow Hopf bifurcation will still be present. Jin and Ghil (1990) note that it is impossible to tell the difference between these two interactions in their barotropic model, but suggest that a baroclinic experiment would be able to do so, due to the wave-zonal flow bifurcation alone leading to jet-shifting. This will be investigated as part of the baroclinic Thermal Topography experiment within this thesis.

Jin and Ghil's (1990) stated objective of finding the mechanism of generation for low-frequency oscillations in the extratropics appears to have been successful, determining that form-drag, wave-zonal flow and wave-wave interactions are all important, and that there are two separate Hopf bifurcations that lead as a period-doubling route to chaos. The results found do not entirely agree with GCM results (such as in Ghil and Mo (1991) or Marcus et al (1990), for example), but do agree well with other high-resolution nonlinear barotropic models (such as Tribbia and Ghil (1990), amongst others), implying that it may be that these discrepancies are caused by the lack of baroclinic instability or asymmetrical thermal forcing of these models. As such, a baroclinic study would be the next logical step to continue this research.

Stratospheric Sudden Warmings

A further phenomenon of the atmospheric circulation is that of stratospheric sudden warmings. Matsuno (1971) describes these events as being an amalgamation of lesser phenomena, including the displacement or collapse of the stratospheric polar vortex and an increase in temperature of the polar air, the latter of which leads to the reversal of the meridional temperature gradient. Unsurprisingly, this has a major impact on the Southern Hemisphere's atmospheric circulation. Stratospheric sudden warmings have strong links to blocking, with papers such as Martius, Polvani and Davies (2009) noting that blocking events in the troposphere often occur before the vortex collapses and always occur before it displaces, but relationships with topographic forcing have also been found. For example, Tung and Lindzen (1979) conclude that the warmings are caused by stationary waves that are resonant with the topography and land-sea temperature difference. This resonant oscillation was suggested to be what generates the unusual time-amplification of the waves, and thus the irregularity of the events. Similarly, Smith (1989) and Esler, Polvani and Scott (2006) both discuss the impact of resonance on the anomalously large stratospheric sudden warmings of the 1979 and 2002 winters, respectively.

As the events occur on the same timescale as seasonal variations, Risch (1999) suggested that slowly changing the temperature difference of an annulus over long periods (i.e. hundreds of rotations) could mimic these seasonal variations, thus leading to a study of stratospheric sudden warmings. This would be especially effective with a topographic base similar to that of the Southern Hemisphere, namely a wavenumber-1 structure. Additionally, improving a laboratory study so that it more closely resembles the long-term atmospheric circulation would benefit the validity of the results gathered, removing a simplification from the atmospheric replication.

2.1.2 Blocking

From the literature, one of the chief areas of interests regarding topography is that of blocking. Egger (1978) described blocking as arising from the nonlinear interactions of slowly drifting free waves and stationary waves caused by "geographic fixed" forcing, such as topographic ridges. Figure 2.3 shows a comparison between the zonal and blocked regimes, showing wavenumber-2 zonal flow being blocked to resemble a wavenumber-4 structure.

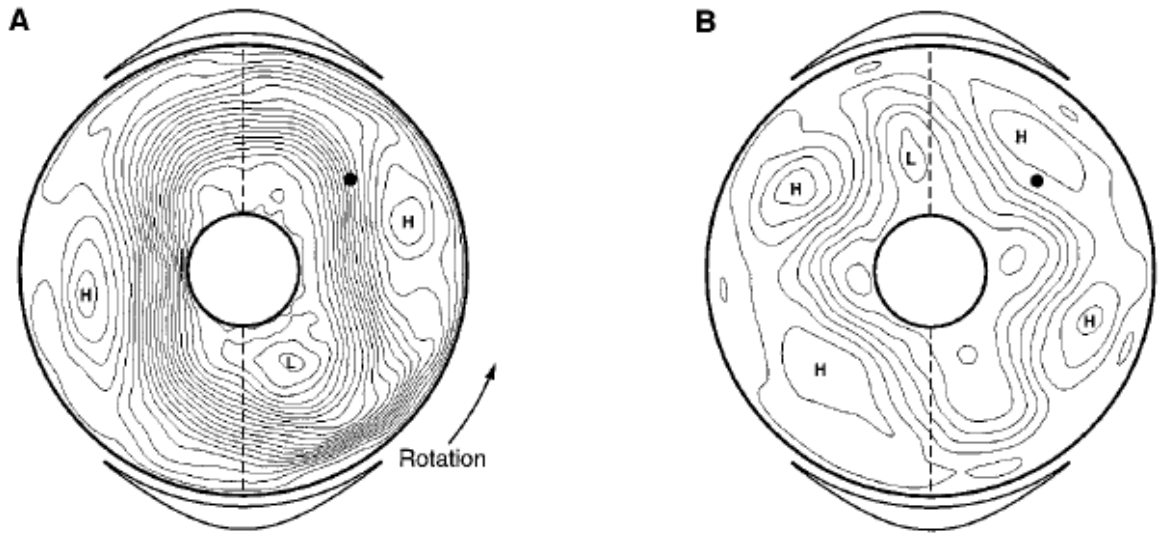

Figure 2.3: Time-averaged streamfunctions illustrating zonal (A) and blocked (B) flow. 'H' denotes streamline maxima and 'L' denotes streamline minima [from Weeks et al (1997)].

Figure 2.3 comes from Weeks et al's (1997) experiments, which served to contrast the annulus to the real atmosphere. As shown in Figure 2.4, the two are very similar, although the real atmosphere exhibits a lot more noise, due to the annulus' simplifications.

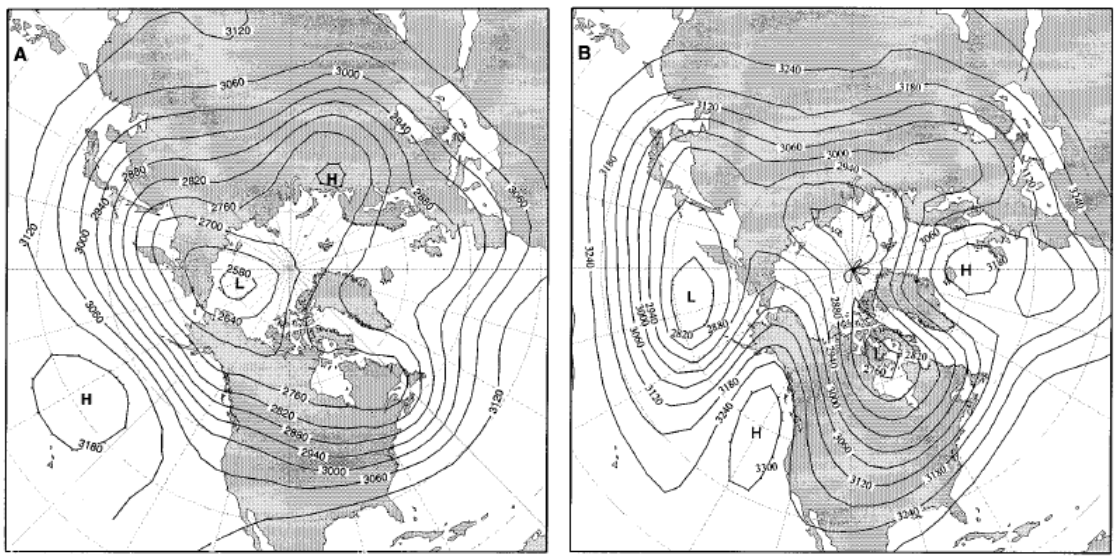

Figure 2.4: Contour plots of the height in metres of the 700-hPa surface of the Northern Hemisphere, illustrating zonal (A) and blocked (B) flow. 'H' denotes contour maxima and 'L' denotes contour minima [from Weeks et al (1997)].

As well as this change in structure, the blocked regime was also found to be defined by reduced jet intensity but larger wave amplitude, along with a noticeable increase in the strength of anticyclonic eddies when compared to the zonal regime. These anticyclonic eddies are the maxima ('H') in both Figure 2.3 and Figure 2.4. The increased persistence and frequency of blocked states, linked to both greenhouse gases and climate change, has been suggested by Woollings (2010) to be an explanation of recent severe weather events, especially in Europe.

Links to Other Processes

Blocking, due to its complex and wide-ranging impacts on the atmospheric circulation, is also sometimes put forward for the explanations of other phenomena, such as Risch's (1999) rogue 'wave-lobe'. In that study, a strange occurrence was found whereby, for low Taylor Number and medium Thermal Rossby Number (both defined in Chapter 3) flows, a wavenumber-3 stationary wave was found to grow an asymmetric fourth 'wave-lobe' (defined as a small cyclonic eddy attached to the main flow's jet) at low levels, but not at high levels. This was suggested to be an example of a

blocking phenomenon due to its resemblance to similar results from the experiments of Weeks et al (1997).

As well as blocking, this discovered rogue ‘wave-lobe’ also bears some similarity to the bifurcations caused by topographic resonance, so spatial period-doubling may be a cause. If these results can be replicated, then it might be possible to link the impacts of topographic resonance to that of blocking. This idea is backed up by the findings of Yang, Reinhold and Källén (1997), who employed a spherical model with an isolated topographic ridge, itself a type of partial barriers experiment. The authors concluded that baroclinic disturbances in their model create “the potential for resonance”, by favouring zonal wave propagation over meridional wave propagation.

In a related way, Weeks et al (1997) note that blocked events (“persistent blocking anomalies”) happen on a timescale of 10-100 days, the same as that of LFV. This implies that transitions between the blocked state and the zonal state are likely to be the cause of LFV in the atmosphere. Blocking, multiple equilibria, LFV and resonance are therefore all strongly interrelated. This being the case, the results of the Resonance experiments and the Partial Barriers experiments will be examined closely for similarities and parallels.

Multiple Equilibria

Possibly the foremost question about blocking found in the literature is the issue of the existence of multiple equilibria. Most notably, CDV, Charney and Straus (1980) and Reinhold and Pierrehumbert (1982) suggested the idea that both the blocked and zonal regimes were stable at the same location, as alternative states that the system could 'choose' to exhibit, depending on the initial conditions. Changing parameters can then lead to bifurcations in which the flow vacillates between the two states, and that these transitions cause most of the atmospheric anomalies that are observed.

On the other hand, Tung and Rosenthal (1985) and Cehelsky and Tung (1987) claimed that multiple equilibria are physically possible, but cannot exist in the real atmosphere. They suggested that previous results of multiple equilibria were caused by unrealistic topography or, in the case of Charney, Shukla and Mo (1981) where the topography used was deemed to be sufficiently 'realistic' (illustrated in Figure 2.5), overly-truncated reproductions of nonlinear interactions. In their models, asserted to be better analogies to the atmosphere, no multiple equilibria are found and the regimes are solitary. The flaw of these papers is that no definition of what is meant by 'realistic' topography is given. Sometimes it appears they are suggesting that the amplitude of the topography in previous studies was overly high, but that of Charney, Shukla and Mo (1981) is similar in scale to that of CDV. As such, it will be assumed that by 'realistic' they mean a complex topography closer to the distribution of mountains on Earth.

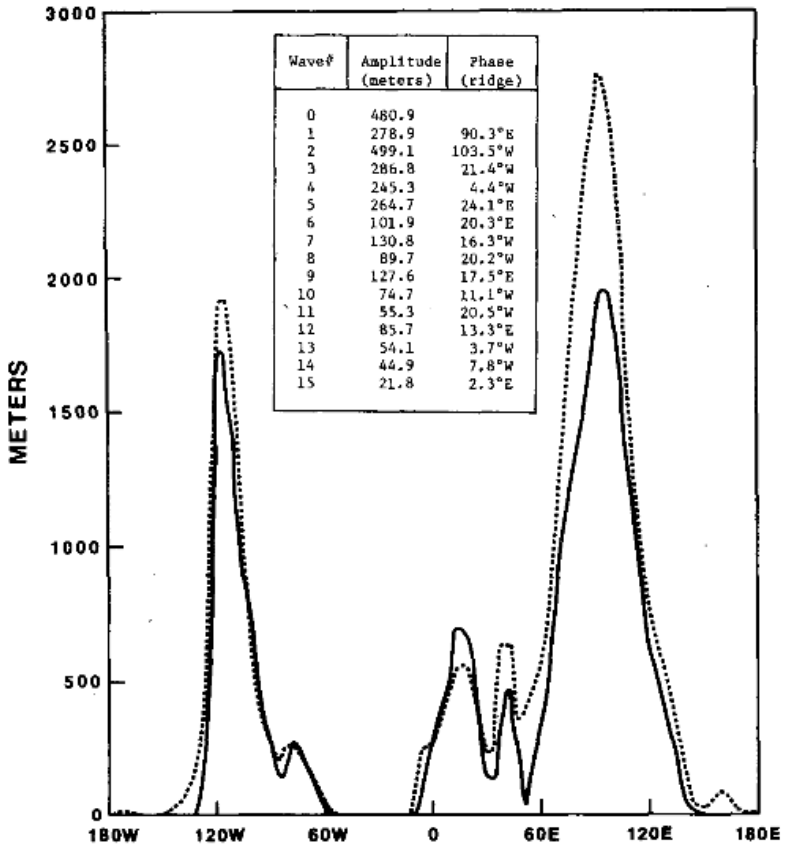

Figure 2.5: 'Realistic' topography, dotted line created from actual topographic measurements [from Charney, Shukla and Mo (1981)].

These papers were in turn rebuffed by Molteni (1996) using high-resolution hemispheric models and employing simple wavenumber-3 topography. Contrary to Tung and Rosenthal (1985) and Cehelsky and Tung (1987), two distinct flow regimes were found, even when a large enough number of degrees of freedom were used to simulate the full range of nonlinear interactions. However, since this was purely a numerical study, it could be argued that the existence of multiple equilibria has only been shown to be possible with a model, not a real fluid.

Furthermore, Risch (1999) claimed to find laboratory evidence for multiple equilibria in a thermally-forced annulus for both with and without topography. The topography used was a simple wavenumber-2 shape, suggesting that (like in Molteni (1996), above) low-order models that found multiple equilibria with similar topography were not merely seeing a false positive due to their 'overly-truncated nonlinear interactions', as alleged by Tung and Rosenthal (1985) and Cehelsky and Tung (1987). By extension, Risch notes that this implies that multiple equilibria should also be possible in the baroclinic atmosphere. The author does admit that the results taken were merely qualitative in nature, however, and suggests that similar experiments should be carried out with quantitative analyses, such as Fourier decomposition.

Supporting the other side of the argument, Tian et al (2001)[7] compared similar numerical and laboratory annulus studies, finding stable multiple equilibria to be prevalent in the former, but not to exist at all in the latter. The physical annulus still produced both zonal and blocked regimes, but they were found to be meta-stable, occurring with sudden and irregular transitions. The lack of genuine and robust multiple equilibria could be due to the fact that the annulus in question was barotropic. Instead of setting up convection via a temperature difference, Tian et al's barotropic annulus created a flow by pumping fluid through several concentric rings of holes that lay between the topographic peaks and troughs, as shown in Figure 2.6. This has the effect of removing any vertical variation in the flow structure and is employed when horizontal thermal gradients and thermal wind shears are assumed to be negligible. Naturally, this removes complexity from the model, allowing other, simpler,

[7] This paper appears to change the meaning of 'meta-stable' from '*can* transition from one regime to another', to '*will* transition between the regimes'. Hence, the 'meta-stable' states in CDV, that allow multiple equilibria, are re-classified as 'stable' by Tian et al (2001).

phenomena to be more easily observed. However, it not known whether multiple equilibria is one of these "simple phenomena", and so a laboratory study using a baroclinic annulus would provide more reliable evidence - either for the existence of multiple equilibria, or against it.

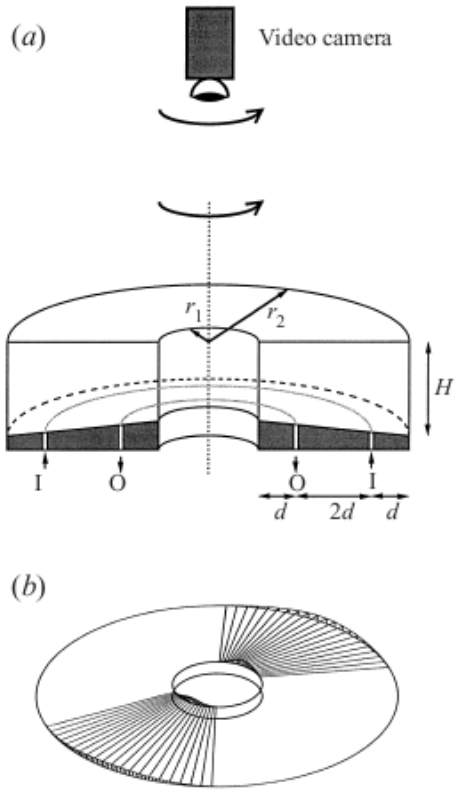

Figure 2.6: Barotropic annulus with sloping base: a.) typical laboratory arrangement, b.) concentric rings of holes in base for pumping in of fluid [from Tian et al (2001)].

In conclusion, the existence of multiple equilibria is still amongst the biggest unresolved questions in the topic of blocking, even if it is not as controversial a topic as it once was in the period after Tung and Rosenthal (1985) and Cehelsky and Tung (1987) published their papers. However, the most immediate aspect of this issue is how best to create a topography for an annulus that can be defined as 'realistic'. Taking the idea of an improved topographic distribution was brought to its logical conclusion in Boyer and Chen (1987), where one mountain range in particular, in this case the Rocky Mountains, was modelled in great detail for a laboratory experiment. Conversely, however, this paper was criticised for bringing *too much* complexity to such a simple simulation of the atmosphere. James (1988), for example, noted that having such a detailed topography was of dubious

worth when the walls of the annulus will produce reflection patterns that simply do not exist in the flow over the Rocky Mountains. From this, the lesson learnt is that less-idealised topography should not be a hyper-realistic reproduction of a planet's surface, in order to reflect the limitations of the physical annulus model.

In an annulus, though the direct geometric and dynamical similarity with the atmosphere is limited and imperfect, the nonlinear interactions will arguably not be truncated, giving a perfectly 'realistic' flow in a number of important respects. This provides a definite advantage over numerical models, regardless of complexity. As such, it appears that the best solution would be to both employ a baroclinic annulus, thus testing Tian et al's (2001) barotropic results, and use quantitative analyses, thus verifying and extending the qualitative findings of Risch (1999). Combining this with the fully nonlinear interactions of a physical annulus, a definitive investigation into the existence of multiple equilibria could be launched, putting to the test the conditions of Tung and Rosenthal (1985) and Cehelsky and Tung (1987).

Oceanic Comparison to the Atmosphere

It should be noted that, since the focus of this thesis is seeking to understand the interactions of topography with the atmospheric circulation, the majority of the literature examined is based on the dynamics of the atmosphere. The oceans experience topography as well, however, and there is plenty of scope for comparison between the two. One of the major differences is the forcing of the flow: atmospheric circulations, like all those mentioned above, are thermally-driven; oceanic circulation systems, like those studied in the work of Völker (1999) who simulated the Antarctic Circumpolar Circulation, are driven by a combination of surface wind stress and thermohaline buoyancy forces. Without that distinction, the latter's study is difficult to distinguish from a standard atmospheric study, employing a baroclinic quasi-geostrophic channel model.

This being the case, it forms an interesting study to compare the oceans and the atmosphere within the annulus. This can be achieved by creating simple ocean-like topography, like the ocean basin experiments of Wordsworth (2008) shown in Figure 2.7, in which the vertical walls used blocked the entire depth of the fluid, representing a continental shelf.

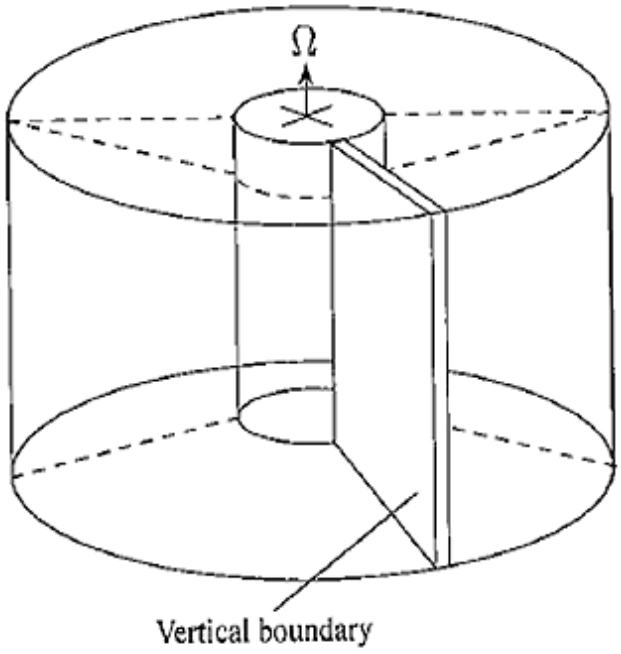

Figure 2.7: Ocean basin experimental arrangement [from Wordsworth (2008)].

Employing both a sloping lid and a sloping base, Wordsworth (2008) encountered a quasi-barotropic jet, despite the obstruction to the circulation, which gained in strength as it flowed towards the upstream of the barrier, and ending with a large persistent azimuthally-trapped gyre. Figure 2.8 gives two examples of this result. The author noted that this trapped flow structure was an equivalent to the western boundary currents of oceanic flows, similar to the observations of Rayer, Johnson and Hide (1998). Since both of those studies found trapped waves independent of height throughout all the obstructed circulation, it is likely that the current experiments with partial barriers will also encounter these azimuthally-trapped waves at the bottom of the tank, if not everywhere. As mentioned in the last chapter, the flow around continental shelves is of great interest in the literature, with these trapped waves and boundary currents being amongst the most prominent effects, as discussed and reviewed in

Huthnance (1989). In addition, Martínez and Allen (2004) note that "the contribution of remotely forced CTWs [coastal trapped waves] in the Gulf of California to the total kinetic energy is comparable to that produced by the wind." Hence, for purposes of comparison, the partial barriers study should allow examination of the relative importance of the trapped wave to the general circulation in an only partially blocked fluid flow.

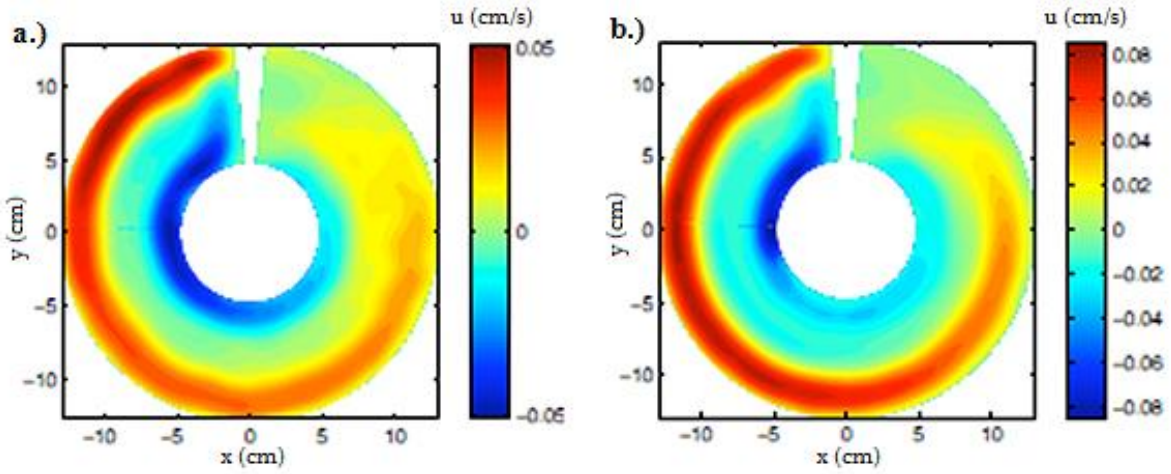

Figure 2.8: Ocean basin time-averaged zonal velocity at mid-depth, with a rotation rate of 1.3rads^{-1} and a temperature gradient of 2K for (a) and 4K for (b) [adapted from Wordsworth (2008)].

2.1.3 Thermal

As mentioned in the last chapter, thermal topography is a fairly recent topic, with few major investigations carried out upon it. This is beginning to improve, however, with additional interest generated by questions concerning the possible origins of current 'extreme weather' conditions associated with climate change. Studies such as Francis and Vavrus (2012) and Liu et al (2012) conclude that a reduction in Arctic sea-ice from global warming has led to significant changes to atmospheric circulation. Francis and Vavrus suggest that the smaller land-sea temperature difference has caused a slower eastward progression of Rossby waves due to weakened zonal winds, and increased wave amplitude. Liu et al note this link to the impacts of blocking, and thus propose that the lack of sea-ice causes more frequent blocked states, in turn leading to cold surges and "recent cold and snowy winters".

The similarities between thermal forcing and topographic forcing, and in particular their generation of stationary baroclinic Rossby waves, were looked at by Holton (1992) and Pedlosky (1987). Notably, both forcings were found to be able to produce both trapped waves and strongly vertically propagating waves, depending on the vertical wavenumber. Mathematically, however, thermal forcing was suggested to have no capability for linear resonance, due to a lack of wavenumber terms in the denominator of its solution (see Equation 1.7 for the topographic case solution). As such, in order to investigate this, it would be worthwhile to examine whether resonant flows and phenomena can be found to occur in a real fluid, such as within the annulus.

As well as land-sea temperature differences, thermal topography can also arise from geothermal or volcanic action. For example, Mashayek et al (2013), via observations and numerical simulations, found that the impact of geothermal heat flux at the ocean bottom is a reduction of stratification throughout the abyssal layer, resulting in a strengthening of the circulation. The authors argue that geothermal heat flux is therefore a vital component for inclusion into oceanic modelling. To examine whether the heating elements of the thermal experiments can replicate this effect, and thus geothermal heat flux in general, signs of vertical-uniformity will be searched for, especially in comparison to the studies without azimuthally-varying heating. Once again, this also will allow the current investigation to extend its focus to oceanic flows, as well as atmospheric circulations.

Annuli with Azimuthally-Varying Heating

Risch (1999) posed a question on the relative importance of the effects of thermal forcing against the effects of topographic forcing on the occurrence of stationary waves, but ultimately decided that such a study would be too ambitious for a standard annulus. However, non-standard annuli have been employed to study azimuthally-varying heating. For example, Boubnov, Golitsyn and Senatorsky (1991) utilised an annulus with four discrete outer cylinders, as opposed to a single continuous one, as shown in Figure 2.9.

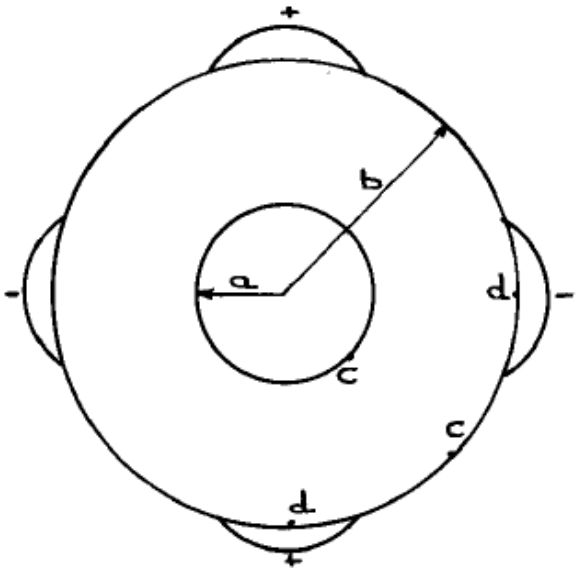

Figure 2.9: Plan view of annulus with azimuthally-varying heating created by two heated outer cylinders (denoted by +) and two cooled outer cylinders (denoted by –) [from Boubnov, Golitsyn and Senatorsky (1991)].

As Figure 2.9 shows, electric wire heaters at the '+' cylinders and cooled water at the '–' cylinders allowed for a controllable azimuthally-varying heating system to be set up in a wavenumber-2 pattern. Not only were baroclinic waves encountered, but the results of the investigation demonstrated drifting waves that interacted with the heaters as they moved past them and stationary waves that occurred along with a reduction in zonal flow, suggesting an appearance of blocking effects. These two findings imply a similarity between thermal and mechanical topography, as the flow reacts in a manner that would be expected with a wavenumber-2 topographic variation at the lower boundary.

Walker Circulation

It was Bjerknes (1969) that first named the Walker Circulation, after noting anomalies in the tropical sea-surface temperatures and equatorial upwelling. The author also discovered that the strength of the circulation was dependent on those sea-surface temperatures, being stronger when the temperatures were lower and weaker when they were higher. Since it is caused by differences

between these temperatures and those of the land in the tropics, the circulation is also closely linked with the El Niño Southern Oscillation (hereafter ENSO). The ENSO is a chaotic oscillation with a timescale on the order of 3-6 years, defined by Philander (1985) as periods of warming (El Niño) and cooling (La Niña) of the Pacific tropics. Whilst the baroclinic annulus more strongly resembles the atmospheric circulation of the mid-latitudes than the tropics, effects of the Walker Circulation can be found outside of the tropics, as discussed by Shulmeister (1999). Furthermore, Meehl (1994), amongst others, linked these mid-latitude land-sea temperature differences to monsoon formation.

Despite there currently not being any notable studies carried out of the Walker Circulation in the annulus, Power and Smith (2007) claimed that "the Walker Circulation is one of the world's most prominent and important atmospheric systems and is closely linked to the mean-state of the equatorial Pacific Ocean". Power and Smith, amongst others, noted that the observed weakening of the Walker circulation, blamed on global warming reducing the land-sea temperature difference, is happening at the same time as a domination of the Southern Hemisphere by the ENSO. With the Walker Circulation and the previously discussed Arctic sea-ice problem both being strongly related to concerns about climate change, the issue of thermal topography is becoming increasingly important. In their review on the topic, Julian and Chervin (1978) stated that "atmospheric response to increased ocean surface temperatures occurs westward of the largest temperature increases, and the subtropical jet stream north of the prescribed change is significantly affected." As such, in the annulus, it would be expected that impacts upon any baroclinic waves or jets formed will be most notable downstream of the thermal topography. This appears to be a similarity to the effects of mechanical topography, comparable to a wake created downstream of mountainous peaks.

Extensions to Other Planets

As mentioned previously, thermal topography also has links to the Martian atmospheric circulation, with Nayvelt, Gierasch and Cook (1997) noting that Martian mountains can act as heat sources (at the peaks) and sinks (at the troughs), as well as obstructions to the flow. Due to this effect,

Mars and Earth have different linear stationary responses, with the former experiencing "global, low wavenumber responses". This has been backed up both by the numerical studies of Webster (1977) and Hollingsworth and Barnes (1995), and by observations, such as from Banfield et al. (1996), finding low wavenumber (wavenumber-1 and wavenumber-2 in the observations) disturbances across the global scale. These disturbances have been linked to the formation of robust stationary eddies (and hence, global dust storms, as discussed earlier) in the Martian atmosphere, especially in the Northern Hemisphere. Nayvelt, Gierasch and Cook also noted that the inclusion of stationary eddies to the zonal mean winds in their Martian linear model caused a dramatic improvement to the large-scale atmospheric reproduction. These effects are suggested to be due to the Martian surface acting as both topographic and thermal forcing, so, in the Thermal Topography experiments, it can be examined how much the latter contributes towards the generation of stationary waves and low wavenumber flows, especially in comparison to the topographic forcing of the Partial Barriers study.

Adaptations to the study of tidally-locked exoplanets, such as those discussed by Cho et al (2008), are also possible, due to the fact that the majority of solar heating occurs only on one side of the planet. This could be replicated by changing the lateral heating profile to only act as a source on the outer wall nearest the bottom heating elements, but these experiments are outside the scope of this study, due to the numerous alterations that would have to be made to the annulus. Alternatively, a more simplified reproduction could be observed in the case where the heat influx from the heating elements is large compared with the lateral heating profile. Under these conditions, Cho et al's results would suggest that the circulation will be somewhat Earth-like, including features such as polar vortices, rather than Jupiter-like, despite the large sizes of the exoplanets investigated. As such, this once again implies that the Thermal Topography experiments will produce similar flow structures to the experiments employing mechanical topography, instead of forming multiple Jupiter-like jets.

Chapter 3

Experimental Arrangement

This chapter will first give an explanation of the apparatus available for this project's investigation, divided into the experimental equipment itself and all the hardware and software needed to actually generate results. After that, the next section will detail the process of how everything was assembled, especially in terms of how the apparatus was rebuilt and modernised between experiments, and the final section will describe how the equipment was employed to achieve meaningful solutions to the problems posed in the previous chapter. Details of the topography specially designed for this project will also be discussed. First of all, however, a brief introduction to some of the more relevant dimensionless numbers will be provided, in order to give context to the parameter space under investigation.

3.1 Non-dimensional Numbers

Whilst the flow of the atmospheric circulation is extremely complicated, for typical annuli experiments (and computational annulus models) the entire system can be reduced to two dimensionless numbers fully describing parameter space. Firstly, the Taylor Number is defined as:

$$\mathcal{T} = \left(\frac{f \cdot L^2}{\nu}\right)^2 \tag{3.1}$$

where L is a characteristic length scale and ν is the kinematic viscosity. The Coriolis Parameter, f, also known as the Coriolis Frequency, describes the effect of the planetary rotation (Ω) depending on latitude (φ). If this latitude variation is ignored, as in an annulus with a flat lid, the Coriolis Parameter is found using the equation:

$$f = 2\Omega \tag{3.2}$$

For an annulus experiment, the Taylor Number can therefore be adapted[8] to the form:

$$\mathcal{T} = \frac{4\Omega^2(b-a)^5}{\nu^2 \cdot d} \tag{3.3}$$

where a is the inner radius, b is the outer radius and d is the height of the annulus and Ω is now the rate of rotation of the annulus. Roughly, the Taylor Number gives the squared ratio of the Coriolis forces (the numerator) to the viscous forces (the denominator) acting upon a fluid. A large value implies a less stable flow, with circulation tending toward higher dominant wavenumbers and the irregular regime. In this way, the Taylor Number can be thought of as a rotational Reynolds Number, as discussed by Hide and Mason (1975).

Secondly, the Rossby Number is defined as:

$$\Theta = \frac{U}{f \cdot L} \tag{3.4}$$

where U is the characteristic velocity scale of the fluid. For an annulus experiment, this can be adapted[9] into the Hide Number (sometimes also known as the Thermal Rossby Number[10]) which takes the form:

$$\Theta_T = \frac{\alpha \cdot g \cdot d \cdot \Delta T}{\Omega^2(b-a)^2} \tag{3.5}$$

where α is the thermal expansion coefficient, g is the gravitational acceleration and ΔT is the temperature difference. Roughly, the Hide Number gives the ratio of the inertial forces (the numerator) to the Coriolis forces (the denominator) acting upon a fluid. At large values the quasi-geostrophic approximation begins to break down, leading Houghton (2002) to refer to the Hide Number as a "measure of the validity of the geostrophic approximation".

[8] As described in Fowlis and Hide (1965), wherein the origin of the $(b-a)^5/_d$ term is also explained.
[9] A full derivation can be found in Holton (1992), for example.
[10] Notably in Hide (1958), but also in more modern works, such as Risch (1999), amongst others.

As most of the quantities are assumed (or fixed) to be constant, the Taylor Number can be simplified to being proportional to Ω^2, and the Hide Number can be simplified to being proportional to $\frac{\Delta T}{\Omega^2}$. For an annulus experiment (or similar) the rotation rate and the temperature difference are the main sources of control, hence these two dimensionless numbers can be taken to fully describe the parameter space within which the experiments take place, as noted by Hide and Mason (1975) in their pioneering study of the annulus.

3.2 Equipment Description

Accounts of the experimental arrangement in question can be found in the theses of two of its previous users - Risch (1999), who used the turntable and heating systems (but not the same annulus), and Wordsworth (2008), who used the current rig in its entirety. The latter is therefore more helpful, not least due to it being more recent, and thus the electronics are more up-to-date. Wordsworth also made several changes to the annulus, replacing the O-ring seals and decreasing the radius of the inner cylinder to permit higher Taylor Numbers to be reached. Figure 3.1 provides two labelled photographs of the annulus, illustrating the apparatus described in this chapter.

a.)

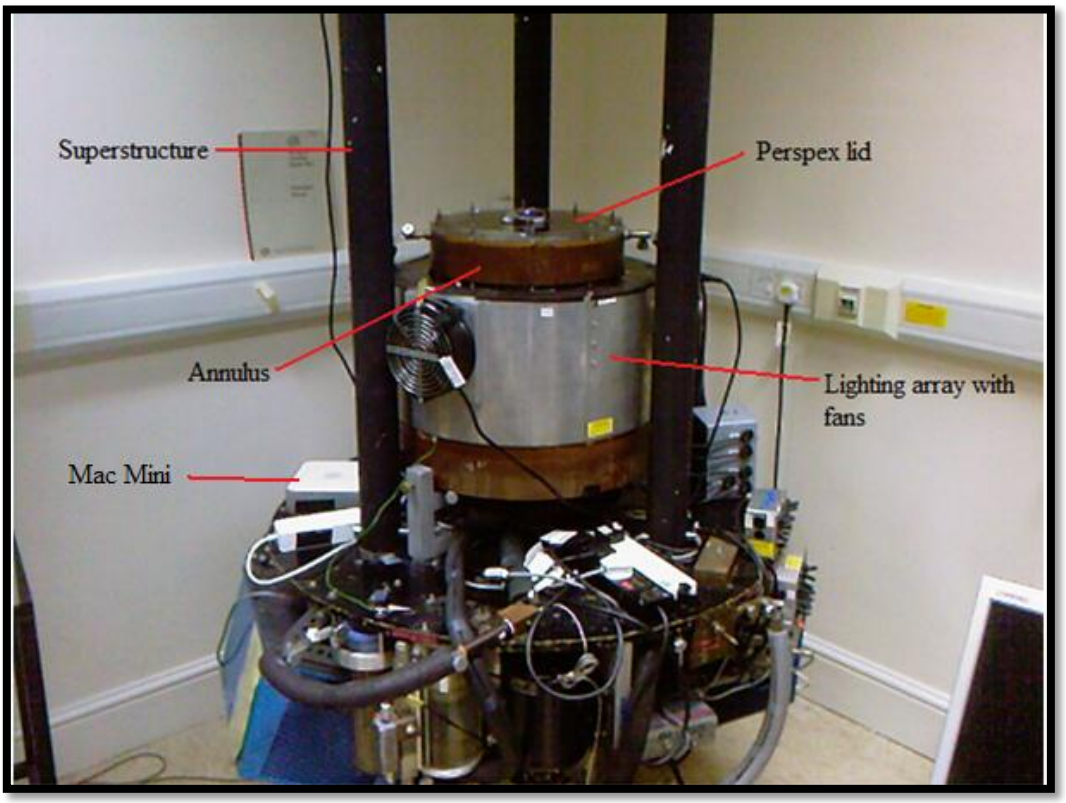

b.)

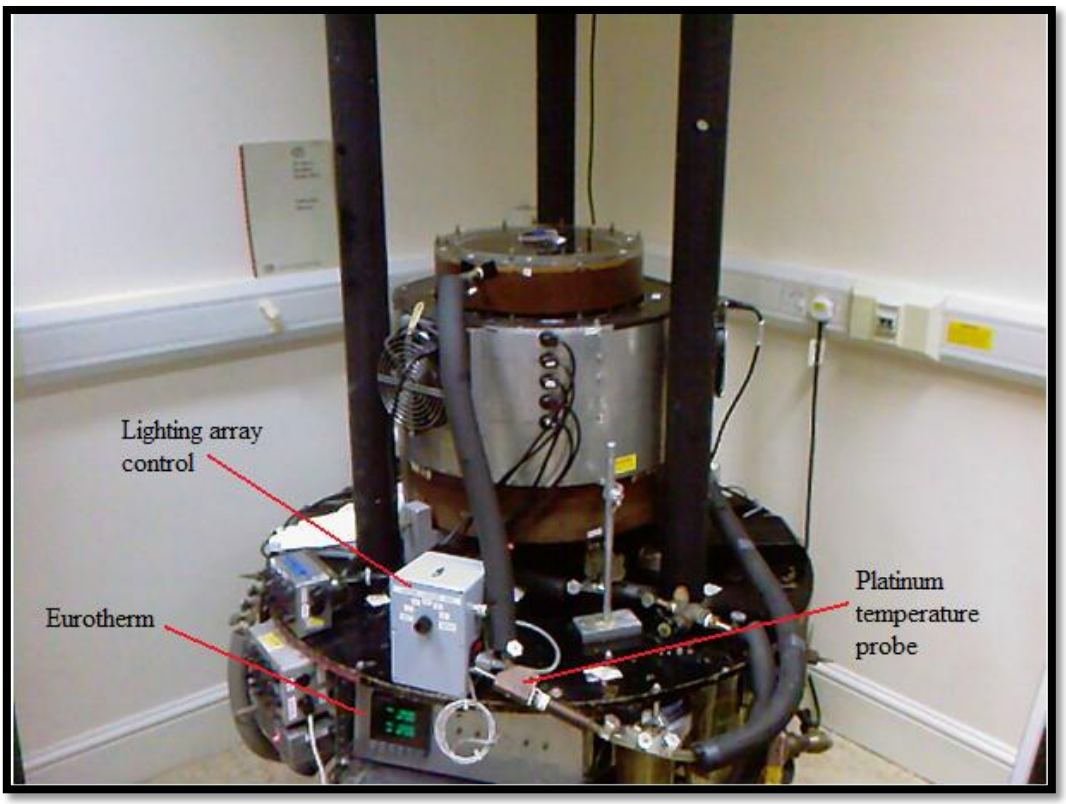

Figure 3.1: Annotated photographs of the annulus from two different sides, with apparatus arranged for the mechanical topographic study.

As explained in Chapter 1, an annulus functions by setting up a temperature difference between the heated outer cylinder and the cooled inner cylinder. This is achieved via two flows of water that each travel through a separate circuit containing a pump, a refrigerator, a heater, a filter and a platinum temperature probe. A feedback system is then created, with the probes sending temperature data of the water entering the cylinders to a Eurotherm 900 EPC Temperature Controller, which compares the readings to any specified value, and then manipulates, via the heaters and fridges, the temperature of the water until the desired value for the outer or inner cylinder is reached. The entire organisation is shown in Figure 3.2.

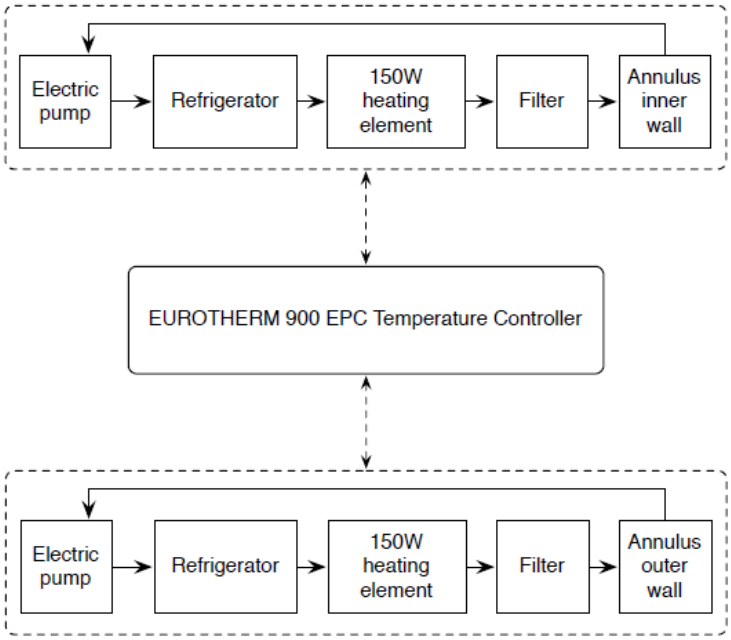

Figure 3.2: Block diagram of heating and cooling flow circuits and feedback system [from Wordsworth (2008)].

The annulus itself is made of Bear grade Tufnol, a resin-bonded multi-layer fabric, and brass, both materials chosen for their thermal properties. The rigid lid is kept in contact with the working fluid and is made of Perspex, employed for its transparency and for being a reasonably good thermal insulator. The working fluid is a mixture of water and glycerol, made up so that its density is $1.044 \pm 5x10^{-4}$ kg m^{-3}. This density allows 350-500 μm diameter pliolite tracer particles to be neutrally buoyant. A sample of working fluid was examined in a viscometer, giving a kinematic viscosity of $1.58x10^{-6} \pm 3x10^{-8}$ m^{2}s^{-1}. This compares well to studies such as Cheng (2008), which calculated

the kinematic viscosity for a mixture with the density in question at 20°C as $1.55\,x10^{-6}$ m^2s^{-1}. Finally, a fungicide solution known as Sanosil S006 was added to the fluid to prevent mould growth. The lid and the inside of the annulus were also treated with this solution.

For the early experiments of this thesis (most notably, the Extended-Regime study), an array of thirty 50 W halogen lamps over five layers surrounded the annulus, allowing light to pass through transparent slits at those layers. This is illustrated by Figure 3.3.

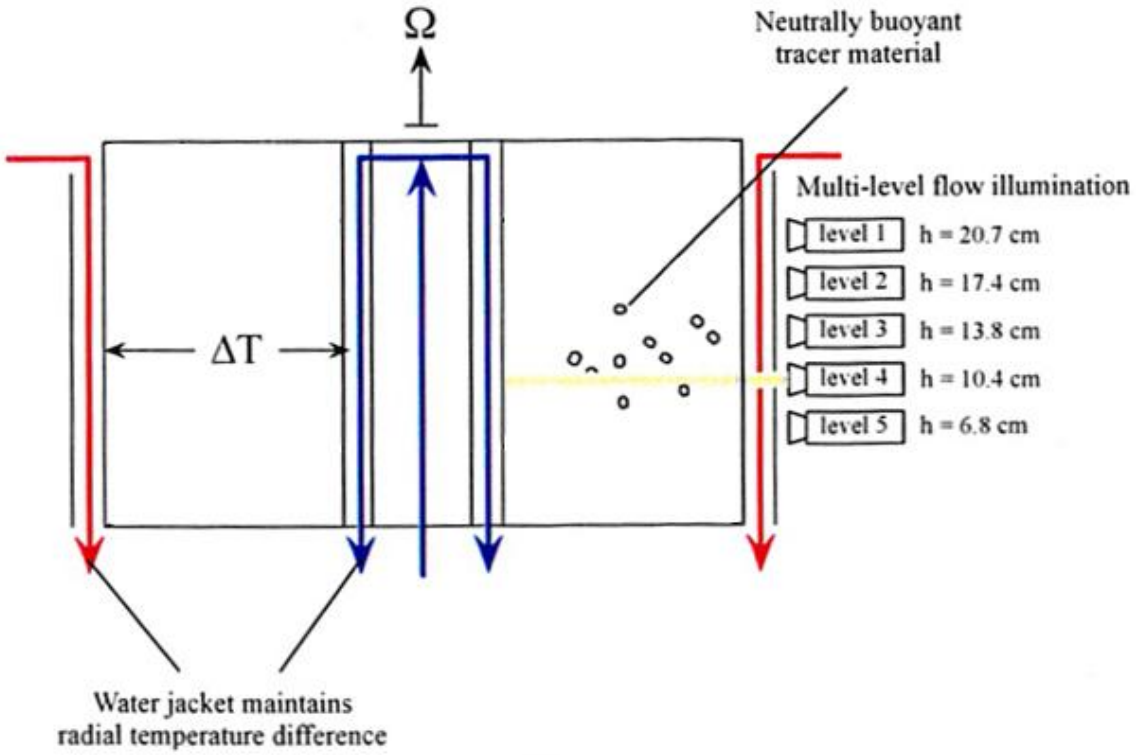

Figure 3.3: Schematic of the lighting array and heating system in side view [adapted from Wordsworth (2008)].

Due to the nature of the halogen lamps, which were very prone to getting hot and thus also causing an additional heat source on the outer wall, three large electric fans were attached to the lighting array as a measure to remove this excess heat. An electronic control box governs which of the five layers is illuminated at a time, with an option for an automatic shift between them at a variable rate. A camera is mounted above the annulus on a tripod-shaped superstructure, with a cone blocking all outside light between it and the Perspex lid. With this arrangement the camera can see the motion

of the tracer particles, and thus the flow structure, at any one of the five levels in Figure 3.3. By switching quickly between the layers the vertical structure can also be resolved.

The annulus to be used was designed to achieve higher Taylor Number values than in some other recent studies, including that of Risch (1999). Its dimensions, as well as several other relevant experimental parameters, are given in Table 3.1.

Table 3.1: Important experimental parameters

Radius of Inner Cylinder	a	4.5 ± 0.05 cm
Radius of Outer Cylinder	b	14.3 ± 0.05 cm
Depth of Annulus	d	26.5 ± 0.05 cm
Density of Water-Glycerol Mixture at 20°C	ρ_g	$1.044 \pm 5x10^{-4}$ kgm^{-3}
Kinematic Viscosity of Water-Glycerol Mixture at 20°C	ν_g	$1.58x10^{-6} \pm 3x10^{-8}$ m^2s^{-1}
Thermal Expansion Coefficient of Water-Glycerol Mixture at 20°C	α_g	$3.16x10^{-4} \pm 1x10^{-6}$ K^{-1}

3.2.1 Data Acquisition

In deference to previous arrangements, a Firewire (type: DFK 31BF03) camera was selected for taking visual results, due to its high picture quality and supposed simplicity of connection with a Mac Mini computer. The Mac Mini, a recent model, is small and light enough to be mounted to the rotating frame, and saved the images and movies to a 500 Gb Seagate Hard Drive. A wireless Local Area Network (LAN) was set up to allow it to communicate with a second computer in the laboratory frame. This stationary computer, a Dell 780 MT 2.66 GHz Core Quad, is known as the 'base station'.

In terms of software, the free TightVNC (Virtual Network Client) package allows the base station to remotely control the Mac Mini, and therefore the camera functions. The digital signal from the camera is picked up on the base station by a software program called BTV Pro, which takes movies of the flow in motion and makes hundreds of frame-by-frame images from them. BTV Pro also ensures the gain of the camera is constant, so that each image occurs under the same conditions. These images are then transferred to a MATLAB program called UVMAT[11], which is an example of

[11] Described in Sommeria (2003), as well as the Coriolis Platform website: http://www.legi.grenoble-inp.fr/web/spip.php?article763

Correlation Image Velocimetry (CIV)[12] – an iterative algorithm that tracks the translation, rotation and shear motion of the tracer particles. From this information, CIV creates a velocity vector field of the flow between each image-pair, with the option of manually removing any false readings. The coding language IDL is then used to analyse this vector field, giving a detailed examination of the flow structure, including the Fourier decomposition. This will be explained more fully in the next chapter.

In addition, a LabVIEW control system was created to give precise, continuous management over the rotation of the annulus. A similar thermal control system was able to wirelessly direct the Eurotherm 900 via the onboard laptop's serial port, but problems were encountered owing to the age of said equipment, which meant that only the temperature of the outer cylinder was able to be changed. Both control systems can be accessed from the base station.

3.3 Process of Re-building and Issues

When the project began, the apparatus had been dismantled to make space for other experiments. Hence, the major task during the first year of work was to restore the equipment to such a point where experiments could be carried out. However, before any of this could begin, the turntable was tested for an inherent 'wobble' noted by Wordsworth (2008). It was found that the reported vibration must have been due to a section of plumbing rubbing against the structure as it rotated. Thus, when the re-build was complete, a second vibration test was carried out, now finding the 'wobble' to be negligible.

To ensure the annulus was positioned exactly in the centre of the turntable, an optical cathetometer (also known as a tracking telescope) was employed. Warping of the Tufnol covering the lower parts of the annulus (where the lighting array rests) had caused a small deviation to the rotation, measured by a Baty Dial Test Indicator to have a maximum of roughly 1.5 mm. As this deviation was confined to the lower section, not the outer or inner cylinders, this was judged to be negligible.

[12] Fincham and Spedding (1997), amongst others, defined the basis of the CIV technique.

Once all the components were fixed in their correct locations, the process of connecting up the plumbing could begin. All the previous pipes and insulation had been lost or discarded when the apparatus was taken apart, so the entire water system was replaced with new material. During this time various leaks were repaired as well as possible and the impellor for the outer cylinder pump was replaced. The electronics were next to be installed, with the camera, Mac Mini and hard drive attached to the superstructure and all of those devices (and the fans, lights etc) then connected to the mains via a slip ring. Lastly, the Firewire camera needed a different attachment to the one used by Wordsworth (2008), so a new aluminium bracket was designed and built.

Unfortunately, after the Extended-Regime experiment (described in the next section), the Mac Mini developed a hardware fault that could not be repaired, and had to be retired. In its place, the Firewire camera was attached to a Lenovo ThinkPad SL510 laptop via a StarTech ExpressCard 1394a Adapter on the rotating frame. To streamline the acquisition process, and to avoid making a second purchase of BTV Pro, it was decided to switch to using MATLAB as a framework for all camera functions. Several scripts were written, employing MATLAB's Image Acquisition Toolbox, to create real-time streakline images and movies, as well as frame-by-frame images from this camera. The Firewire camera was set to use a frame-rate of 3.75 frames/second and it was found that the optimal images were made via 11 captures with a 3 frame interval between each, giving effective streaks of roughly 8.8 seconds. Hence the images show where the particles have travelled in the last 8.8 seconds - long streaks denote a quickly travelling particle, whilst shorter streaks and dots denote slower particles. The streakline images are excellent at characterising the type of flow at a given point: which wavenumber most resembles the motion, whether the waves are stationary or drifting and whether any kind of vacillation is observed. In addition, the new framework greatly speeds up the process of data acquisition, as the files created can immediately be fed into UVMAT without any post-processing, and without any compression or loss in quality.

During the change from the Mac Mini to the laptop, it was decided to update the lighting array. The halogen lamps were replaced by five strips of Maxilux Prostrip 120 white light LEDs, which could achieve a much more reliable and uniform light sheet, and at a much higher brightness. This required the use of a step-down transformer from mains power to 24V, but also removed the need for the cooling fans of the original array. The new lighting array is shown in Figure 3.4, with the configuration for the Thermal Topography experiment (discussed later). Repeat readings using identical conditions at explored areas of parameter space were taken after all changes, to make sure that the same flow structures and phenomena were observed and that the results generated were unchanged.

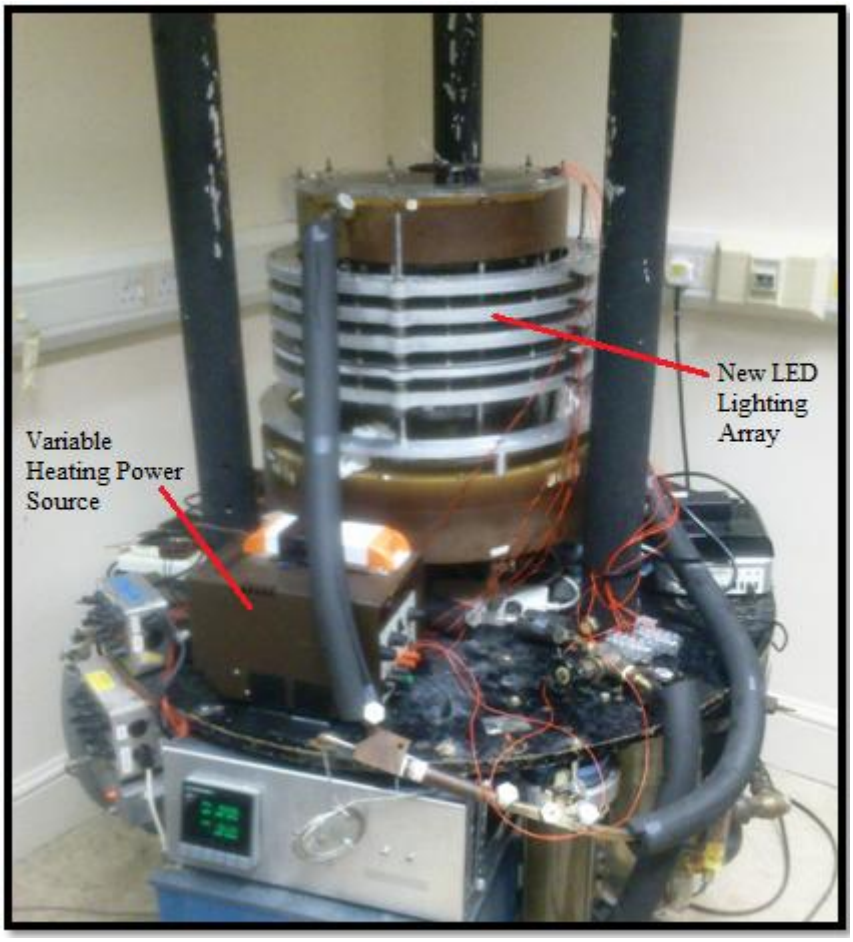

Figure 3.4: Annotated photograph of the annulus, illustrating the new lighting array.

3.4 Topographic Arrangement

This section will expand upon the basic experimental ideas put forward in the previous chapter. The reasoning for the design of the topography that was built is given, as well as how this design influenced the arrangements for each experiment.

3.4.1 Topographic Design

The design of the topography to be used was motivated chiefly by the desire to permit a lot of flexibility in allowing different bases to be constructed with a minimum of effort. Experiments were planned for both a wavenumber-3 and a wavenumber-1 topography (the Resonance experiment and the Partial Barriers experiment, respectively), but it was decided that making those two bases by themselves would limit the flexibility of the experiments. Instead it was planned that the bases could be designed as to be able to separate and combine into numerous forms. Hence, three distinct Perspex bases were built (flat, low amplitude wavenumber-3 and high amplitude wavenumber-3), specifically designed so that they could be taken apart and reassembled to form a variety of shapes. The three bases, as they were modelled in the CAD software Inventor, are shown in Figure 3.5. All three bases have an outer radius of 14.3 cm and an inner radius of 4.675 cm to allow a 2.5 mm gap from the sides of the annulus, in case of expansion of the Perspex. In addition, the minimum thickness of each base is 1 cm, to permit seamless inter-changeability.

a.)

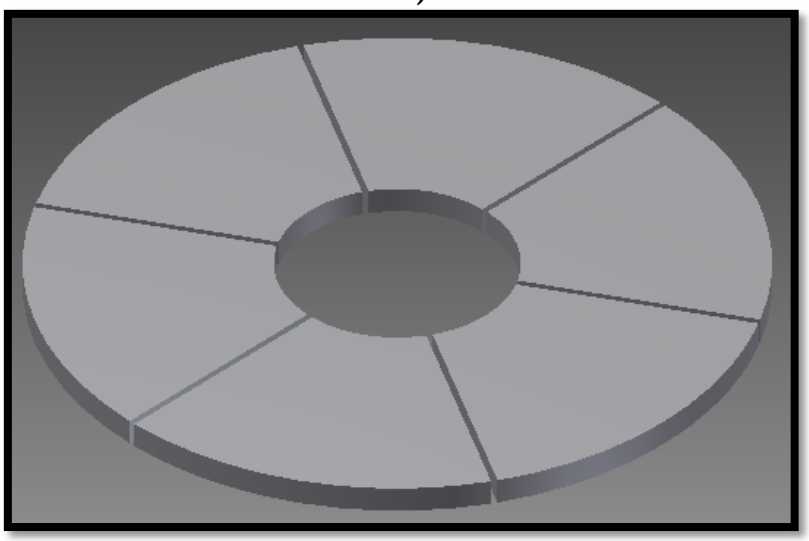

b.)

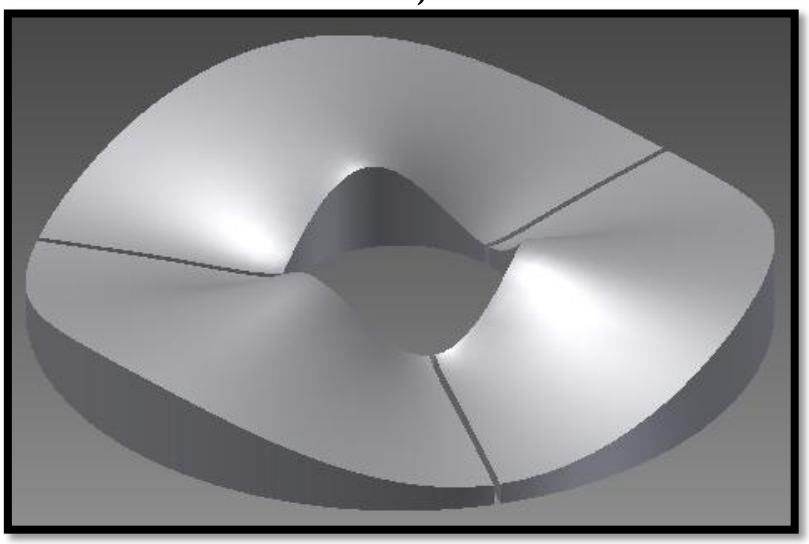

c.)

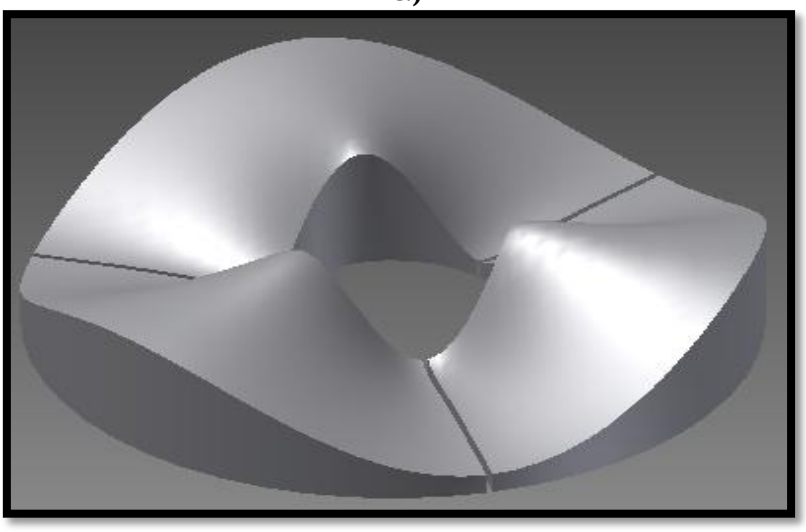

Figure 3.5: Topographic bases: (a) flat base, (b) low amplitude wavenumber-3 with maximum peak-trough difference of 30 mm and (c) high amplitude wavenumber-3 with maximum peak-trough difference of 50 mm.

3.4.2 Extended-Regime Experiment

In order to create a reference point to which all the studies can be compared, it was decided that a control experiment with some simple sinusoidal mechanical (i.e. non-thermal) topography would be employed. This control experiment would also be used to check the readings being obtained against a similar investigation in the literature, and to expand upon the parameter space explored in that work's regime diagram. For this purpose, the recent study of Read and Risch (2011) was chosen. Their topography was a wavenumber-3 style, with the peak at 3.1 cm and the trough at 0.9 cm. In turn, their annulus had an inner radius of 2.5 cm, outer radius of 8 cm and a mean depth of 12 cm. As this is roughly half the size of this investigation's annulus, using the high-amplitude wavenumber-3 topography (as shown in Figure 3.5 (c), with the peak at 6 cm and the trough at 1 cm) should match the topographic aspect ratio of those experiments. For reference, an extended version of Read and Risch's regime diagram is shown in Figure 3.6, illustrating the amount of parameter space investigated (red outline), and the location of the most notable results (green outline).

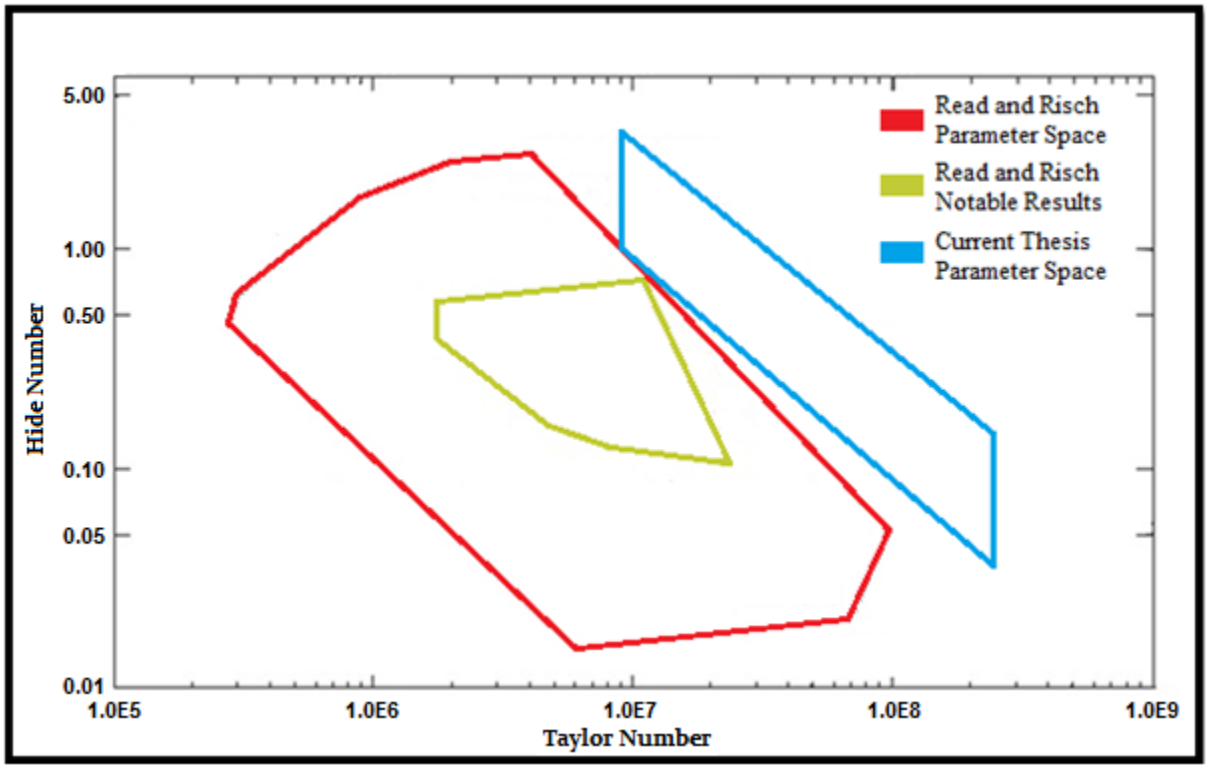

Figure 3.6: Extended regime diagram, showing Read and Risch's parameter space (red outline), Read and Risch's notable results (green outline) and the parameter space to be investigated (blue outline), [adapted from Read and Risch (2011)].

It was initially hoped that the whole of the green-lined "anvil-shaped" structure could be explored, as Read and Risch (2011) found it to contain a sequence of transitions between different flow structures. Unfortunately, preliminary experiments found that, at the low rotation rates and temperature differences needed to reach that region of parameter space, the evolved wave structure was too weak to maintain the floating tracer and most of the particles fell to the bottom of the annulus. This was due to this project's annulus being significantly larger than that used by Read and Risch, and was designed to be able to reach significantly greater Taylor Numbers. Instead, experiments were carried out as close as possible to the original studies, but with the advantage of being able to explore additional parameter space at these higher Taylor Numbers. The location of these results is shown in Figure 3.6 as the blue outlined shape.

In this way, the effect of increasing the Taylor Number on the flow could be examined. Once the expanded regime diagram was fully mapped, this provided a large parameter space which could then be used for all the other experiments within this thesis, as described below. By performing the same scans with the various different topographies, the corresponding effect on the observed flow regimes could be investigated. As such, the Extended-Regime experiments were carried out first of all, both to compare with and expand upon earlier experiments presented in Read and Risch (2011), as well as to set up this reference point for all the following studies.

3.4.3 Resonance Experiment

In order to study the effects of resonance, it was necessary to add a beta effect via a sloped lid, as opposed to the flat lid of the Extended-Regime experiment. The slope has the effect of changing depth with radius, which acts as an equivalent to the previously ignored (in the flat lid) variation with latitude from Equation 3.2. The Perspex sloped lid was the same as that used by Wordsworth (2008), with a 22° slope on the bottom and 3.5° slope on the top, to cancel out any optical distortions at a set camera height. For comparison with the Extended-Regime experiment, the

larger-amplitude wavenumber-3 topography and the parameter space was kept the same. This allowed the impact of the beta effect on the flow to be easily visualised. Furthermore, a sinusoidal (in azimuthal terms) base was believed to be preferable when searching for resonant effects, since non-sinusoidal geometry (such as in the Partial Barriers experiment) will cause additional nonlinear influences, which could obscure those due to topographic resonance. In the channel model used in the investigation of Jin and Ghil (1990), as mentioned previously, there is a single central peak between the boundaries - this can be thought of as representing a section equal to one third of the base of the current experiments. It should be noted, however, that the channel model's base was not laterally-uniform, so comparison with that paper will also serve to illustrate the difference between flows over radially-varying topography and those over radially-uniform topography.

3.4.4 Partial Barriers

Since the topography to be built is in the form of wave-segments, it also allows adaption of the Partial Barriers experiment to that of an isolated ridge one. By combining the flat base with a single peak from one of the other bases, a barrier of sinusoidal cross-section can be implemented, as illustrated in Figure 3.7. The height of the wall can be varied by simply swapping between whether the high or the low amplitude base is used for the single wave. This method removes the need for separate barriers to be made, and also allows for comparison of the effects of a curved wall with a sheer one (as utilised in previous works: Rayer, Johnson and Hide (1998), for example), and a partial barrier with a full-depth one (as found in Wordsworth's (2008) ocean basin experiments, amongst others). Similarly, Harlander et al (2012) conducted free-surface experiments using an 'L-shaped' wall, combining both a partial vertical barrier and a partial radial one. Any dissimilarities found from the results of that study should therefore be due to either the impact of the addition of the second partial barrier or the lack of a lid. The motivation for having a single ridge is twofold - firstly it creates a contrast with the wavenumber-3 base of the Resonance experiment, and secondly it serves to make obvious where (in terms of upstream or downstream of the peak) and how the flow interacts with the

topography, both at the bottom level where the circulation is blocked, and the higher levels where it is unobstructed. As well as permitting the investigation of oceanic blocking, the curved wall is a more realistic simulation of general blocking structures in the atmosphere, and has rough parallels to the topographic impact of the Andes in the Southern Hemisphere.

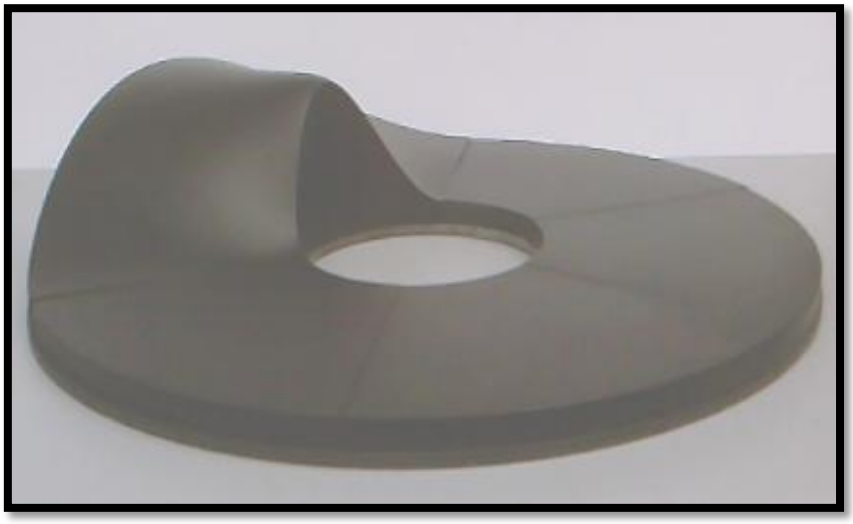

Figure 3.7: Bases arranged to produce a partial barrier.

3.4.5 Thermal Topography

To achieve the azimuthally-varying heating profile needed for thermal topography, flat heating elements on the base of the annulus were employed. These elements were stretched from the inner to the outer wall over a sector one third of the area of the base, forming a rough parallel with a single peak of mechanical topography, as described in the Partial Barriers experiment. This arrangement was chosen to allow immediate comparison between the Thermal Topography experiments and the isolated ridge, especially in regards to the question of whether blocking features can occur without a physical peak obstructing the flow. Once again, this should also make visually clear the locations (in terms of upstream or downstream of the elements) and dynamics of the flow's interactions with the topography. The elements utilised are Kapton Insulated Flexible Heaters, chosen due to their flexibility, thinness (~ 1 mm) and water-proofing. The voltage across the elements can be altered, allowing a range of possible input heat fluxes for each radial thermal profile. Three

rectangular elements of 3 cm by 10 cm were utilised; each rated 10 W/in^2 (1.55 W/cm^2). The arrangement is shown in Figure 3.8.

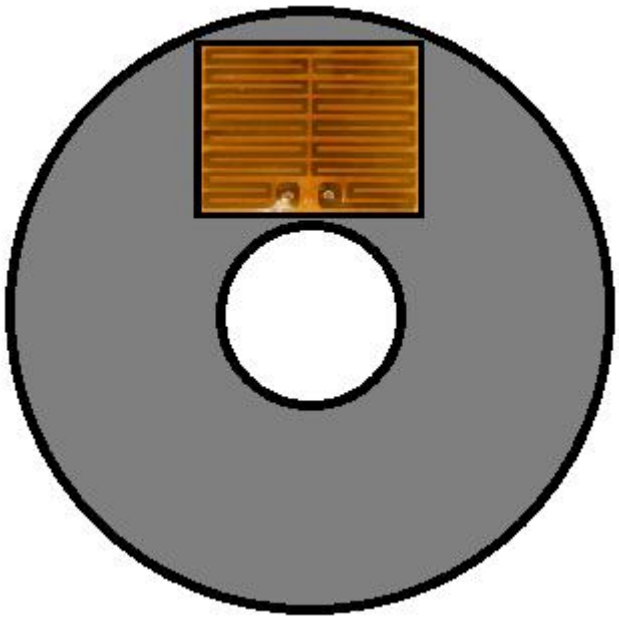

Figure 3.8: Location of the heating elements on the annulus base.

This arrangement gives an isolated ridge of thermal topography, as discussed, creating a comparable profile to the Partial Barriers experiment. In addition, this also contrasts with Boubnov, Golitsyn and Senatorsky's (1991) wavenumber-2 azimuthally-varying heating, which was an azimuthal modulation of the temperature of the outer boundary that was constant at all heights, rather than being an input heat flux constrained to the base.

3.4.6 Methodology

For each experiment, the relevant arrangement of topography was placed at the bottom of the annulus. The required density of water-glycerol mixture would then be added, and the inner and outer cylinder temperatures would be set. To ensure the particles were well mixed throughout the tank at the start of the experiment, the annulus would be briefly spun up to an arbitrary high rotation rate before being slowed to the relevant speed under examination. In the case of the thermal experiments, the

heating elements were turned on at this point. The apparatus would be then left for one hour to allow the fluid to achieve solid-body rotation and to permit the wave structure to become fully baroclinic. After this point, results were taken as a movie file at that specific point in parameter space, switching between the five light levels, or as a scan over a changing dimensionless number, depending on the experiment (explained in the next chapter). The movie files were then split into an array of images, allowing CIV to determine vector velocity field measurements in the form of netcdf files, which in turn were used to create velocity vector diagrams of the flow and real-time streakline images, as well as permitting further analysis, such as Fourier analysis, via scripts written in IDL.

Chapter 4

Flow Regimes and Phenomena

Contained within this chapter are the results of the early experiments completed in order to understand parameter space and the basic flow structures of the fluid. These experiments are comprised of the Extended-Regime investigation and a drift-rate study. The former was motivated by questions about how the various flow regimes and phenomena change with regards to increasing Taylor Number, as an expansion of existing literature on the annulus. This also allowed the creation of a control study, for the purposes of comparison to the subsequent Resonance, Partial Barriers and Thermal investigations. The drift-rate investigation was designed to examine how the drift-rates of the dominant waves alter under different input parameters, especially in terms of their reduction in speed as the flow becomes stationary. After each study, a short analysis will be given, describing what is observed and noting any trends discovered. For the Extended-Regime experiment it was decided not to include baroclinic data by taking readings at different levels of the flow, in order to allow a greater extent of parameter space, and with smaller intervals, to be explored. As such, all images were taken at the clearest height – level 2, at 17.4 cm above the base (16.4 cm above the troughs of the topography). The other experiments, however, feature data taken from every level. More detail on the presented Figures will be explained in the introduction to each section.

4.1 Extended-Regime Experiment

As discussed in the last chapter, this experiment set out to compare the results taken with the current annulus to those of Read and Risch (2011) under the same conditions, namely a sinusoidal wavenumber-3 topographic base and a flat lid, as well as to extend that study's existing regime diagram. This expansion allowed for the flow patterns generated to be studied over a wider range of parameters, especially in regards to increased Taylor Number, in addition to creating a control study

to which the later experiments with different lids and topographic bases can be compared. For each point in parameter space, three velocity vector images, each using CIV from two images separated by a time gap of one second, were created – the first just after the one hour spin up at 3600 s, the second 30 minutes after that at 5400 s, and the third another 30 minutes after that at 7200 s. Clearly anomalous or 'false' vectors flagged by the software were manually removed. As well as the above readings, acquisition and qualitative visualisation was also achieved by creating streakline images via MATLAB. As these readings are taken in real-time, slowly developing flow characteristics, such as vacillation, can be more easily observed. Each Figure is captioned with the time and light level at which it was taken, as well as the rotation rate, temperature difference, Taylor Number and Hide Number (dimensionless numbers calculated to 3s.f.). For sake of space and clarity, not every result that was taken will be given in this section. Instead, the regime diagram of Figure 4.1 has been compiled from the dominant flow structure at each investigated point of parameter space.

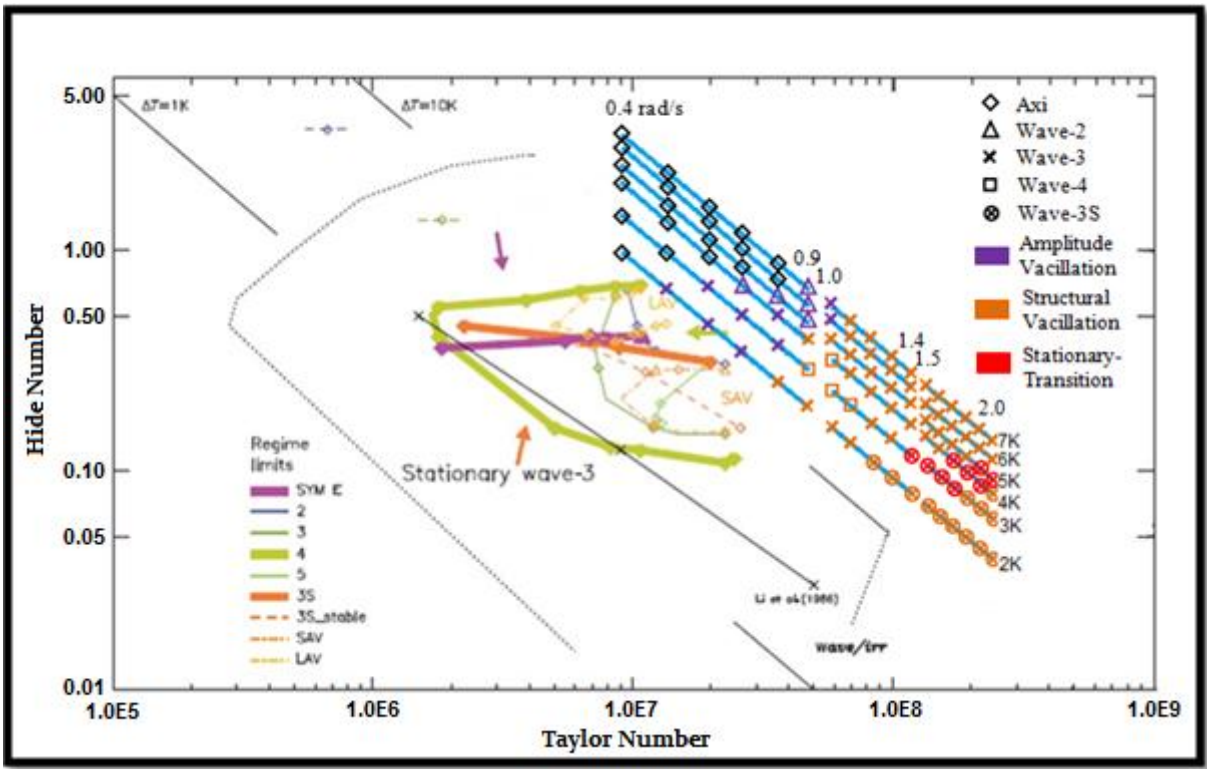

Figure 4.1: Extended regime diagram adapted from Read and Risch (2011), with locations and dominant flow characteristics of the results of the Extended-Regime experiments shown as blue diagonal lines. All flows are drifting except for the stationary 'Wave-3S' region. Each point along the lines of constant temperature difference is 0.1 rads^{-1} apart.

For comparison, from Read and Risch's (2011) section of the regime diagram, Figure 4.1 shows three major regions: an axisymmetric regime above the top of the green 'anvil', a drifting wave regime within the 'anvil' and a stationary wavenumber-3 regime below it. There is also amplitude and structural vacillation evident at the upper and lower parts of the 'anvil', respectively. In this way, the Extended-Regime experiment was used to check for all these flow structures, though it has been noted[13] that transitions may occur in different locations for different annuli.

In the current experiments, the blue lines in Figure 4.1, the flow types are confined to well-defined regions. The circulation was found to start off as axisymmetric, gaining a drifting wave structure as rotation rate increases, with possible transitions between wavenumber-2, wavenumber-3 and wavenumber-4 along the way. It can be noted, however, that wavenumber-3 is by far the most common. As the rotation rate increases even higher, the flow eventually becomes "locked" to a stationary wavenumber-3 type. To further illustrate these regions, an example of each flow structure containing baroclinic instability is given below.

In a similar way, Figure 4.1 shows that the vacillation types also occur in well-defined regions. As soon as the flow changes from axisymmetric to drifting, a form of amplitude vacillation (purple) can be observed. Similarly, as rotation rate increases further, this gives way to a form of structural vacillation (orange), which continues for the rest of the readings. Within the structural vacillation region, another regime was discovered. This 'stationary-transition' regime (red) also undergoes structural vacillation, but is notable for its irregular oscillation between drifting and stationary waves. Once again, to further illustrate these regions, an example of each flow structure is given below.

[13] By Hignett et al (1985), for example.

Drifting Waves

a.) **b.)** **c.)**

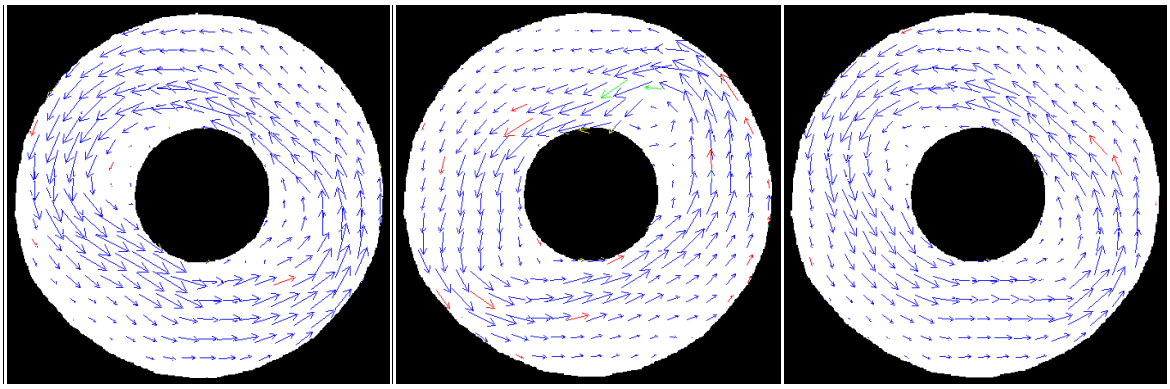

Figure 4.2: Flow visualisation with arrows showing relative fluid velocity at Level 2, $\Omega = 0.7$ rads^{-1}, $\Delta T = 4K$, $\mathcal{T} = 2.783x10^{7}$, $\Theta_T = 0.645$; a.) $t = 3600s$, b.) $t = 5400s$, c.) $t = 7200s$.

a.) **b.)** **c.)**

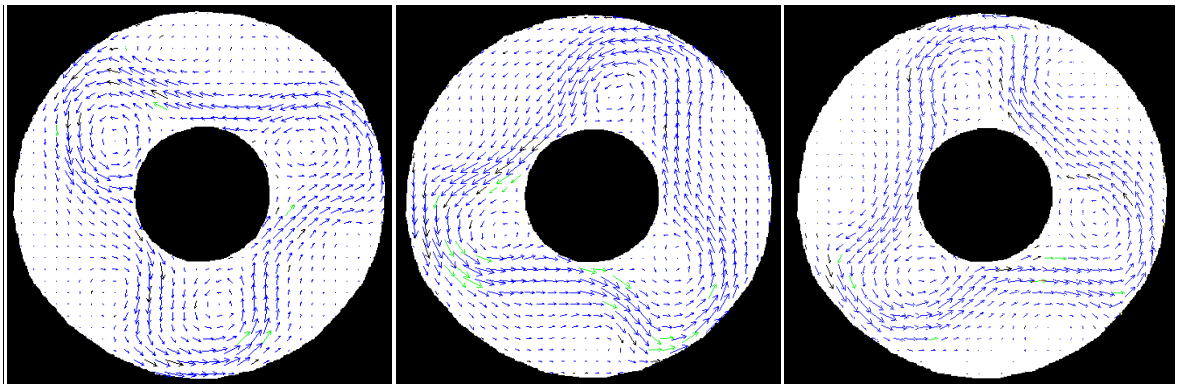

Figure 4.3: Flow visualisation with arrows showing relative fluid velocity at Level 2, $\Omega = 0.6$ rads^{-1}, $\Delta T = 2K$, $\mathcal{T} = 2.045x10^{7}$, $\Theta_T = 0.439$; a.) $t = 3600s$, b.) $t = 5400s$, c.) $t = 7200s$.

a.) **b.)** **c.)**

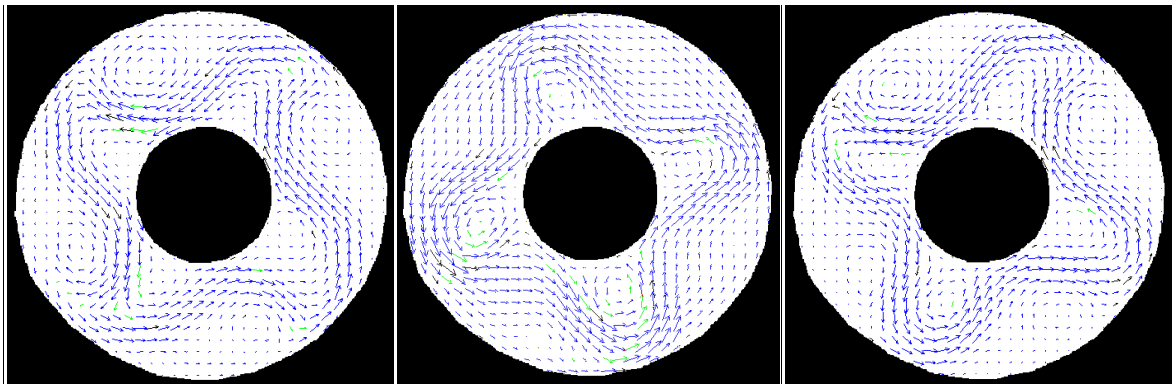

Figure 4.4: Flow visualisation with arrows showing relative fluid velocity at Level 2, $\Omega = 1$ rads^{-1}, $\Delta T = 3K$, $\mathcal{T} = 5.680x10^{7}$, $\Theta_T = 0.237$; a.) $t = 3600s$, b.) $t = 5400s$, c.) $t = 7200s$.

Figures 4.2, 4.3 and 4.4 are examples of flows that continually drift counter-clockwise (i.e. in the same direction that the annulus rotates). As shown by Figure 4.1, the most common drifting flow is a wavenumber-3, illustrated in Figure 4.3. This is possibly due to the flow becoming "locked" to the shape of the topography, but not strongly enough to become stationary, though Hignett et al (1985), amongst others, note that drifting wavenumber-3 flows are common even with a complete absence of topography. In addition, whilst wavenumber-3 can occur seemingly anywhere within the drifting region, the number of waves present does appear to be linked to the value of the Hide Number. A high value near to the axisymmetric regime (such as in Figure 4.2) gives wavenumber-2 flows more frequently, whilst a lower Hide Number (such as in Figure 4.4) is more likely to produce wavenumber-4 structures. An even lower Hide Number once again returns to a domination of wavenumber-3, as the circulation prepares to enter the stationary wavenumber-3 regime. Figure 4.1 also shows that transitions between azimuthal and drifting baroclinic flows are found where would be expected if the upper line of Read and Risch's (2011) 'anvil' was to be extended in Taylor Number, occurring at a fairly constant $\Theta_T \approx 0.65$. In these diagrams blue vectors are those with the best correlation (0.66 and above, where 1 is perfect image correlation), green vectors denote reasonable correlation (0.3 to 0.6) whilst red vectors have poor correlation (0.33 or below). Any vector with less correlation than 0.2 has been removed.

Quasi-Stationary Waves

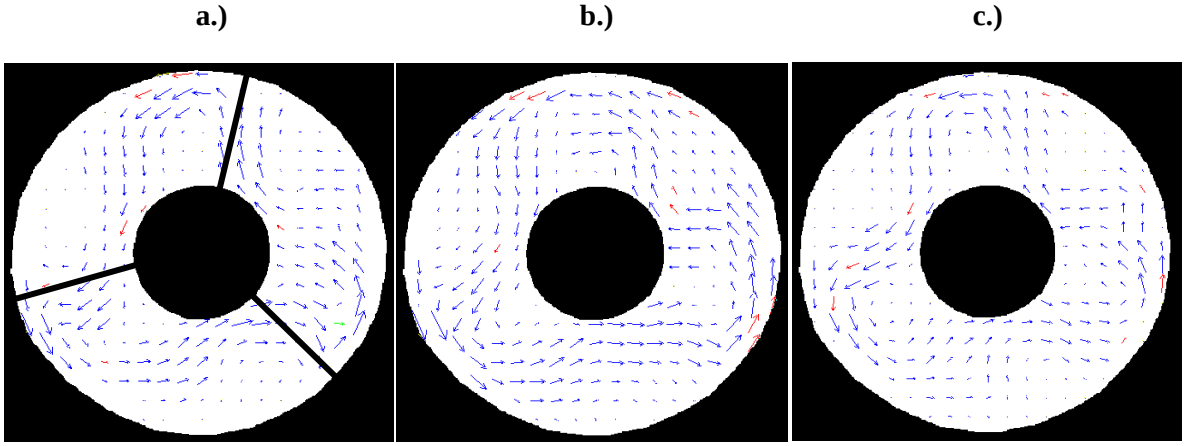

Figure 4.5: Flow visualisation with arrows showing relative fluid velocity at Level 2, $\Omega = 1.2$ *rads*$^{-1}$, $\Delta T = 2K$, $\mathcal{T} = 8.179x10^7$, $\Theta_T = 0.110$*; a.)* $t = 3600s$*, b.)* $t = 5400s$*, c.)* $t = 7200s$.

Figure 4.5 provides an example of a quasi-stationary wavenumber-3 flow structure. It can be observed that, whilst the waves do not move location, their shape changes noticeably over time. This is especially clear for the wave at the bottom-left from (a) to (c) and is likely evidence for a form of structural vacillation at this point in parameter space. An indication of where the peaks of the topography lie has been added to (a). From this it can be seen that, since drifting eddies were found to travel anti-clockwise, the cyclonic stationary waves occur slightly downstream from the corresponding wavenumber-3 shape of the topography, indicating a small phase-shift. As for the drifting wave regime, Figure 4.1 shows that transitions between drifting and stationary flows are found at a Hide Number consistent with an extrapolation in Taylor Number of the results of Read and Risch (2011), if the lower line of their 'anvil' was to be extended, occurring at a fairly constant Hide Number of roughly 0.11.

Amplitude Vacillation

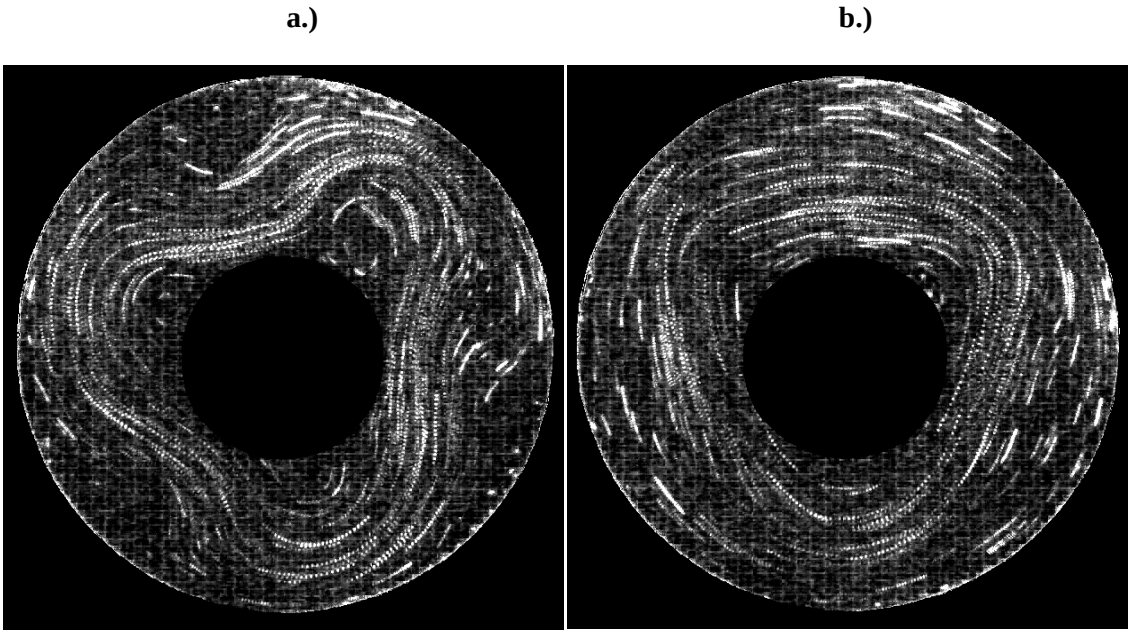

Figure 4.6: Streakline images at Level 2, $\Omega = 0.6$ *rads*$^{-1}$, $\Delta T = 2K$, $\mathcal{T} = 2.045x10^{7}$, $\Theta_T = 0.439$*; a.)* $t = 4140s$*, b.)* $t = 4260s$.

Lu and Miller (1998) characterise amplitude vacillation as a periodic oscillation in the growth and decay of wave amplitude. To demonstrate this, the two images in Figure 4.6 show the maximum (a) and minimum (b) amplitude of a wavenumber-3 structure as it drifts downstream. The oscillation is regular, with a period of about 240 seconds, over which time the cyclonic wave amplitude can be observed to halve in magnitude. The eddy drift-rate for this flow is $0.094 \pm 5x10^{4}$ rad/s, which corresponds to a drift-period (i.e. time taken for a complete revolution) of 668 ± 33 seconds. For a wavenumber-3 structure, this means that the flow travels one wavelength every 223 ± 11 seconds. If this value were the same as the vacillation period, it would suggest that the oscillation was largely due to simple superposition between a drifting wavenumber-3 component and a stationary wavenumber-3 component, with constructive interference at the maximum amplitude and destructive interference at the minimum amplitude. As the period to travel one wavelength and the vacillation period are similar, but not identical (i.e. outside of the calculated error bars), it can be assumed that there are indeed some superposition effects, but there also must exist some additional impact from the mean flow in order to cause the amplitude vacillation that was found. From Figure 4.1 it can be observed that amplitude vacillation occurs in an area confined to the top half of Read and Risch's (2011) 'anvil', if said 'anvil' was to be extended in Taylor Number. Like in the regime diagram of Read and Risch, amplitude vacillation only dominates the flow structure for drifting waves under low rotation rates and temperature differences, with structural vacillation becoming dominant under stronger forcing.

Structural Vacillation

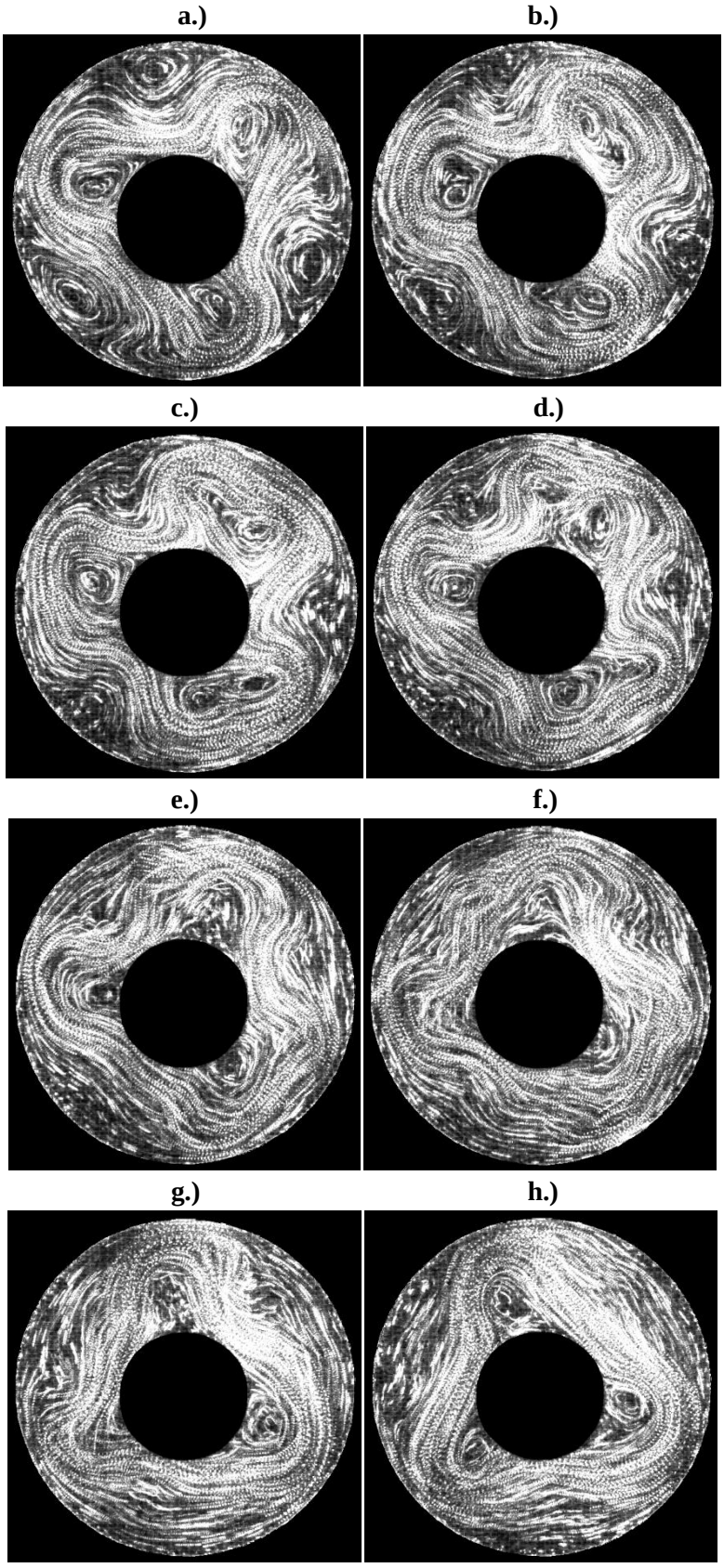

Figure 4.7: Streakline series at Level 2, $\Omega = 1.4$ rads^{-1}, $\Delta T = 7K$, $\mathcal{T} = 1.113x10^{8}$, $\Theta_T = 0.282$; a.) $t = 4920s$, b.) $t = 4940s$, c.) $t = 4960s$, d.) $t = 4980s$, e.) $t = 5000s$, f.) $t = 5020s$, g.) $t = 5040s$, h.) $t = 5060s$.

Figure 4.7 provides an image sequence illustrating one example of structural vacillation, defined in Read et al (2004) as "irregular, small-scale secondary instabilities or eddies" that affect the main flow pattern. The drifting flow in (a) starts off as a regular wavenumber-3 structure, but then begins to deform over time: (b) and (c) show the shape of the waves dramatically change; (d) and (e) show smaller eddies, independent of the main baroclinic waves, appearing on the flow's jet, as well as eddies breaking off from the main waves in the downstream direction; (f) and (g) show the locations of the waves change relative to each other, forming a straighter jet along the bottom of the images. In (h), 140 seconds after the first image, the flow has returned to a regular wavenumber-3 structure. This oscillation is not as regular as the equivalent one from amplitude vacillation, and has no clear progression in terms of how the structure will deform during the vacillation. The eddy drift-rate for this flow is $0.013 \pm 5x10^4$ rad/s, which corresponds to a drift-period of 483 ± 18 seconds. For a wavenumber-3 structure, this means that the flow travels one wavelength every 161 ± 6 seconds. Hence, once again, the fact that this value and the vacillation period are similar but outside of the calculated error suggests that the structural vacillation is more than merely a simple superposition between a drifting wavenumber-3 component and a stationary wavenumber-3 component, but must also include some additional impact from the mean flow. From Figure 4.1 it can be observed that structural vacillation first begins to occur in the bottom half of Read and Risch's (2011) 'anvil', if said 'anvil' was to be extended in Taylor Number. However, the size of the structural vacillation region can also be noted to have expanded with the increase in Taylor Number, now taking up the entirety of the stationary wave regime as well as the low Hide Number section of the drifting wave regime.

Stationary-Transition

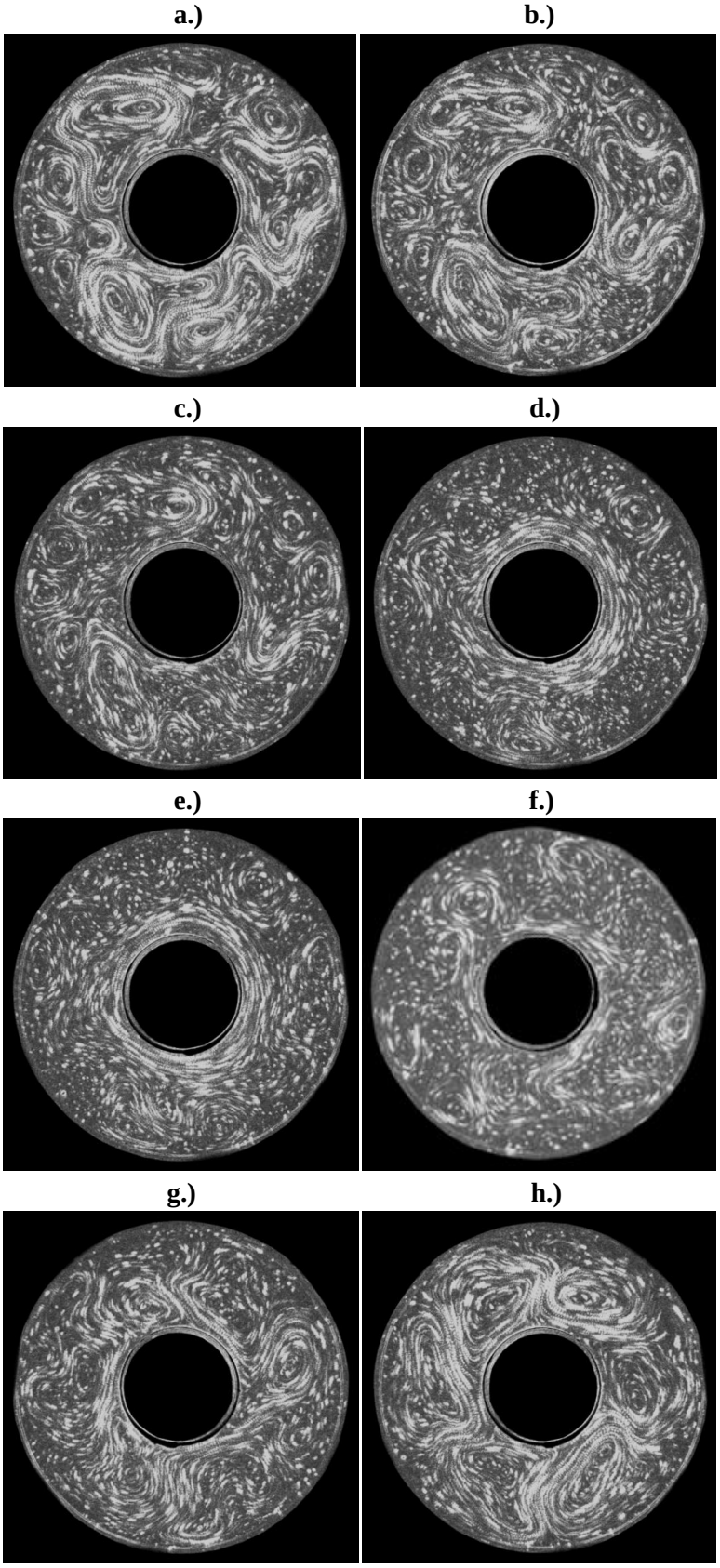

Figure 4.8: Streakline series at Level 2, $\Omega = 1.5$ *rads*$^{-1}$, $\Delta T = 3K$, $\mathcal{T} = 1.278x10^{8}$, $\Theta_T = 0.105$; *a.)* $t = 4000s$, *b.)* $t = 4040s$, *c.)* $t = 4080s$, *d.)* $t = 4120s$, *e.)* $t = 4160s$, *f.)* $t = 4200s$, *g.)* $t = 4240s$, *h.)* $t = 4280s$.

Of particular note in Figure 4.1 is the section with red symbols. This was observed to be some manner of ‘stationary-transition’ region where the flow was dominated by a stationary wavenumber-3 flow, but would periodically transition into a drifting flow or a chaotic structure (depending on the magnitude of the input parameters), and then return to the locked state, as part of an intermittent bursting phenomenon. An example of this behaviour is shown in Figure 4.8.

As illustrated by Figure 4.8, the flow in (a) starts off as a stationary wavenumber-3, but this structure begins to weaken in (b), and by (c) it is almost completely dissipated. During this time, the flow appears to undergo strong structural vacillation until small eddies can be observed to break off and travel anticlockwise – this is the same direction of travel as the drifting waves in Figure 4.4, referred to as downstream. In (d) and (e) the flow appears to have become almost axisymmetric, with no evidence of baroclinic activity, and featuring a reduced jet strength, which continues until (f) and (g), when a weak wavenumber-3 is formed in the same location as the initial stationary wave, and begins to strengthen. By (h), after a period of 300s, this stationary wavenumber-3 structure has returned to full strength, appearing much the same as in (a), and the pattern then repeats itself. In other examples of the ‘stationary-transition’ regime at higher rotation rates and temperature differences, a chaotic structure is set up instead of the almost axisymmetric flow at (d) and (e). The pattern of transformation for the rest of the oscillation is mostly unchanged. Due to the dominance of a stationary wave with the same wavenumber mode as the topographic base, it is assumed that the ‘stationary-transition’ oscillation is associated with resonant interactions with the topography. As such, more investigation of this regime will take place in the Resonance experiments of the next chapter.

Whilst the ‘stationary-transition’ region is believed to be a newly found regime, the structure does bear some resemblance to two of Read and Risch’s (2011) noted regimes: Low Frequency Amplitude Vacillation (LAV) and Stationary Amplitude Vacillation (SAV). LAV, shown in Figure 4.9, is visually similar to the image sequence in Figure 4.8, but features a dominant drifting wavenumber-4 component, as opposed to a stationary wavenumber-3 component. As such, the cause of LAV is unlikely to be topographic resonance, in contrast to the ‘stationary-transition’ oscillation.

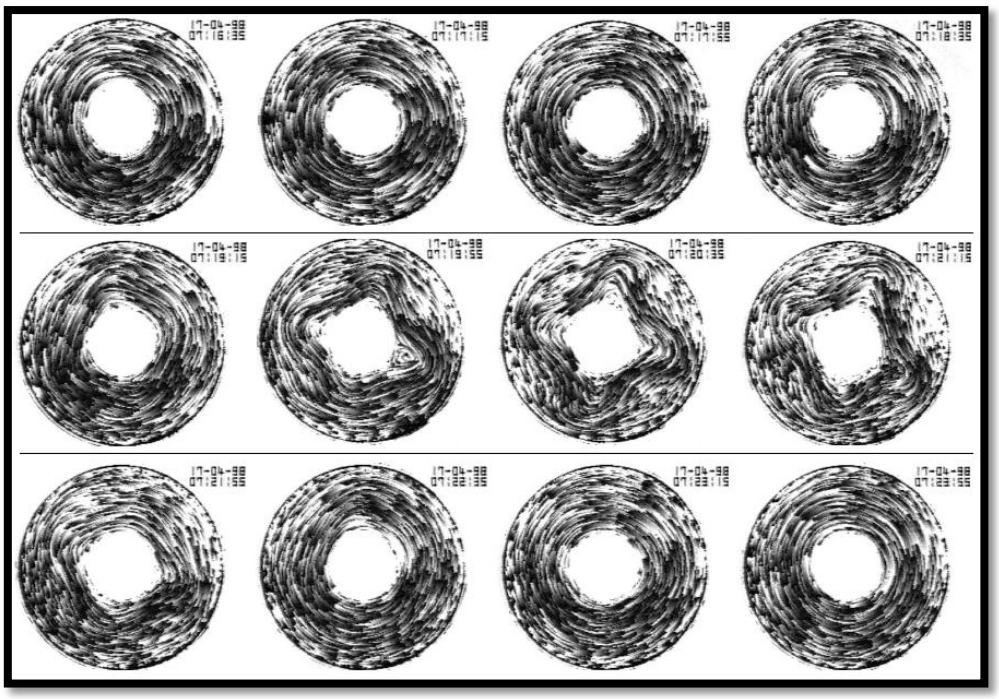

Figure 4.9: Low Frequency Amplitude Vacillation image sequence with each frame 20s apart, $\mathcal{T} = 8.95x10^6$, $\Theta_T = 0.44$ *[adapted from Risch and Read (2014)].*

SAV, on the other hand, was found to have a dominant stationary wavenumber-3 component, as illustrated in Figure 4.10. However, the SAV oscillation can be observed to have a much more defined flow structure between those stationary elements than the 'stationary-transition' equivalent, appearing as clear drifting baroclinic waves rather than azimuthal or chaotic flow. As such, Read and Risch (2011) suggested that SAV had an origin in the interference between stationary and drifting waves, with the stationary points of the oscillation being caused by the superposition of the two.

Further investigation of the similarities and differences between the 'stationary-transition' regime and the LAV and SAV regimes found at lower Taylor Numbers will take place in the Resonance experiments of the next chapter.

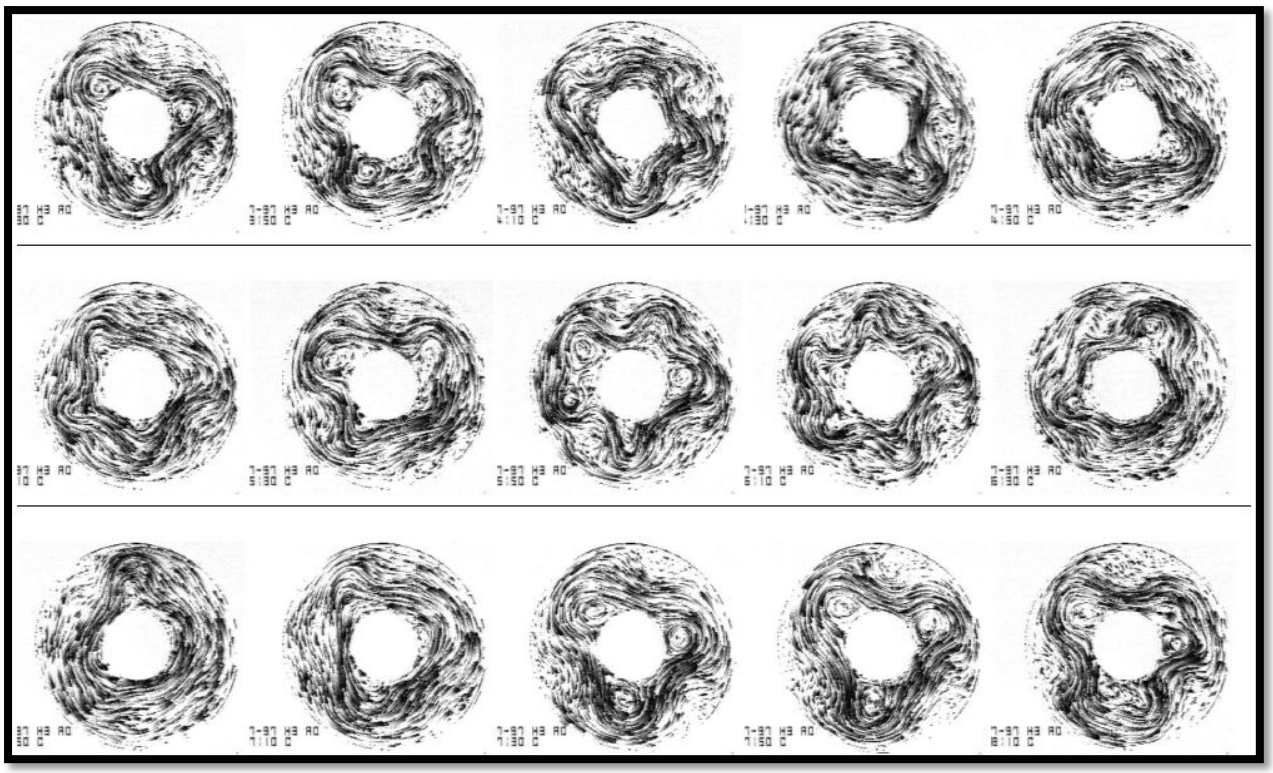

Figure 4.10: Stationary Amplitude Vacillation image sequence with each frame 20s apart, $\mathcal{T} = 2.4x10^7$, $\Theta_T = 0.17$ *[from Risch and Read (2014)].*

4.1.1 Hysteresis

Hysteresis, in terms of the annulus, is the process whereby the flow is demonstrably able to support more than one type of structure at the same point in parameter space, and the particular structure that occurs is strongly dependent on the flow's initial conditions: whether it was spun up from rest, or was adjusted from some other part of parameter space. Hignett et al (1985) explains that "if, at constant temperature difference, the rotation rate is progressively reduced until the dominant wavenumber changes to the next lowest value, the rotation rate can then be increased (gradually) to much higher values without a corresponding increase in the wavenumber". As an example, if a flow is at solid-body rotation in a wavenumber-2 regime, then spun up into what would be expected to be a wavenumber-3 regime, the flow may remain in a wavenumber-2 state. This is more commonly noticed in free-surface experiments (i.e. those without a lid) and has been interpreted as being caused by barotropic interactions removing kinetic energy from the baroclinic waves to the mean flow,

inhibiting their growth, as described by Miller and Butler (1991). However, in these Extended-Regime experiments this was tested, and the regions where flows occur were found to be robust. Evidence of hysteresis was not found, regardless of whether the experiment was spun up from rest, increased in rotation rate, or decreased in rotation rate.

4.2 Discussion – Extended-Regime Experiment

From Figure 4.1, an easy comparison can be made between the results of the Extended-Regime experiment and those of Read and Risch (2011). This comparison shows that the flow structures and vacillation types occur almost exactly where would be expected if the green 'anvil' were to be extrapolated, tending to occur roughly across lines of constant Hide Number. The axisymmetric regime occurs above the 'anvil', the drifting waves (wavenumbers-2, -3 and -4, as predicted) lie within the 'anvil' and stationary wavenumber-3 flows appear beneath the 'anvil'. Similarly, amplitude and structural vacillation were found across from the regions in which they were noted by Read and Risch, provided that the structural vacillation region is assumed to expand as Taylor Number increases (a reasonable assumption since an increase in Taylor Number corresponds to a relative reduction in viscous diffusion and dissipation within the fluid, and thus an increase in nonlinearity), to the extent that it begins to occur outside of the 'anvil' and within the stationary regime as well. This expansion would also be consistent with why Read and Risch found areas with no vacillation, but the Extended-Regime experiment did not. In addition, the large spread of structural vacillation would account for the relatively common occurrence of atypical wave structures and additional 'wave-lobes', especially in regions of high rotation rate and temperature difference, where structural vacillation increases in intensity.

The results gathered also agree well with established topographic theory. As discussed in Chapters 1 and 2, the most notable effect of the addition of topography is the formation of stationary topographic waves, locked at locations determined by the shape and position of the base. This is the spatial symmetry-breaking effect on the zonal flow mentioned by Benzi et al (1986). The small phase

shift noticed in the stationary waves of Figure 4.5 can be explained by the fact that, in the Northern Hemisphere, topographic waves slope westward (i.e. downstream) with height, as noted by Reinhold and Pierrehumbert (1982), amongst others. The direction of the slope is due to the waves that are forced by the topography having an upward-propagating group velocity, and thus a poleward heat transport[14]. This phase-shift has also been observed in other annuli experiments, such as those of Leach (1981).

The most unexpected discovery of the Extended-Regime experiment was the 'stationary-transition' region, discovered whilst searching for vacillations. Within the 'stationary-transition' region, located inside the larger stationary wavenumber-3 regime, a periodic transition was found to occur between stationary waves and drifting waves or chaotic structure. It is possible that this region is caused by resonance with the topography, due to the fact that a quasi-stationary oscillating structure is set up, even though resonance was unexpected for experiments with a flat lid, since the lack of a beta plane effect gives rise to the propagation of free waves which cannot resonate with the topography. The occurrence of stationary waves with the same mode of the topography suggests that the flow is near the location of linear resonance, whilst instability of the resonant mode, as discussed in Chapter 2, could be the cause of the chaotic transitions. The oscillation sequence resembles the quasi-stationary wavenumber-4 oscillation found in Li, Kung and Pfeffer's (1992) baroclinic annulus experiments, which was also suggested to be caused by resonance with a wavenumber-2 base. Unlike the spatial period-doubling of Jin and Ghil (1990) discussed earlier, which would involve a doubling of the dominant period of the flow caused by nonlinear interactions between the main wave structure and its lesser harmonics, it is also possible that this region demonstrates temporal period-doubling, whereby the bifurcation that led to the oscillation continues to transform its frequency until chaos is reached. As discussed previously, the oscillation sequence has similarities to Read and Risch's (2011) SAV and LAV regimes, but with some noticeable differences in terms of the origin of the phenomena. These differences could be further examined by performing a Fourier analysis in azimuth and exploring how the dominant wavenumber components vary over time. This would also allow

[14] This process is derived and discussed in detail by Holton (1992) and Pedlosky (1987).

investigation into the origin of the 'stationary-transition' regime, especially in regards to the presence of resonant interactions. In addition, the early part of the oscillation in which the stationary structure begins to weaken and deform, shown in Figure 4.8a-c, also bears some resemblance to Keppenne et al's (2000) topographic-forced 'tilted-trough vacillation', illustrated by Figure 2.1. This suggests a similarity to LG's resonant 36-40 day extratropical LFV as well, which again could be examined in more detail by performing an azimuthal Fourier analysis and studying the time-series of the resonant modes, searching for bifurcations and frequency cascades. However, as the rotation rate is increased further (roughly until the Hide Number drops to 0.079), the flow appears to move out of linear resonance, and the stationary structure no longer breaks down. This region will be studied in more detail in the Resonance investigation and so provides a good starting place for the subsequent investigation into resonant flows.

4.3 Drift Rate Study

This study was carried out to determine the rate at which baroclinic waves drifted in the regions between the axisymmetric flows and the stationary waves, over a range of rotation rates and temperature differences. This is important information, as a necessary condition for resonance is that the combined effect of wave propagation and net zonal mean flow is to bring the wave drift to a standstill relative to the apparatus frame, i.e. generate stationary waves, in order that topographic forcing can exchange energy coherently with the original wave. The drift-rates were studied by taking long time-series of the flow and combining them to create a movie, then timing how long the drifting eddies took to complete one revolution of the annulus. The initial study employed the Extended-Regime experiment's flat lid with the same sinusoidal wavenumber-3 base.

4.3.1 Drift Rate Results

Three separate temperature differences at 2K, 4K and 6K were investigated, and the rotation rate was varied between 0.4 $rads^{-1}$ and 2 $rads^{-1}$ in intervals of 0.1 $rads^{-1}$, just like for the Extended-Regime experiment. Figure 4.11 shows the results of this investigation.

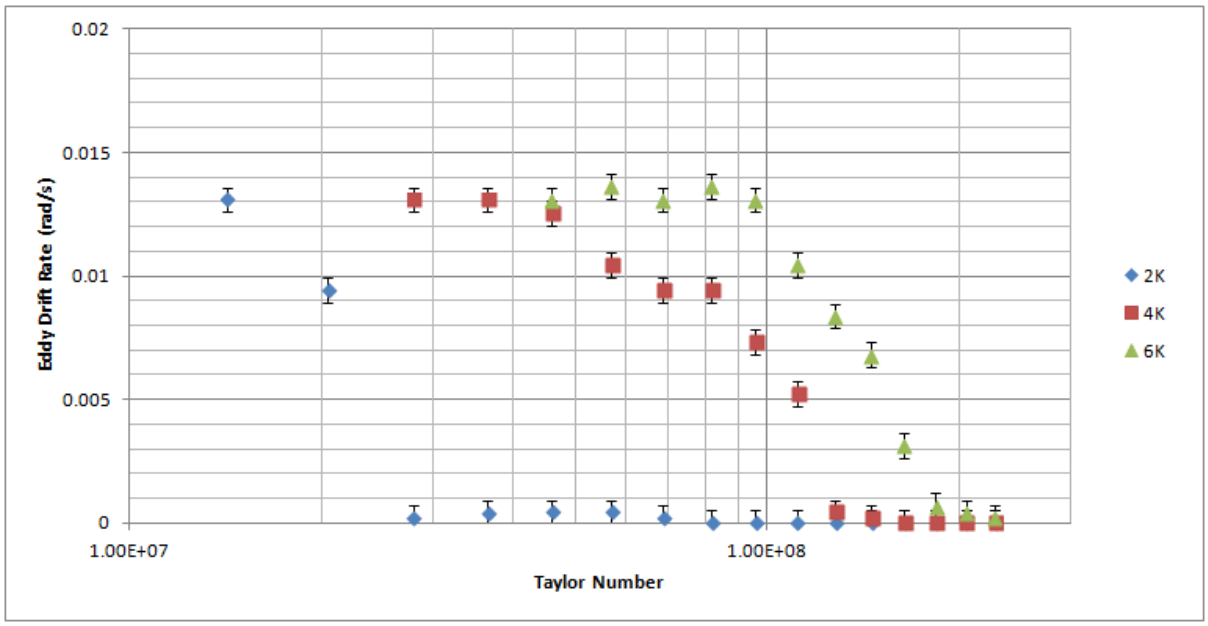

Figure 4.11: Eddy drift rate against Taylor Number over a range of temperature differences. Axisymmetric flows (i.e. the leftmost ends of each line) have been removed for clarity.

In the Figure 4.11, it can be observed that, once baroclinic waves are set up, the drifting regime is encountered first, then the flow becomes stationary (i.e. the eddy drift rate becomes zero), and these transitions happen at lower rotation rates for smaller temperature differences, so that a roughly constant critical Hide Number is maintained, as expected from the Extended-Regime study (Figure 4.1). In addition, throughout the drifting regime, there appears to be a fairly robust maximum drift speed. This drift rate is reached almost as soon as the baroclinic waves appear, at which point the speed plateaus, before gradually slowing to become stationary, rather than undergoing a sharp transition.

Figure 4.11 also shows that stationary waves were found to occur only at relatively high Taylor Numbers, and thus topographic linear resonance, which takes place within regions of stationary flows, would be possible only in a small area of examined parameter space. As such, it was desirable for the Resonance experiments to find a way to reduce the Taylor Number needed to achieve stationary waves, in order to be effective. One method to accomplish this was to employ a sloped lid, as the topographic beta effect that is added by the sloping boundary to the fluid acts to slow down the drift of the waves relative to the apparatus, allowing slower wave propagation and mean flow to be needed in order to reduce this drift to zero. Hence, under a sloped lid it should be easier to find resonant wave patterns, with them occurring more readily in the examined parameter space and at lower Taylor Numbers. Due to this, results employing the sloped lid from the Resonance experiments, as described in the Experimental Arrangement Chapter, were added to the drift-rate study for additional comparison.

4.3.2 Sloped Lid Experiments

During the first experiments with the sloped lid, an unusual occurrence was noted. Evidence of baroclinic waves was either extremely weak or not found at all, even in regions where they would be expected to dominate the flow, such as between the axisymmetric and chaotic regimes of Figure 4.1. Figure 4.12 gives one example of this phenomenon, alongside the equivalent result from the flat lidded Extended-Regime experiment.

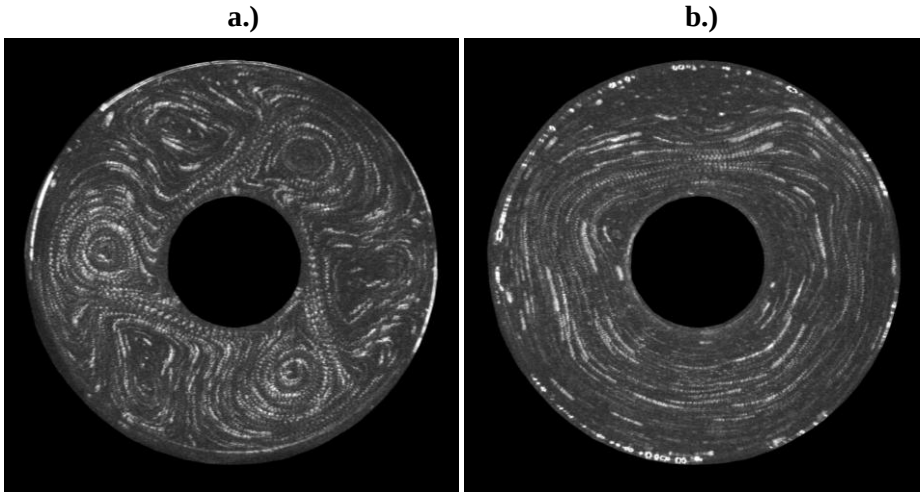

Figure 4.12: Streakline images at Level 3 (mid-depth), $\Omega = 1.2$ rads^{-1}, $\Delta T = 2K$, $\mathcal{T} = 8.179x10^{7}$, $\Theta_T = 0.110$, $t = 3600s$; a.) flat lid b.) sloped lid.

The flow pattern shown in Figure 4.12b was predominant at mid-depth over all of examined parameter space. It is believed that this effect was caused by the precise arrangement of the annulus when using the sloped lid, namely that, to retain the same topographic base as the Extended-Regime experiment, only the lid and not the base was sloped, and said lid was sloped towards the inner radius, forming a deeper tank at the outer edge. Referring back to Figure 1.2, it can be observed that the slope of the lid is therefore in the opposite direction to that of the slope of the isotherms within the fluid. Linear instability studies, such as Mason (1975), suggest that this can lead to a stabilisation of the flow, as well as a reduction in baroclinic growth rates. As such, the slope of the lid has a damping effect on baroclinic activity, causing a reduction on the formation of baroclinic waves. As this would make it more difficult to study resonance using a sloped lid, not least due to resulting flow structures and phenomena being hard to observe, the direction of either the sloped lid or the sloping convection must be altered. As the former represented a significant cost in terms of money and time (and could theoretically lead to stationary waves being less likely to occur, due to the reversal of the direction of the beta effect, and hence of the wave drift), it was decided to reverse the temperature gradient of the annulus, so that the inner cylinder became a heat source and the outer cylinder became a heat sink, with the understanding that the convection currents set up would be mirrored. Preliminary experiments showed that this solution had been successful, and baroclinic waves were found

throughout parameter space once again. As a comparison, Figure 4.13 shows the same experiment as in Figure 4.12 but with a reversed temperature gradient, illustrating the expected wavenumber-3 flow.

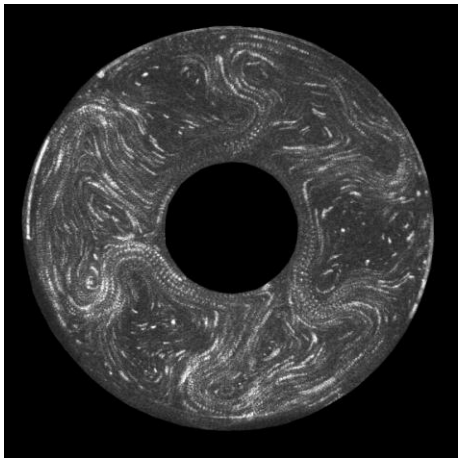

Figure 4.13: Streakline image for experiment with sloped lid and reversed temperature gradient at Level 3 (mid-depth), $\Omega = 1.2$ *rads*$^{-1}$, $\Delta T = 2K$, $\mathcal{T} = 8.179x10^{7}$, $\Theta_{\mathrm{T}} = 0.110$, $t = 3600s$.

Figure 4.13 also shows evidence of increased amplitude of the equilibrated wave, consistent with Mason's (1975) predictions that increased baroclinic growth rates would result if the slope of the lid is in the same direction to that of the slope of the isotherms within the fluid. This should aid in the search for resonance by making baroclinic activity more intense, as well as the previously stated reduction in wave drift rates making resonant effects more commonly found. This appears to be confirmed by Figure 4.13 showing signs of the 'stationary-transition' regime, which is believed to have an association with topographic resonant instability (further investigated in the next chapter), with eddies breaking off to drift downstream, even though it is outside the region where that regime was previously found (see Figure 4.1). The reversed temperature gradient is therefore crucial to experiments employing the sloped lid, especially in terms of the investigation of near-resonant flows, and will be utilised throughout the rest of this thesis' experiments.

4.3.3 Combined Drift Rate Results

Once again, three separate temperature differences at 2K, 4K and 6K were investigated for the sloped lid, and the rotation rate was varied between 0.4 rads^{-1} and 2 rads^{-1} in intervals of 0.1 rads^{-1}, in the same way as for the Extended-Regime experiment. Figure 4.14 shows the results of this investigation.

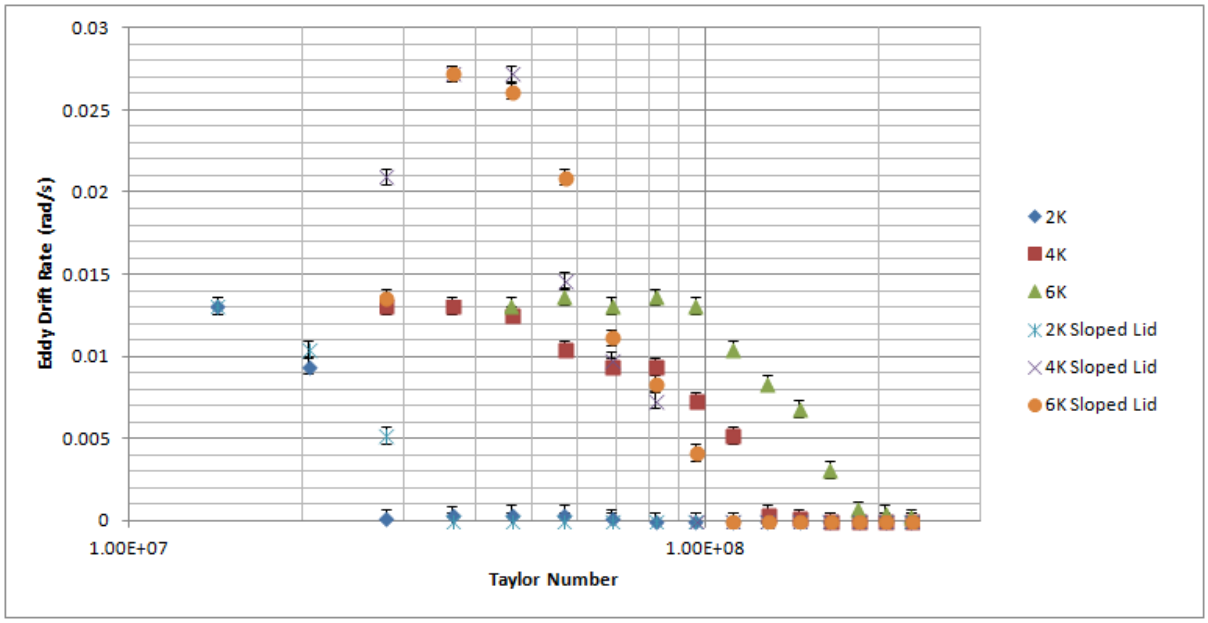

Figure 4.14: Eddy drift rate against annulus rotation rate over a range of temperature differences, for both the flat lid and the sloped lid. Axisymmetric flows (i.e. the leftmost ends of each line) have been removed for clarity.

In Figure 4.14, it can be noted that flows under a sloped lid cease drifting at lower rotation rates and temperature differences than those under a flat lid, especially in the case with a temperature difference of 6K. However, when the sloped lid's baroclinic waves do drift, they tend to travel much quicker, at roughly twice the rotation rate (0.027 rads^{-1} for the sloped lid compared to 0.013 rads^{-1} for the flat lid) at a temperature difference above 2K. In addition, the drift-rate plateaus for the sloped lid experiments are also much narrower in Taylor Number relative to their decline to zero, whereas the flat lid experiments produce much larger plateaus. This last result may be due to the 'stationary-transition' regime from the previous section occurring over a larger area of parameter space with the sloped lid in place, as will be discussed in the next chapter. The regime was regarded as having zero

mean drift in Figure 4.14, due to the stationary part of the oscillation being dominant, and it being difficult to accurately determine the drift-rate over a short time interval. As such, when the drift speed becomes zero in the three sloped lid experiments, it can be assumed that the flow is approaching the location of linear resonance in parameter space. As these stationary flows occur at reduced forcings, it follows that topographic resonance should be therefore easier to find and study in the next chapter, employing both the sloped lid and the reversed temperature gradient.

Chapter 5

Topographic Resonance

Continuing from the preliminary results of the Extended-Regime experiment and drift-rate study, this chapter will investigate the occurrence of topographic resonance and associated phenomena in the annulus. This study is motivated by questions concerning the conditions under which resonance occurs in a differentially-heated annulus, whether Hopf bifurcations can be found and the mechanism for generation of topographically resonant flows within the annulus. The results of the experiments are also hoped to be able to go some way to answering the open questions of the literature, such as the role resonance plays in the atmospheric circulation, the existence of multiple equilibria in the annulus and the mechanism of generation for LFV. First of all, a general outline of the method of experimentation will be given, which will be followed by the results gathered. These results will then be analysed in detail, with comparison to both the Extended-Regime experiment and the literature. More detail on the presented Figures will be explained in the introduction to each section.

5.1 Experimental Arrangement

In the Extended-Regime experiment, a region of parameter space was encountered which showed evidence, namely an oscillatory structure about a quasi-stationary flow, of being topographically resonant in nature. From previous theoretical studies on topographic resonance, such as Jin and Ghil (1990), it was believed that resonant influences will feature more strongly with a beta plane effect[15]. As such, the area of parameter space dubbed the 'stationary-transition' region was chosen to be explored more thoroughly with a sloped lid providing the beta plane effect, but retaining

[15] In theory, a beta plane effect is a necessary condition for resonance, as otherwise free waves will tend to propagate and cannot resonate with the stationary topography.

the Extended-Regime experiment's sinusoidal wavenumber-3 base. To this end, the results of the drift-rate study were used to determine where stationary flows may be found under the sloped lid, and thus where the investigation should be focussed. Also from the preliminary results of the drift-rate study, it was noted that the use of the sloped lid can lead to a reduction in baroclinic activity, which was considered undesirable because it could have the effect of suppressing or inhibiting the full nonlinear effects of the topographic resonance. Accordingly, the technique of reversing the impressed temperature gradient was employed as well, which had the effect of enhancing baroclinic activity.

In contrast to the Extended-Regime experiment, however, a new method of mapping parameter space was utilised. If the regime in question is truly resonant in nature, it is possible that the flow may undergo other bifurcations, such as period-doubling, as it moves into and through the region. As such, a Hovmöller time series is needed, in which a scan through parameter space over time is carried out, and in this way the flow's evolution over time can be revealed. To achieve this, instead of taking discrete points in parameter space, as previously, the Resonance experiments were taken as continuous scans along a constant dimensionless number, in this case the Hide Number, chosen so that the scan would hopefully begin as a simple steady flow, then encounter resonance, and then continue on to chaos. Maintaining an unvarying Hide Number has the advantage of keeping a constant Rossby deformation radius for the flow, whilst increasing the Taylor Number moves the system in the direction of nonlinearity, via a relative decrease in frictional forces. This allows for a detailed exploration of the changes to near-resonant flows as nonlinearity is slowly increased. A regime diagram showing the relative positions of the chosen scans in parameter space is shown in Figure 5.1.

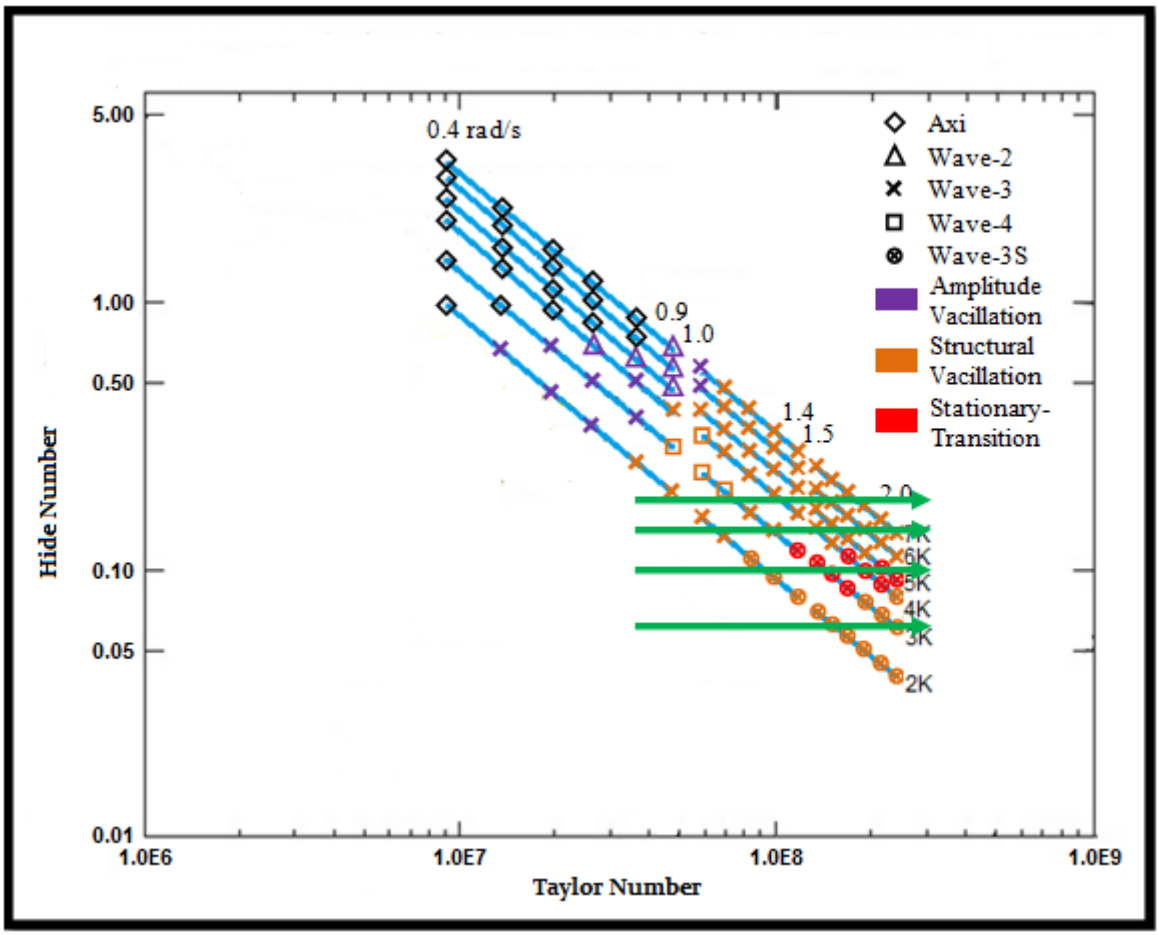

Figure 5.1: Resonance investigation scans shown on a background of the Extended-Regime experiment's regime diagram.

As Figure 5.1 shows, four scans were carried out, at Hide Numbers of 0.18, 0.14, 0.1 and 0.6, each starting at a rotation rate of 0.8 rads^{-1} (a Taylor Number of $3.64x10^7$) and ending at a rotation rate of 2.2 rads^{-1} (a Taylor Number of $2.75x10^8$). To achieve this, both the rotation rate and the temperature difference must be altered simultaneously. Whilst the optimal solution would be completely continuous scans, it was believed that this would add too much noise to the readings, as the thermal feedback system would have trouble keeping up with a continually changing input temperature, and create 'bounce', in a similar way to an underdamped mechanism. As such, the scans were designed to be stepwise, settling on a value for 15 minutes (judged to be enough to observe multiple oscillation periods), then increased by 0.05 rads^{-1} and the corresponding temperature change (which varies in amount depending on the Taylor Number), and then left for 30 minutes to resettle

before the next reading. Preliminary results showed that this proved to be a good compromise, allowing rapid scanning of parameter space, whilst not introducing too much error to the results.

5.2 Constant Hide Number Scans

Both real-time streakline images and vector velocity maps created by CIV were used to collect the initial flow structure data. Each Figure illustrating the results is captioned with the time from spin-up, as well as the light level, rotation rate, temperature difference, Taylor Number and Hide Number (dimensionless numbers calculated to 3s.f.). For sake of space and clarity, not every result that was taken will be given in this section. Instead, the regime diagram of Figure 5.2a has been compiled from the dominant flow structure at each investigated point in parameter space. For added comparison, Figure 5.2b shows the corresponding section of parameter space from the Extended-Regime study.

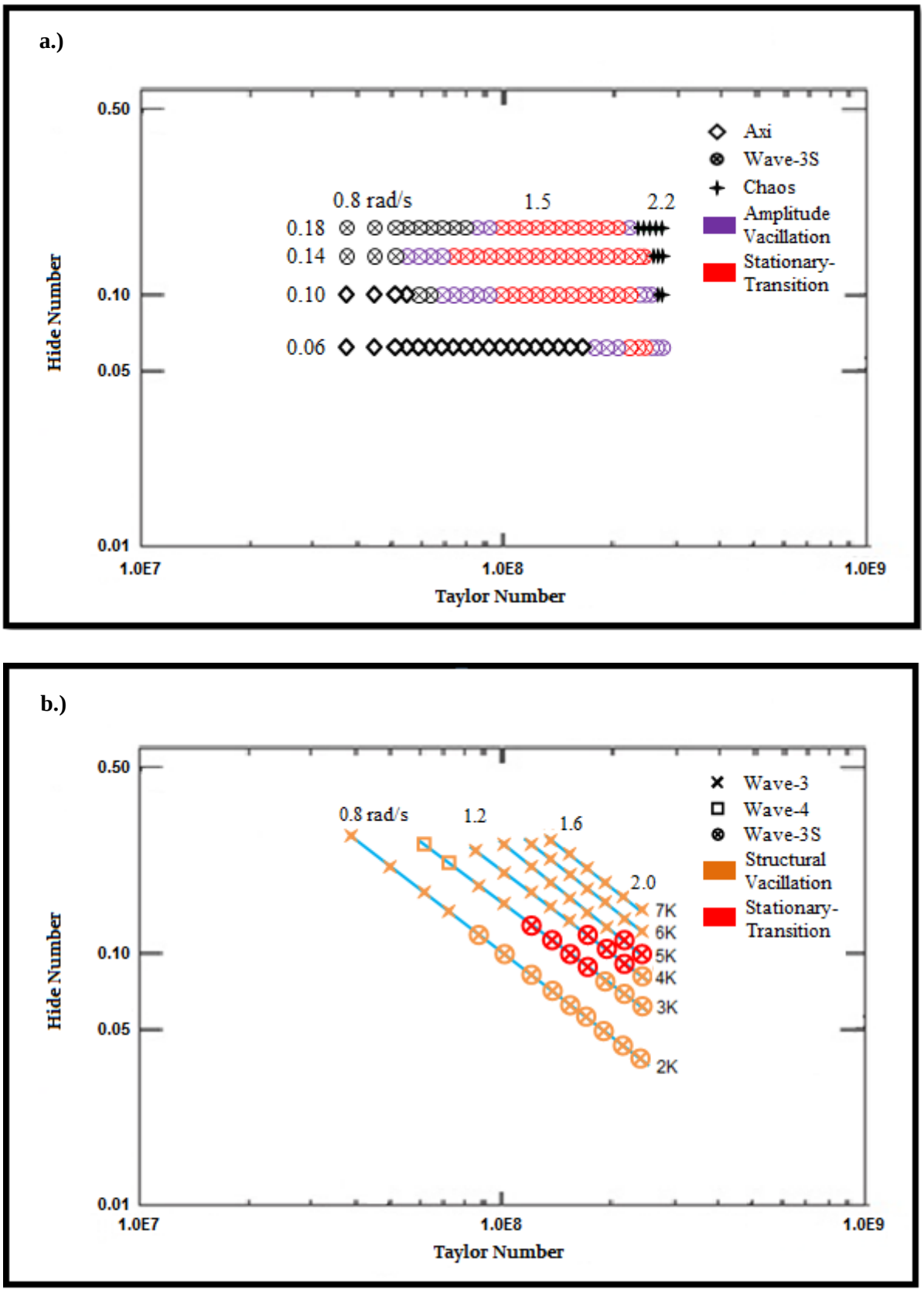

Figure 5.2: a.) Regime diagram with locations and dominant flow characteristics of the results of the Resonance experiment. Each point along the scans is 0.05 rads^{-1} apart. b.) Corresponding section of Extended-Regime study parameter space, otherwise same as Figure 4.1.

In Figure 5.2a, a large region of axisymmetric flow can be observed in the low-Taylor Number, low-Hide Number section of parameter space. This is due to the temperature difference being so small in that area that baroclinic activity cannot occur, with the weak forcing unable to overcome the strength of damping effects of viscous and thermal diffusion, much like in the low rotation rate section of the Extended-Regime experiment, referred to as a lower symmetric transition by Hide and Mason (1975). Comparing (a) to (b) also shows that the 'stationary-transition' region has indeed increased in size, now covering a significant section of parameter space. The regular stationary wavenumber-3 structure is also more common, and is stable in areas where drifting flows were expected under a flat lid. As well as this, in contrast to the Extended-Regime experiment, there are no longer any transitions to wavenumber-4 in the examined parameter space, with wavenumber-3 dominant everywhere that baroclinic waves are found. Amplitude vacillation is also common, whereas structural vacillation is not found, although this may be due to difficulties in distinguishing by visual inspection between the latter and the 'stationary-transition' regime. These results suggest that the addition of a sloped lid, and hence the beta effect, acts to increase the locking of the flow to the topography, presumably by reducing the angular propagation speed of the free baroclinic waves relative to the annulus, strongly favouring stationary wavenumber-3 flows with simple vacillation. In turn, this would also be consistent with the apparent increase in the size of the 'stationary-transition' region, especially if it is topographically resonant in nature. To further illustrate this regime, an example of the time variation of the flow structure is given in Figure 5.3.

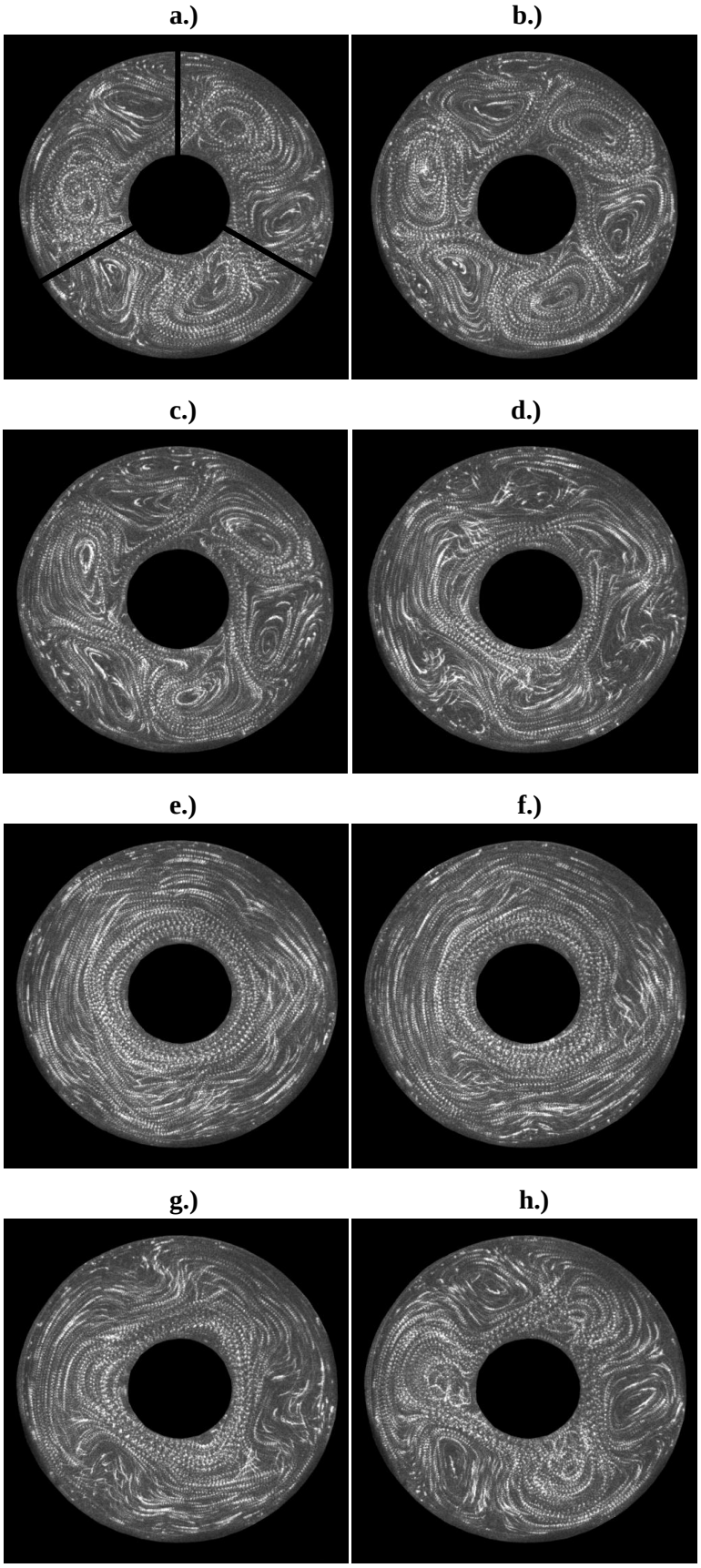

Figure 5.3: Streakline series at Level 3 (mid-depth), $\Omega = 1.3$ *rads*$^{-1}$, $\Delta T = 2.99K$, $\mathcal{T} = 9.599x10^{7}$, $\Theta_T = 0.14$, *a.)* $t = 3900s$, *b.)* $t = 3940s$, *c.)* $t = 3980s$, *d.)* $t = 4020s$, *e.)* $t = 4060s$, *f.)* $t = 4100s$, *g.)* $t = 4140s$, *h.)* $t = 4180s$.

From Figure 5.3, the main aspects of the ‘stationary-transition’ regime can be observed. The flow in (a) starts off as a stationary wavenumber-3, but over (b), (c) and (d) the structure of the waves collapses as eddies break off and drift downstream, in a visually similar way, for example, to how vortices separate from the main meandering jet of the Gulf Stream in the Northern Atlantic. In (e) and (f) the flow appears to become almost axisymmetric, with the baroclinic waves weakening considerably (but yet not disappearing altogether), and featuring a reduced jet strength, until (g), when a weak wavenumber-3 is formed in the same location as the initial stationary wave. By (h), after a period of about 300s, the stationary wavenumber-3 structure has grown enough to resemble the original, and the cyclic oscillation is complete, which then repeats indefinitely. In other examples of the ‘stationary-transition’ regime at higher rotation rates and temperature differences, a chaotic structure is set up instead of the nearly axisymmetric flow at (e) and (f). The organisation of the rest of oscillation is mostly unchanged. It should be noted that the oscillation is the same as in the Extended-Regime experiment although, due to the reversed temperature gradient, the travelling waves are now found to drift clockwise, and thus the definition of ‘downstream’ has been reversed as well. In addition to the structural variation of the oscillation, the period is also unchanged by the slope of the lid, remaining constant at about 300s.

Once again, for clarity, an indication of where the peaks of the topography lie has been added to (a). Hence it can be seen that, when the stationary waves do occur, they arise slightly downstream from the topography, indicating a small phase-shift. The flow in (b) and (c) can also be observed to be visually similar to the ‘tilted-trough vacillation’ shown in Figure 2.1, mentioned in the last chapter as a possible link to LG’s topographically resonant oscillation. In addition, the flow patterns demonstrate stronger anti-cyclonic eddies and weaker jets when compared to the majority of the Extended-Regime experiment results. This effect can also be observed outside of the ‘stationary-transition’ regime, and thus appear to be a feature of the inclusion of the sloped lid, rather than an impact of resonance.

Time-Averaged Flow Structure

Taking a time-average of the flow structure over the period of the observed oscillation (about 300s), has the effect of removing the drifting wave elements and leaving only the stationary components. As such, Figure 5.4 gives an example of the time-averaged flow, using azimuthal velocity, radial velocity and a kinetic energy map, for the parameters given in Figure 5.3.

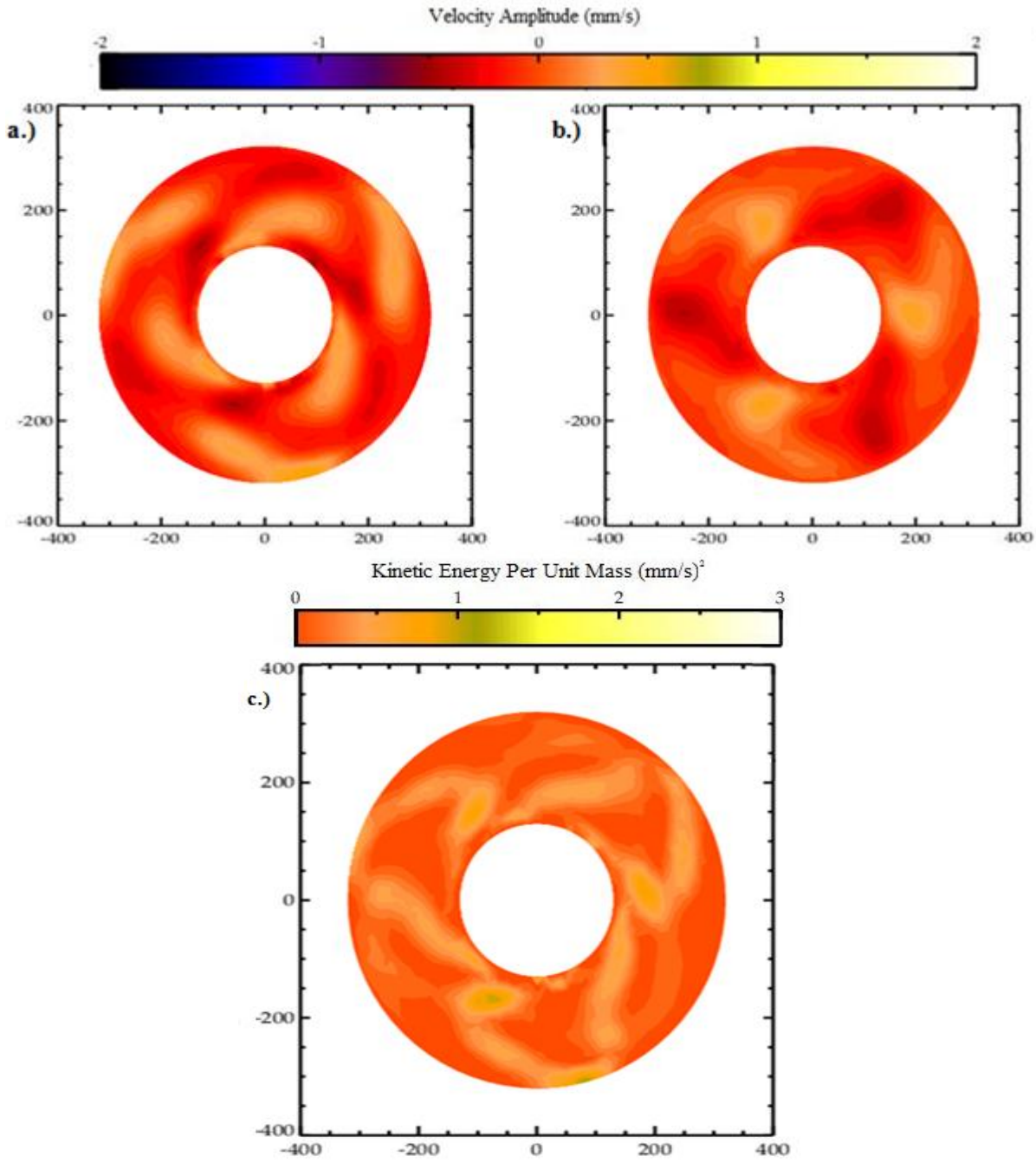

Figure 5.4: Azimuthal velocity (a), radial velocity (b) and kinetic energy (c) averaged over 300s for Level 3 (mid-depth), $\Omega = 1.3$ *rads*$^{-1}$, $\Delta T = 2.99K$, $\mathcal{T} = 9.599x10^{7}$, $\Theta_T = 0.14$.

As Figure 5.4 illustrates, everything aside from the stationary wavenumber-3 component has been removed by the time-averaging, leaving only the azimuthal and radial wavenumber-3 in (a) and (b) respectively. In (c), which combines the previous two examples into a kinetic energy map to illustrate the total flow structure, the circulation strongly resembles what is shown in the streakline image in Figure 5.3a, during the stationary part of the oscillation. In this way, the previously-noted slope with height can also be observed, via the downstream shift of the locations of the eddies compared to the topographic peaks.

In order to examine how the time-averaged flow changes with increased Taylor Number, Figure 5.5 shows a time-average of the flow structure over the same period (300s) for a point in parameter space with a larger Taylor Number within the same scan – once again using azimuthal velocity, radial velocity and a kinetic energy map.

Figure 5.5 illustrates that the time-averaged flow structure is very similar across the entire examined region of parameter space, due to the strong stationary wavenumber-3 element found throughout. In the velocity components, (a) and (b), the only notable difference to the equivalent results in Figure 5.4 is that the amplitude has increased, especially in the peak positive and negative areas. This corresponds to the increased forcing from the greater Taylor Number leading to a faster flow structure and stronger jets. In the kinetic energy map of (c), this increase in amplitude can be seen as well. In addition, there appear to be more secondary stationary components visible, possibly due to the proximity of the chaotic region. However, the main stationary wavenumber-3 structure is still clear and strongly similar to that of Figure 5.4 and the relevant streakline images in Figure 5.3, and the downstream slope of the locations of the eddies is unchanged as well.

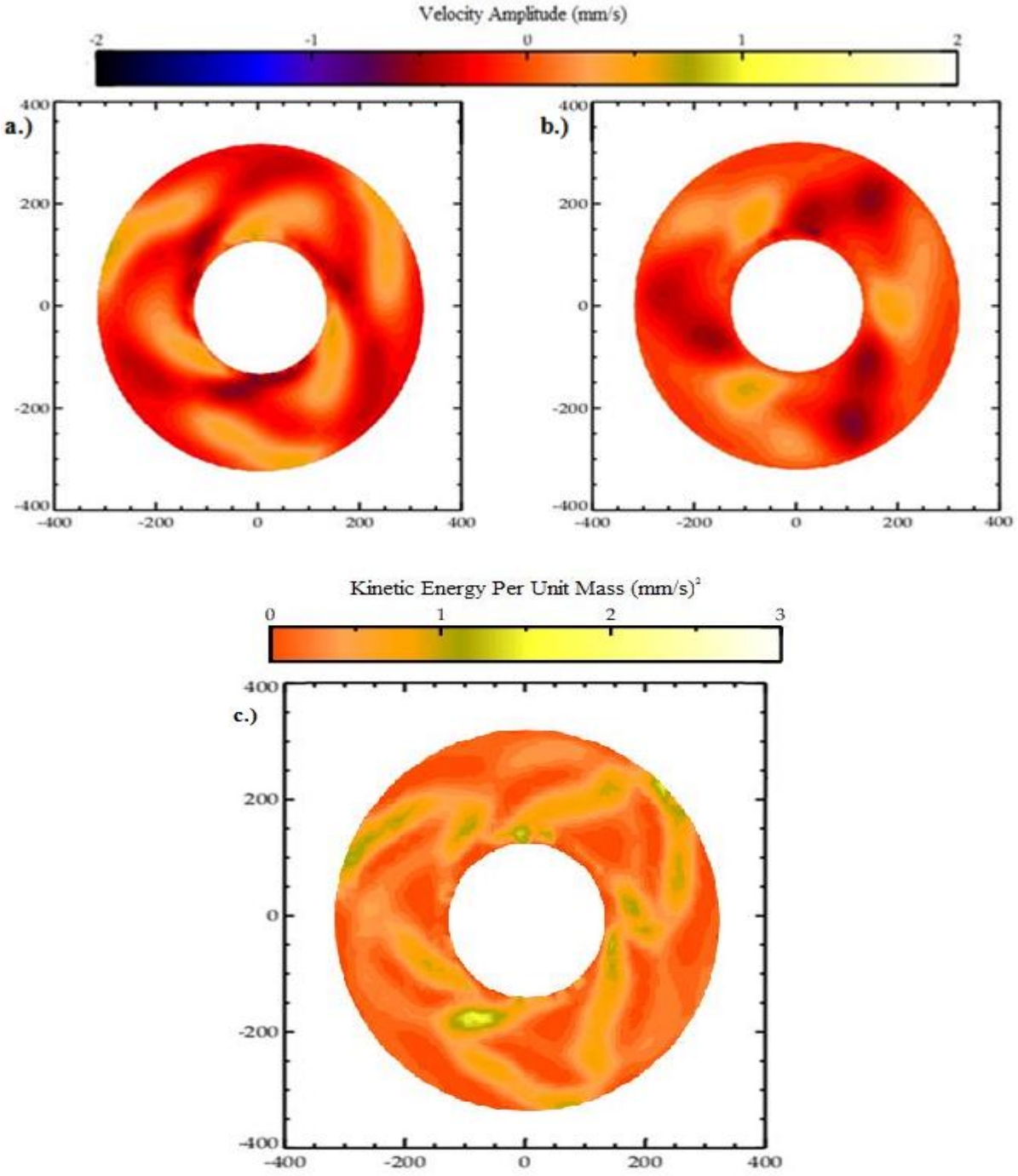

Figure 5.5: Azimuthal velocity (a), radial velocity (b) and kinetic energy (c) averaged over 300s for Level 3 (mid-depth), $\Omega = 1.8$ *rads*$^{-1}$, $\Delta T = 5.74K$, $\mathcal{T} = 1.840x10^{8}$, $\Theta_T = 0.14$.

5.2.1 Time Variations of Resonant Modes

For further understanding of the oscillation, a deeper analysis must be undertaken. First, the outputs from the UVMAT CIV program were converted to polar coordinates on a regularly-spaced grid, and the units of the velocities changed from pixels / time step to mms^{-1}. The zonal background mean flow and any anomalous readings were then removed. An azimuthal Fourier analysis of the wavenumber structure in terms of amplitude and phase could then be carried out for every time step - combining these analyses allows the evolution of the flow over time to be observed. Azimuthal and radial velocity components were calculated at a quarter of the radial distance between the inner wall and the outer wall (closer to the inner wall) and at mid-radius respectively, chosen to avoid nodes in the radial direction and because the patterns found were indicative of the rest of the flow. Figure 5.6 shows an example of the time variations in the amplitude of the first ten wavenumbers, for the point in parameter space used to create the image sequence in Figure 5.3.

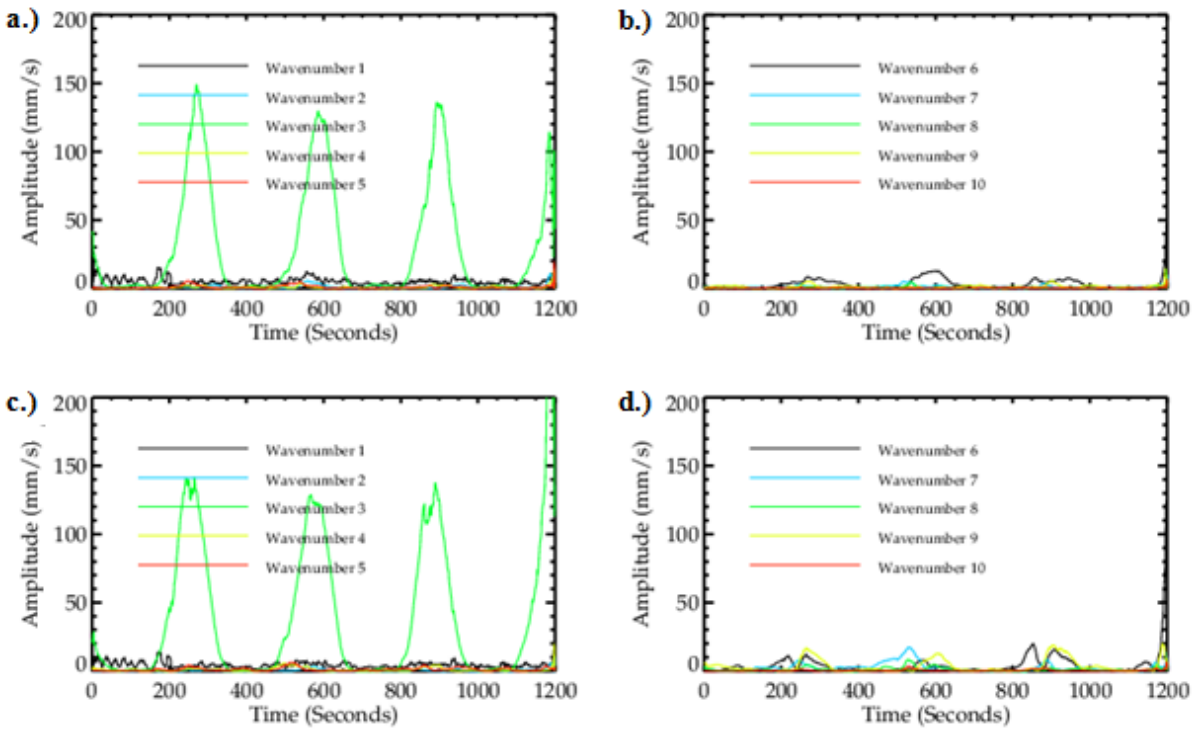

Figure 5.6: Velocity amplitude for Level 3 (mid-depth), $\Omega = 1.3\ rads^{-1}$, $\Delta T = 2.99K$, $\mathcal{T} = 9.599x10^{7}$, $\Theta_T = 0.14$, a.) azimuthal velocity for wavenumbers 1-5, b.) azimuthal velocity for wavenumbers 6-10, c.) radial velocity for wavenumbers 1-5, d.) radial velocity for wavenumbers 6-10.

As can be seen in Figure 5.6, there is an oscillation in amplitude that has a fairly regular period, and is associated with the growth and decay of the wavenumber-3 component, with wavenumber-6 and wavenumber-9 being harmonics that evidently follow the behaviour of the wavenumber-3 component[16]. Both azimuthal and radial velocities are roughly identical throughout the entire time-step. The wavenumber-3 amplitude is periodic, oscillating between periods of dominating the flow and periods of being interchangeable in amplitude with the other components (wavenumber-6 and wavenumber-9 also experience this, but to a lesser extent). However, since the amplitude variation can be observed to not be purely sinusoidal in nature, as is often the case for some amplitude vacillations and all simple linear interference interactions, there must be also some nonlinear impacts on the flow causing the oscillation, such as from topographic resonance. As expected from the image sequence in Figure 5.3, the amplitude oscillation period is found to be about 300s. At a rotation rate of 1.3 $rads^{-1}$, this gives a period of 36.7 'days', which is both in the range of LFV (10-100 days) and, specifically, LG's resonant 36-40 day extratropical LFV as well. At this point, the amplitude variation over time for the 'stationary-transition' oscillation can be compared with that of Read and Risch's (2011) SAV and LAV regimes, as discussed in the previous chapter. Figure 5.7 gives an example of the amplitude time-series for each of the SAV and LAV regimes.

[16] There is also evidence of a time lag between the oscillation of the wavenumber-9 and wavenumber-3 components, indicating that the former may be 'slaved' to the activity of the latter.

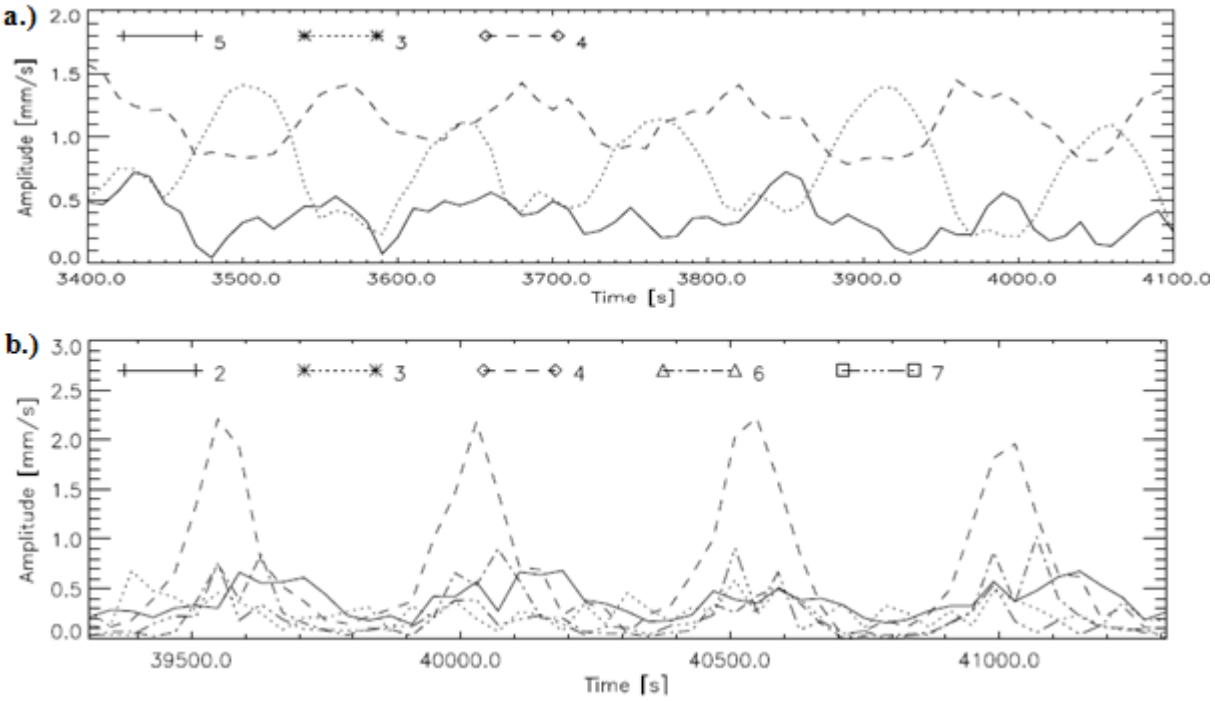

Figure 5.7: Velocity amplitudes for selected wavenumbers during a.) SAV at $\mathcal{T} = 1.23x10^7$, $\Theta_T = 0.22$ *and b.) LAV at* $\mathcal{T} = 8.95x10^6$, $\Theta_T = 0.44$ *[from Risch and Read (2014)].*

As can be observed in Figure 5.7, the dominant wavenumbers of both the SAV and LAV regimes produce a similar oscillation to that of the quasi-stationary wavenumber-3 component of the 'stationary-transition' regime shown in Figure 5.6. Surprisingly, it is the LAV's drifting wavenumber-4 component from (b) that appears the most similar, as the stationary wavenumber-3 component SAV in (a) is only barely greater at the peaks than the wavenumber-4 amplitude, allowing the latter component to dominate the flow for most of the observed time. Hence, it is likely, as suggested by Read and Risch (2011), that the SAV regime is mostly caused by interference between the stationary wavenumber-3 and the other large drifting waves, rather than topographic resonance. As such, the 'stationary-transition' regime is clearly distinct from the LAV and SAV regimes. However, it is also possible that, due to the visual similarities of the oscillations, both LAV and SAV are non-resonating counterparts to the 'stationary-transition' regime, found only at lower Taylor Numbers.

By examining the time variation of the azimuthal phases of the ten wavenumbers of Figure 5.6, most of the wave components were found to be steadily drifting, with the exception of wavenumber-1 and wavenumber-3. Figure 5.8 shows the phase of these notable wavenumbers, for the same flow example as previously.

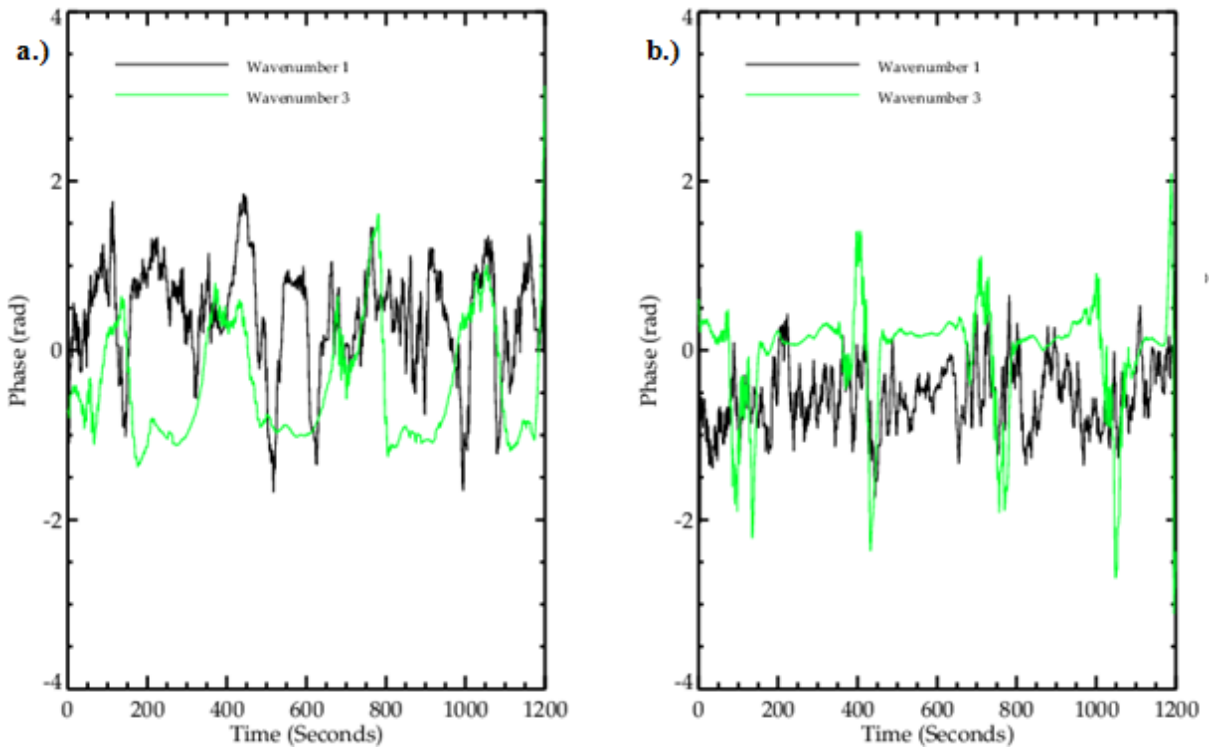

Figure 5.8: Velocity phase for Level 3 (mid-depth), $\Omega = 1.3\ rads^{-1}$, $\Delta T = 2.99K$, $\mathcal{T} = 9.599x10^{7}$, $\Theta_T = 0.14$, a.) azimuthal velocity for wavenumber-1 and wavenumber-3, b.) radial velocity for wavenumber-1 and wavenumber-3.

From the phase diagram in Figure 5.8, it can be observed, despite a large amount of noise, that the wavenumber-1 component is essentially quasi-stationary, and the dominant wavenumber-3 component is rocking back and forth between two stationary points in azimuth. This is shown most clearly in the phase of the radial velocity components, (b), which will be focused on from this point. The rocking between phase locations could be the origin of the structure of the oscillation, which resembles the appearance of a stationary 'tilted-trough vacillation'. The peaks of the oscillation occur when the wavenumber-3 component is at its most positive phase, roughly 0 rad, where it appears to be most stable, and the troughs occur around the most negative phase, roughly -2 rad, where it is less

stable (the phase of the wavenumber-3 azimuthal velocity component has the opposite change, with the peaks being at -1 rad and the troughs at +0.5 rad). For comparison, the position of the topography at the base corresponds to a phase of about $+¾\,\pi$ rad. This agrees well with Figure 5.3, as the stationary wavenumber-3 part of the oscillation, (a), was found to occur downstream of the topographic peaks, due to a clockwise shift with height.

For further analysis, Figure 5.9 gives the radially-averaged kinetic energy for the first 10 wavenumbers of the same flow.

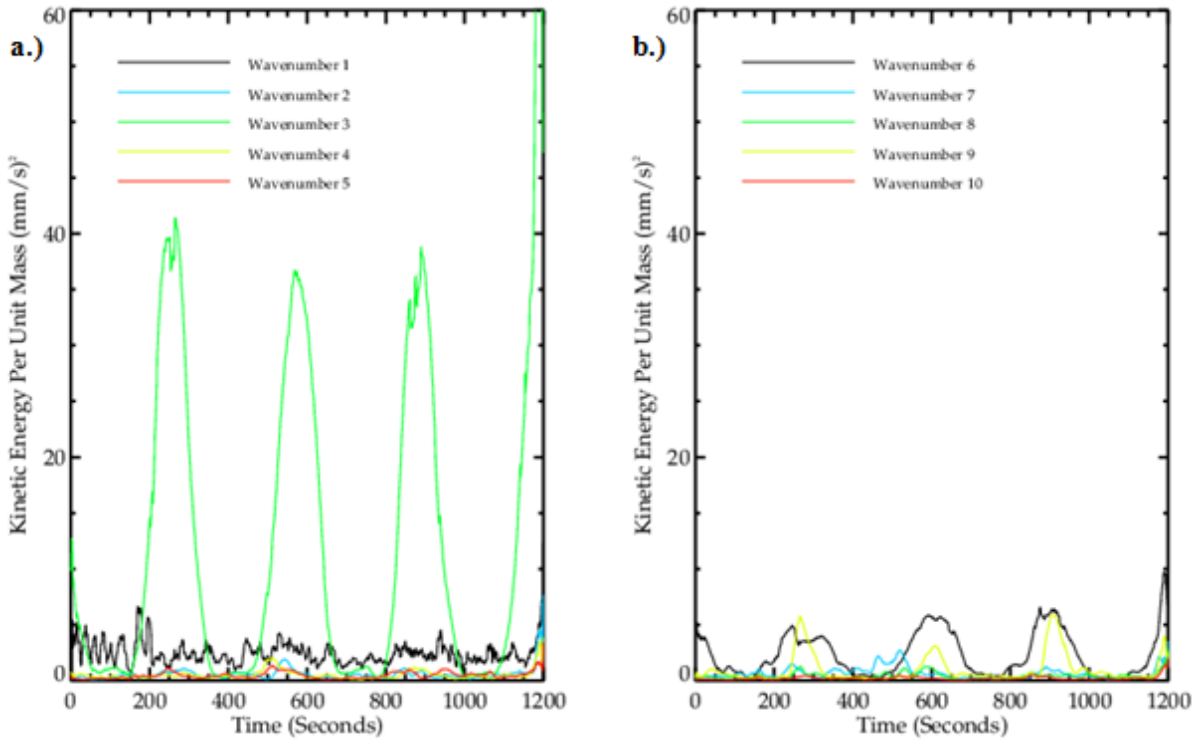

Figure 5.9: Radially-averaged kinetic energy for Level 3 (mid-depth), $\Omega = 1.3\ rads^{-1}$, $\Delta T = 2.99K$, $\mathcal{T} = 9.599x10^{7}$, $\Theta_T = 0.14$, a.) wavenumbers 1-5, b.) wavenumbers 6-10.

As can be seen in Figure 5.9, the kinetic energy in the flow is almost entirely contained within the oscillation, especially in the wavenumber-3 component (the wavenumber-3 peak at about 1200 seconds is anomalous, thought to be due to an accidental capture of change in input parameters for the subsequent time-step). During the troughs of the oscillation, the kinetic energy is presumed to be

transferred to potential energy, as explained in Chapter 1. This is likely to be the mechanism for why the drifting structure of the flow appears to slow down during the 'stationary-transition' sequence, with the jet and eddies weakening until almost axisymmetric behaviour is reached. Furthermore, a contrast can be made between the time variations of the kinetic energy of the dominant wavenumber-3 component and the kinetic energy of the zonal mean flow. At mid-depth, this zonal mean is found to fluctuate in direction from positive to negative and vice versa, due to being acted upon by both the topographically-forced waves from the bottom and the free baroclinic waves from the top and middle of the tank. As such, Figure 5.10 shows the time variation of the kinetic energy of the zonal mean component of the flow, from the same point in parameter space as in Figure 5.9, but at the higher Level 2, and with a superposition of the wavenumber-3 kinetic energy for comparison.

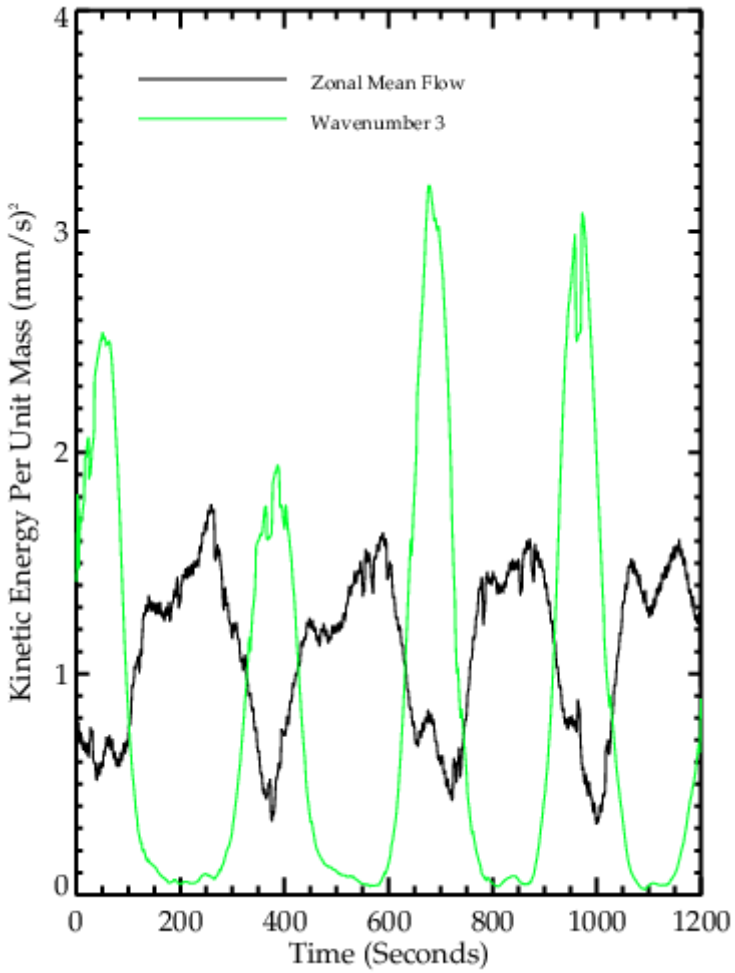

Figure 5.10: Radially-averaged kinetic energy of zonal mean flow (black) with wavenumber-3 total kinetic energy (green, not to scale) as comparison, for Level 2, $\Omega = 1.3$ *rads*$^{-1}$, $\Delta T = 2.99K$, $\mathcal{T} = 9.599x10^{7}$, $\Theta_T = 0.14$.

Figure 5.10 shows that the kinetic energy of the zonal mean flow oscillates exactly in antiphase with the kinetic energy of the dominant mode. Not only does this further show where energy is being transferred to during the oscillation's troughs, it also strongly implies that the oscillation is comprised of nonlinear wave-zonal flow interactions, associated with resonance with the topography.

Oscillation Evolution

Aside from the number of results that encountered the 'stationary-transition' regime for each scan, the major difference between the four scans conducted is in the relative strength of the oscillation, in terms of wavenumber amplitude and dominance of the flow structure. Of these, the scan of $\Theta_T = 0.14$ exhibits the strongest oscillations, with a very clear oscillation throughout. By contrast, the scan of $\Theta_T = 0.10$ is second strongest, and the scans of $\Theta_T = 0.18$ and $\Theta_T = 0.06$ are much weaker, the latter two in particular being difficult to visually discern between the 'stationary-transition' regime and structural vacillation. It is therefore possible that the centre of the oscillation region, and hence where it is has the largest effect, is near where the scan of $\Theta_T = 0.14$ cuts through parameter space. Since the oscillation is believed to have a resonant origin, as discussed previously, it is also likely that this centre is where the peak of the topographic linear resonance is located. As such, the scan of $\Theta_T = 0.14$ will be the major focus of this investigation. It should be noted that this also implies that the centre of the oscillation occurs at a point in parameter space where no 'stationary-transition' activity occurred in the Extended-Regime experiment, suggesting that the sloped lid causes resonance to occur at a larger Hide Number than with the flat lid, as was discussed during the drift-rate study in the last chapter.

To illustrate how the 'stationary-transition' oscillation arises and changes as Taylor Number is increased, Figure 5.11 presents a selection of mid-depth azimuthal velocity wavenumber-3 component amplitudes over time, each 0.1 $rads^{-1}$ apart, over the course of the scan of $\Theta_T = 0.14$.

Rather than showing the separate azimuthal and radial components at a single radial location, as used in Figure 5.6, Figure 5.11 is comprised of the RMS of the velocities at each individual radial location, creating radially-averaged velocities so that no information is lost.

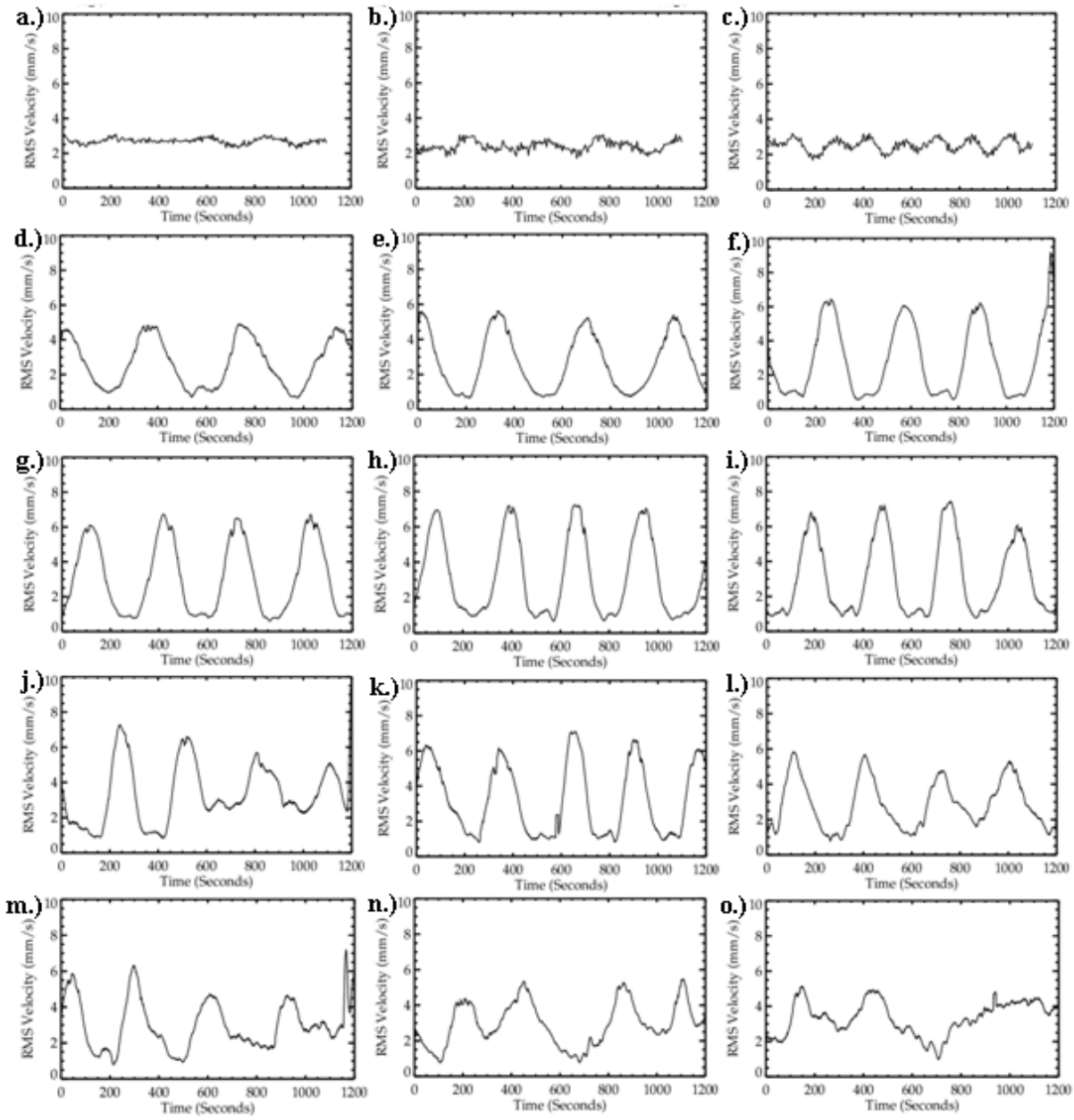

Figure 5.11: Wavenumber-3 component RMS velocities for constant Hide Number $= 0.14$ *at Level 3 (mid-depth);* *a.)* $\Omega = 0.8$ *rads*$^{-1}$, $\Delta T = 1.13K$, $\mathcal{T} = 3.635x10^7$, *b.)* $\Omega = 0.9$ *rads*$^{-1}$, $\Delta T = 1.43K$, $\mathcal{T} = 4.601x10^7$, *c.)* $\Omega = 1.0$ *rads*$^{-1}$, $\Delta T = 1.77K$, $\mathcal{T} = 5.680x10^7$, *d.)* $\Omega = 1.1$ *rads*$^{-1}$, $\Delta T = 2.14K$, $\mathcal{T} = 6.673x10^7$, *e.)* $\Omega = 1.2$ *rads*$^{-1}$, $\Delta T = 2.55K$, $\mathcal{T} = 8.179x10^7$, *f.)* $\Omega = 1.3$ *rads*$^{-1}$, $\Delta T = 2.99K$, $\mathcal{T} = 9.599x10^7$, *g.)* $\Omega = 1.4$ *rads*$^{-1}$, $\Delta T = 3.47K$, $\mathcal{T} = 1.113x10^8$, *h.)* $\Omega = 1.5$ *rads*$^{-1}$, $\Delta T = 3.98K$, $\mathcal{T} = 1.278x10^8$, *i.)* $\Omega = 1.6$ *rads*$^{-1}$, $\Delta T = 4.53K$, $\mathcal{T} = 1.454x10^8$, *j.)* $\Omega = 1.7$ *rads*$^{-1}$, $\Delta T = 5.12K$, $\mathcal{T} = 1.641x10^8$, *k.)* $\Omega = 1.8$ *rads*$^{-1}$, $\Delta T = 5.74K$, $\mathcal{T} = 1.840x10^8$, *l.)* $\Omega = 1.9$ *rads*$^{-1}$, $\Delta T = 6.39K$, $\mathcal{T} = 2.050x10^8$, *m.)* $\Omega = 2.0$ *rads*$^{-1}$, $\Delta T = 7.08K$, $\mathcal{T} = 2.272x10^8$, *n.)* $\Omega = 2.1$ *rads*$^{-1}$, $\Delta T = 7.81K$, $\mathcal{T} = 2.505x10^8$, *o.)* $\Omega = 2.2$ *rads*$^{-1}$, $\Delta T = 8.57K$, $\mathcal{T} = 2.749x10^8$.

Figure 5.11a shows that, outside of the 'stationary-transition' regime, in the stationary wavenumber-3 regime of Figure 5.2a, the dominant wavenumber-3 component remains more uniform over time and shows no evidence of the oscillation. The maximum amplitude reached is also much lower for this area of parameter space. Similarly, the phase diagram at this point displays a completely stationary wavenumber-3, with no rocking encountered at all. This, and the fact that all the other wavenumbers are also drifting more regularly, once again suggests that the oscillation is linked to the interactions of drifting and stationary waves. In (b) and (c), the flow is now evidently within an amplitude vacillation regime, as noted by the occurrence of an oscillatory structure. This vacillation oscillation is notably much weaker and more sinusoidal than the 'stationary-transition' oscillation shown in Figure 5.6, suggesting the flow is still far from linear resonance and undergoing few nonlinear interactions. As the Taylor Number increases further, the flow enters the 'stationary-transition' region, and the peak amplitude in (d) and (e) suddenly increases greatly, whilst the trough values similarly drop towards zero. This transition appears to be accompanied by a period-doubling event, as the frequency of the amplitude oscillation can be observed to halve as the flow moves from (c) to (d). Throughout (f), (g) and (h) the peak amplitudes continue to increase until the maximum point of the oscillation is reached. At this maximum, (i), the amplitude of the wavenumber-3 component is larger than in previous points in parameter space, but otherwise the oscillation structure is mostly the same. Most notably, the period is unchanged, being still roughly 300s. The phase time-series at this point of parameter space shows that the phase rocking of wavenumber-3 is still occurring, but is now even larger, with the radial case showing at least -3 rad of difference between the peak and trough states. In (j), (k) and (l) the amplitude of the wavenumber-3 oscillation begins to become smaller and more irregular over time as the rotation rate is increased. In particular, at about 650s and 950s in (j), the troughs of the oscillation no longer cause the wavenumber-3 to lose its dominance compared with the other wavenumbers. At those points, the structure resembles that of (a), in the region of parameter space before the oscillation was formed. Furthermore, the phase diagram at this point of parameter space shows that the phase rocking of the wavenumber-3 component is now sporadic in occurrence, and elsewhere the phase is constant, at -1 rad for the radial case. This may show that the flow is leaving the oscillation regime, and that this is the upper limit of the 'stationary-

transition' region. By the final three cases, (m), (n) and (o), Figure 5.2a shows that the parameter space has reached a chaotic flow regime and the oscillatory structure is now very irregular, becoming difficult to discern from the chaos of the flow.

In summary then, as the Taylor Number is increased, the flow changes from a dominant wavenumber-3 without regular oscillations at Figure5.11a, to one in which notable oscillations in wavenumber-3 (and harmonics) appear at (d), which then grow in strength until a maximum amplitude is reached at (i), whilst the period continues to remain constant. In the case of the scan of $\Theta_T = 0.14$, this maximum occurs at 1.6 rads^{-1} (a Taylor Number of $1.454x10^8$). For comparison, the maximum of the oscillation in the scan of $\Theta_T = 0.1$ occurs at 1.7 rads^{-1} (a Taylor Number of $1.641x10^8$), and the maxima of the other scans are hard to define, as mentioned previously. After the oscillation reaches a maximum, increasing the Taylor Number further causes the amplitude to begin to decrease again at (j), continuing until the oscillations become less regular, in turn leading to regions where the wavenumber-3 component does not disappear into the background flow at the troughs. Eventually, at very large Taylor Numbers, this leads to chaos at (m), and finally the oscillatory structure of the wavenumber-3 component dies out at (o). For all scans that encountered the oscillation, this basic evolution of the flow over increasing parameters is the same.

As the above evolution would appear to suggest a bifurcation sequence of a near-resonant flow, a bifurcation diagram was produced, showing the amplitude of both the peaks and troughs of the wavenumber-3 RMS velocities as the Taylor Number is increased. This bifurcation diagram is shown in Figure 5.12.

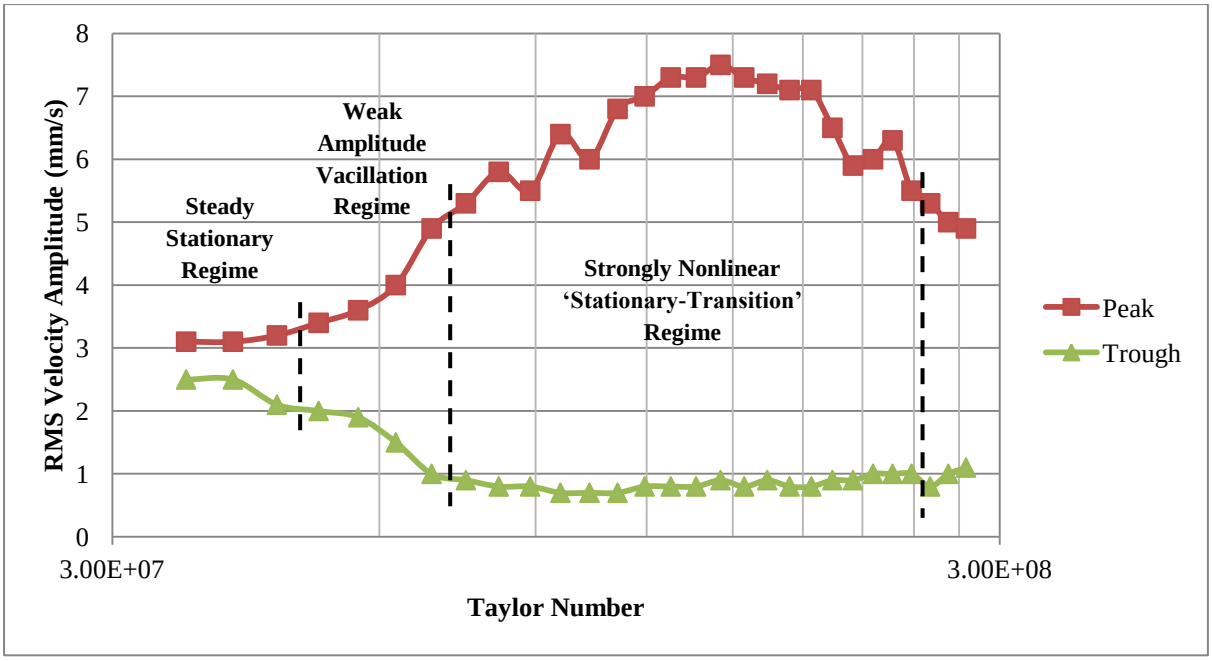

Figure 5.12: Bifurcation diagram of wavenumber-3 component RMS velocities at Level 3 (mid-depth), for peak and trough amplitudes against Taylor Number during the $\Theta_T = 0.14$ *scan.*

Figure 5.12 shows clearly the bifurcation sequence of the $\Theta_T = 0.14$ scan, and suggests a resonance origin from the peaked amplitude response near the maximum. This maximum is then assumed to be the point closest to the location of linear resonance, with the period-doubling event witnessed in Figure 5.11d highlighting the beginning of the near-resonant flow, and the route to chaos starting in Figure 5.11m marking its end. As the bifurcations shown are oscillatory in nature, they are therefore Hopf bifurcations, and hence Figure 5.12 is also evidence that the mechanism of generation for resonant nonlinear interactions in the annulus may be similar to what was found by Jin and Ghil (1990) in a barotropic channel model.

Existence of Resonant Wave-Triads

It has been discussed that the oscillation is linked to the interactions of quasi-stationary waves - it is therefore possible that these waves form part of a resonant wave-triad. From Equation 2.1 it is known that the wave-triad must be composed of three components with wavenumber modes that have a summation or difference that equals zero. Since it can be assumed that such a triad would include

interactions between a component forced by the wavenumber-3 base and the dominant wavenumber-3 component, this suggests observation of the phase of the wavenumber-6 component. As such, Figure 5.13 shows the phase from near the maximum amplitude of the oscillations, with the phase of the wavenumber-3 component compared to the phase of the wavenumber-6 component, along with the amplitude of the wavenumber-3 component (not to scale) for illustration of where the peaks and troughs of the oscillation lie.

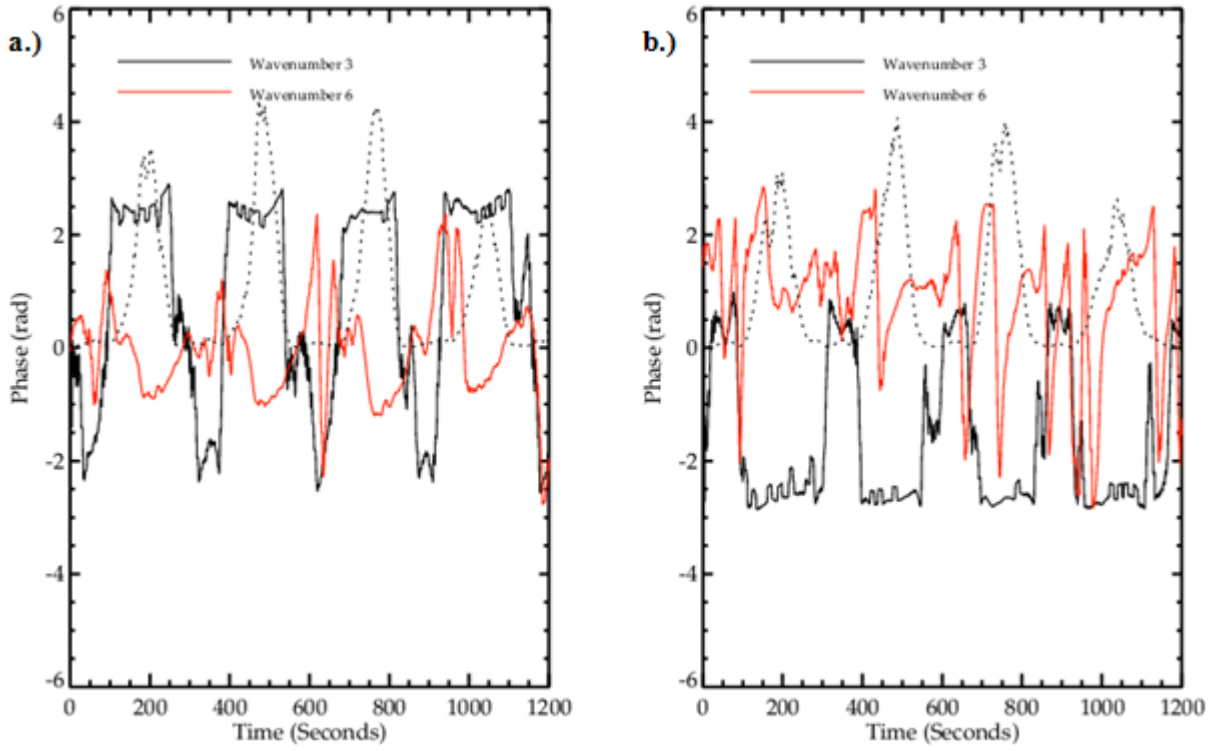

Figure 5.13: Wavenumber-3 phase (black) against wavenumber-6 phase (red), along with the amplitude of the wavenumber-3 (dotted black) for $\Omega = 1.6$ *rads*$^{-1}$, $\Delta T = 4.53K$, $\mathcal{T} = 1.454x10^8$, $\Theta_T = 0.14$*; a.) azimuthal velocity, b.) radial velocity.*

As can be seen in Figure 5.13, for both the radial and the azimuthal velocity cases, the phase of the wavenumber-3 component oscillates almost discretely between two points, depending on whether the wavenumber-3 amplitude is at a peak or a trough. This observation was previously shown in Figure 5.6 for a lower Taylor Number, and appears to be a robust feature of the oscillation. At the same time, the phase of the wavenumber-6 component is quasi-stationary, with a noisy periodic oscillation around a constant value (at about 0 rad for the azimuthal case and about $+1$ rad for the

radial cases) that undergoes frequent phase-slips. The most substantial of these slips appear to occur at regular intervals and happen at the same time as (in the azimuthal velocity case) or a constant interval after (in the radial velocity case) the change in phase of the wavenumber-3 component. This would seem to further suggest a relationship between a quasi-stationary wavenumber-6 and a quasi-stationary wavenumber-3. For further investigation, Figure 5.14 gives the phase difference between the two components against time for the same example.

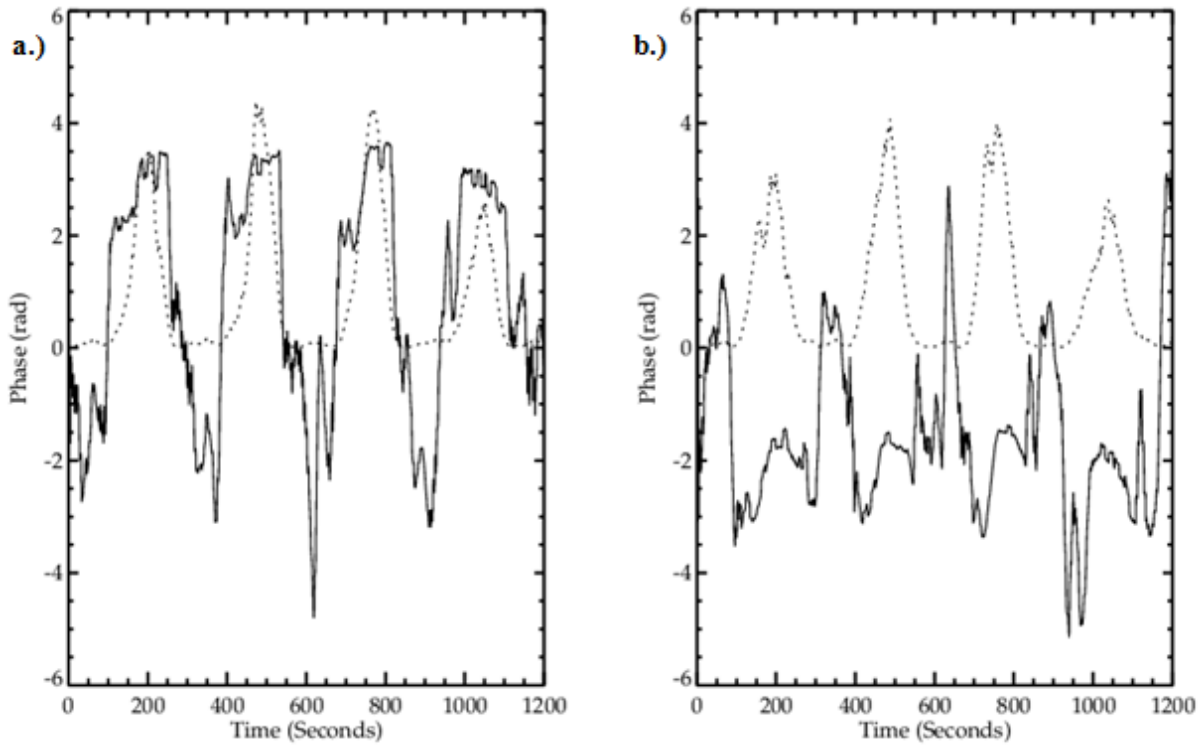

Figure 5.14: Phase difference between wavenumber-3 component and wavenumber-6 component (black), along with the amplitude of the wavenumber-3 (dotted black) for $\Omega = 1.6$ *rads*$^{-1}$, $\Delta T = 4.53K$, $\mathcal{T} = 1.454x10^{8}$, $\Theta_T = 0.14$, *a.) azimuthal velocity, b.) radial velocity.*

Especially clearly in the azimuthal case, Figure 5.14 shows that the phase difference is strongly periodic over time and over a limited range[17]. Hence, the phases of the wavenumber-3 and wavenumber-6 components vary coherently both with each other and with the amplitude variation of the oscillation. This suggests that the first condition for the existence of a resonant wave-triad is met.

[17] If both components were drifting independently of each other at a steady rate, the phase difference would also appear periodic, but only because the phase difference would jump every time the difference exceeded $+2\pi$. However, in this case, the range of variation is only between 0 and $+\pi$.

The second condition for a resonant wave-triad, given in Equation 2.2, is that the drifting frequencies of the wave modes must also have a summation or difference that equals zero. Since both wave components of the triad are quasi-stationary, and the barotropic component is forced directly by the stationary topography, all parts of the triad can be assumed to have negligible drift frequency, within a given frame of reference. Thus, the second condition for resonance is also confirmed to be met.

Hence, with both conditions met, the oscillation appears to contain a self-interacting resonant wave-triad between both the baroclinic and topographically-forced barotropic components of the topographically resonant quasi-stationary wavenumber-3 and the quasi-stationary wavenumber-6 baroclinic component. In this way, the three zonal wavenumbers (3, 3, and 6) can be summed to zero, satisfying the first condition for the occurrence of the resonant wave-triad[18]. This wave-triad only appears at a specific location in parameter space, referred to as the 'stationary-transition' region, where the flow enters a near-resonant state. Moving closer to the centre of the linear resonance causes the wave-triad to strengthen and the oscillation to increase in amplitude, and moving further away weakens the wave-triad, allowing the circulation to return to a non-resonating state. In this way, the nonlinear resonant interactions that cause the oscillation are noted to involve resonant triad wave-wave interactions, as well as the wave-zonal flow interactions shown in Figure 5.10.

Vertical Structure

By observation of the vertical structure, the changes to the oscillation and flow structure at different heights can be investigated. Figure 5.15 gives a snapshot of the vertical structure in the 'stationary-transition' regime, quickly switching between levels so that all images are taken at the same time, as much as physically possible. Each image is roughly 10 seconds apart, to allow for a streakline picture, and, considering the slow speed of drifting and oscillation, this was determined to be sufficient.

[18] It can be noted that the three vertical wavenumbers can also be summed to zero as well, satisfying another resonant interaction condition.

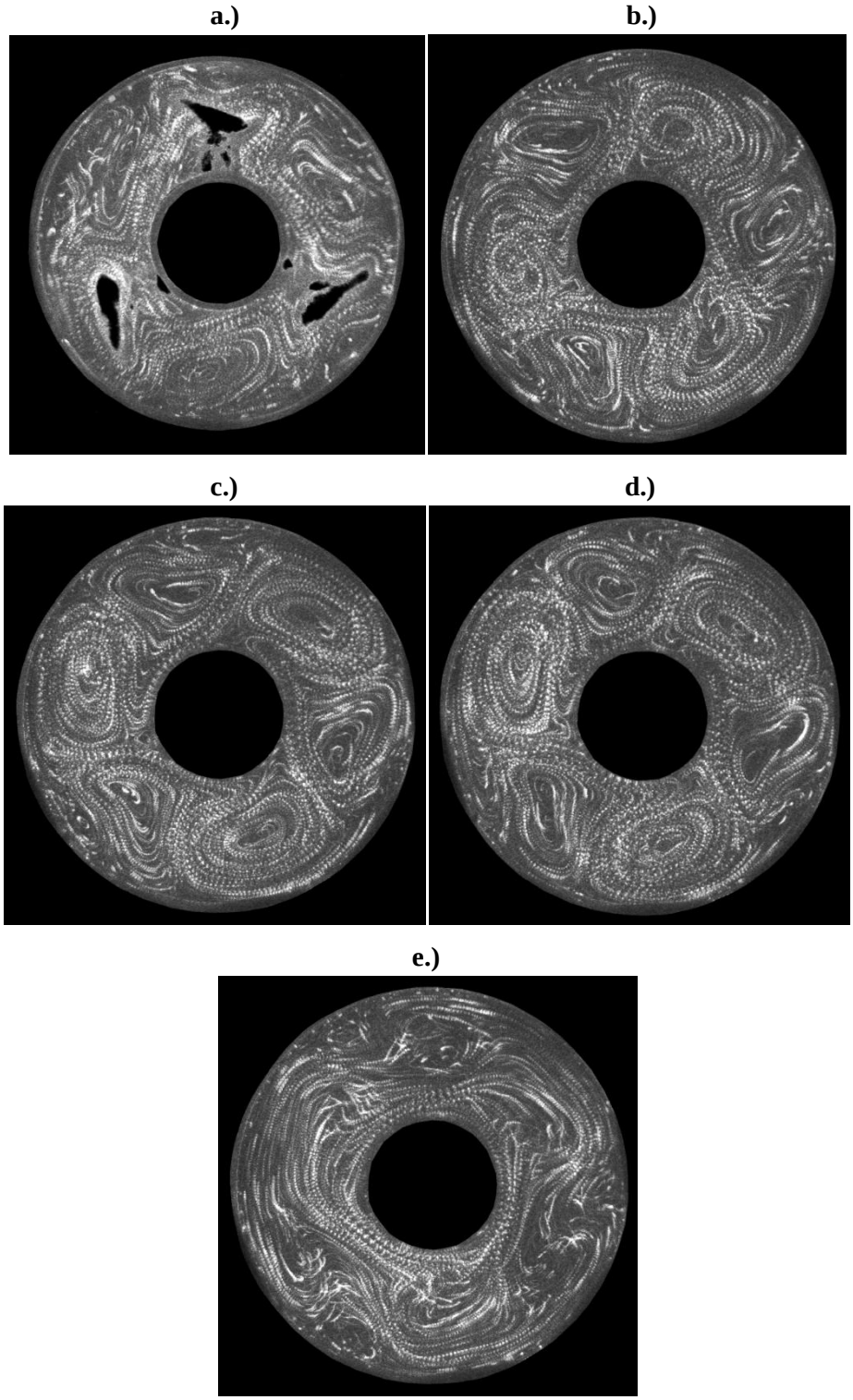

Figure 5.15: Streakline images for $\Omega = 1.3$ rads^{-1}, $\Delta T = 2.99K$, $\mathcal{T} = 9.599x10^{7}$, $\Theta_T = 0.14$; a.) Level 5, b.) Level 4, c.) Level 3, d.) Level 2, e.) Level 1.

Figure 5.15a highlights the location of the topographic peaks via particles that have settled on the base, creating three black shadows. At this level, there is a wavenumber-3 structure, with each wave centred directly over the topographic peaks. Above this height, the dominant wavenumber-3 component remains, as seen in (b), but the baroclinic waves can be observed to increase in strength until the mid-depth (c), as well as showing a shift with height, with the cyclonic eddies in each example occurring slightly further downstream (clockwise). This downstream shift continues with (d), whilst the rest of the flow structure is unchanged. Near the sloped lid, however, (e) shows a very weak wavenumber-3 structure, suggesting that proximity to the lid can act to suppress baroclinic wave activity. This is most likely to be associated with the reduced zonal mean flow that would be expected to be found near the lid, due to the upper boundary layer. The baroclinic eddies at this height, whilst weak, are still found to occur in locations downstream of the previous levels. From these five images, the quasi-stationary wavenumber-3 section of the 'stationary-transition' regime can be observed to be fairly uniform with height.

Similarly, over a longer timescale, Figure 5.16 shows the variation over time of the radial velocity amplitudes of the first ten wavenumbers, in the same manner as in Figure 5.6, for runs at each height.

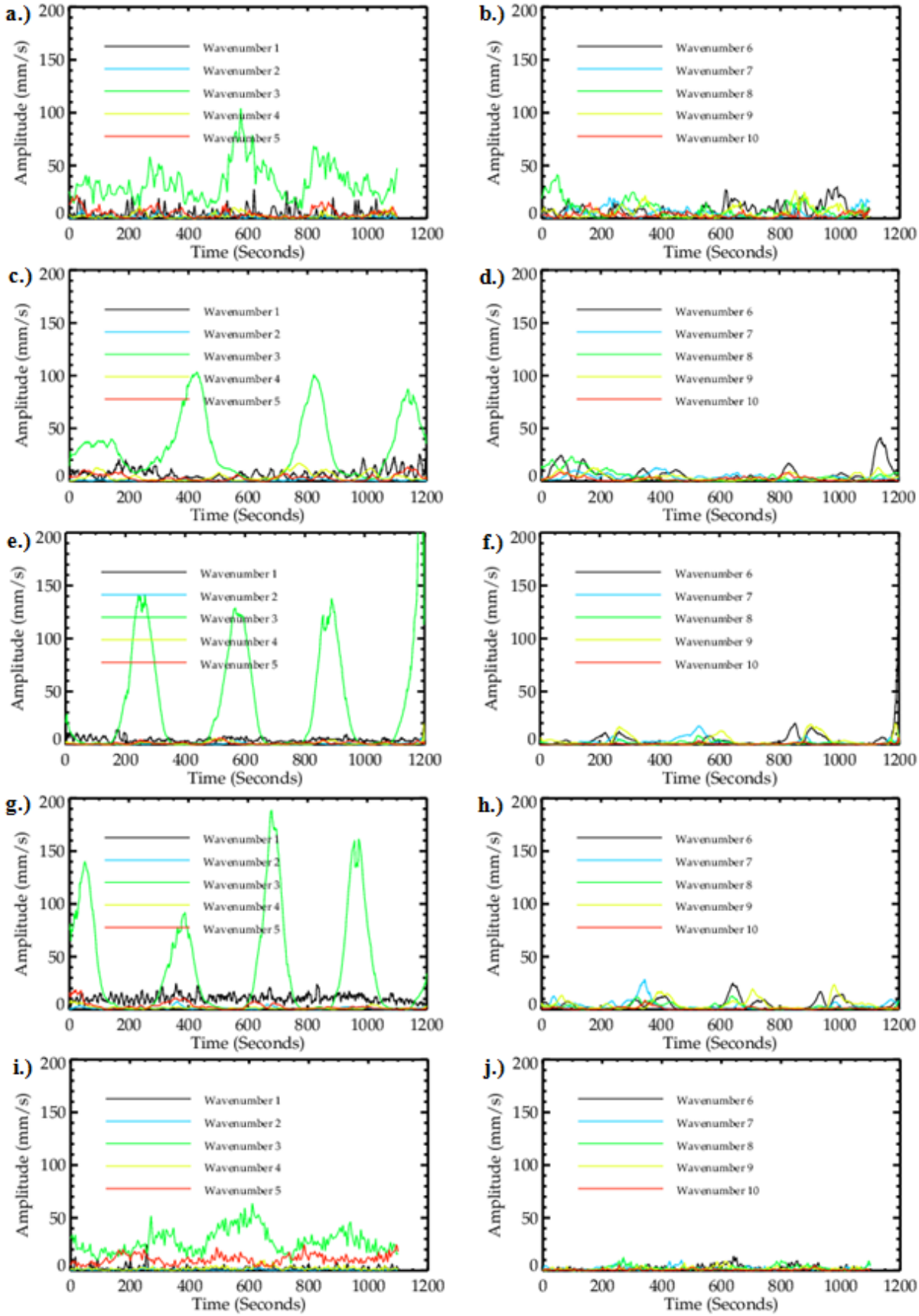

Figure 5.16: Radial velocity amplitude for $\Omega = 1.3\ rads^{-1}$, $\Delta T = 2.99K$, $\mathcal{T} = 9.599x10^{7}$, $\Theta_T = 0.14$; a.) Level 5 wavenumbers 1-5, b.) Level 5 wavenumbers 6-10, c.) Level 4 wavenumbers 1-5, d.) Level 4 wavenumbers 6-10, e.) Level 3 wavenumbers 1-5, f.) Level 3 wavenumbers 6-10, g.) Level 2 wavenumbers 1-5, h.) Level 2 wavenumbers 6-10, i.) Level 1 wavenumbers 1-5, j.) Level 1 wavenumbers 6-10.

Figure 5.16 shows that the oscillation associated with the 'stationary-transition' region is felt most strongly at the centre of the annulus, especially at Level 3 (e) and Level 2 (g). Those heights also exhibit the largest amplitudes of the wavenumber-3 velocity component. By contrast, due to the impact of proximity to the topography and the sloped lid, respectively, Level 5 (a) and Level 1 (i) are much more irregular, though wavenumber-3 is still dominant. As such, with the exception of areas close to the top and bottom of the annulus, the flow structures and oscillation dynamics are once again found to be reasonably uniform in the vertical direction over time.

5.3 Analysis – Resonance Experiment

By comparing Figure 5.2a to Figure 4.7, the effect of the addition of a sloped lid can be observed. It was found that, over a well-sampled section of parameter space, there was a greater preference for stationary wavenumber-3 structures with little to no vacillation. It is suggested that this is due to the sloped lid making topographic resonance more likely to occur, via a reduction in the drift speed of the baroclinic waves. This in turn would cause an increase in nonlinear interactions between the near-resonant drifting waves and the stationary topography, thus increasing the flow's locking to the topography. In addition, the major difference between the regime diagrams was the extension of the 'stationary-transition' region. This regime, under Fourier analysis, was discovered to be associated with an oscillation of the wavenumber-3 component and its harmonics. Over scans of constant Hide Number, the strongest oscillation was found at $\Theta_T = 0.14$. The period of this oscillation is about 300s, and so is equivalent to 29.8 'days' for the case at its maximum amplitude at 1.6 rads^{-1}, with a minimum of 23.3 'days' at its upper limit of 2.2 rads^{-1}, and a maximum of 41.5 'days' at its lower limit of 1.15 rads^{-1}. This 23.3 to 41.5 'day' oscillation is therefore well within the 10-100 day timescale for atmospheric LFV, and, perhaps more importantly, overlaps LG's resonant 36-40 day extratropic oscillation, again suggesting a resonant origin. Furthermore, Tian et al (2001) gives an equation for roughly calculating the location in parameter space where a flow's jet velocity becomes linearly resonant with its topography, as follows:

$$U_r = \frac{2 \cdot \Omega \cdot s}{d({k_x}^2 + {k_y}^2)} \quad (5.1)$$

where U_r is the "optimal" resonant jet velocity, s is the topographic slope, and k_x and k_y are the topographic wavenumbers in Cartesian coordinates. Tian et al defined k_x as the zonal wavenumber of the base over the mean radial jet location, and assumed that k_y was negligible. Making the same assumptions for the current experimental analysis, this gives values of $k_x = 3/69.5 = 0.0432$ mm^{-1} and $k_y = 0$. Using 1.6 rads^{-1} for the rotation rate, the depth given in Chapter 3, as well as the slope of the lid (the lid has an angle of 22°, thus $s = tan22 = 0.404$), this formula gives a resonant jet velocity of 2.61 mms^{-1}. At the peaks of the resonant oscillation, the maximum jet velocity reached was found to be 5.97 mms^{-1}. Hence, by this method, the flow is in a super-resonant state at the peaks, and drops to a sub-resonant state as the jet dissipates during the troughs. Once again, this suggests that the location of greatest topographic resonance in parameter space is somewhere close to the maximum oscillation, 1.6 rads^{-1}, of the scan at $\Theta_T = 0.14$. For comparison, Tian et al found their zonal states to be super-resonant, and their blocked states to be sub-resonant. This would seem to imply that there is a link between the blocked and zonal states of multiple equilibria, discussed in Chapter 2, and the peaks and troughs of the current oscillation. This was also suggested by Li, Kung and Pfeffer (1992) for their similar quasi-stationary oscillation with an assumed topographically resonant origin. As such, it may be possible that the oscillation observed is a shift between the two states, with the peaks forming the zonal flow and the troughs the blocked flow, but without either state being discrete or permanent, as would be required for multiple equilibria. Again, this has some basis in atmospheric observations, with Weeks et al (1997) noting that atmospheric blocking events and LFV have the same timescale, that of 10-100 days. As such, it has been suggested that the transitions between the blocked state and the zonal state are likely to be the manifestation of LFV in the atmosphere. Despite being unable to display a case of multiple equilibria in the annulus, due to a lack of notable hysteresis, the current investigation's resonant oscillation can be described not only as part of LFV, but also as an example highlighting the link between LFV and multiple equilibria.

Further analysis suggests that the oscillation has both nonlinear wave-zonal flow interactions, characterised by kinetic energy transfer between the dominant resonating mode and the mean flow, and nonlinear wave-wave interactions, characterised by the occurrence of a resonant wave-triad between the baroclinic and barotropic components of the quasi-stationary wavenumber-3 and the baroclinic quasi-stationary wavenumber-6 component. A Hopf bifurcation sequence was also discovered as the Taylor Number was increased, with a peaked amplitude response near the maximum suggested as the location for linear resonance. In this way, the mechanism for the impact of topographic resonance on the flow agrees well with the study described in Jin and Ghil (1990), despite that work being a numerical investigation, and employing a barotropic channel model. Futhermore, over the course of the bifurcation sequence, a period-doubling event was witnessed as the flow transitioned from amplitude vacillation to the near-resonant oscillation, and routes to chaos, like those found in Feigenbaum (1979) and Lin, Busse and Ghil (1989), were observed as the flow reached Taylor Numbers larger than the maximum amplitude location. In addition to the period of the oscillation being within the LFV limits, similarities to Keppenne et al's (2000) topographic-forced 'tilted-trough vacillation' were also noted. According to Rhines (1975) and Wordsworth (2008) resonant triad wave-wave interactions are suggested as one of the causes of the onset of turbulence, but this effect was not found in the current study, as even the maximum impact of the resonance caused a fairly stable oscillation. However, as mentioned previously, a route to chaos was noted to occur after the Taylor Number was increased further than this maximum, as well as greater irregularity to the oscillation structure, and this may signify the beginnings of a form of turbulence. The results also show some preliminary evidence of parallels to stratospheric sudden warmings, as discussed by Risch (1999), as the collapse or vortex-shedding of the dominant wavenumber-3 component during the oscillation can be thought of as analogous to the collapse or displacement of the stratospheric polar vortex that leads to the atmospheric warming. This would imply that the troughs of the oscillation also correspond to the noted increase in temperature of the polar air, which in turn leads to the reversal of the meridional temperature gradient. Further temperature data would be needed to confirm this. Finally, it can be noted that, in this investigation, topography, sloped lid and reversed temperature gradient were all necessary for the oscillation regime to be robust.

In the vertical structure, the results gathered also agree well with established topographic theory. Once again, a small phase shift with height can be observed in the stationary waves of Figure 5.15 since, as discussed by Leach (1981), Reinhold and Pierrehumbert (1982) and found in the previous chapter's Extended-Regime experiment, topographic waves slope westward (i.e. downstream) with height. In the case of the Resonance experiments, however, the reversed temperature gradient means that 'downstream' is the opposite to that of the Extended-Regime experiment, as the direction of convection has been reversed. Aside from the weakened flow structures found in the levels nearest the base and lid, the 'stationary-transition' region and its corresponding resonant oscillation were found to be fairly uniform in the vertical direction.

As for real-world atmospheric context to the oscillation, the results of this study have a parallel to the intraseasonal, topographic-forced waves and flows in the Northern Hemisphere Extratropics. The Northern Hemisphere has essentially a wavenumber-2 topography, however, so it is unlikely that wavenumber-3 and wavenumber-6 components will make up any atmospheric wave-triads, if they exist. Wavenumber-2 and wavenumber-4 would fit better, and these are what are observed during the zonal and blocked states, respectively, of the atmosphere, as shown in Figure 2.4. The oscillation is also put forward as a possible mechanism for the occurrence of LFV, the nonlinear interactions of the resonant wave-triad between the topography and the circulation giving rise to atmospheric zonal flow vacillation and transitions between multiple equilibria regimes. Petoukhov et al (2012) also give the resonant wave-triad a context in terms of climate change, with evidence that resonance of high wavenumbers in the atmosphere (wavenumber-6, wavenumber-7 and wavenumber-8 in that study) leads to persistent blocked events, in turn leading to extreme weather events in certain locations. In order to continue this investigation, the Partial Barriers and Thermal Topography experiments will also be examined for topographically resonant effects, especially the occurrence of oscillations, wave-zonal flow interactions and wave-triads.

Chapter 6

Partial Barriers and Blocking

This chapter will focus on experiments utilising a single isolated ridge, as a way of studying the effect of topographic partial barriers on the structure and behaviour of a baroclinic flow. Due to topographic resonance impacts being found in the last chapter with a periodic, fully-sinusoidal wavenumber-3 base, this study is motivated by questions concerning whether resonance can still occur with complex, partially sinusoidal topography, such as the isolated ridge. Any comparisons or contrasts to the previous investigation into resonant phenomena will therefore be examined. In addition, characterisation of the contrast between the azimuthally-trapped bottom flow and the rest of the unobstructed circulation caused by employing partial barriers in the annulus will allow the study of both blocking and the effects of continental shelves on the thermohaline circulation in an ocean basin, as well as investigation into the unresolved questions about the existence of multiple equilibria. First of all, a general outline of the method of experimentation will be given, followed by the results gathered. After that the results will be analysed in detail, with comparison to both the Extended-Regime experiment and the literature. The experiments will be presented in such a manner as to allow immediate comparison of the similarities and differences between the topographic forced results and those forced by azimuthally-varying heating in the thermal experiments, which will be discussed in the next chapter. More detail on the presented Figures will be explained in the introduction to each section.

6.1 Experimental Arrangement

As described in Chapter 3, these experiments replaced the sinusoidal wavenumber-3 topography with a single isolated ridge, with the rest of the base being flat, as shown in Figure 3.7. Seeing as how resonance was not the sole focus of these experiments, the constant Hide Number scans of the previous chapter were dropped in favour of the Extended-Regime experiment's investigation at single parameter space points. The sloped lid and reversed temperature gradient, however, were kept, as it was believed that the addition of the beta effect would increase the chance of observing resonant oscillations. In this way, the Partial Barriers experiment could be compared to both of the previous studies.

6.2 Results and Analysis

The results taken followed a similar procedure to those of the Extended-Regime experiment, investigating from 0.4 $rads^{-1}$ to 2 $rads^{-1}$, at intervals of 0.2 $rads^{-1}$, and from 2K to 7K, at intervals of 1K. Both real-time streakline images and vector velocity maps created by CIV were used to collect the initial flow structure data, starting at 3600s after spin up. Each Figure is captioned with this time, as well as the light level, rotation rate, temperature difference, Taylor Number and Hide Number (dimensionless numbers calculated to 3s.f.). For sake of space and clarity, not every result that was taken will be given in this section. Instead, the regime diagram of Figure 6.1 has been compiled from the dominant flow structure at each investigated point of parameter space.

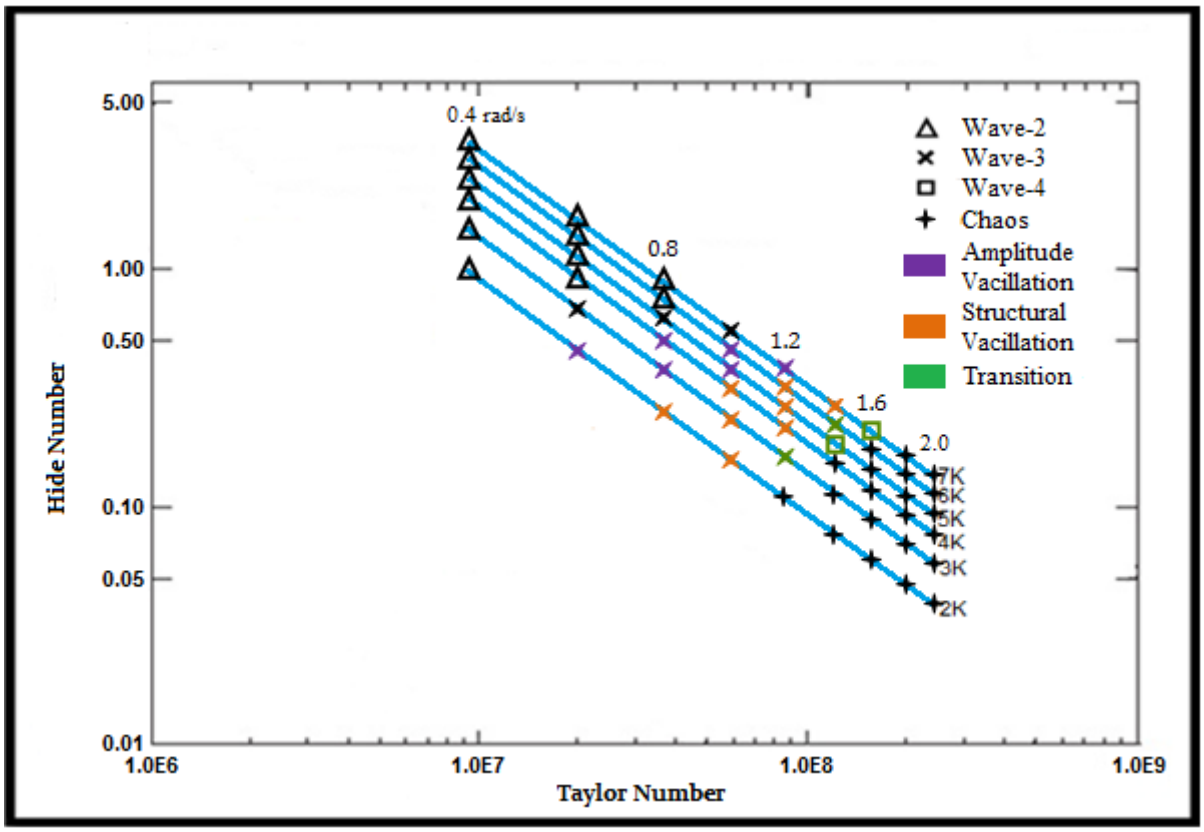

Figure 6.1: Regime diagram with locations and dominant flow characteristics of the results of the Partial Barriers experiments.

Figure 6.1 is comprised of two major sections: an 'interference' region, at larger Hide Numbers, where the impact of the isolated wave is strongly observable throughout the flow; and an 'irregular' region, at lower Hide Numbers, where the flow is erratic in time and space. During the former regime baroclinic waves can be observed, though the circulation does not ever become an axisymmetric flow (almost certainly due to the asymmetrical topography), but instead contains a drifting wave structure for the whole region, transitioning from wavenumber-2 to wavenumber-3, and with occasional transitions to wavenumber-4, as the rotation rate increases. Compared to the Extended-Regime experiment with the wavenumber-3 base, amplitude and structural vacillation are encountered in the same areas, but some points in parameter space, denoted in Figure 6.1 as the green Transition region, exhibit a greatly increased number of transitions between wavenumbers over time. In these flows, which lie near the 'irregular' region, the dominant wavenumber is only foremost for part of the time, with other wavenumbers irregularly dominating the structure. This is especially

common between wavenumber-3 and wavenumber-4, as those are the wavenumbers most often encountered before chaos takes over. Typically, the transitions are between adjacent wavenumbers, so that wavenumber-2 may transition to wavenumber-1 or wavenumber-3 and wavenumber-3 may transition to wavenumber-2 or wavenumber-4. This could suggest a low-dimensional wavenumber competition via wave-zonal flow nonlinear interactions. Dominant wavenumbers higher than four were not found.

'Interference' Flow Structure

In addition to the above, it can be noted that the drifting waves are modified as they encounter and cross the topography, creating temporary flow structures, even at the middle and upper levels of the annulus. To illustrate this effect, an example of the time variations of the flow structure from this region is given in Figure 6.2.

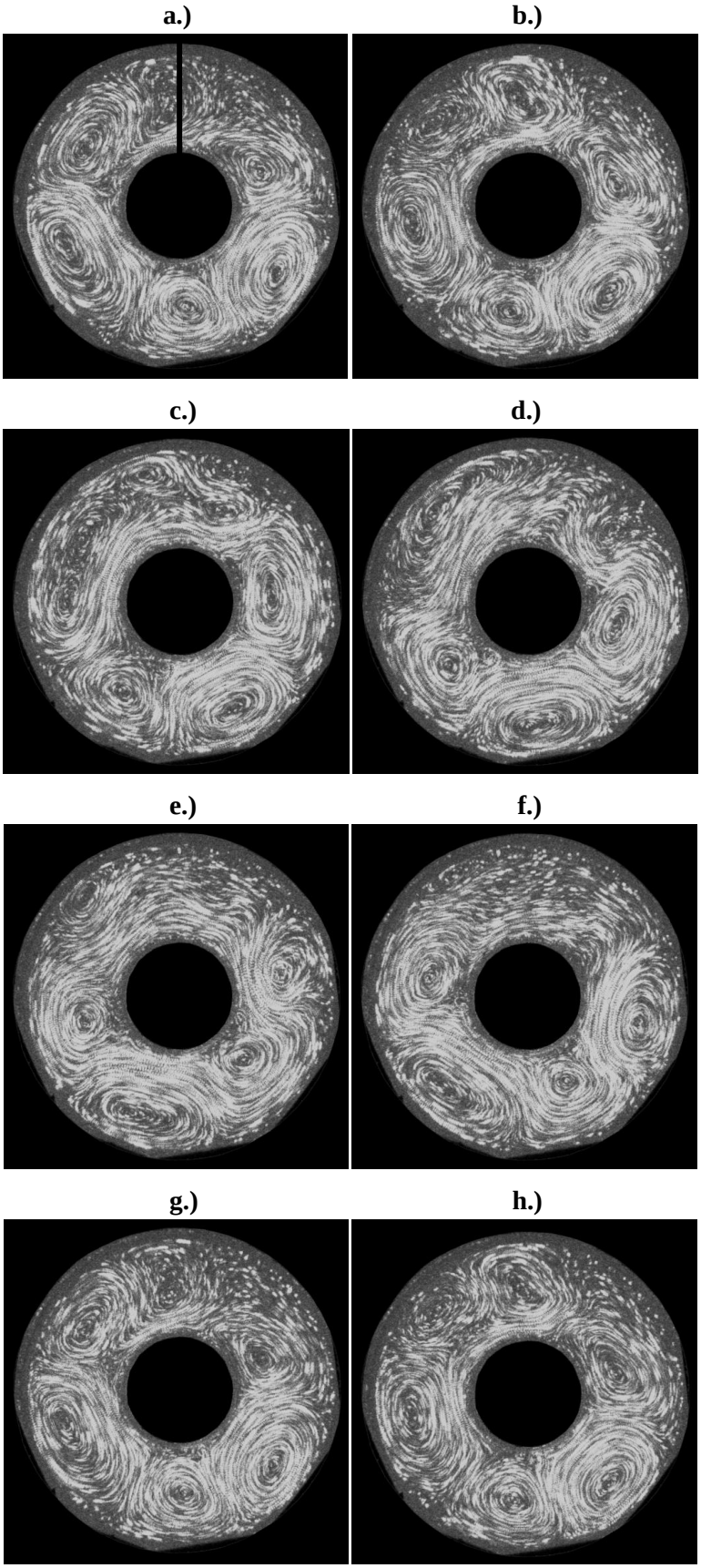

Figure 6.2: Streakline series at Level 3 (mid-depth), $\Omega = 0.8$ rads^{-1}, $\Delta T = 4K$, $\mathcal{T} = 3.635x10^{7}$, $\Theta_T = 0.494$; a.) $t = 3650s$, b.) $t = 3680s$, c.) $t = 3710s$, d.) $t = 3740s$, e.) $t = 3770s$, f.) $t = 3800s$, g.) $t = 3830s$, h.) $t = 3860s$.

For clarity, an indication of where the peak of the topography lies has been added to Figure 6.2a, so that the main aspects of the 'interference' regime can be observed. The flow in (a) starts off as a clockwise-drifting wavenumber-3, but during (b) one of the cyclonic eddies (at the upper left of the image) encounters the topography and weakens until it disappears. At the same time, the weak anticyclonic eddy directly above the topography strengthens. In (c) this anticyclonic eddy joins up with a second further upstream (anticlockwise). The flow then appears to be a skewed wavenumber-2 which steadily continues drifting throughout (d) and (e). This continues until (f), where the disappeared cyclonic eddy seems to reappear on the other side (downstream) of the topography - the flow now resembling a wavenumber-3, but still remaining skewed. By (g), the flow has drifted far enough that the original wavenumber-3 structure has returned, and will continue until the next eddy encounters the topography, as in (h) whereby the cycle repeats itself. The example given in Figure 6.2 is at mid-depth, but can be found at all levels except the bottom, which is physically blocked by the peak of the base and will be discussed later. At lower rotation rates, the dominant component is a wavenumber-2, and so when the waves disappear when encountering the topography the flow resembles a skewed wavenumber-1. This is an example of the topographic effect of jet shifting, also known as jet deflection, as discussed by Tian et al (2001). This jet-shifting was also noted in the experiments with partial vertical and radial barriers of Harlander et al (2012), who found similar transitions from wavenumber-3 to a skewed wavenumber-2 as the waves crossed the topographic peak. In addition, as can be seen, the flow patterns demonstrate stronger anti-cyclonic eddies and weaker jets when compared to the Extended-Regime experiment, especially during the wavenumber-3 structure of the flow, i.e. (a), (b), (g) and (h). This may again be a feature of the inclusion of the sloped lid, as it was also observed in the Resonance experiment.

To illustrate the 'interference' regime flow structure over a longer timescale than the image sequence in Figure 6.2, Figure 6.3 shows the radial velocity for every point on a complete azimuthal circle at mid-radius, for the same parameters over the entire 1100s run. Azimuthal position is given in

degrees where positive is anticlockwise, and wherein the centre of the topographic peak occurs at about 100°.

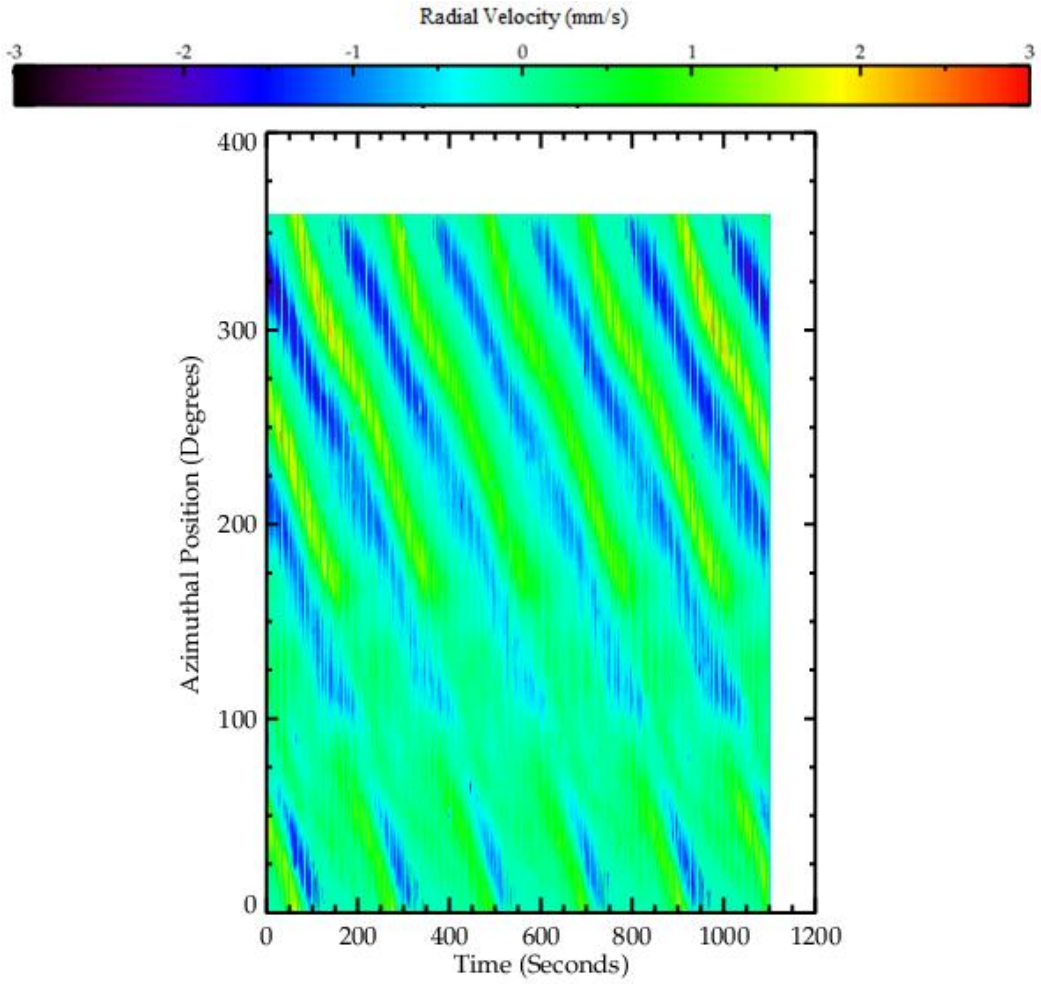

Figure 6.3: Radial velocity over time against azimuthal position for Level 3 (mid-depth), $\Omega = 0.8$ *rads*$^{-1}$, $\Delta T = 4K$, $\mathcal{T} = 3.635x10^{7}$, $\Theta_T = 0.494$.

Figure 6.3 shows the clockwise drifting wavenumber-3 structure of the flow throughout the entire run, becoming more negative in azimuthal position over time, and also highlights the impact upon the wave as it encounters the topography, which begins at around an azimuthal position of 150°. At this point, the drifting wave can be observed to greatly reduce in strength, becoming difficult to discern from the flow between waves. This is equivalent to the apparent visual disappearance of the wave as it encounters the topographic peak shown in Figure 6.2. The phase of the drifting wave is also notably modified as it crosses the topographic peak. In addition, Figure 6.3 suggests that the wave that

disappears when crossing the topography is indeed the same wave that reappears once the flow has moved on, due to the unbroken line connecting the drifting flow on either side of the topography.

‘Irregular’ Flow Structure

The flow in Figure 6.1 never becomes stationary, nor encounters the ‘stationary-transition’ regime, with the areas where these regions would be expected to be found covered by the ‘irregular’ regime. In addition, simple linear Rossby wave resonance cannot occur, as the partial barrier is forcing a predominantly wavenumber-1 stationary flow, but the free baroclinic wave flow appears to favour different, higher zonal wavenumbers throughout parameter space, as shown in Figure 6.1. The ‘irregular’ region appears abruptly, and at much lower rotation rates and temperature differences than would be expected for such an erratic flow. To further illustrate some of the unusual properties of this regime, a brief example of the flow structure is given in Figure 6.4.

Figure 6.4 highlights some of the notable features of the ‘irregular’ regime. Firstly, (a) shows what is either a skewed wavenumber-3, or a wavenumber-4 in which the eddy above the topography is missing. This lack of activity above the topography continues in (b), where what appears to be a skewed wavenumber-4 can be seen, but this quickly dissipates. Until this point, the flow structure has had noticeable fine features, such as small, asymmetrically-placed eddies, but in (c) these features dominant the circulation. Starting at (d) it can be noted that the eddies downstream of the topography (clockwise) are generally larger in linear size than those upstream of it. In addition, by (e) and (f) a large persistent stationary eddy has appeared directly above the topography. Throughout all the images, however, a large eddy or a jet can be seen just upstream of the topographic peak – this occurrence seems to be a permanent feature of the flow.

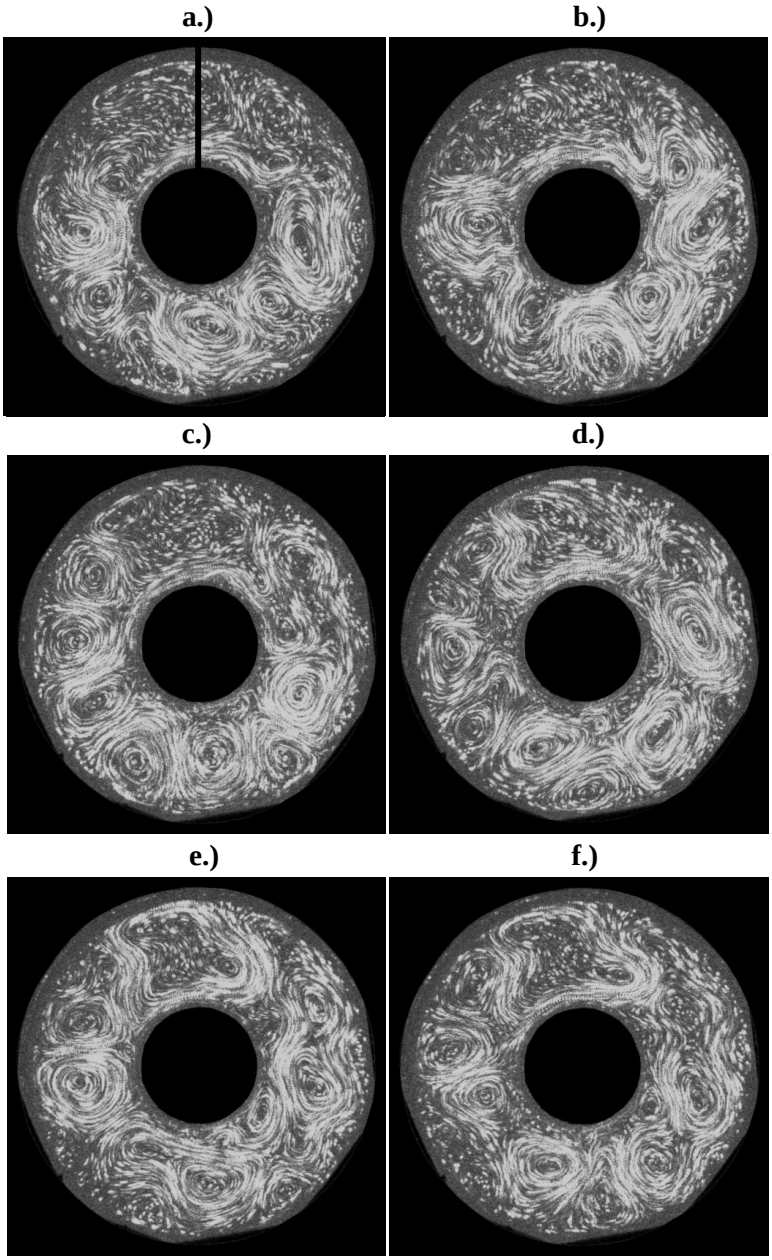

Figure 6.4: Streakline series at Level 3 (mid-depth), $\Omega = 1.6$ *rads*$^{-1}$, $\Delta T = 4K$, $\mathcal{T} = 1.454x10^{8}$, $\Theta_T = 0.124$; *a.)* $t = 3600s$, *b.)* $t = 3680s$, *c.)* $t = 3760s$, *d.)* $t = 3840s$, *e.)* $t = 3920s$, *f.)* $t = 4000s$.

The most notable aspect of the 'irregular' regime, however, is that it occurs so suddenly, since readings were as close as 0.2 rads^{-1} apart, and neither flow shows any evidence of the structure of the other, apart from limited transitions between wavenumbers. Furthermore, each flow regime was found to develop directly from the other, forming simply by incrementing the rotation rate, and without requiring a stop of the apparatus. This would appear to imply a discontinuous transition or bifurcation between the 'interference' and 'irregular' regions. As such, further runs were carried out at smaller

intervals of 0.05 rads^{-1}, and yet chaos was still found to appear suddenly, for example occurring between 1.2 rads^{-1} and 1.25 rads^{-1} when at a temperature difference of 4K (a change equal to values of $\mathcal{T} = 6.958x10^{6}$ and $\Theta_T = 1.722x10^{-2}$). This is surprising for such a dramatic change as, for example, the transition to a more standard chaotic regime is preluded by steadily increasing vacillation and noise, such as was noted in the Resonance investigation in the previous chapter. In addition, hysteresis, found to be negligible in the Extended-Regime experiment, was observed throughout this small area of parameter space, in regards to the beginning of the 'irregular' regime. For example, the result at a rotation rate of 1.25 rads^{-1} and with a temperature difference of 4K was found to have an 'irregular' flow structure (appearing as in Figure 6.4) when the rotation rate was increased, as discussed above, but an 'interference' structure (appearing as in Figure 6.2) when the annulus was spun up from rest. As such, it appears that the initial conditions of the fluid have an effect on where the transition between the regimes occurs, with the 'irregular' regime occurring at lower Taylor Numbers during a scan with increasing rotation rate.

To illustrate the 'irregular' regime flow structure over a longer timescale than the image sequence in Figure 6.4, Figure 6.5 shows the radial velocity for every point on a complete azimuthal circle at mid-radius, for the same parameters over the entire 1100s run. Once again, azimuthal position is given in degrees where positive is anticlockwise, and wherein the centre of the topographic peak occurs at about 100°.

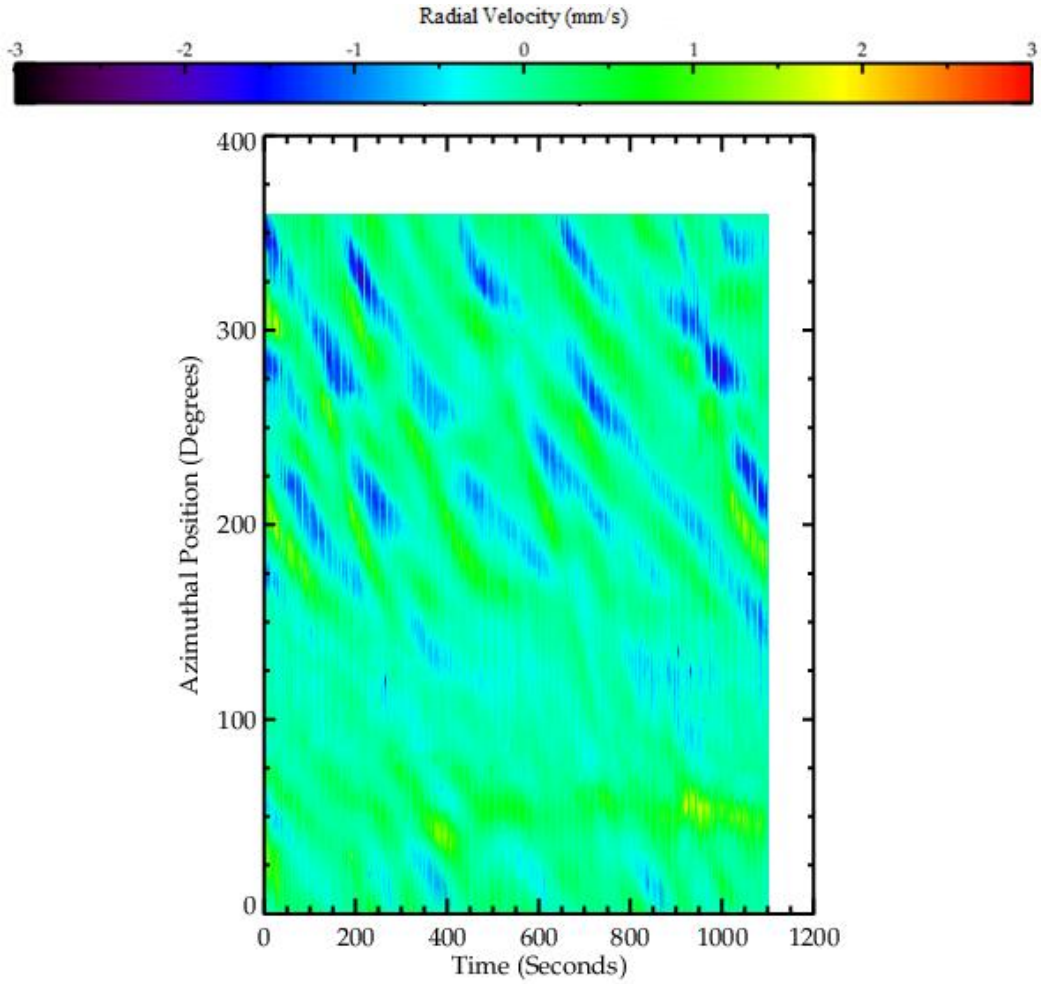

Figure 6.5: Radial velocity over time against azimuthal position for Level 3 (mid-depth), $\Omega = 1.6\ rads^{-1}$, $\Delta T = 4K$, $\mathcal{T} = 1.454x10^{8}$, $\Theta_{\mathrm{T}} = 0.124$.

Figure 6.5 shows a far more erratic flow structure throughout the entire run than in the 'interference' regime case in Figure 6.3, but also shows that the flow is not purely random and chaotic. Some clockwise drifting wave structure of several different wavenumber components can be observed, especially far from the topography, at around an azimuthal position of 300°. These different wavenumber components have varying drifting rates, and often overlap each other, contributing to the erratic nature of the flow. Nearer the topography, however, the flow structure becomes too erratic to be able to observe any drifting flow, with only the impact of the topographic peak (a weakening and then reappearance of the waves) being visible.

Time-Averaged Flow Structure

Taking a time-average of the flow structure over the period of the drifting waves (about 200s), has the effect of removing the drifting wave elements and leaving only the stationary components. As such, Figure 6.6 gives an example of time-averaged flow for the 'interference' regime, using azimuthal velocity, radial velocity and a kinetic energy map, for the parameters given in Figure 6.2.

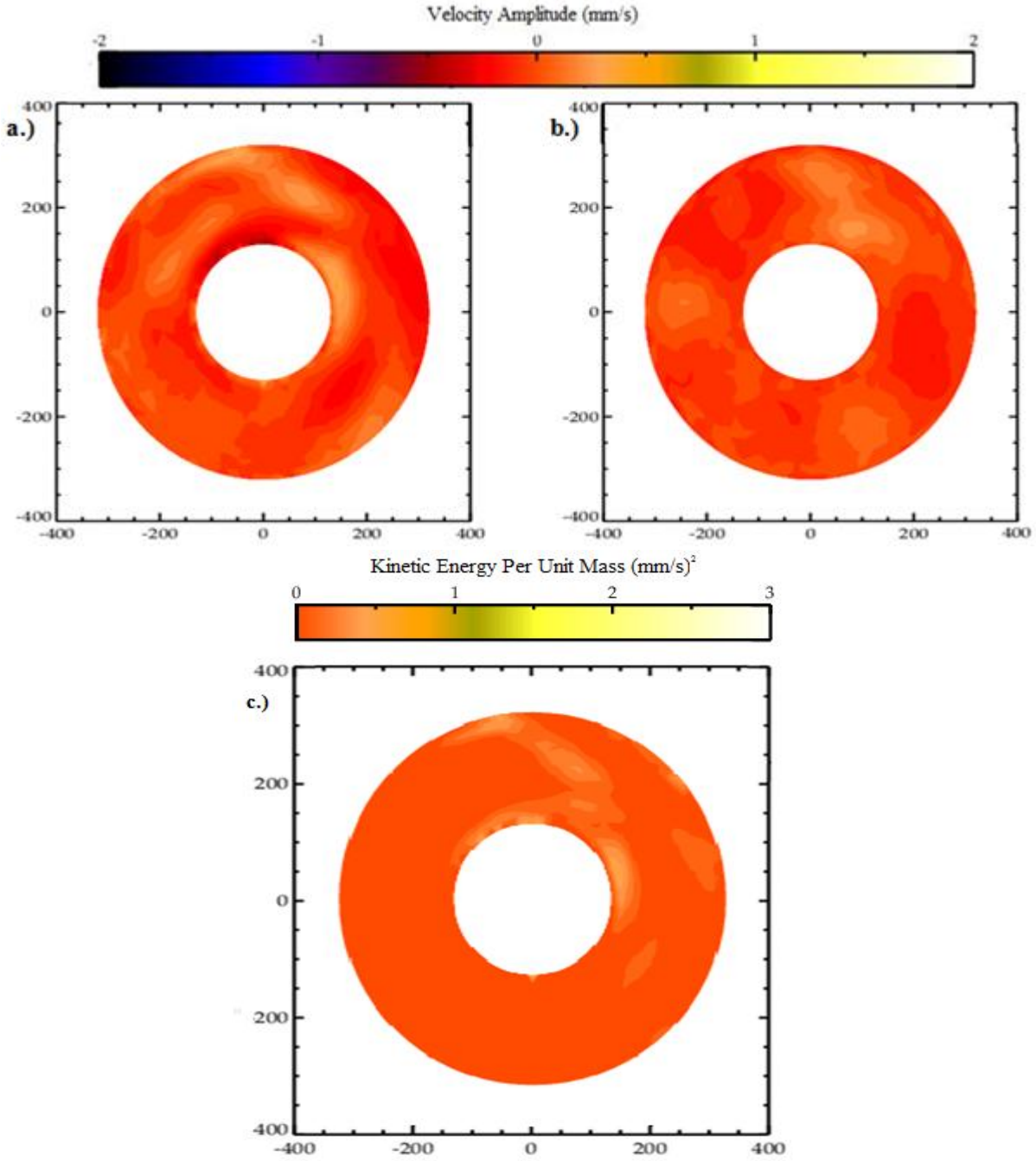

Figure 6.6: Azimuthal velocity (a), radial velocity (b) and kinetic energy (c) averaged over 200s for Level 3 (mid-depth), $\Omega = 0.8$ *rads*$^{-1}$, $\Delta T = 4K$, $\mathcal{T} = 3.635x10^{7}$, $\Theta_T = 0.494$.

As Figure 6.6 illustrates, with the drifting wave components removed by the time-averaging, a great deal of the flow structure is removed, with (a) showing a weak quasi-wavenumber-1 structure, and (b) showing a weak wavenumber-3 structure. In (c), which combines the previous two examples into a kinetic energy map to illustrate the total flow structure, only a single notable persistent jet remains, directly above the bottom topography. This is evidence for a pressure drop as the flow crosses the topographic peak (since the radial and azimuthal velocities show that it is a cyclonic wave), and also highlights the relative lack of stationary wave elements, in contrast to Figure 5.4 and Figure 5.5 from the Resonance experiment. In addition, the stationary "imaginary cylinder" occurring in the flow directly above the actual topography gives an example of a Taylor column, as originally described in Taylor (1923).

Similarly, Figure 6.7 shows a time-average of the flow structure over the period of the drifting waves (about 200s) for the 'irregular' regime, using azimuthal velocity, radial velocity and a kinetic energy map, for the parameters given in Figure 6.4.

Figure 6.7 demonstrates that the 'irregular' region has a very similar time-averaged structure to the 'interference' region, with a weak stationary elements throughout, a quasi-wavenumber-1 structure in (a) and a single notable persistent jet occurring as a Taylor column directly above the bottom topography in (c). The jet and corresponding pressure drop as the flow crosses the topographic peak are significantly larger in amplitude for the 'irregular' regime, however, most likely due to the increased Taylor Number, and a downstream (clockwise) wake can also be noted in (c). This suggests that the impact of the topography upon the flow becomes greater as the forcings from the rotation rate are increased.

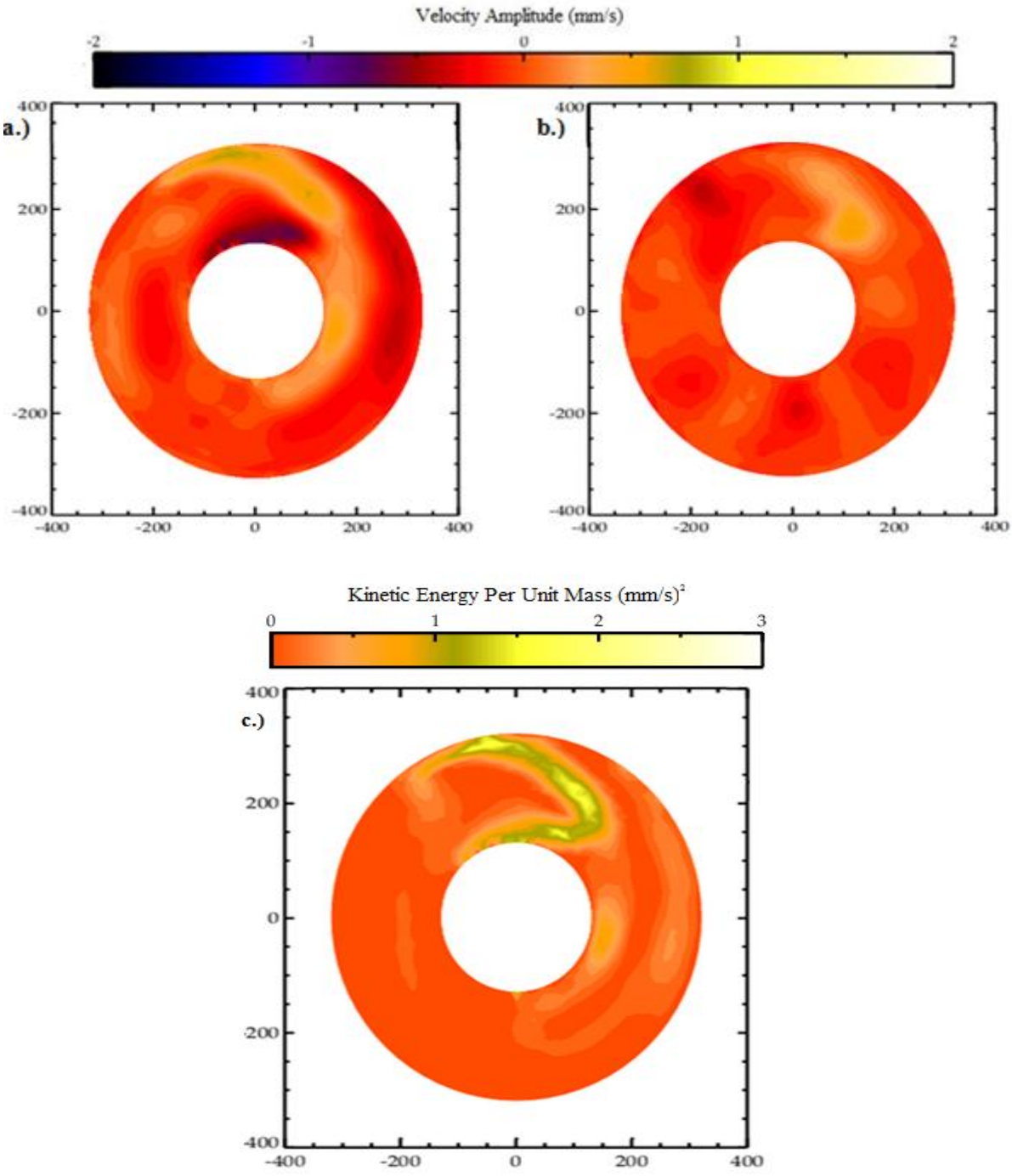

Figure 6.7: Azimuthal velocity (a), radial velocity (b) and kinetic energy (c) averaged over 200s for Level 3 (mid-depth), $\Omega = 1.6$ *rads*$^{-1}$, $\Delta T = 4K$, $\mathcal{T} = 1.454x10^{8}$, $\Theta_T = 0.124$.

Bottom Flow Structure

At the lowest light level, the horizontal flow is physically blocked by the topographic peak of the base. As such, the flow is forced to create an azimuthally-trapped structure (though fluid can be driven upwards over the ridge by the slope of the barrier), different to that found at the higher unobstructed levels. Figure 6.8 gives an example of this flow, at a point in parameter space close to the boundary between the 'interference' and 'irregular' regimes.

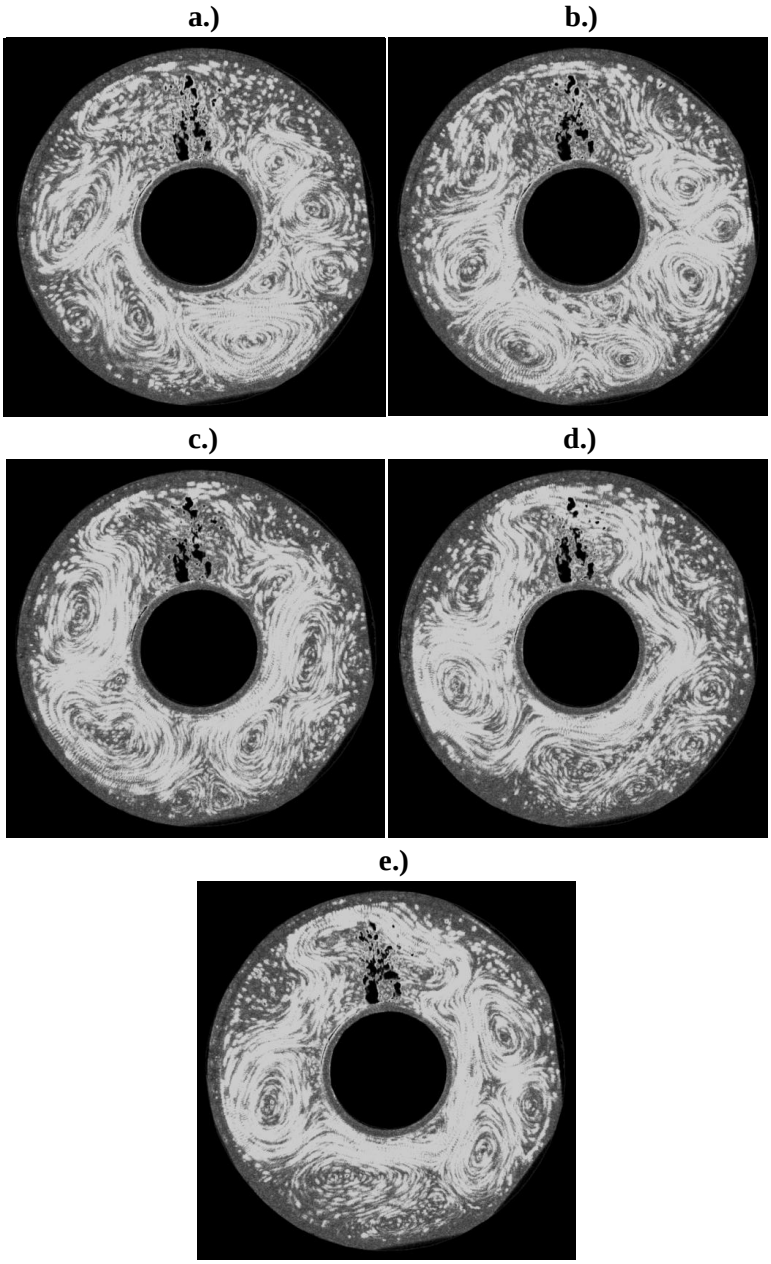

Figure 6.8: Streakline series at Level 5 (bottom), $\Omega = 1.1$ *rads*$^{-1}$, $\Delta T = 4K$, $\mathcal{T} = 6.873x10^{7}$, $\Theta_T = 0.261$; *a.)* $t = 3600s$, *b.)* $t = 3680s$, *c.)* $t = 3760s$, *d.)* $t = 3840s$, *e.)* $t = 3920s$.

Figure 6.8 shows the main aspects of the trapped flow, and highlights the location of the topographic peak via particles that have settled on the base, creating a black shadow. Whilst the flow structure in (a) appears to be irregular at first, it can be noted that the eddies downstream (clockwise) of the topography are smaller than those upstream of it. This continues through (b) until (c), when the upstream cyclonic eddies grow in size to form a skewed wavenumber-2 structure, with a jet that wraps around the topographic peak. In (d) and (e) this wavenumber-2 becomes more skewed, as the upstream eddy slowly drifts, but the jet above the peak does not. Due to this persistent azimuthally-trapped wave, as well as the clear asymmetry between the smaller and larger eddies seen throughout, the flow has many of the features of the 'irregular' regime, as shown in Figure 6.4. If the wavenumber-2 collapses, the flow will return to the arrangement of (a). This occurrence is universal for all parameters, though the flow in the 'interference' regime favours the structure found in (c), (d) and (e), and the flow in the 'irregular' regime shows more of the smaller eddies of (a) and (b). Once again, this is similar to the results Harlander et al (2012), who observed a trapped wave and smaller downstream eddies. However, in contrast, the trapped wave was found at mid-depth and was surrounded by a large jet similar to that of Wordsworth's (2008) ocean basin experiments. These differences are likely due to Harlander et al's addition of the partial radial barrier.

6.2.1 Azimuthal Time Variations

For further understanding of the 'interference' and 'irregular' regimes, a deeper analysis must be undertaken. Once again, the measurements from UVMAT were converted to polar coordinates on a regularly-spaced grid, and the units of the velocities changed from pixels / time step to mms^{-1}. The zonal background mean flow and any anomalous readings were then removed. An azimuthal Fourier analysis of the wavenumber structure in terms of amplitude and phase could then be carried out for every time step - combining these analyses allows the evolution of the flow over time to be observed. Azimuthal and radial velocity components were calculated at a quarter of the radial distance between the inner wall and the outer wall (closer to the inner wall) and at mid-radius respectively, chosen to

avoid nodes in the radial direction and because the patterns found were indicative of the rest of the flow.

'Interference' Regime

Figure 6.9 shows an example of the time variations of the amplitude of the first ten wavenumbers, for the flow used to create the 'interference' image sequence in Figure 6.2.

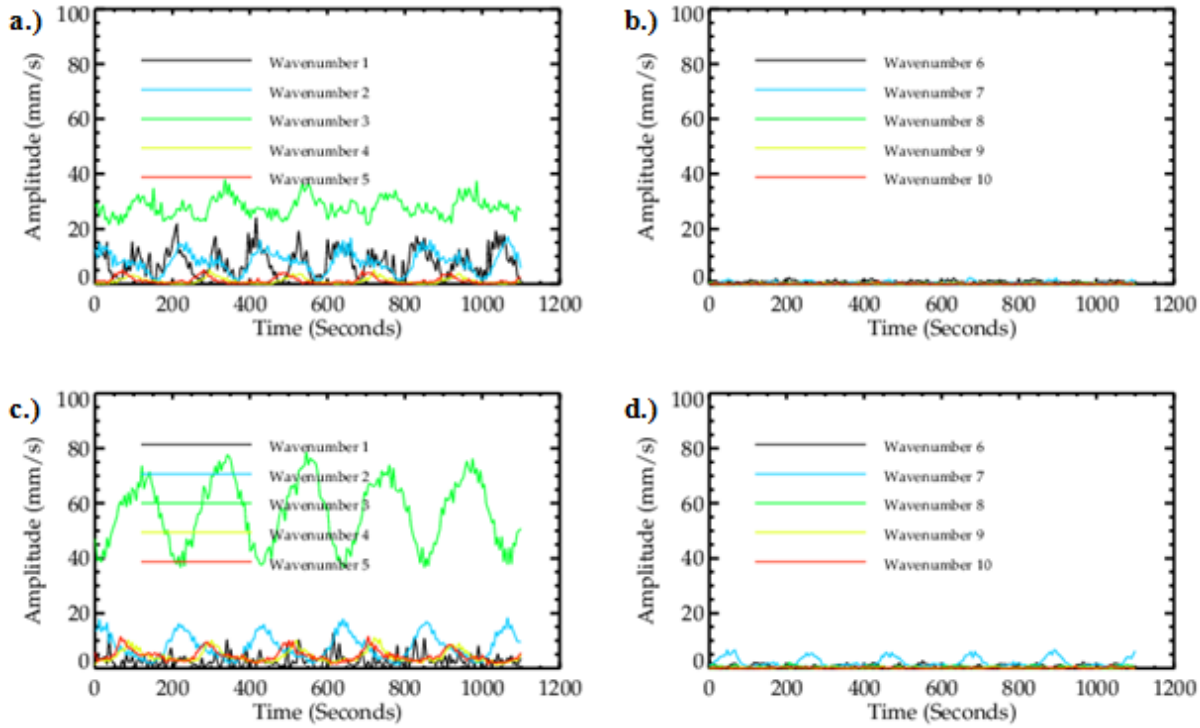

Figure 6.9: Velocity amplitude for Level 3 (mid-depth), $\Omega = 0.8$ *rads*$^{-1}$, $\Delta T = 4K$, $\mathcal{T} = 3.635x10^7$, $\Theta_T = 0.494$*; a.) azimuthal velocity for wavenumbers 1-5, b.) azimuthal velocity for wavenumbers 6-10, c.) radial velocity for wavenumbers 1-5, d.) radial velocity for wavenumbers 6-10.*

As can be seen in Figure 6.9, the flow is comprised of wavenumber-1, wavenumber-2 and wavenumber-3 components, with the latter strongly dominant throughout. The amplitudes can be seen to have a regular oscillatory nature, though this is different to the oscillations of the Resonance experiment, where the dominant wavenumber amplitude disappeared into the background noise during the oscillation's troughs, as such behaviour was not observed in these isolated ridge

experiments. Instead the oscillation here appears to be associated with the flow's topographic interactions, as evidenced by the peaks of the wavenumber-2 component (and the wavenumber-1 component, in the azimuthal velocity case) matching the troughs of the wavenumber-3 component. As such, the transitions between the dominant wavenumber-2 and wavenumber-3 components would seem to correspond to the interactions with the topography shown in Figure 6.2, visually appearing as transitions between a temporary skewed wavenumber-2 structure and a more regular wavenumber-3 structure as the waves cross the topographic peak.

By examining the phases over time of the ten wavenumbers of Figure 6.9, most of the wave components were found to be steadily drifting. As the flow is dominated by wavenumber-1, wavenumber-2 and wavenumber-3 components, Figure 6.10 shows the phase of these notable wavenumbers, for the same flow example as previously.

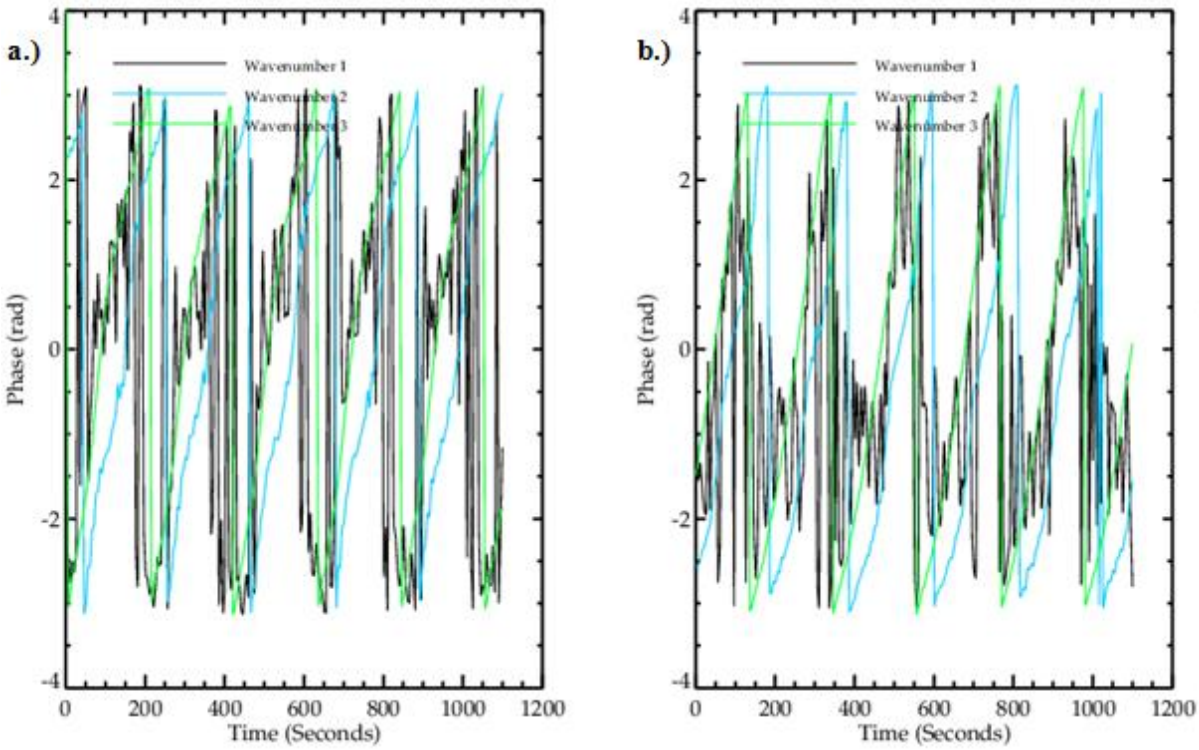

Figure 6.10: Velocity phase for Level 3 (mid-depth), $\Omega = 0.8$ rads^{-1}, $\Delta T = 4K$, $\mathcal{T} = 3.635x10^{7}$, $\Theta_T = 0.494$; a.) azimuthal velocity for wavenumbers 1-3, b.) radial velocity for wavenumbers 1-3.

Figure 6.10 illustrates that all of the wave components are constantly drifting with the same frequency, despite the fact that the amplitude variations of the wavenumber-2 and wavenumber-3 components are in antiphase, and that the phases would be expected to follow the Rossby wave dispersion relationship. It is also surprising that the wavenumber-1 component at mid-height is not stationary, despite the strong wavenumber-1 element of the topographic base. The studies of the bottom of the annulus showed that there is an azimuthally-trapped stationary wave just upstream of the topography, so this 'interference' flow structure is therefore likely an interaction between these drifting waves and the effects of the bottom-trapped wave, extending the reach of the topography far beyond its physical dimensions. During periods where the two are out of phase, they constructively interfere, creating a wavenumber-3 flow. In periods where they are in phase, they destructively interfere, creating the visually-skewed wavenumber-2 flow.

For further investigation, Figure 6.11 shows the variations of the radially-averaged kinetic energy of the first ten wavenumbers over time.

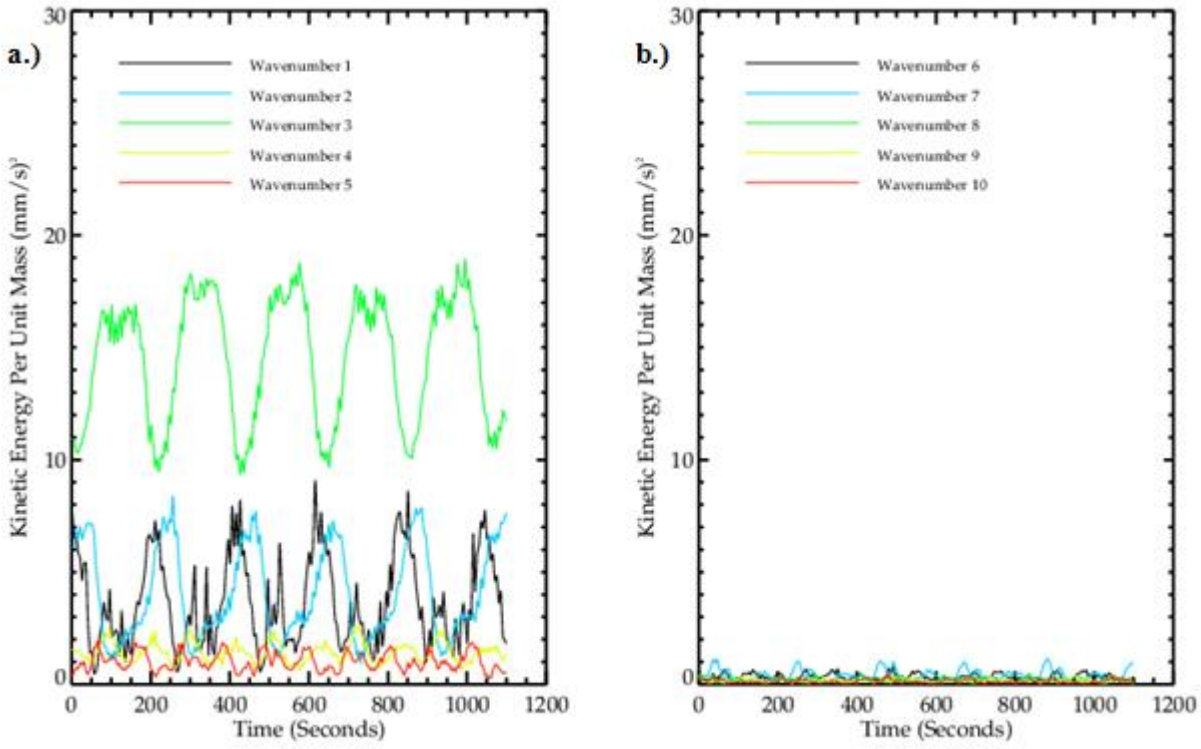

Figure 6.11: Radially-averaged kinetic energy for Level 3 (mid-depth), $\Omega = 0.8$ *rads*$^{-1}$, $\Delta T = 4K$, $\mathcal{T} = 3.635x10^{7}$, $\Theta_T = 0.494$*; a.) wavenumbers 1-5, b.) wavenumbers 6-10.*

Figure 6.11 reinforces what was just described, with the kinetic energy of the flow being transferred back and forth between the wavenumber-3 component and the wavenumber-1 and wavenumber-2 components. Indeed, the relationship between the two oscillations is even easier to discern in the graph of kinetic energy. Once again, a contrast can be made between the time variations of the kinetic energy of the dominant wavenumber-3 component and the kinetic energy of the zonal mean flow. At mid-depth, this zonal mean is found to fluctuate in direction from positive to negative and vice versa, due to being acted upon by both the topographically-forced waves from the bottom and the free baroclinic waves from the top and middle of the tank. As such, Figure 6.12 shows the variation over time of the kinetic energy of the zonal mean from the same point in parameter space as in Figure 6.11, but at the higher Level 2, and with a superposition of the wavenumber-3 kinetic energy time-series for comparison.

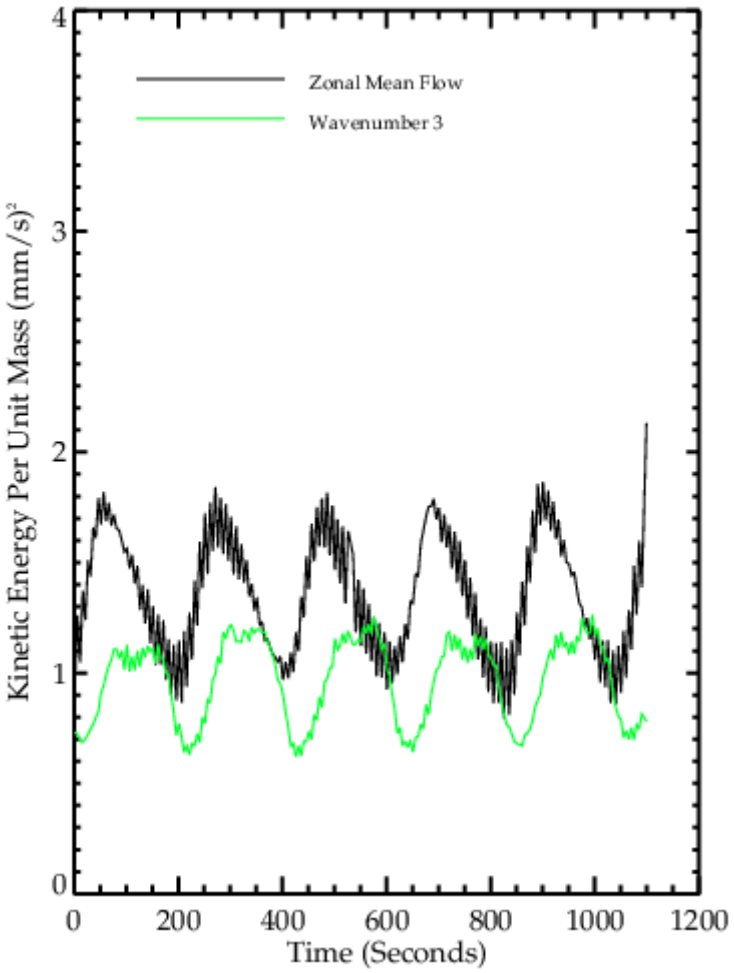

Figure 6.12: Radially-averaged kinetic energy of zonal mean flow (black) with wavenumber-3 total kinetic energy (green, not to scale) as comparison, for Level 2, $\Omega = 0.8$ *rads*$^{-1}$, $\Delta T = 4K$, $\mathcal{T} = 3.635x10^{7}$, $\Theta_T = 0.494$.

Figure 6.12 shows that the kinetic energy of the zonal mean flow oscillates effectively in quadrature with the kinetic energy of the dominant mode, with the zonal mean kinetic energy peaks occurring where the wavenumber-3 kinetic energy is changing most rapidly, and vice versa. This is consistent with strong nonlinear wave-zonal flow interactions and an exchange of energy between the waves and the mean zonal flow, similar to that found in the Resonance experiments.

'Irregular' Regime

For contrast, Figure 6.13 gives the time variations of the amplitude of the first ten wavenumbers of a flow in the 'irregular' regime, for the point in parameter space illustrated in the image sequence of Figure 6.4.

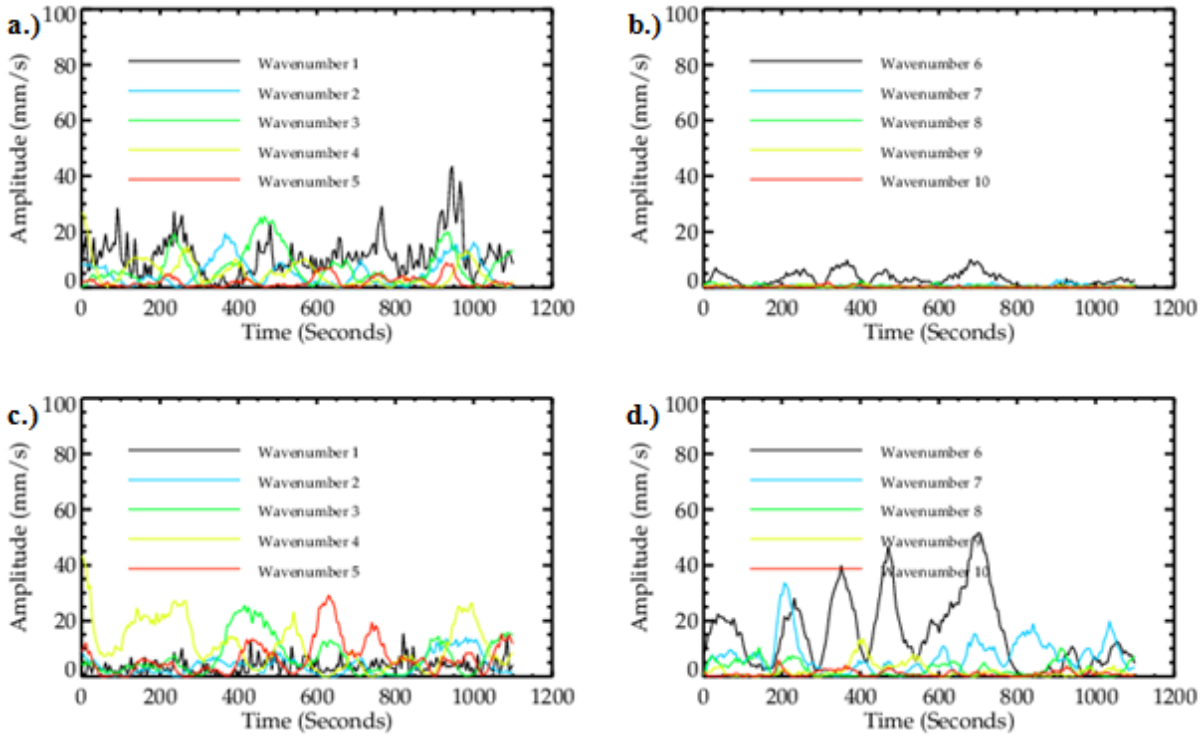

Figure 6.13: Velocity amplitude for Level 3 (mid-depth), $\Omega = 1.6$ rads^{-1}, $\Delta T = 4K$, $\mathcal{T} = 1.454x10^{8}$, $\Theta_T = 0.124$; a.) azimuthal velocity for wavenumbers 1-5, b.) azimuthal velocity for wavenumbers 6-10, c.) radial velocity for wavenumbers 1-5, d.) radial velocity for wavenumbers 6-10.

From Figure 6.13, it can be determined where the ‘irregular’ regime originates. It can be noted that the previously dominant wavenumber-3 component is no longer the largest in amplitude for either the azimuthal or the radial case. The former is now dominated for most of the time by an irregularly-varying wavenumber-1, and the latter is dominated by much higher wavenumbers, chiefly wavenumber-4, wavenumber-5 and wavenumber-6. These high wavenumber radial velocity amplitudes are also now much larger than the azimuthal amplitudes, which is also consistent with the irregularly-spaced small eddies and other fine features found in the ‘irregular’ regime. Hence, the transition between the two regimes can be assumed to be caused when the large wavenumber radial velocity components become dominant over the small wavenumber azimuthal components. If the Hide Number is increased, these radial components can be seen to steadily increase in amplitude as well, much like the evolution of the oscillation in the Resonance experiments as Taylor Number was increased. A parallel can therefore be made between the rise of the ‘stationary-transition’ regime from a stationary wavenumber-3 flow in that study, and the emergence of the ‘irregular’ regime from the more regular ‘interference’ state in this one.

By examining the phases over time of the ten wavenumbers of Figure 6.13, most of the wave components were found to be steadily drifting, with the exception of wavenumber-1. As the ‘irregular’ regime flow is dominated by radial wavenumber-4, wavenumber-5 and wavenumber-6 components, Figure 6.14 shows the phase of these notable wavenumbers, as well as the wavenumber-1 component, for the same flow example as previously.

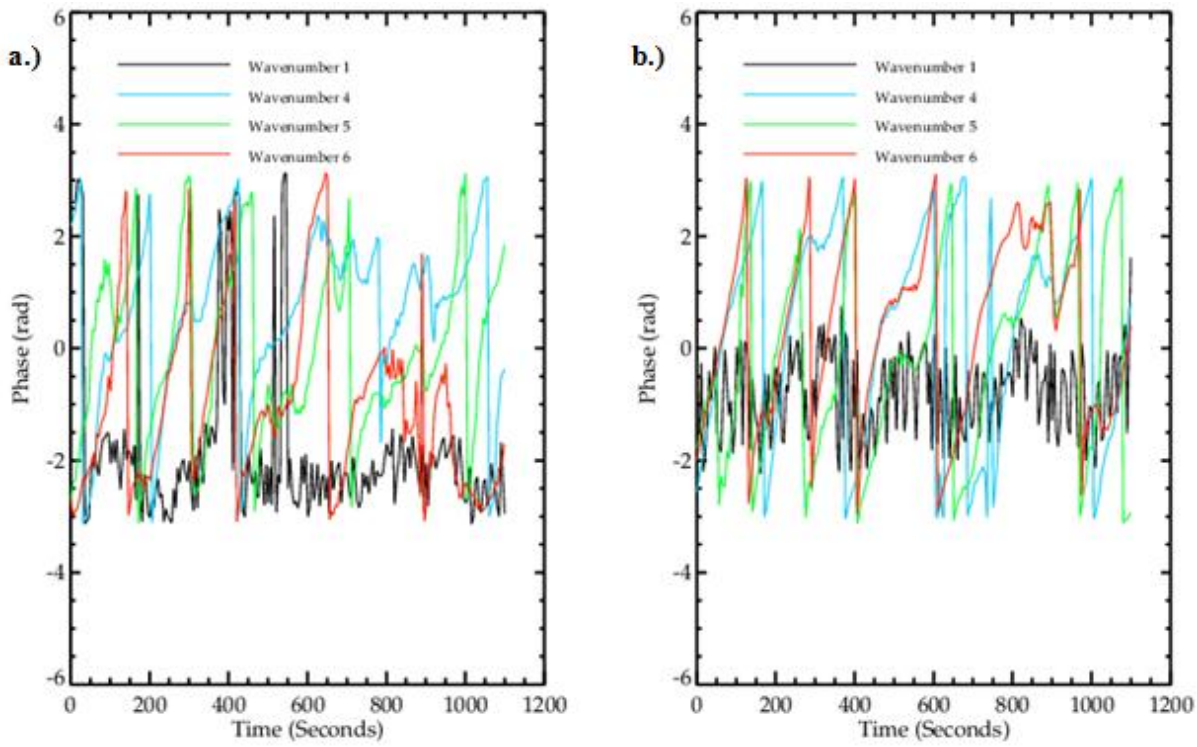

Figure 6.14: Wavenumber-1 phase (black) against wavenumber-4 phase (blue), wavenumber-5 phase (green) and wavenumber-6 phase (red), for Level 3 (mid-depth), $\Omega = 1.6$ *rads*$^{-1}$, $\Delta T = 4K$, $\mathcal{T} = 1.454x10^{8}$, $\Theta_T = 0.124$*; a.) azimuthal velocity b.) radial velocity.*

Figure 6.14 shows that the wavenumber-1 component is stationary, but the majority of the other components are still drifting. This stationary wavenumber-1 component is likely associated with the wavenumber-1 component of the topographic base (though said base is not wholly wavenumber-1 in structure), possibly as a result of the azimuthally-trapped wave at the bottom level. Furthermore, by looking at the radial phase in (b), it can be noticed that wavenumber-4, wavenumber-5 and wavenumber-6 appear to show good evidence of phase synchronisation, despite the noise of the experiment, suggesting the activity of wave-triads. Assuming that the wavenumber-1 topography plays a role in the interactions (which is judged to be reasonable due to the dominant stationary azimuthal velocity wavenumber-1 component), Equation 2.1 gives two likely triads: wavenumber-4, wavenumber-5 and the stationary, topographically anchored wavenumber-1 component, and wavenumber-5, wavenumber-6 and the stationary, topographically anchored wavenumber-1 component. To confirm this, Equation 2.3 stated that the relative importance of a wave-triad to the dynamic evolution of the flow can be measured by how constant the summation or difference of the

phases of the component wave modes remains over time. Therefore, if the phases are 'unwrapped' (removed from the constraints of fitting between $+\pi$ rad and $-\pi$ rad)[19], then this difference over time between them can be observed, as in Figure 6.15, which shows the differences between the wavenumber-5, wavenumber-4 and wavenumber-1 components and between the wavenumber-6, wavenumber-5 and wavenumber-1 components. These differences are both found by subtracting the unwrapped phase of the two middle wavenumber components (wavenumber-4 and wavenumber-5, respectively) from the sum of the unwrapped phase of the higher wavenumber (wavenumber-5 and wavenumber-6, respectively) and wavenumber-1 components.

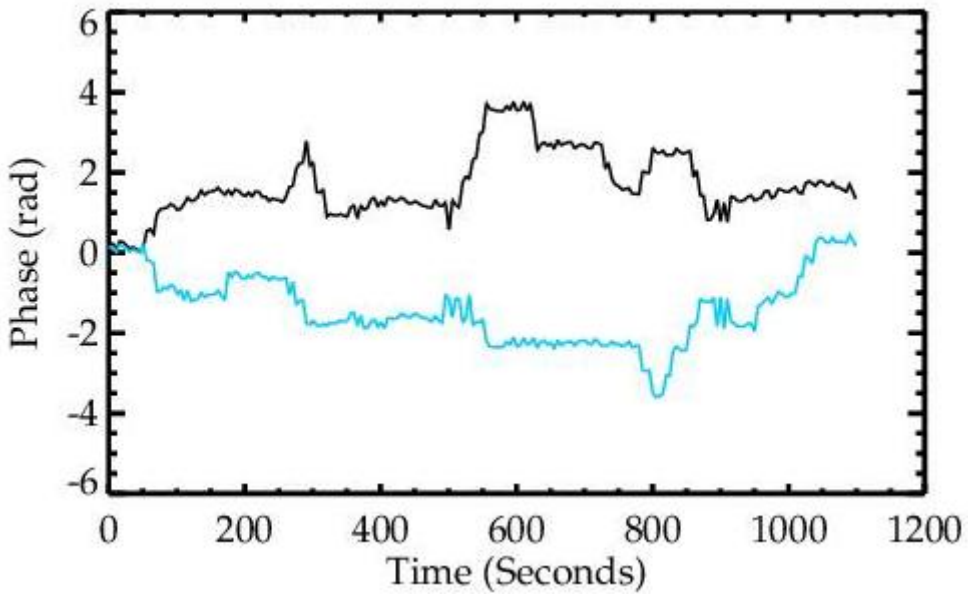

Figure 6.15: Unwrapped radial wavenumber-5, wavenumber-4 and wavenumber-1 phase difference ($\varphi_1 + \varphi_5 - \varphi_4$, black) against unwrapped radial wavenumber-6, wavenumber-5 and wavenumber-1 phase difference ($\varphi_1 + \varphi_6 - \varphi_5$, blue) for $\Omega = 1.6$ rads^{-1}, $\Delta T = 4K$, $\mathcal{T} = 1.454x10^8$, $\Theta_T = 0.124$.

Whilst Figure 6.15 shows a large amount of noise, as the experiment is in general fairly noisy (assumed to be due to small vibrations caused as the annulus rotates), both phase differences have long areas of stationarity, giving evidence that these are indeed components of important wave-triads for the evolution of the flow. Besides the noise, there are also frequent phase-slips where the phase difference suddenly changes to a new constant value - these often occur at the same time for both

[19] This is achieved via the addition of 2π rad every time the phase completes one drift cycle, i.e. the phase changes from $+\pi$ rad to $-\pi$ rad.

lines, and with fairly regular intervals of about 150 - 200s. From Figure 6.2, it was found that the time taken for one cycle of the topographic interaction is roughly 180s, so it is therefore likely that these phase-slips may be associated with the topography interactions as the flow drifting over the peak of the base.

Hence, it appears that the 'irregular' regime contains two resonant wave-triads: one between the stationary wavenumber-1 component forced by the topographic base, and the drifting wavenumber-4 and wavenumber-5 components; and the other again between the stationary wavenumber-1 component forced by the topographic base, but instead with the drifting wavenumber-5 and wavenumber-6 components. In the literature, clusters of two triads that are connected by a common mode are referred to as "butterflies". Kartashova and L'vov (2007), for example, found three such "butterflies" in their numerical investigation into LFV. Kartashova and L'vov put forward the idea that intraseasonal atmospheric oscillations could be described via "periodical energy exchange" within various planetary wave-triads, including between the three "butterflies" that were able to exchange energy through their shared common modes. Once again, this gives evidence that the nonlinear interactions that cause the transition from the 'interference' regime to the 'irregular' regime have strong wave-wave components, with energy being transferred between the different wavenumber modes.

In addition, for the 'irregular' regime, a contrast can be made between the time variations of the kinetic energy of the dominant wave components and the kinetic energy of the zonal mean flow. Figure 6.16 shows the variation over time of the kinetic energy of the zonal mean from the same point in parameter space as in Figure 6.13, but at the higher Level 2, and with a superposition of the total kinetic energy from the first ten wavenumbers (since there is no clear dominant wavenumber component) for comparison.

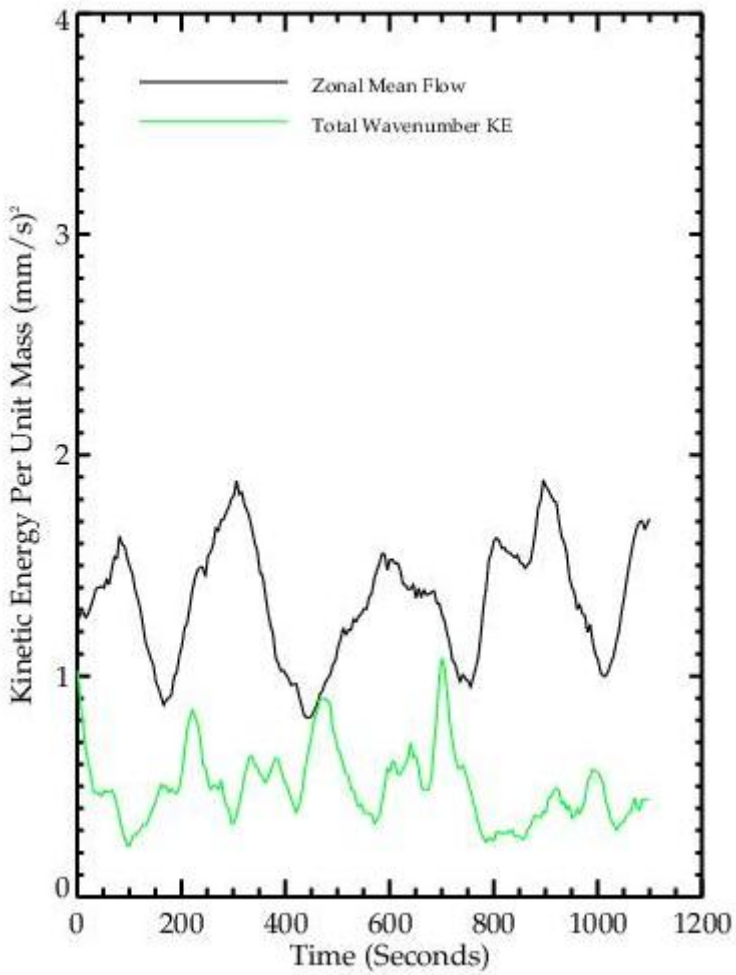

Figure 6.16: Radially-averaged kinetic energy of zonal mean flow (black) with total kinetic energy (green, not to scale) as comparison, for Level 2, $\Omega = 1.6$ *rads*$^{-1}$, $\Delta T = 4K$, $\mathcal{T} = 1.454x10^{8}$, $\Theta_T = 0.124$.

Within the 'irregular' region, Figure 6.16 shows that there is a much less pronounced correlation between the activity of the dominant component and the mean flow. However, some weak oscillating in quadrature still seems to occur, though much less obviously than for the 'interference' regime (Figure 6.12) or for the Resonance study (Figure 5.10). As such, it is possible that the flow structure and resulting phenomena of the 'irregular' regime are associated more with nonlinear wave-wave interactions, rather than with wave-zonal flow interactions, but the latter interactions are by no means absent from the dynamics of the flow.

Vertical Structure

By observation of the vertical structure, the difference between the blocked and unblocked parts of the flow can be investigated. Figure 6.17 gives a snapshot of the vertical structure close to the location of transition between the 'interference' and 'irregular' regimes, quickly switching between levels so that all images are taken at approximately the same time, as much as physically possible. Each image is roughly 10 seconds apart, to allow for a streakline picture, and, considering the slow speed of drifting and oscillation, this was determined to be sufficient.

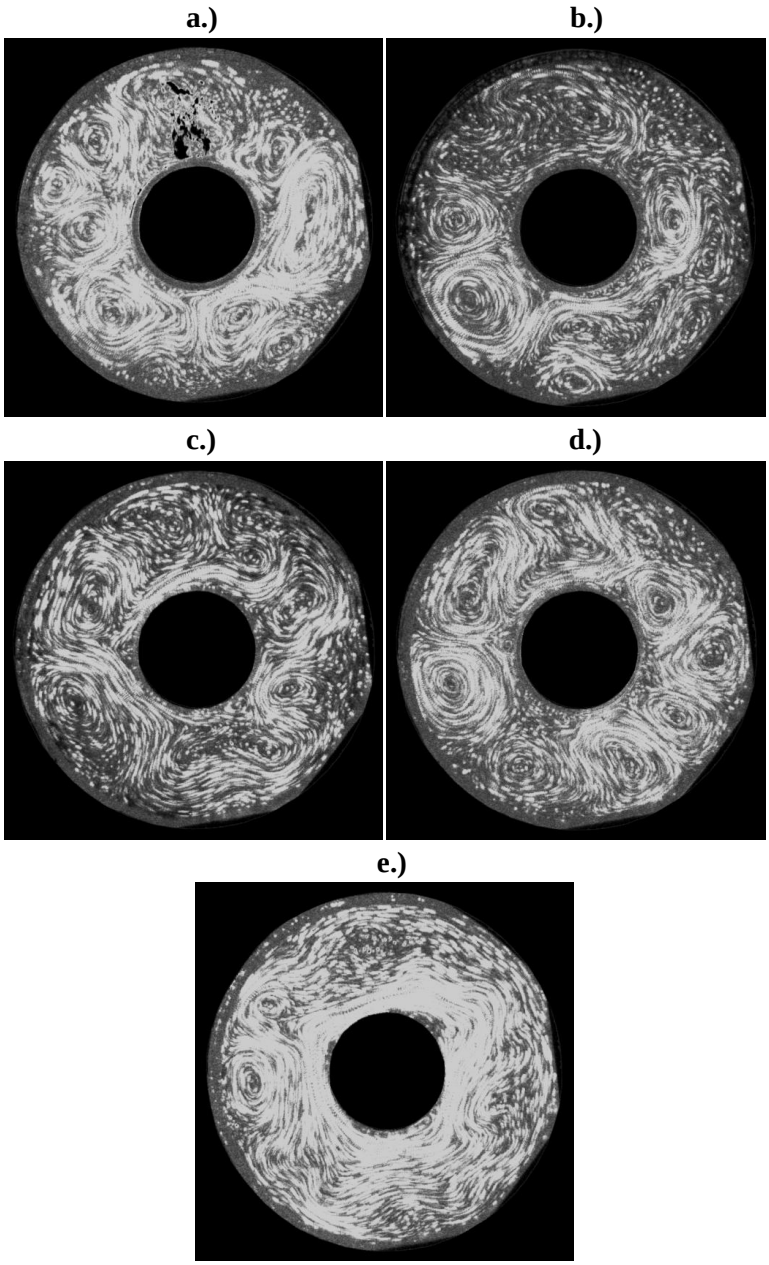

Figure 6.17: Streakline images for $\Omega = 1.1$ rads^{-1}, $\Delta T = 4K$, $\mathcal{T} = 6.873x10^{7}$, $\Theta_T = 0.261$; a.) Level 5, b.) Level 4, c.) Level 3, d.) Level 2, e.) Level 1.

Figure 6.17 shows the azimuthally-trapped wave in (a) is also felt at Level 4, in (b), despite the topography not physically extending that high. The wave is visibly weaker, however, probably due to increased distance from the topography, and slightly shifted downstream (clockwise). Above that, the middle Level 3, at (c), gives a more regular wavenumber-3, as expected from this point in parameter space, with little visible evidence of the trapped wave. The wavenumber-3 has yet to encounter the topography as it drifts, being the equivalent of (a) or (g) in Figure 6.2. Higher still, (d) shows that the wavenumber-3 has been shifted further downstream, and has become more irregular. It appears the flow is transitioning to wavenumber-4, which again is not unusual for this area of parameter space, as it is so close to the 'irregular' regime and the 'transition' region in Figure 6.1. At the top of the annulus, (e) shows that the sloped lid appears to suppress baroclinic activity, with the flow showing a very weak wavenumber-3 or wavenumber-4. This is most likely to be associated with the reduced zonal mean flow that would be expected to be found near the lid, due to the upper boundary layer. Once again, the wave's locations can be seen to have been shifted downstream as the height is increased.

Similarly, over a longer timescale, Figure 6.18 shows the variation in amplitude over time of the first five wavenumbers for runs at each height.

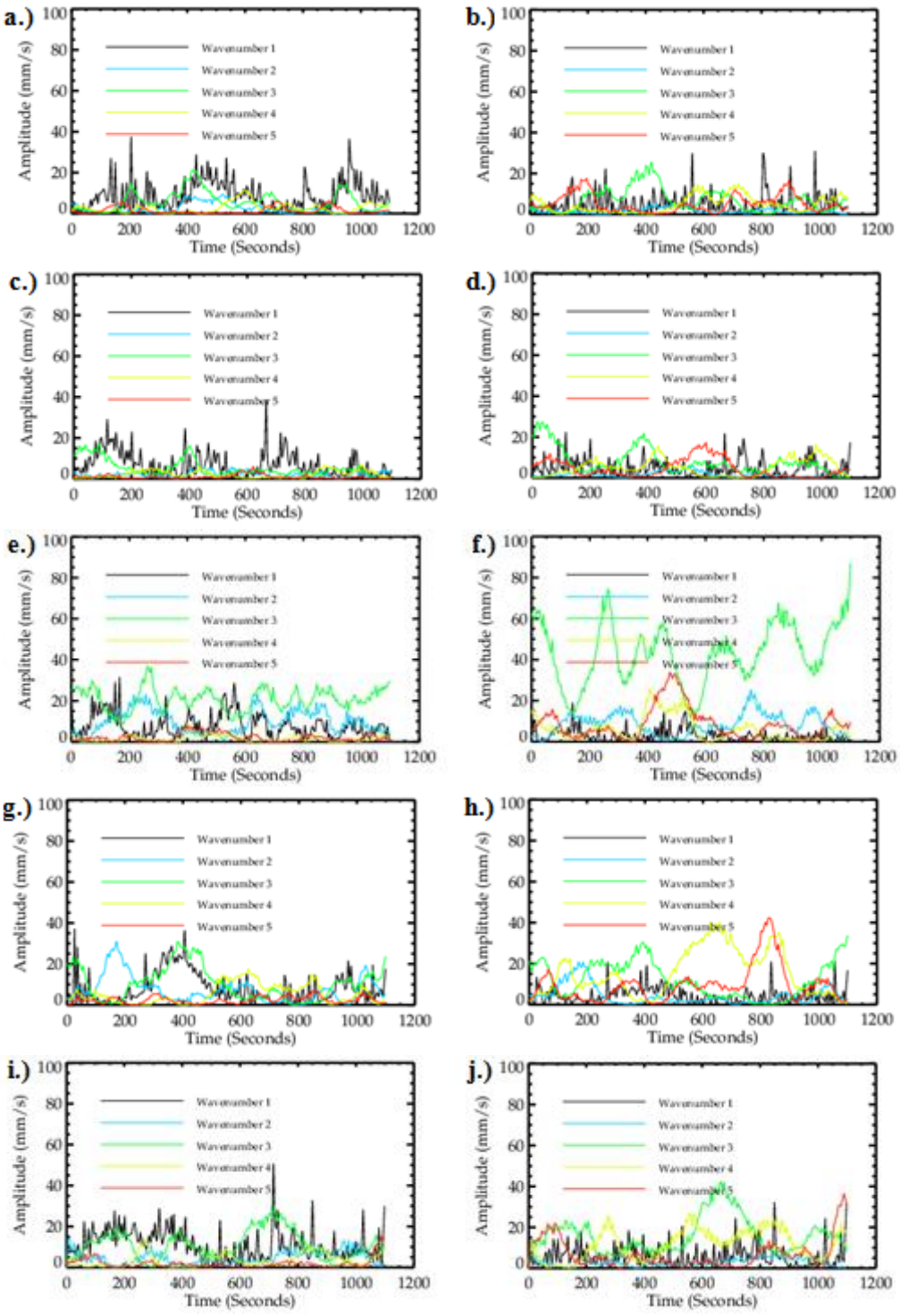

Figure 6.18: Velocity amplitude for $\Omega = 1.1\ rads^{-1}$, $\Delta T = 4K$, $\mathcal{T} = 6.873x10^{7}$, $\Theta_T = 0.261$, *a.) Level 5 azimuthal velocity for wavenumbers 1-5, b.) Level 5 radial velocity for wavenumbers 1-5, c.) Level 4 azimuthal velocity for wavenumbers 1-5, d.) Level 4 radial velocity for wavenumbers 1-5, e.) Level 3 azimuthal velocity for wavenumbers 1-5, f.) Level 3 radial velocity for wavenumbers 1-5, g.) Level 2 azimuthal velocity for wavenumbers 1-5, h.) Level 2 radial velocity for wavenumbers 1-5, i.) Level 1 azimuthal velocity for wavenumbers 1-5, j.) Level 1 radial velocity for wavenumbers 1-5.*

Figure 6.18 shows a flow in parameter space closer to the 'irregular' regime than Figure 6.9, and thus illustrates aspects of both regimes. For example, at the middle depth flow, (e) and (f), there is a strongly dominant vacillating wavenumber-3 reminiscent of the 'interference' regime, as noted in Figure 6.9, as well as evidence of the 'irregular' regime's typical azimuthal velocity wavenumber-1 in (e) and radial velocity higher wavenumbers in (f), both as noted in Figure 6.13. As mentioned previously, this is an extremely rare occurrence, only found directly on the boundary between the two regimes (for reference, the 'irregular' region was defined to begin at a rotation rate merely 0.05 $rads^{-1}$ faster than the above case). At the bottom of the annulus, especially in the azimuthal velocity cases (a) and (c), Levels 5 and 4 are dominated by a wavenumber-1 component, with the former having a larger amplitude than the latter, which corresponds to the azimuthally-trapped wave observed at those heights. By contrast, especially in the radial velocity cases (h) and (j), Levels 2 and 1 show a more chaotic flow, with higher constituent wavenumbers, but with reduced amplitude in absolute terms compared to the mid-depth flow of (f). This appears to be due to the effects of the proximity of the sloping lid, as discussed previously. In addition, the phase variations over time are fairly uniform throughout the vertical scale, with a reasonably stationary wavenumber-1 component at all heights, and the other wavenumber components constantly drifting at the same frequency. As such, despite the effects of the topography and the lid, the flow shows little variation with height over time, with the major difference between the blocked and unblocked flows being the azimuthally-trapped wave in the former.

6.3 Discussion

As opposed to the waveumber-3 topography of the Resonance study, the isolated ridge experiments showed no dominant stationary regimes, despite Luo's (2005) statement that large-scale topography often acts to lock the atmospheric circulation into creating a stationary wave. However, the topography clearly still has major impacts on the flow, causing jet-shifting as the waves cross the peak of the base. For example, Figure 6.2d, where the dominant wavenumber amplitude is at its

weakest, resembles a typical blocked structure, such as may be found in the atmosphere, with notable similarities to Figure 2.4b. When the waves are not interacting with the topography, the flow resembles more the zonal state of Figure 2.3a or Figure 2.4a, the latter showing another parallel to the real atmosphere. Atmospheric blocked and zonal states, however, are by nature stationary. As discussed in Chapter 2, Egger (1978) described blocking as arising from the nonlinear interactions of slowly drifting free waves and stationary waves caused by "geographic fixed" forcing, such as topographic ridges. Hence, the foremost wavenumber-1 component of the topographic base in this study creates a non-dominant stationary wavenumber-1, which in turn interacts with the drifting dominant wavenumbers to form an oscillation between the blocked and zonal states. When the waves are in phase, visually denoted by one of the cyclonic eddies crossing the peak of the topography, they destructively interfere, creating a blocked flow. When they are out of phase, during the rest of the eddy's drift, they constructively interfere, creating the zonal flow state. This agrees well with the results of Harlander et al (2012) and the observations of Leach (1981), who stated that "as a wavelobe approached from the west it slowed down and then broke up as it passed over the ridge and did not reform until about 90° to the east". The results of this study also agrees with the literature in other ways, with the flows that resemble the blocked state exhibiting reduced jet intensity but larger wave amplitude, along with a noticeable increase in the strength of anticyclonic eddies when compared to those that resemble the zonal state, as noted by Weeks et al (1997). Evidence was also found of Risch's (1999) rogue 'wave-lobe', with many of the flow structures discovered having additional, temporary 'wave-lobes'. This was often associated with topographic interactions close to the 'irregular' regime, giving rise to strong vacillation and frequent wavenumber transitions.

In terms of multiple equilibria, within the region of parameter space occupied by the 'interference' regime evidence was found of both blocked and zonal flows as part of a regular oscillation caused by topographic interactions, as described above, but not as discrete or permanent alternative states that the circulation 'chooses' to adopt based on initial conditions. However, within the small area of parameter space between the 'interference' and 'irregular' regimes, hysteresis was

noted in the experiments. In that area, whether the flow structure ended up as an ‘interference’ regime or an ‘irregular’ regime did appear to be dependent on the initial conditions, namely whether the flow had been spun up from rest or from some other point in parameter space respectively. As such, there is some evidence of multiple equilibria in this study, although not as widespread in location as was suggested by studies such as Risch (1999). The current study also adds quantitative Fourier analysis to Risch’s qualitative findings and Tian et al’s (2001) barotropic results, suggesting that the zonal and blocked states themselves come about from interactions between the drifting dominant waves and a stationary wave. Evidence of this stationary wave is present at all depths and all sections of parameter space, and was found to dominate at the bottom of the annulus, where the flow is azimuthally blocked. In the current study, this stationary wave was a wavenumber-1, assumed to be due to the dominant wavenumber-1 component of the topography.

A further comparison that can be made with the Resonance experiments is the question of the presence of topographic resonance under partial barriers. Whilst the base used was not entirely wavenumber-1 in structure, it would be reasonable to assume that resonant interactions would occur mainly between the topography and a wavenumber-1 flow. However, despite a topographic-forced stationary wavenumber-1 component being noted, especially at high Taylor Numbers, this component was never noted to dominate the flow structure, and thus no clear evidence of topographic resonance was discovered. On the other hand, in Figure 6.2, the time taken for one cycle of the topographic interaction within the ‘interference’ regime is roughly 180s. At a rotation rate of 0.8 $rads^{-1}$, this corresponds to 35.8 ‘days’ for the annulus. This, like the oscillation found in the Resonance study and LG’s resonant 36-40 day oscillation, corresponds with the timescale for LFV, and so gives a second alternative possible mechanism of generation for LFV in the non-resonating case, in the form of interference effects between a stationary flow forced by topography and a drifting baroclinic wave. This also serves to highlight a relationship between both topographic resonance and LFV, which have already been linked by the Resonance study, to the multiple equilibria states of blocked and zonal flows. In addition, further analysis suggests that an aspect of the ‘irregular’ regime is the occurrence

of two resonant wave-triads: the first between the stationary wavenumber-1 forced by the topography, and the drifting wavenumber-4 and wavenumber-5 components; and the second between the stationary wavenumber-1 forced by the topography, and the drifting wavenumber-5 and wavenumber-6 components. This 'butterfly' is another link to LFV, as Kartashova and L'vov (2007) found three such "butterflies" in their numerical investigation into LFV, and also acts to illustrate the difference between the two different arrangements of topography. For a wavenumber-3 base, like that of the Resonance experiments, a single wave-triad of the baroclinic and topographically-forced barotropic components of wavenumber-3 and the baroclinic component of wavenumber-6 was associated with the formation of the 'stationary-transition' regime; for a base with a strong wavenumber-1 component, like that of the Partial Barriers experiments, two wave-triads of wavenumber-4, wavenumber-5, wavenumber-6 and a stationary wavenumber-1 forced by the topography were associated with the formation of the 'irregular' regime. Once again it can be noted that, in this investigation, topography, the sloped lid and a reversed temperature gradient were all necessary for the 'interference' and 'irregular' regimes to appear. As such, this would appear to indicate that the flows are dominated by nonlinear wave-wave interactions involving a stationary wave forced by the topography.

The Partial Barriers experiment was designed to block part of the working fluid, allowing comparison between blocked flow at the lower levels and unblocked flow at the higher levels. The blocked bottom flow was found to be defined by a large persistent azimuthally-trapped wave upstream of the topographic peak, as well as smaller, irregularly-spaced downstream eddies. This is quite different to the results of Wordsworth's (2008) fully blocked ocean basin experiments, which found a quasi-barotropic jet rather than trapped waves. It is likely, therefore, that in a Partial Barriers experiment, the existence of the unblocked flow affects the structure of the blocked flow. Similarly, the azimuthally-trapped wave extends further vertically than the topography, as shown in Figure 6.17, weakening as it crosses into the unblocked flow. This bears similarity to the real oceanic flow, as discussed by Huthnance (1989) and Martínez and Allen (2004). These lower levels are found to be

dominated by a stationary wavenumber-1 component, presumably associated with the trapped wave, which is also found at a reduced amplitude at all other heights. Further into the unblocked flow, the circulation is far more regular, with structure depending on the location in parameter space, and with little visible evidence of the azimuthally-trapped wave, due to its weakened state. Above this point, the flow is reasonably uniform in the vertical direction, appearing mostly the same in structure at all heights, except for a notable reduction in wave amplitude near the sloped lid. Once again, a small phase shift with height can be observed since, as discussed by Leach (1981) and Reinhold and Pierrehumbert (1982), topographic waves slope westward (i.e. downstream) with height. As such, the major difference between the blocked and unblocked flows was found to be the notable azimuthally-trapped wave in the former.

Chapter 7

Thermal Topography

This chapter will focus on experiments utilising thermal topography, as a way of studying the effect of azimuthally-varying heating upon the flow structure. This study is motivated by questions concerning the influence of the Walker Circulation on the atmospheric circulation, as well as the topographic heating of the Martian atmosphere. In addition, the experiment was designed in such a manner as to allow immediate comparison between the results forced by azimuthally-varying heating and the topographic forced results of the Partial Barriers experiments, discussed in the last chapter. Using the same parameter space, and a similar shape of base (i.e. the heating elements on the flat base occupy the same azimuthal area as the Partial Barriers experiment's isolated ridge), any differences to the previous investigation will therefore be due to the influx of heating, and the lack of a bottom trapped flow. First of all, a general outline of the method of experimentation will be given, followed by the results gathered. After that, the results will be analysed in detail, with comparison to both the previous conducted experiments and the literature.

7.1 Experimental Arrangement

As described in the experimental arrangement chapter, these experiments replaced the single isolated ridge topography with a section of heating elements with roughly the same extent in azimuth, so that the whole of the base was flat. Once again, like for the Partial Barriers experiments, the constant Hide Number scans of the resonance chapter were dropped in favour of the Extended-Regime experiment's investigations at single points in parameter space. The sloped lid and reversed temperature gradient were kept, as it was believed the beta effect would increase the chance of

observing resonant oscillations. In this way, the Thermal Topography experiment could be compared to all of the previous studies, as well as the obvious parallels to the blocking investigation.

7.1.1 Heating Element Calculations and Testing

As mentioned in the Experimental Arrangement chapter (and shown in Figure 3.8), three rectangular elements of 3 cm by 10 cm were utilised; each rated up to 10 W/in^2 (1.55 W/cm^2). This therefore provides a maximum possible power of 140W. However, it was not the aim of the heating elements to overwhelm the flow completely since, as mentioned in Chapter 1, Boubnov, Golitsyn and Senatorsky (1991) note that, at its maximum, "the temperature contrast between continents and oceans is of the same order as the temperature difference between tropical and polar regions." As such, it was decided to generate an azimuthal thermal contrast of roughly 2K via the elements, so that the azimuthal heating is on a similar scale to that of the radial heating during a typical 2K temperature difference experiment (the weakest of the temperature differences used). This also means that increasing the temperature difference for the experiments will in turn change the amount of relative heating (for example, making radial heating weakly dominant at 4K and strongly dominant at 7K), allowing the impacts of this effect to be observed.

The calculation for achieving 2K of heating is found by rearranging the definition of the Nusselt Number in an annulus, from Hide and Mason (1975), in terms of total heat transport, as follows:

$$H = \frac{2 \cdot \pi \cdot Nu \cdot D \cdot \kappa \cdot \rho \cdot c (T_b - T_a)}{\ln(b/a)} \tag{7.1}$$

where H is the total heating power, Nu is the Nusselt Number, defined as the ratio of the total heat transfer to the conductive heat transfer in the fluid, D is the annulus depth, κ is the thermal diffusivity of the working fluid, ρ is the density of the fluid, c is the specific heat capacity of the

fluid, and T_a and T_b are the temperatures at the inner and outer walls, respectively. This can be simplified by using the identity:

$$\kappa \cdot \rho \cdot c = \alpha \tag{7.2}$$

where α is the thermal conductivity of the fluid. Substituting this into Equation 7.1 gives:

$$H = \frac{2 \cdot \pi \cdot Nu \cdot D \cdot \alpha (T_b - T_a)}{\ln(b/a)}. \tag{7.3}$$

Assuming a value of order 10 for the Nusselt Number (judging from previous experiments such as Hide and Mason (1975) and Read (2003), for example), and using a value of 0.5 $WK^{-1}m^{-1}$ for the thermal conductivity of a 17.5/72.5% glycerol/water mixture, from Glycerine Producers' Association (1963), gives a heating power of 15W for the equivalent of 2K of radial temperature difference. The resistance of each element was determined to be 19 ohms, and the maximum voltage is 28 V, which gives a maximum current of 1.5 A. For effectively uniform heating, it was decided to wire the three elements in parallel, giving an effective resistance of 6.$\dot{3}$ ohms - hence, for 15W of heat input, the voltage should be 9.74 V and the current should be 1.54 A. This was achieved by using a variable power supply attached to the annulus.

As the value used for the Nusselt Number was just an assumption, and to make sure that the heating generated would act as thermal topography, a range of experiments were carried out at the same point in parameter space, but employing a range of input powers from 5-25W, in 5W increments. Figure 7.1 gives a selection of the results found, with the location of the heating elements indicated.

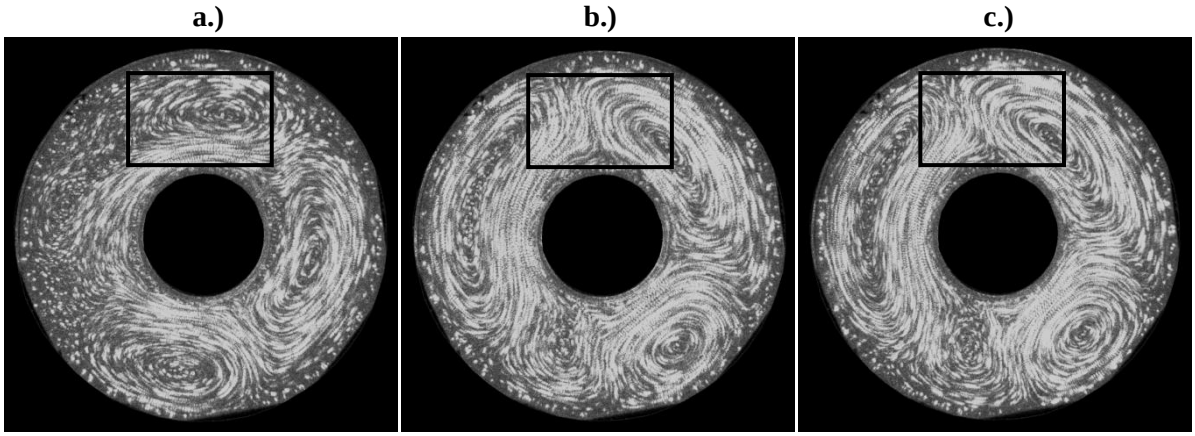

Figure 7.1: Streakline images at Level 3 (mid-depth), $\Omega = 0.6$ rads^{-1}, $\Delta T = 4K$, $\mathcal{T} = 2.044x10^7$, $\Theta_T = 0.878$; a.) 5W heating, b.) 15W heating, c.) 25W heating.

As Figure 7.1 illustrates, all results at this point in parameter space showed either a drifting wavenumber-1, as in (a), or drifting wavenumber-2, as in (b) or (c). Not only did the runs at 5W and 10W (not shown) produce the lower of the wavenumbers found, they also demonstrated no evidence of the flow interacting with the thermal topography. By contrast, the experiments at 15W and above were all extremely similar, with no additional effects found by increasing the heat input further, and the impact of the topography upon the flow (which will be discussed in the next section) was clear. As such, it was decided that the use of 15W of heating in the azimuthal direction was justified; producing a discernible effect qualitatively equivalent to the mechanical isolated ridge.

7.2 Results and Analysis

The results taken followed a similar procedure to those of the Extended-Regime and Partial Barriers experiments, investigating from 0.4 rads^{-1} to 2 rads^{-1}, at intervals of 0.2 rads^{-1}, and from 2K to 7K, at intervals of 1K. Both real-time streakline images and vector velocity maps created by CIV were used to collect the initial flow structure data, starting at 3600s after spin up. Each Figure is captioned with this time, as well as the light level, rotation rate, temperature difference, Taylor Number and Hide Number (dimensionless numbers calculated to 3s.f.). For sake of space and clarity, not every result that was taken will be given in this section. Instead, the regime diagram of Figure 7.2 has been compiled from the dominant flow structure at each investigated point of parameter space.

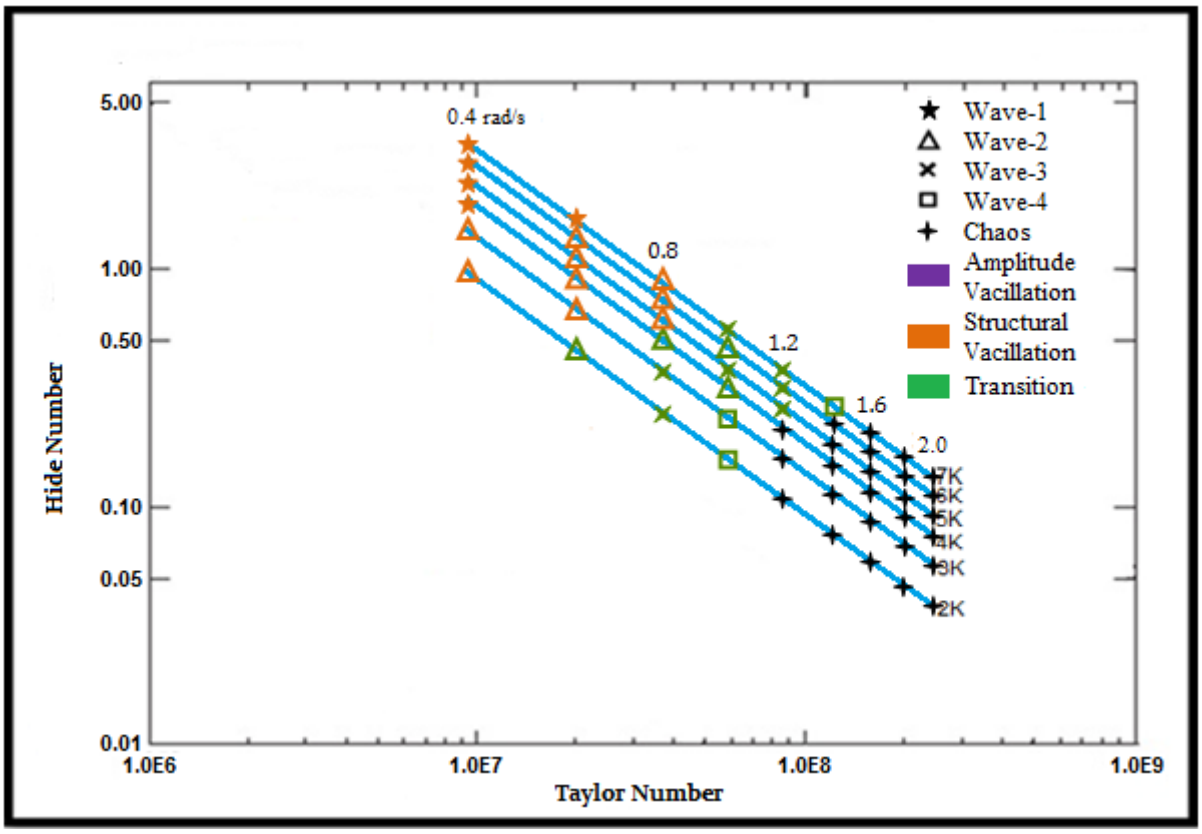

Figure 7.2: Regime diagram with locations and dominant flow characteristics of the results of the Thermal Topography experiment.

Surprisingly, Figure 7.2 shows no real evolution of the flow as the temperature difference is increased, beyond that what was observed in the Extended-Regime study in Figure 4.7. At both the temperature difference of 2K, where the radial and azimuthal heatings are equal, and the temperature difference of 7K, where the radial heating is strongly dominant, the flow shows a steady progression from small wavenumbers to higher ones, with increasing vacillation, as the rotation rate increases. As such, the effects of the azimuthal heating seem to be independent of the amount of radial heating. Instead, the impact of the thermal topography manifests by once again inducing two major regimes and associated transitions: an 'interference' region where the effects of the isolated topography on the drifting waves are strongly observable throughout the flow, and an 'irregular' region where the flow is erratic in time and space. These regimes are mostly the same as in the Partial Barriers experiment, with the same interactions with topography shown in Figure 6.2 and Figure 6.4, except with a wider range of possible wavenumbers during transitions for the 'interference' regime, including wavenumber-1, wavenumber-4 and even, rarely, wavenumber-5. The major difference between the

two studies is that the transition to the 'irregular' regime occurs both more gradually, leading in turn to larger vacillation and transition regions, and at a higher Hide Number, possibly due to the thermal topography reducing the static stability of the fluid flow. As such, many of the flows near the transition between regimes suffer from strong vacillation and themselves transition frequently between wavenumbers. To illustrate this effect, an example of the time variations of the flow structure from this transition region is given in Figure 7.3.

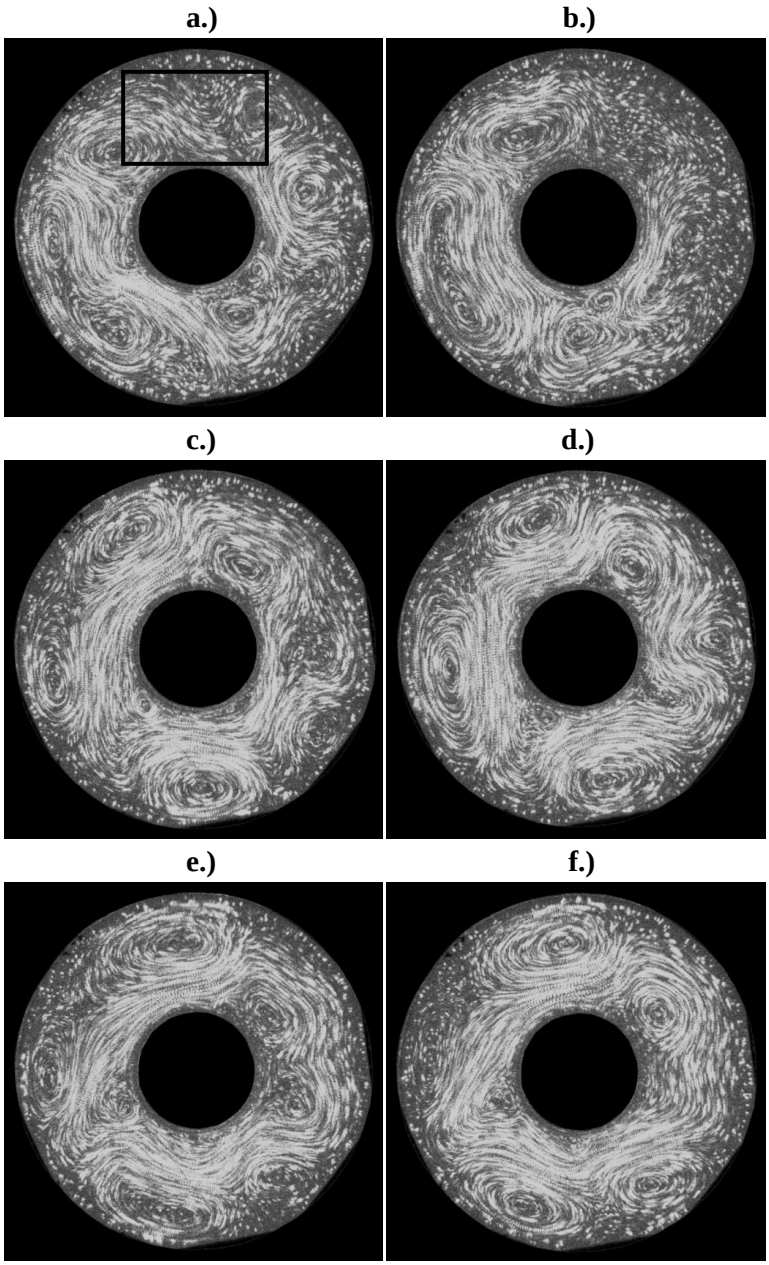

Figure 7.3: Streakline series at Level 3 (mid-depth), $\Omega = 1.0$ *rads*$^{-1}$, $\Delta T = 4K$, $\mathcal{T} = 5.680x10^{8}$, $\Theta_T = 0.316$; *a.)* $t = 3700s$, *b.)* $t = 3760s$, *c.)* $t = 3820s$, *d.)* $t = 3880s$, *e.)* $t = 3940s$, *f.)* $t = 4000s$.

For clarity, an indication of where the heating elements of the thermal topography lie has been added to Figure 7.3a, so that the main aspects of the ‘interference’ regime near the ‘irregular’ regime can be observed. The flow in (a) starts off as a clockwise drifting wavenumber-2, experiencing heavy structural vacillation presumably due to its proximity to chaos, and is therefore more irregular than its wavenumber-3 equivalent from the Partial Barriers experiment, Figure 6.2a. As one of the cyclonic eddies approaches the thermal topography in (b), it begins to decay, and a new eddy begins to grow just downstream of the heating elements. Notably, at this point, the circulation becomes extremely asymmetrical, with a very large anticyclonic eddy upstream of the topography (anticlockwise), and barely any eddy activity downstream of the topography. This effect is temporary, as it has disappeared by (c), wherein the flow returns to being a wavenumber-2 structure, rather than a skewed wavenumber-1, like in the Partial Barriers study. These processes are again likely due to the influences of the nearby ‘irregular’ regime. By (d), further vacillation has occurred, causing the circulation to transition to an irregular wavenumber-4 structure. This image is noteworthy in particular, as it strongly resembles the blocked state found by Weeks et al (1997), as reproduced in Figure 2.3b. This form is again temporary, with (e) showing a structure that appears to be a wavenumber-1 and wavenumber-2 superposition. As the flow drifts further still, in (f), the flow again becomes a wavenumber-2. The example given in Figure 7.3 is at mid-depth, but can be found at all levels including the bottom, as the replacement of the isolated ridge with the thermal topography means the lower depths of the annulus are no longer physically blocked. This will be discussed in the next section. At lower rotation rates, these transitions are less common, and lower wavenumbers are seen to be dominant.

Once again, like in the Partial Barriers experiment, the flow patterns demonstrate stronger anti-cyclonic eddies and weaker jets when compared to the Extended-Regime experiment, which may again be a feature of the inclusion of the sloped lid. Another similarly to the Partial Barriers experiment is that the flow also never becomes stationary, nor encounters the ‘stationary-transition’ regime, possibly due to the fact that the regions where these would be expected are covered by the ‘irregular’ regime. Said ‘irregular’ regime is also the same as before in Figure 6.4, with fine features

such as small, asymmetrically-placed eddies downstream of the heating elements and a permanent large eddy or a jet just upstream of the elements. In turn, the 'irregular' regime appears far less abruptly, with a noticeable but slow transition from one regime to the other, so that Figure 7.3 shows aspects of the impact of both regimes. In addition, hysteresis, found to be negligible in the Extended-Regime experiment, was once again observed throughout this area of parameter space, in regards to the beginning of the 'irregular' regime. For example, the result at a rotation rate of 1.1 $rads^{-1}$ and with a temperature difference of 4K was found to have an 'irregular' flow structure when the rotation rate was increased, as discussed above, but an 'interference' structure when the annulus was spun up from rest. As such, much like for the case with mechanical topography, it appears that the initial conditions of the fluid have an effect on where the transition between the regimes occurs, with the 'irregular' regime occurring at lower Taylor Numbers during a scan with increasing rotation rate.

To illustrate the 'interference' regime flow structure over a long timescale, Figure 7.4 shows the radial velocity for every point on a complete azimuthal circle at mid-radius, over the entire 1100s run. Once again, azimuthal position is given in degrees where positive is anticlockwise, and wherein the centre of the heating elements occurs at about 100°.

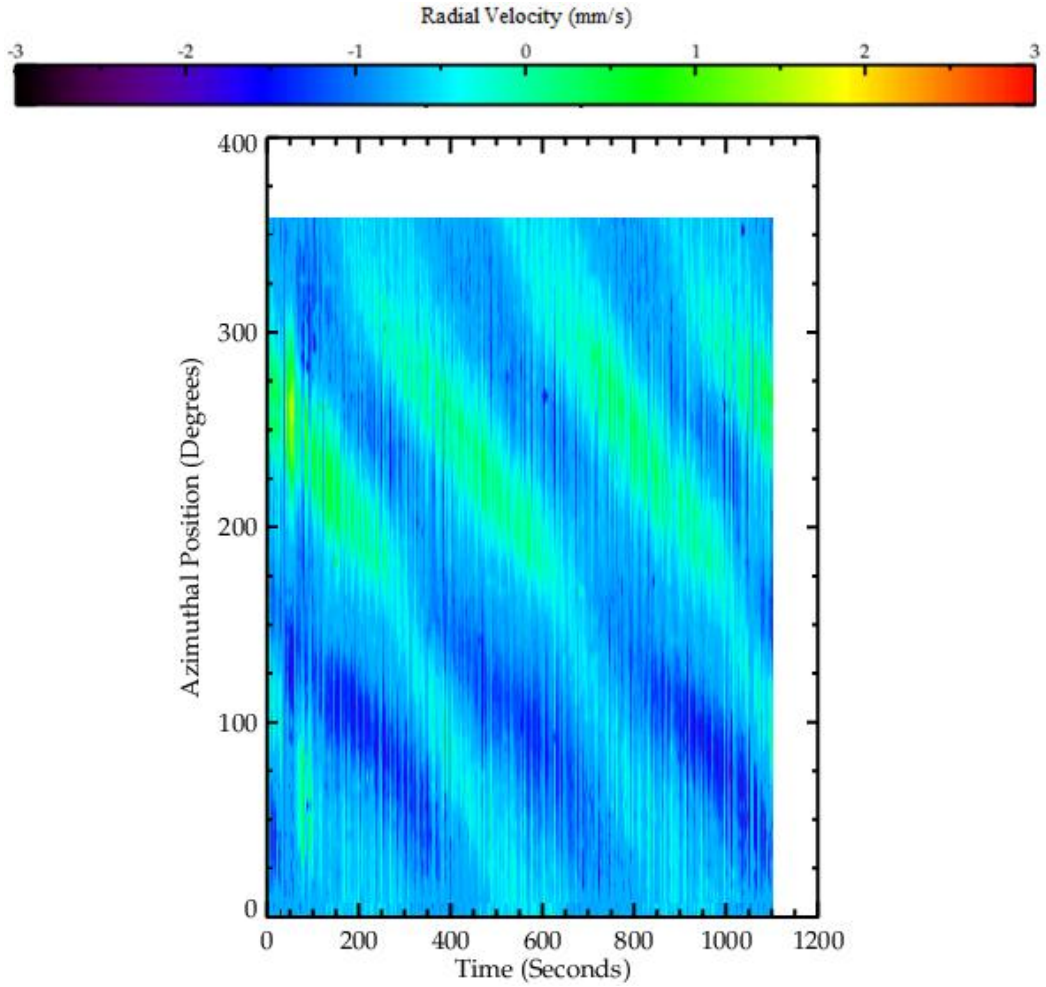

Figure 7.4: Radial velocity over time against azimuthal position for Level 3 (mid-depth), $\Omega = 0.4$ *rads*$^{-1}$, $\Delta T = 4K$, $\mathcal{T} = 9.088x10^{6}$, $\Theta_{\mathrm{T}} = 1.976$.

Figure 7.4 shows that the flow at this point in parameter space is mainly comprised of a clockwise drifting wavenumber-2 structure, which becomes more negative in azimuthal position over time. As the rotation rate is very slow, the drifting waves travel with a lower drift rate than the Partial Barriers example, shown in Figure 6.3. For the thermal topographic case the impact of the wave encountering the topography begins at around an azimuthal position of 175°, where the drifting wave can be observed to decrease in strength and be altered in phase. This is the same as the wave progression found in the Partial Barriers experiments, and the visual disappearance and reappearance of the wave as it encounters the topographic peak is also similar. Once again, the wave that disappears when crossing the topography is indeed the same wave that reappears once the flow has moved on, due to the unbroken line connecting the drifting flow on either side of the thermal topography. In

Figure 7.4, however, the drifting wave takes a much greater time and distance to regain its original strength after reappearing, only doing so at around an azimuthal position of 250°.

Similarly, for a point in parameter space inside the 'irregular' regime, Figure 7.5 shows the radial velocity for every point on a complete azimuthal circle at mid-radius, over the entire 1100s run.

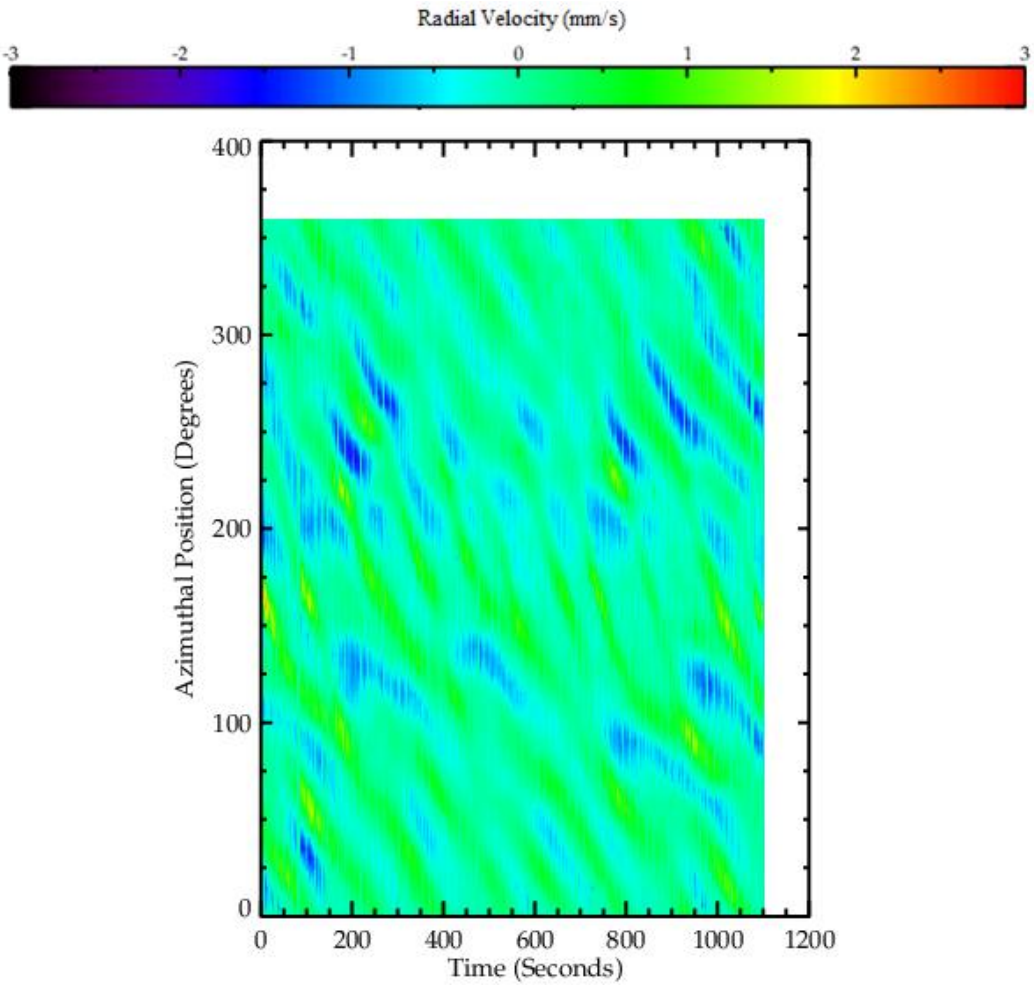

Figure 7.5: Radial velocity over time against azimuthal position for Level 3 (mid-depth), $\Omega = 1.6$ *rads*$^{-1}$, $\Delta T = 4K$, $\mathcal{T} = 3.635x10^{7}$, $\Theta_{\mathrm{T}} = 0.494$.

Like for the 'irregular' regime in the Partial Barriers experiments, shown in Figure 6.5, Figure 7.5 shows a far more erratic flow structure than in the 'interference' regime case in Figure 7.4, but also shows that the flow is not purely random and chaotic. Once again, some clockwise drifting wave structure of several different wavenumber components with varying drifting rates can be observed,

often overlapping to contribute to the erratic nature of the flow. Interestingly, however, the impact of the topography seems to be greatly reduced compared to the other experiments and regime, with the strongly erratic flow structure near the heating elements appearing very similar to the structure far away from them.

Time-Averaged Flow Structure

Taking a time-average of the flow structure over the period of the drifting waves (about 200s) has the effect of removing the drifting wave elements and leaving only the stationary components. As such, Figure 7.6 gives an example of time-averaged flow for the 'interference' regime, using azimuthal velocity, radial velocity and a kinetic energy map.

Figure 7.6 further illustrates the similarities between the Thermal Topography and the Partial Barriers experiments, with (a) and (b) showing a weak quasi-wavenumber-1 structures and (c), which combines the previous two examples into a kinetic energy map to illustrate the total flow structure, showing a single stationary vortex occurring directly above the heating elements. This is again evidence for a pressure drop as the flow crosses the heat influx, as well as highlighting that the sole stationary component is the topographically-forced wavenumber-1. This shows that Taylor columns can occur even without mechanical topography, creating an "imaginary cylinder" purely from azimuthally-varying thermal forcing. In contrast to the experiments with an isolated ridge, however, the jet is now stronger and more circular in nature, creating a full persistent gyre over the thermal topography. This can be assumed to be due to a lack of a physically trapped bottom circulation.

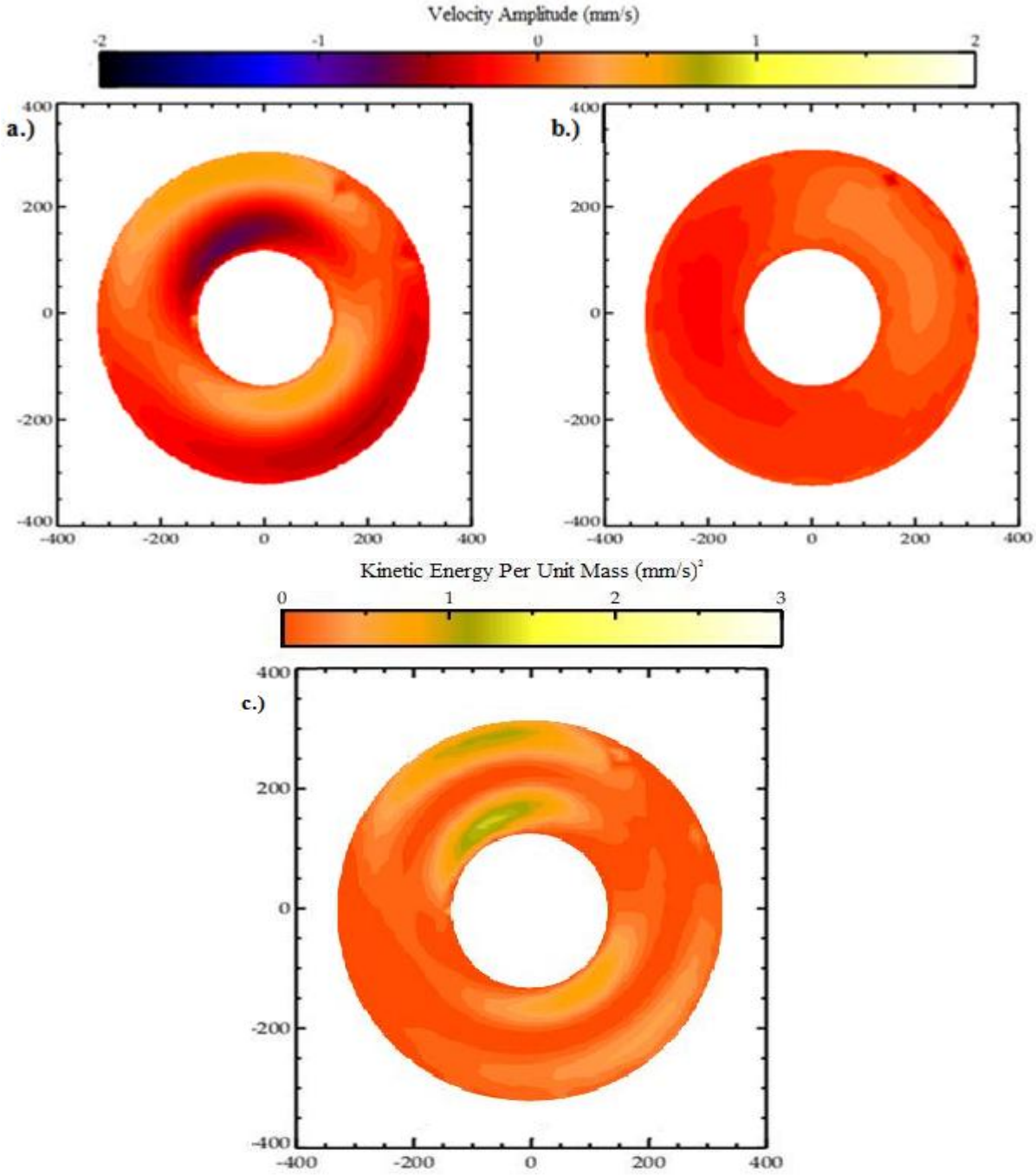

Figure 7.6: Azimuthal velocity (a), radial velocity (b) and kinetic energy (c) averaged over 200s for Level 3 (mid-depth), $\Omega = 0.4$ *rads*$^{-1}$, $\Delta T = 4K$, $\mathcal{T} = 9.088x10^{6}$, $\Theta_T = 1.976$.

Similarly, Figure 7.7 shows a time-average of the flow structure over the period of the drifting waves (about 200s) for the 'irregular' regime, using azimuthal velocity, radial velocity and a kinetic energy map.

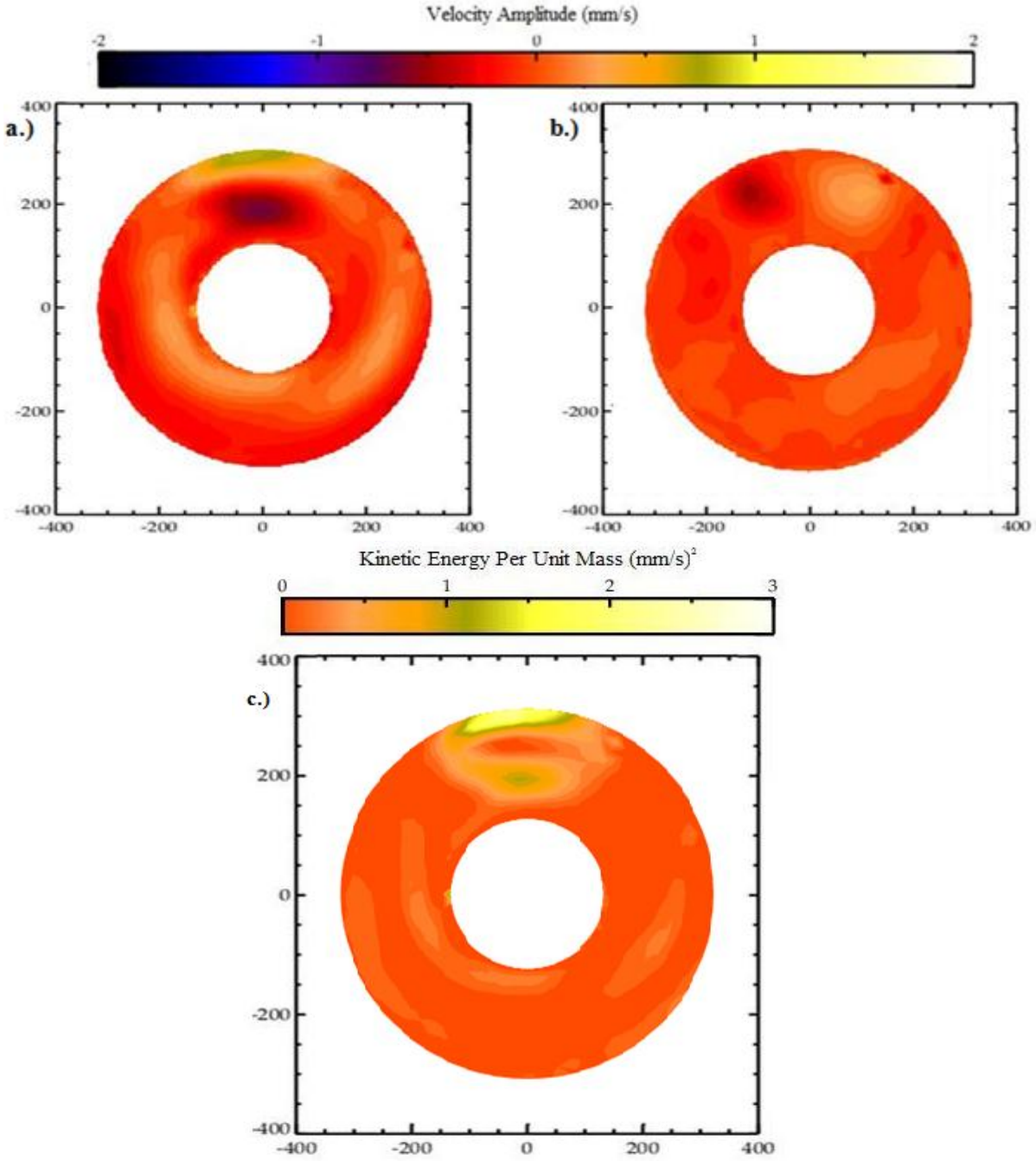

Figure 7.7: Azimuthal velocity (a), radial velocity (b) and kinetic energy (c) averaged over 200s for Level 3 (mid-depth), $\Omega = 1.6$ *rads*$^{-1}$, $\Delta T = 4K$, $\mathcal{T} = 3.635x10^{7}$, $\Theta_T = 0.494$.

Figure 7.7 demonstrates that the 'irregular' region has a very similar time-averaged structure to the 'interference' region, with a quasi-wavenumber-1 structure in (a) and a stationary vortex occurring as a Taylor column directly above the bottom topography in (c), much like what was found for mechanical topography. Another similarity to the Partial Barriers experiment is that the vortex and corresponding pressure drop as the flow crosses the topographic peak are significantly larger in amplitude for the 'irregular' regime, again most likely due to the increased Taylor Number. This

further suggests that the impact of the topography upon the flow becomes greater as the forcings from the rotation rate are increased.

Bottom Flow Structure

At the lowest light level, the flow is now uninterrupted, whilst it was physically blocked by the topographic peak of the base in the Partial Barriers study. Figure 7.8 gives an example of this flow, at the same parameters as Figure 7.3.

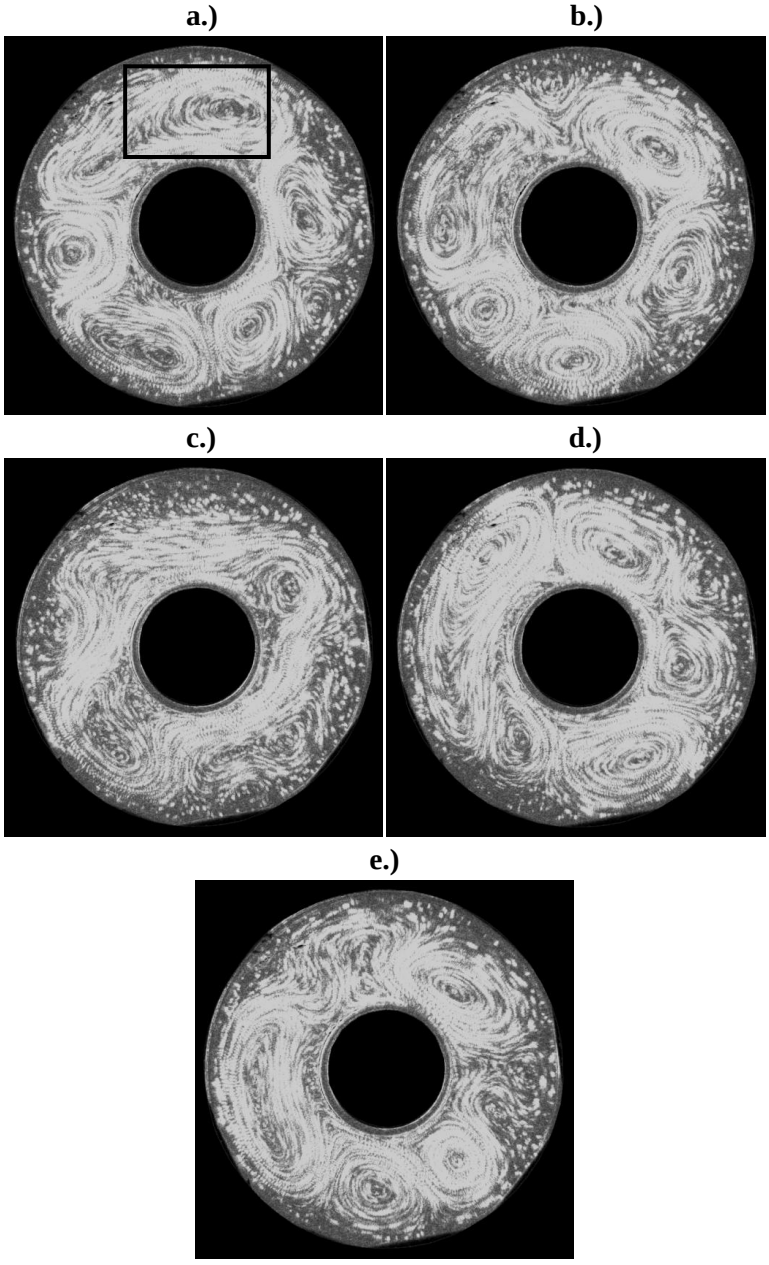

Figure 7.8: Streakline series at Level 5 (bottom), $\Omega = 1.0$ *rads*$^{-1}$, $\Delta T = 4K$, $\mathcal{T} = 5.680x10^{8}$, $\Theta_T = 0.316$*; a.)* $t = 4100s$*, b.)* $t = 4180s$*, c.)* $t = 4260s$*, d.)* $t = 4340s$*, e.)* $t = 4420s$*.*

Figure 7.8 shows the main aspects of the bottom flow under thermal topography, with an indication of where the heating elements lie added to (a). Without the physical barrier to the flow's progression, as in Figure 6.8, the circulation no longer creates a persistent azimuthally-trapped wave upstream (anticlockwise) of the peak, nor does it gives rise to the smaller downstream eddies. Instead the flow resembles more the image sequence in Figure 7.3, with irregular drifting wavenumber-2 components, seen most clearly in (c), but with notable vacillation and transitions due to the impact of the 'irregular' regime. This suggests that the flow is more uniform in the vertical direction than in the Partial Barriers experiments, as there is no separation between blocked and unblocked flow. However, the structure at the bottom of the annulus does appear to be undergoing stronger chaotic effects than at higher levels. This is likely to be caused by the proximity to the base's heat source, injecting additional energy into the flow. Whilst the above just gives a single example of one point in parameter space, the bottom level being mostly identical to the higher levels, except with increased vacillation and transitions, is a typical arrangement throughout the entire area of investigation.

7.2.1 Azimuthal Time Variations

For further understanding of the 'interference' and 'irregular' regimes, a deeper analysis must be undertaken. Once again, the measurements from UVMAT were converted to polar coordinates on a regularly-spaced grid, and the units of the velocities changed from pixels / time step to mms^{-1}. The zonal background mean flow and any anomalous readings were then removed. A Fourier analysis of the wavenumber structure in terms of amplitude and phase could then be carried out for every time step - combining these analyses allows the evolution of the flow over time to be observed. Azimuthal and radial velocity components were calculated at a quarter of the radial distance between the inner wall and the outer wall (closer to the inner wall) and at mid-radius respectively, chosen to avoid nodes in the radial direction and because the patterns found were indicative of the rest of the flow.

‘Interference’ Regime

Figure 7.9 shows an example of the time variations of the amplitude of the first ten wavenumbers, for a typical flow in the ‘interference’ regime, far away from the boundary with the ‘irregular’ regime.

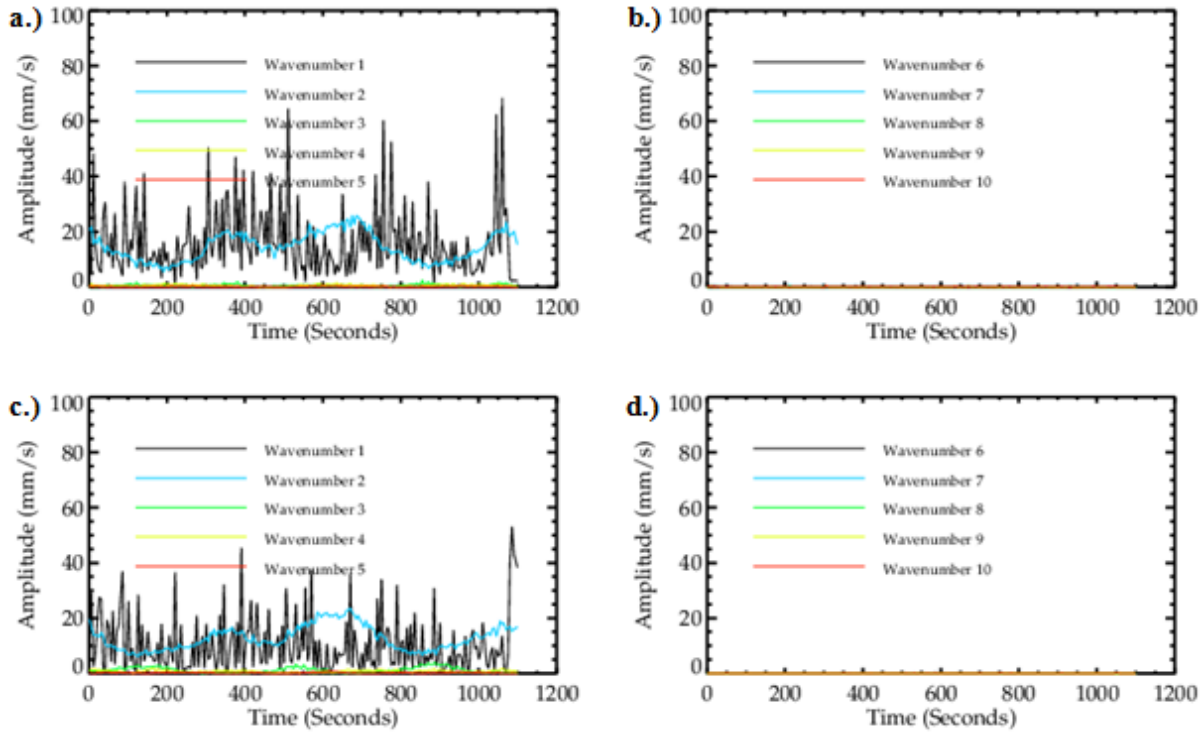

Figure 7.9: Velocity amplitude for Level 3 (mid-depth), $\Omega = 0.4$ rads^{-1}, $\Delta T = 4K$, $\mathcal{T} = 9.088x10^{6}$, $\Theta_T = 1.976$; a.) azimuthal velocity for wavenumbers 1-5, b.) azimuthal velocity for wavenumbers 6-10, c.) radial velocity for wavenumbers 1-5, d.) radial velocity for wavenumbers 6-10.

As can be seen in Figure 7.9, the flow is comprised of wavenumber-1 and wavenumber-2 components, with the wavenumber-1 dominant in the azimuthal case, and both roughly equal in the radial case. It can be noted that the amplitudes of the former are higher than the amplitudes of the latter, whereas, in the ‘interference’ region of the Partial Barriers study (Figure 6.9), it was the opposite. This wavenumber-1 dominance was also not observed in any of the Partial Barriers experiments, but the rest of the structure is familiar. There is again the oscillation from the flow’s topographic interactions, with the peaks of the wavenumber-2 component matching the troughs of the wavenumber-1 component, although to a lesser extent than in the Partial Barriers experiment case,

presumably due to the weaker forcing conditions. As before, this is caused by eddies encountering the topography and transitioning between a wavenumber-1 and a wavenumber-2 structure. Figure 7.9 also shows that the wavenumber-1 component is unusually noisy, both in comparison to previous experiments and the other wavenumbers. The reason for this was found to be spurious errors in the CIV process adding additional noise to the wavenumber-1 component, but only for this result.

As the 'interference' regime flow at this location in parameter space is dominated by wavenumber-1 and wavenumber-2 components, Figure 7.10 shows the phase of these notable wavenumbers, for the same flow example as previously.

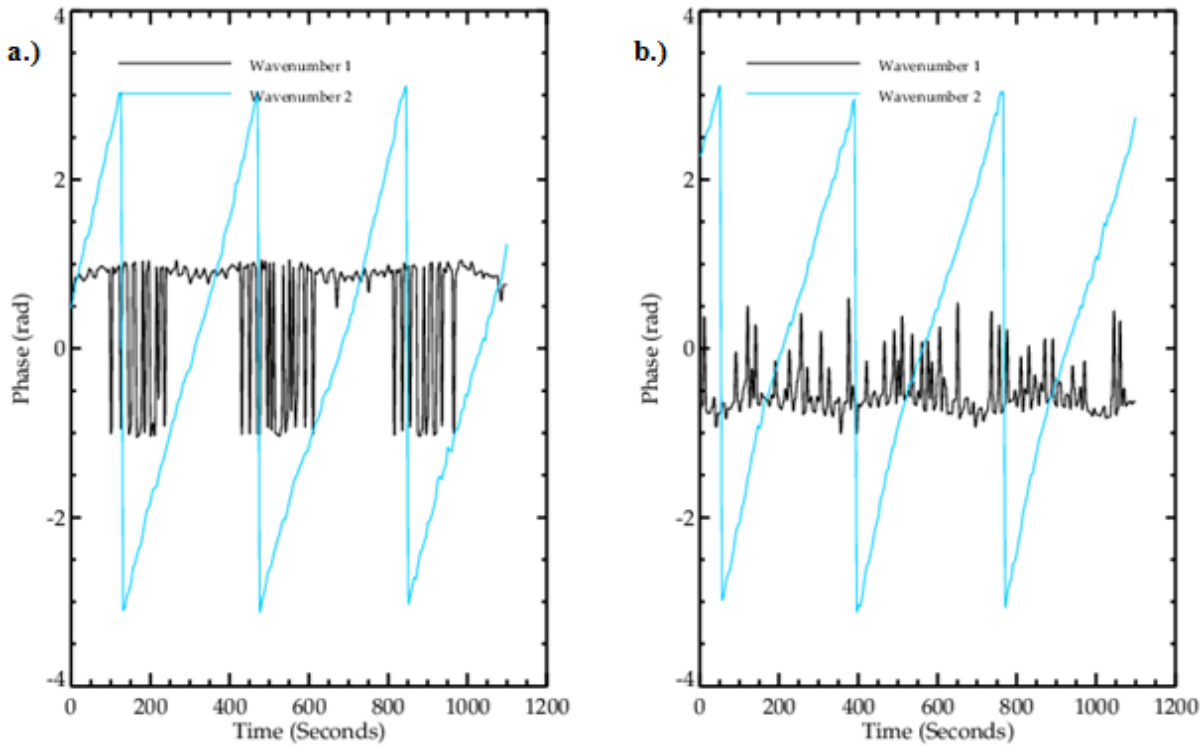

Figure 7.10: Velocity phase for Level 3 (mid-depth), $\Omega = 0.4$ rads^{-1}, $\Delta T = 4K$, $\mathcal{T} = 9.088x10^6$, $\Theta_T = 1.976$; a.) azimuthal velocity for wavenumber-1 and wavenumber-2, b.) radial velocity for wavenumber-1 and wavenumber-2.

Figure 7.10 gives the phase of the flow, which shows that the wavenumber-2 component, like the other components not shown, is constantly drifting, but the wavenumber-1 component is stationary (quasi-stationary in the azimuthal case). This is of interest, as the studies of the bottom of

the annulus showed no azimuthally-trapped wave, so this stationary wavenumber-1 component must arise directly from the forcing of the topography, not merely its physical presence in the arresting of a drifting structure. The 'interference' flow structure is therefore caused by interactions between the drifting waves and a locked stationary wavenumber-1 component, much like the stationary wavenumber-3 of the Resonance experiment, and arises regardless of whether the topography is mechanical or thermal. During periods where the drifting waves and stationary wave are out of phase, they constructively interfere, creating a wavenumber-2 flow in this case. In periods where they are in phase, they destructively interfere, creating the skewed wavenumber-1 flow.

For further reference, Figure 7.11 shows the radially-averaged kinetic energy of the flow at this point in parameter space.

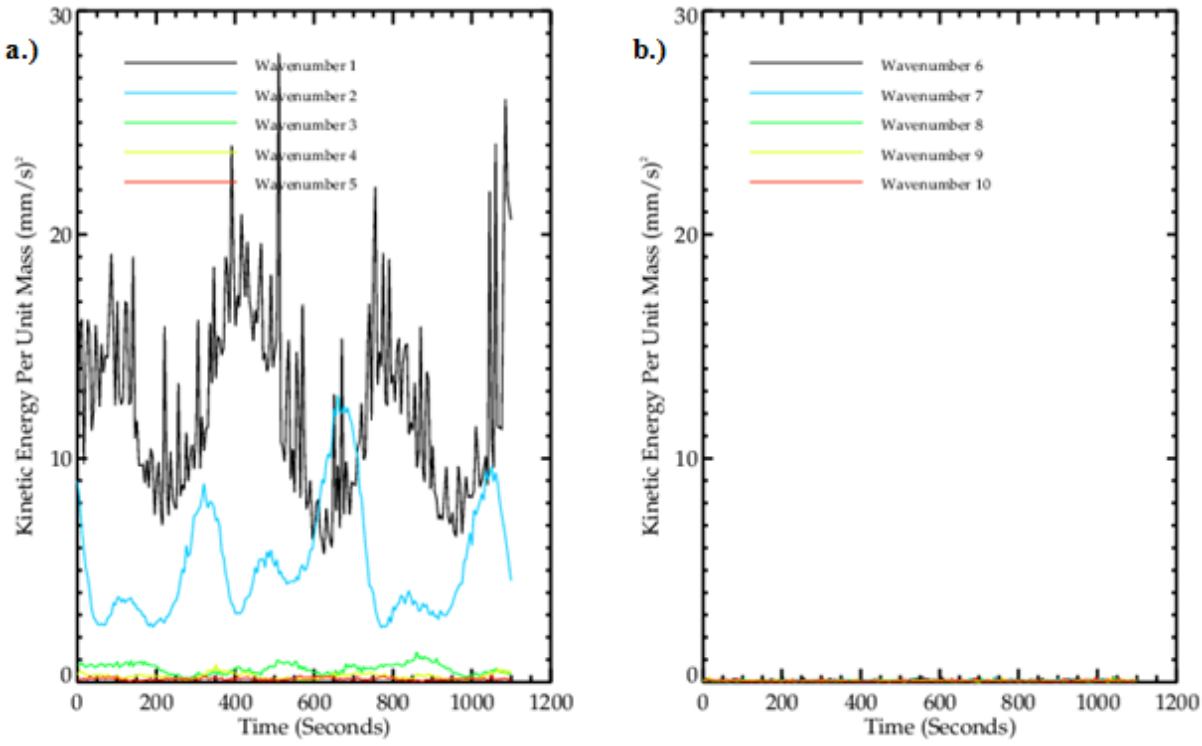

Figure 7.11: Radially-averaged kinetic energy for Level 3 (mid-depth), $\Omega = 0.4$ rads^{-1}, $\Delta T = 4K$, $\mathcal{T} = 9.088x10^{6}$, $\Theta_T = 1.976$; a.) azimuthal velocity for wavenumbers 1-5, b.) azimuthal velocity for wavenumbers 6-10.

Just like in the Partial Barriers experiment, Figure 7.11 shows the kinetic energy of the flow being transferred back and forth between the wavenumber-1 component and the wavenumber-2 component, with the peaks of one aligning with the troughs of the other. This indicates that the same process of topographic interaction is occurring, regardless of whether the oscillation is forced by mechanical or thermal topography. In addition, the time variation of the wavenumber-2 kinetic energy component appears to contain a period-doubled oscillation, only found at this large Hide Number region in parameter space. This is possibly evidence for a weak form of topographic resonance, as the wavenumber-1 component, which is forced by the topography, is dominant at this point. Once again, a contrast can be made between the time variations of the kinetic energy of the dominant wavenumber-1 component and the kinetic energy of the zonal mean flow. At mid-depth, this zonal mean is found to fluctuate in direction from positive to negative and vice versa, due to being acted upon by both the topographically-forced waves from the bottom and the free baroclinic waves from the top and middle of the tank. As such, Figure 7.12 shows the kinetic energy of the zonal mean from the same point in parameter space as in Figure 7.11, but at the higher Level 2, and with a superposition of the wavenumber-1 kinetic energy time-series for comparison.

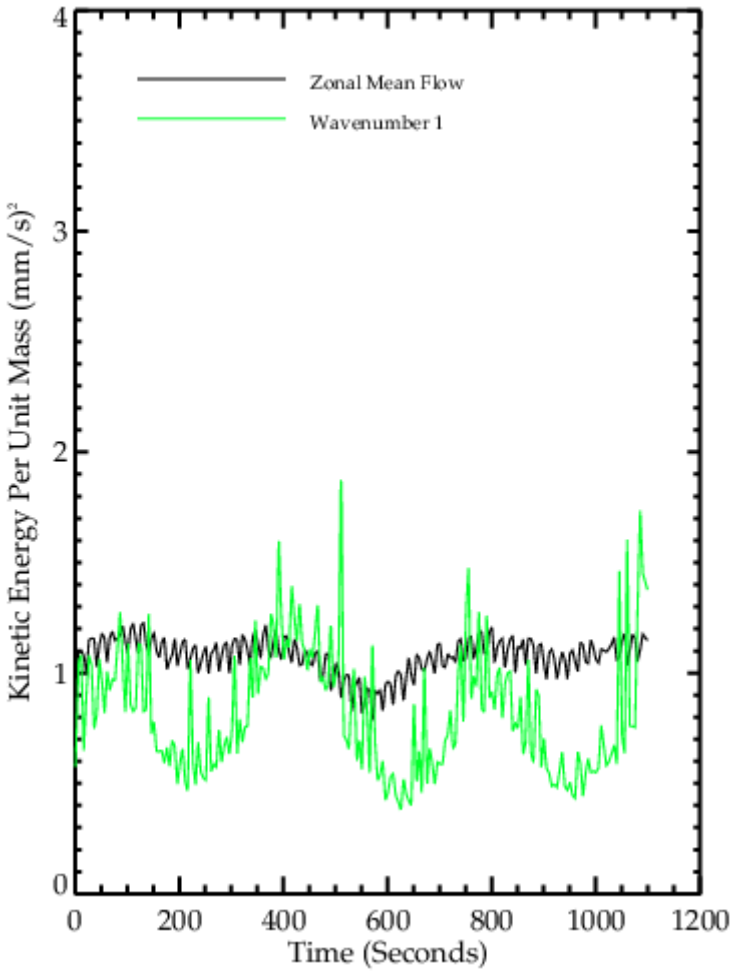

Figure 7.12: Radially-averaged kinetic energy of zonal mean flow (black) with wavenumber-1 total kinetic energy (green, not to scale) as comparison, for Level 2, $\Omega = 0.4$ *rads*$^{-1}$, $\Delta T = 4K$, $\mathcal{T} = 9.088x10^{6}$, $\Theta_T = 1.976$.

Figure 7.12 shows a correlation between the kinetic energy of the zonal mean flow and the kinetic energy of the dominant mode, oscillating effectively in quadrature like the equivalent example from the 'interference' regime of the Partial Barriers experiment (Figure 6.12). As such, this is consistent with elements of nonlinear wave-zonal flow interactions and an exchange of energy between the waves and the mean zonal flow, as in both of the previous experiments. In addition, there is also now a higher frequency component to the zonal mean flow kinetic energy, with a period of around 30s. However, the correlation in the case with heating elements is much weaker than the case with the isolated ridge, suggesting that the nonlinear wave-zonal flow interactions occurring are of

less importance to the overall flow structure, compared to wave-wave interactions for example, for thermal topography than for mechanical topography.

'Irregular' Regime

Figure 7.13 gives the time variations of the amplitude of the first ten wavenumbers for a typical flow in the 'irregular' regime, again at a location in parameter space fairly distant from the boundary between regimes.

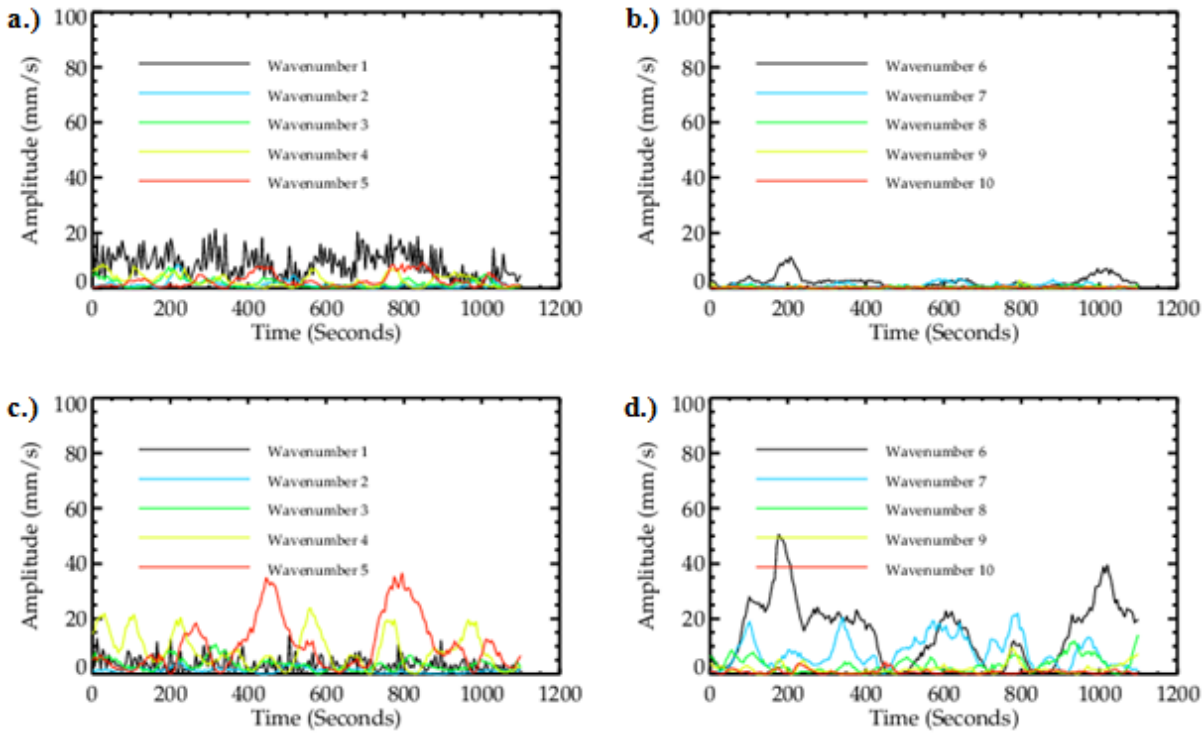

Figure 7.13: Velocity amplitude for Level 3 (mid-depth), $\Omega = 1.6$ rads^{-1}, $\Delta T = 4K$, $\mathcal{T} = 1.454x10^{8}$, $\Theta_T = 0.124$; a.) azimuthal velocity for wavenumbers 1-5, b.) azimuthal velocity for wavenumbers 6-10, c.) radial velocity for wavenumbers 1-5, d.) radial velocity for wavenumbers 6-10.

Once again, Figure 7.13 shows the azimuthal case dominated by a wavenumber-1 component, and the radial case dominated by wavenumber-4, wavenumber-5 and wavenumber-6. These higher wavenumber radial amplitudes are also much larger than the azimuthal amplitudes, despite the azimuthal amplitudes being larger in the 'interference' case of Figure 7.9. This is notably the same as

in the Partial Barriers experiment (Figure 6.13), and is arguably even clearer in this case, possibly due to the slower transition between the two regimes with thermal topography. As such, transitions from the 'interference' regime to the 'irregular' regime for both mechanical topography and thermal topography are found to be associated with the locations in parameter space where large wavenumber radial components become dominant over small wavenumber azimuthal components.

By examining the phases over time of the ten wavenumbers of Figure 7.13, most of the wave components were found to be steadily drifting, with the exception of wavenumber-1. As the 'irregular' regime flow is dominated by radial wavenumber-4, wavenumber-5 and wavenumber-6 components, Figure 7.14 shows the phase of these notable wavenumbers, as well as the wavenumber-1 component, for the same flow example as previously.

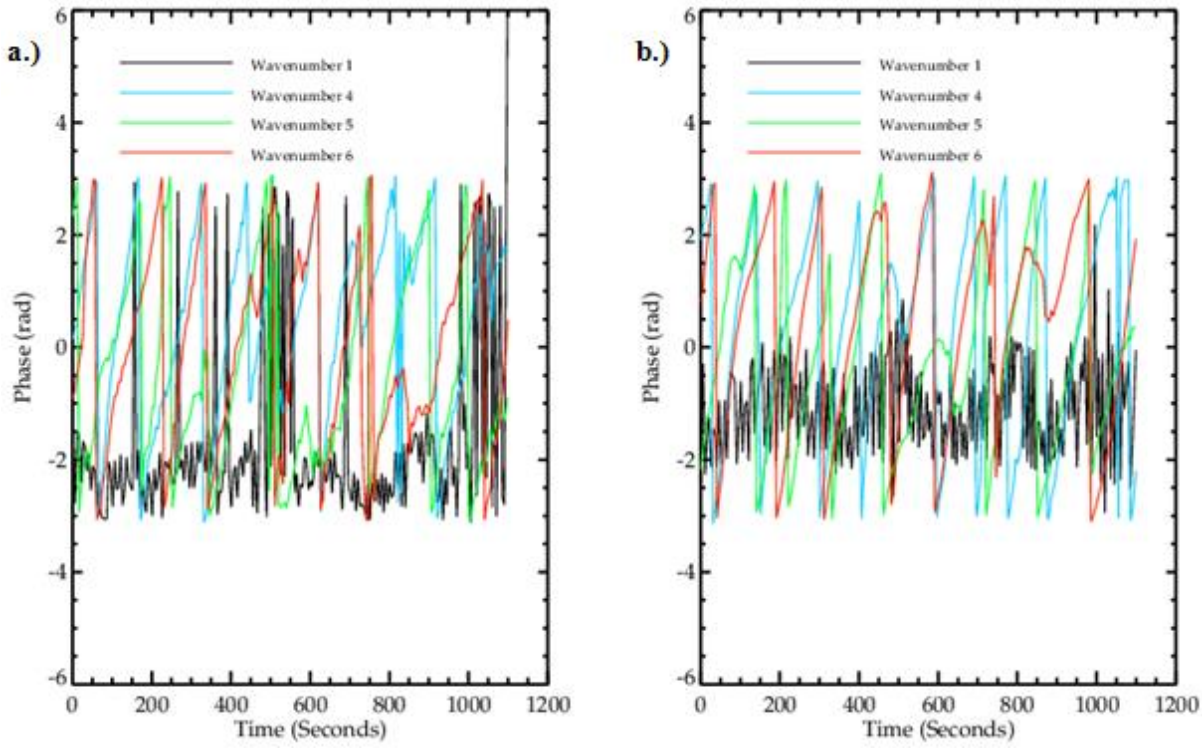

Figure 7.14: Wavenumber-1 phase (black) against wavenumber-4 phase (blue), wavenumber-5 phase (green) and wavenumber-6 phase (red), for Level 3 (mid-depth), $\Omega = 1.6$ *rads*$^{-1}$, $\Delta T = 4K$, $\mathcal{T} = 1.454x10^{8}$, $\Theta_T = 0.124$*; a.) azimuthal velocity b.) radial velocity.*

Figure 7.14 shows that the azimuthal velocity wavenumber-1 component is stationary and the high radial velocity wavenumbers are drifting, seemingly in sync. Again, this is the same as in the Partial Barriers experiment (Figure 6.14), and shows an even better agreement, especially in the radial velocity case, which will be used solely in discussions from now on. Once again, assuming that the two active resonant triads involve the drifting wavenumber-4 and wavenumber-5 components and the stationary wavenumber-1 component forced by the thermal topographic base, and the drifting wavenumber-5 and wavenumber-6 components and the stationary wavenumber-1 component forced by the thermal topographic base, the phases were 'unwrapped', and the phase differences between them over time were observed, as shown in Figure 7.15. These differences are both found by subtracting the unwrapped phase of the two middle wavenumber components (wavenumber-4 and wavenumber-5, respectively) from the sum of the unwrapped phase of the higher wavenumber (wavenumber-5 and wavenumber-6, respectively) and wavenumber-1 components.

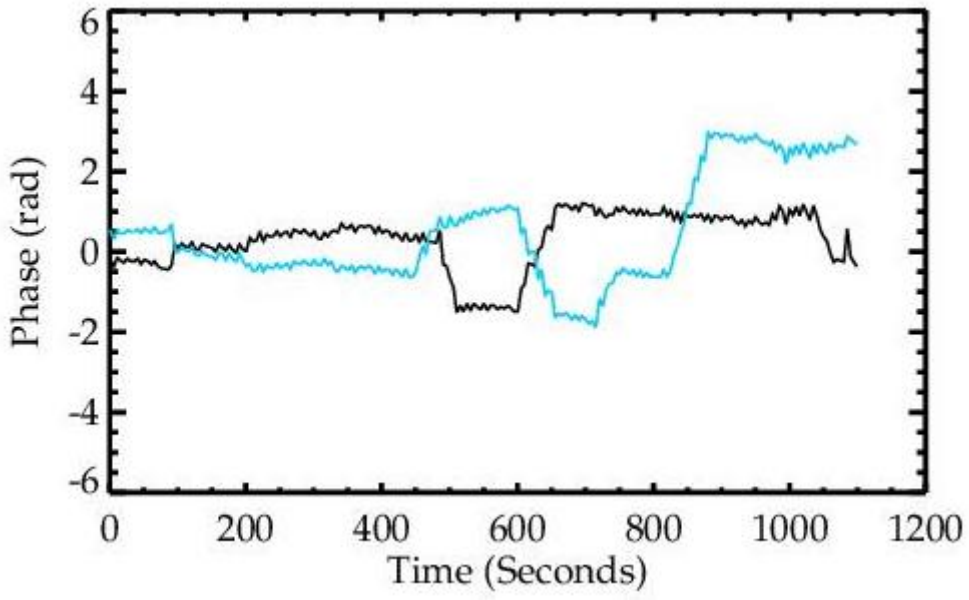

Figure 7.15: Unwrapped radial wavenumber-5, wavenumber-4 and wavenumber-1 phase difference ($\varphi_1 + \varphi_5 - \varphi_4$, black) against unwrapped radial wavenumber-6, wavenumber-5 and wavenumber-1 phase difference ($\varphi_1 + \varphi_6 - \varphi_5$, blue) for $\Omega = 1.6$ rads^{-1}, $\Delta T = 4K$, $\mathcal{T} = 1.454x10^8$, $\Theta_T = 0.124$.

Once again, Figure 7.15 shows a large amount of noise from the experiment, but also that both phase differences have long areas of stationarity, giving evidence that the same two resonant wave-triads are indeed important for the evolution of the flow under thermal topography. It can also be observed that there is much less noise than the Partial Barriers case (Figure 6.15), and there is a clearer structure, although the phase-slips no longer appear to have particularly regular intervals. From the study with mechanical topography, it was determined that these phase-slips may be due to the topography interactions as the dominant wave drifts over the peak of the base, so it is possible that the phase-slips in the thermal topography case are less regular due to the lack of a physical peak.

Hence, it appears that this 'irregular' regime, regardless of whether the topography used is mechanical or thermal in origin, contains two resonant wave-triads: one between the stationary wavenumber-1 forced by the thermal topography, and the drifting wavenumber-4 and wavenumber-5 components; and the other again between the stationary wavenumber-1 forced by the thermal topography, but instead with the drifting wavenumber-5 and wavenumber-6 components. This "butterfly" is independent of any azimuthally-trapped waves, occurring under any topography with a dominant wavenumber-1 structure. Once again, this gives evidence that the nonlinear interactions that are associated with the transition from the 'interference' regime to the 'irregular' regime have wave-wave components, with energy being transferred between the different wavenumber modes.

In addition, for the 'irregular' regime, a contrast can be made between the time variations of the kinetic energy of the dominant wave component and the kinetic energy of the zonal mean flow. Figure 7.16 shows the kinetic energy of the zonal mean from the same parameter space as in Figure 7.13, but at the higher Level 2, and with a superposition of the total kinetic energy from the first ten wavenumbers (since there is no clear dominant wavenumber component) for comparison.

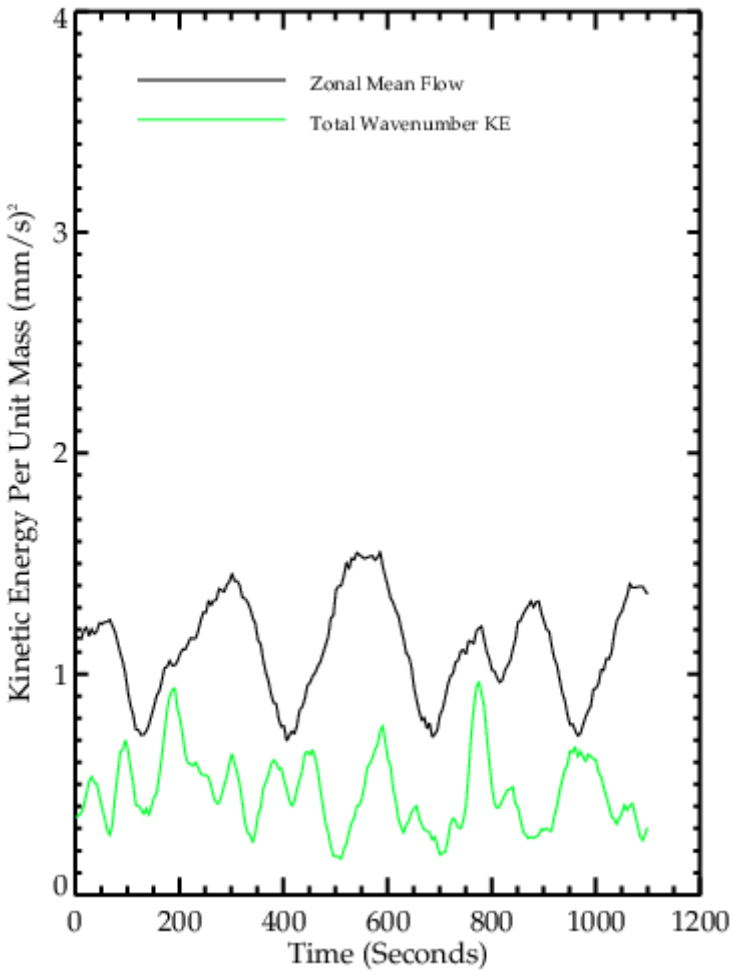

Figure 7.16: Radially-averaged kinetic energy of zonal mean flow (black) with total kinetic energy (green, not to scale) as comparison, for Level 2, $\Omega = 1.6$ *rads*$^{-1}$, $\Delta T = 4K$, $\mathcal{T} = 1.454x10^{8}$, $\Theta_T = 0.124$.

Within the 'irregular' region, Figure 7.16 shows that there is very little correlation between the kinetic energy activity of the sum of the wavenumber components and the zonal mean flow. As such, wave-zonal flow interactions appear to have less influence in the 'irregular' regime than in the 'interference' regime, in a similar way to what was found for the Partial Barriers experiment (Figure 6.16) but to a much greater extent. As such, it is possible that the flow structure and resulting phenomena of the 'irregular' regime are associated more with nonlinear wave-wave interactions, rather than with wave-zonal flow interactions. Overall, therefore, throughout the entire examined parameter space of the experiments using thermal topography there seems to be evidence for a reduction in the impact of nonlinear wave-zonal flow interactions when compared to mechanical topography.

Vertical Structure

The vertical structure of the Thermal Topography experiment, which is unblocked throughout, allows for the comparison with the vertical structure of the Partial Barriers experiment, which had both blocked and unblocked sections. Figure 7.17 gives a snapshot of the vertical structure in the 'interference' regime, quickly switching between levels so that all images are taken at approximately the same time, as much as physically possible. Each image is roughly 10 seconds apart, to allow for a streakline picture, and, considering the slow speed of drifting and oscillation, this was determined to be sufficient.

Figure 7.17 shows that the vertical structure of the experiments with thermal topography is more uniform than those with partial barriers, due to the lack of the azimuthally-trapped wave in the latter. As such, (a), (b) and (c) all show an irregular wavenumber-2 structure having just interacted with the topography, with a downstream (clockwise) shift as height is increased. This structure is familiar for this area of parameter space, also appearing in Figure 7.8a at the bottom of the tank and Figure 7.3e at mid-depth. Nearing the lid, as for the Partial Barriers experiments, the flow becomes weaker and more irregular, with both (d) and (e) showing an irregular wavenumber-1 with reduced amplitude, once more with a downstream shift. This again is associated with the reduced zonal mean flow due to the upper boundary layer near the sloped lid appearing to suppress baroclinic activity.

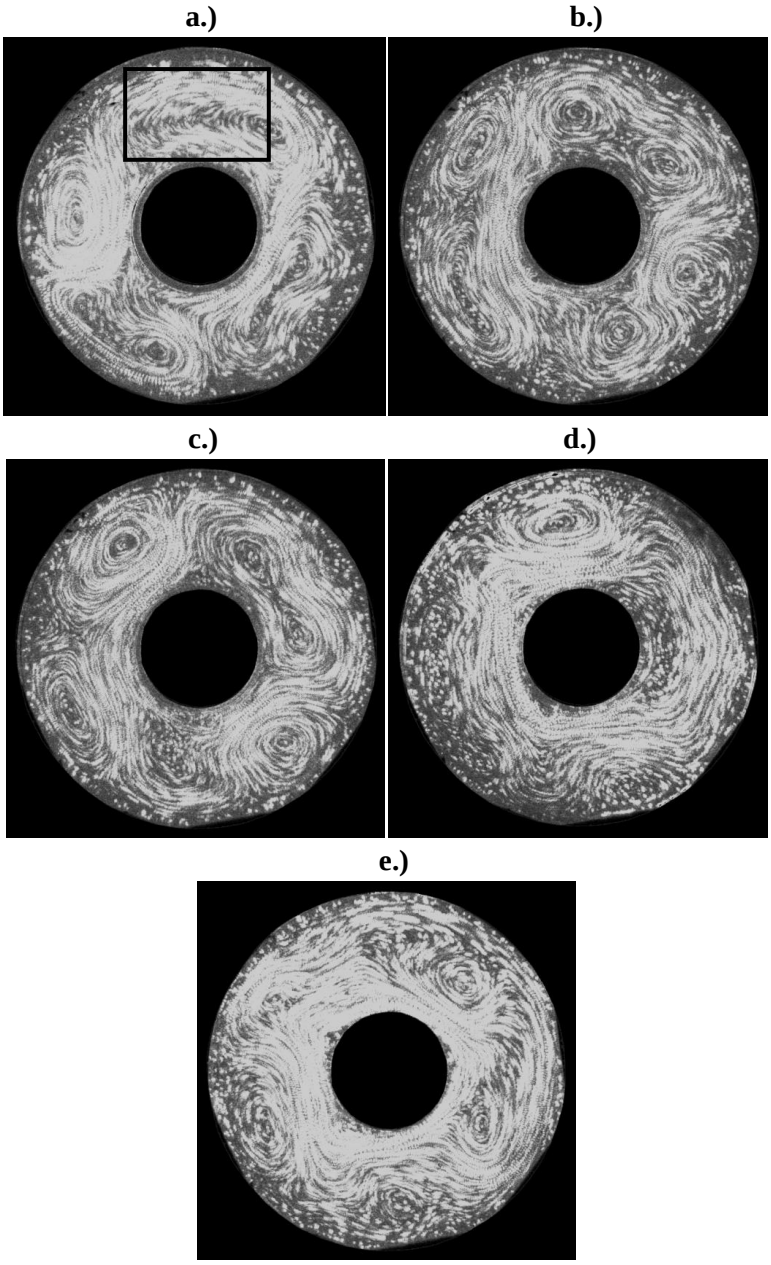

Figure 7.17: Streakline images for $\Omega = 1.0$ *rads*$^{-1}$, $\Delta T = 4K$, $\mathcal{T} = 5.680x10^{7}$, $\Theta_T = 0.316$*; a.) Level 5, b.) Level 4, c.) Level 3, d.) Level 2, e.) Level 1.*

Similarly, over a longer timescale, Figure 7.18 shows the time variations of the amplitude of the first five wavenumbers for runs at each height.

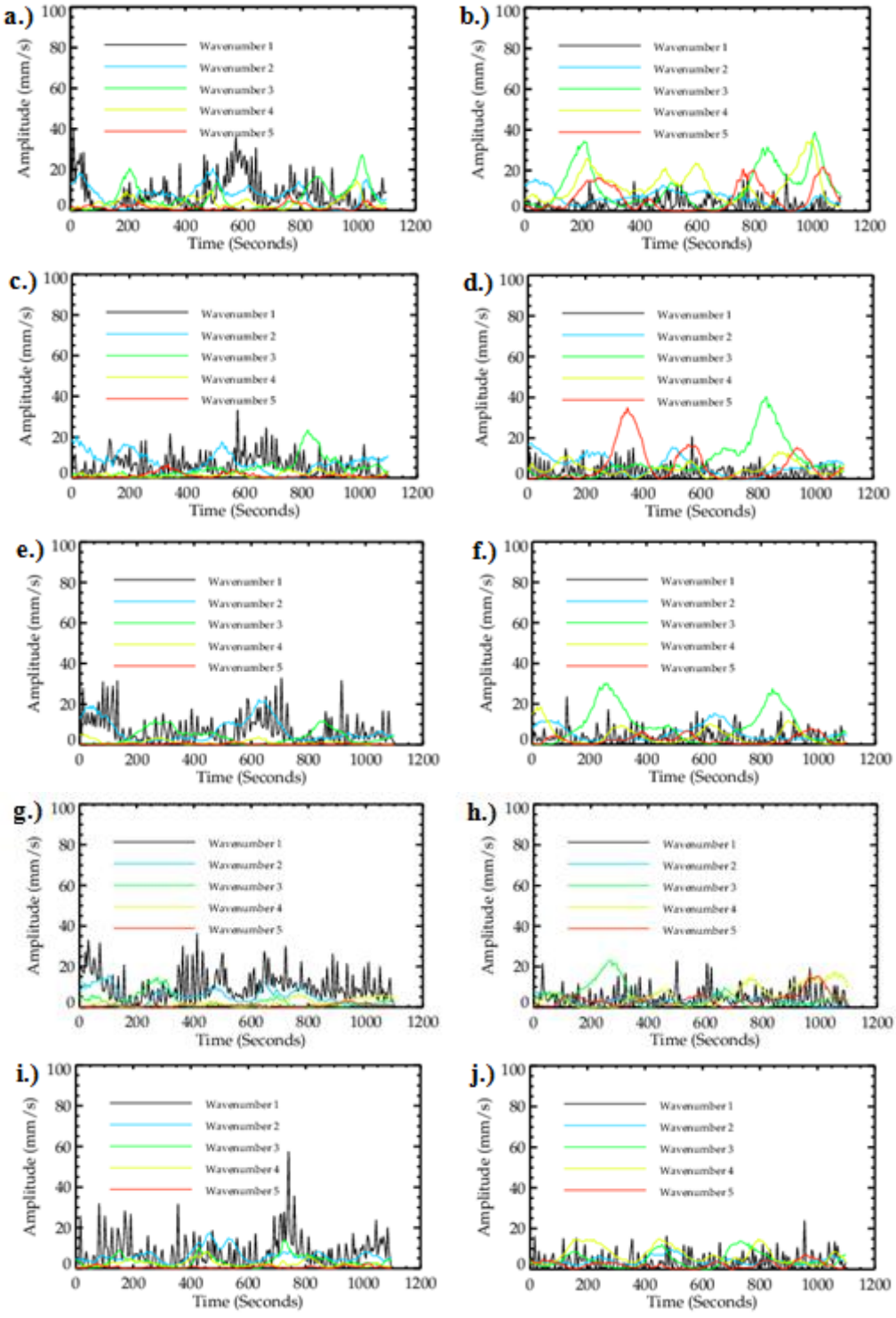

Figure 7.18: Velocity amplitude for $\Omega = 1.0$ *rads*$^{-1}$, $\Delta T = 4K$, $\mathcal{T} = 5.680x10^{7}$, $\Theta_T = 0.316$, *a.) Level 5 azimuthal velocity for wavenumbers 1-5, b.) Level 5 radial velocity for wavenumbers 1-5, c.) Level 4 azimuthal velocity for wavenumbers 1-5, d.) Level 4 radial velocity for wavenumbers 1-5, e.) Level 3 azimuthal velocity for wavenumbers 1-5, f.) Level 3 radial velocity for wavenumbers 1-5, g.) Level 2 azimuthal velocity for wavenumbers 1-5, h.) Level 2 radial velocity for wavenumbers 1-5, i.) Level 1 azimuthal velocity for wavenumbers 1-5, j.) Level 1 radial velocity for wavenumbers 1-5.*

Figure 7.18 again illustrates that the vertical flow structure is more uniform than for the Partial Barriers experiment, as shown in Figure 6.18, varying only slightly with height. At all levels there is an azimuthal velocity wavenumber-1 dominance for most of the time, but with frequent transitions to wavenumber-2, such as in (e), (g) and (i), as well as transitions to wavenumber-3 at the lower depths (a) and (c). These transitions are associated with the proximity in parameter space of the 'irregular' regime, although the flow is not located close enough that the higher radial velocity wavenumbers have risen to dominate the structure, even at the middle depth, as shown in (f). The effect of the lid can be seen in Levels 2 and 1, where the amplitudes are generally weaker, especially in the radial cases (h) and (j), as discussed previously. Similarly, the phase variations of the wavenumber components over time are fairly uniform throughout the vertical scale, though the wavenumber-1 component was found to be less stationary than in the Partial Barriers experiment, with large amounts of phase-slips and noise. This is likely due to the lack of an azimuthally-trapped wave when compared to the mechanical topography. All other wavenumbers are found to be constantly drifting at all heights.

7.3 Discussion

In this experiment, many parallels can be drawn with the previous Partial Barriers study. To begin with, the azimuthally-varying heating used was indeed able to create notable flow structures and dynamics, such as forced stationary baroclinic waves, Taylor columns and topographic interference, comparable to mechanical topography. Considering this, as a comparison between mechanical and thermal topography over the same parameter space, this study showed a great deal of similarities. Most notably, both experiments have a lack of dominant stationary activity, both show topographic interactions as the flow structure drifts over the peak / heating elements, creating flows similar to the blocked and zonal states, and both have the same general shape of regime diagram, separated into 'interference' and 'irregular' regions. The mechanism for generation of the latter regime is also the same, being associated with the rise of coupled resonant wave-triads between the topographically-

generated wavenumber-1 and the wavenumber-4, wavenumber-5 and wavenumber-6 drifting components. The differences between the Thermal Topography and the Partial Barriers study are twofold. Firstly, without any physical peak at the base, there is no blocked low-level circulation at the bottom of the annulus. This makes the vertical structure for the Thermal Topography experiments a lot more uniform, aside from a small shift downstream with height, as well as showing that the topographic interactions and 'interference' flows discovered are independent of the azimuthally-trapped bottom wave. Secondly, the boundary between the 'interference' and 'irregular' regimes is significantly more gradual with thermal topography, leading to more transitions between a wider range of wavenumbers, and stronger vacillation throughout. This more variable flow may be caused by the additional heat flux into the system. In regards to topographic resonance, unlike in the Partial Barriers investigation, some limited evidence was discovered. Whilst the heating elements used were not entirely arranged with a wavenumber-1 structure, it would be reasonable to once again assume that topographic resonant interactions would mainly occur between the thermal topography and a wavenumber-1 flow, if at all. As such, when the wavenumber-1 component was found to dominate the flow structure at high Hide Numbers, period-doubling of the wavenumber-2 amplitude component was observed. Period-doubling is a phenomenon commonly associated with topographic resonance, as noted in the Resonance experiment, though the region in question was too small to observe a bifurcation sequence, or other conclusive evidence of topographic resonance.

The results gathered also agree well with the few experiments reported in the literature with azimuthally-varying heating. Boubnov, Golitsyn and Senatorsky (1991) found similar topographic interactions between the drifting baroclinic waves their experiments encountered and the azimuthally-varying heating, in addition to noting evidence of nonlinear blocking effects, such as interactions occurring along with a reduction in zonal flow. They also reported stationary wave regimes, which were not found in the current study, but this is likely the result of the location of the thermal topography - along the outer wall for their investigation, and attached to the base for this one. As such, Boubnov, Golitsyn and Senatorsky's experiment had a fully periodic topographic structure in

azimuth, much like this thesis' Resonance investigation wavenumber-3 base, which was found to be more likely to produce stationary waves than the more aperiodic isolated ridge from the Partial Barriers investigation, of which the heating elements take their shape.

In terms of the Walker Circulation, Bjerknes (1969) discovered that the strength of said circulation was dependent on sea-surface temperatures, being stronger when the temperatures were lower and weaker when they were higher. This is similar to the jet-shifting found in this study, as when the flow was not interacting with the thermal topography (i.e. the immediate temperature difference was lower) the zonal state with strong jet circulation occurred, and when the flow did interact with the thermal topography (i.e. the immediate temperature difference is higher) the blocked state with reduced jet circulation was found. As suggested by Julian and Chervin (1978), this jet-shifting occurs downstream of the heating elements, though Figure 7.6 and Figure 7.7 both show that the stationary elements of the flow are locked to appear directly above the elements. Since the thermal topography results gathered were so similar to those with mechanical topography, this highlights the importance of the often overlooked Walker Circulation on the atmospheric circulation, with a land-sea temperature difference on the order of the polar-Equator temperature difference producing comparable flow patterns to that of a major mountain range. This also possibly suggests that the ENSO, which, as discussed in Chapter 2, is a chaotic oscillation with a timescale on the order of 3-6 years, could have some relationship with the frequent transitions and strong vacillation of many of the flows found, or may occur as the equivalent of the advent of the 'irregular' regime. However, the real ENSO is likely to be more complicated than this, as it involves coupled oscillations in both the oceans and the atmosphere interacting with each other.

One of the major similarities with the Partial Barriers study was the occurrence of the two resonant wave-triads, or "butterfly", that seem to occur and become active within the 'irregular' regime. This shows that resonant wave-triads can still occur with thermal topographic forcing, and is not dependant on mechanical topography, as was put forward by Jin and Ghil (1990). On the other hand, Jin and Ghil also suggested that a thermally-forced study would not observe the wave-zonal flow interactions of a topographic-forced equivalent, due to the removal of form-drag effects, but would still see wave-wave interactions. Whilst the occurrence of resonant wave-triads do indeed give evidence of wave-wave interactions occurring under thermal topographic conditions, only limited correlation between the kinetic energies of the zonal mean flow and the dominant wave component was also noted. In this way nonlinear wave-zonal flow interactions were found to be reduced in importance to the flow structure compared to wave-wave interactions, but not to be entirely absent, especially within the higher Hide Number 'interference' regime. This appears to contradict the conclusions of Jin and Ghil's purely numerical study. Furthermore, the wave-triad interactions act in the same way as for the Partial Barriers experiment, backing up the assertion that it is the shape of the topography that determines whether it encounters a 'stationary-transition' regime and corresponding oscillation, or an 'irregular' regime. The existence of the wave-triads also constitutes thermal topography's relationship to LFV and impacts on the real atmosphere. This is especially noteworthy, as a reduction in sea-ice from climate change will reduce the atmosphere's equivalent to azimuthally-varying heating, thus in turn causing significant changes to LFV and the global circulation. One possible outcome of the decreased atmospheric thermal topography is suggested by studies such as Power and Smith (2007), Francis and Vavrus (2012) and Liu et al (2012) to be the recent rise in number and longevity of persistent blocked states, leading to severe weather across the world.

Chapter 8

Conclusions and Further Work

In this chapter the various results and observations of Chapters 4, 5, 6 and 7 will be examined in greater detail, with a discussion on what has been learnt from the studies so far. The success of the thesis' stated aims and objectives will also be analysed, in the form of answers to the motivating questions posed in Chapter 1, reproduced here for convenience. After that, the physical relevance of the results gathered to planetary atmospheres and oceans will be discussed. A final section will then highlight the outstanding issues of the experiments, especially in terms of further extensions to the studies in order to investigate other aspects of topographic impact upon large-scale flow.

8.1 Resolutions of Motivating Questions

The most important objective of the Extended-Regime experiment was to expand the parameter space of a similar topographic annulus study, Read and Risch (2011), especially in terms of increasing the Taylor Number. To achieve this, a regime diagram was compiled, finding that the transitions between regimes, both in terms of dominant flow structure and vacillations, happened in locations that could be estimated by extrapolating the results of the previous work, with clear progression and reliable transition points. However, within a region of structural vacillation at large Taylor Numbers, a new regime was discovered, featuring an oscillation between stationary elements and axisymmetric or chaotic structures, later found to have an origin in nonlinear instabilities of a topographic resonance. This 'stationary-transition' regime was noted to be distinct from Read and Risch's Low Frequency Amplitude Vacillation and Stationary Amplitude Vacillation regimes, due to LAV having a different dominant wavenumber to the topographic base and SAV having a much more defined flow structure between dominant stationary elements. However, a number of similarities were observed between the regimes, in particular the visual similarities of the flow structures and

oscillation behaviour over time, which leads to the suggestion that those phenomena are low Taylor Number non-resonating variants of the 'stationary-transition' regime, found further from the location of linear resonance.

As a secondary outcome, the Extended-Regime experiment was able to explore a large, varied area of parameter space in order to create a basis for comparison for the later experiments. This permitted investigation of the motivating questions that this thesis set out to attempt to find solutions to, as given below:

- Can topographic resonance and associated Hopf bifurcations be found in a differentially-heated annulus and, if so, under what conditions?

Continuing on from the results of the Extended-Regime study, the Resonance experiment sought to find evidence of topographic resonance and associated Hopf bifurcations under beta-plane conditions using a sloping lid. Preliminary investigation from the drift-rate study showed that the addition of the sloping lid, whilst retaining $dT/dr > 0$, caused a reduction in baroclinic activity, making stationary waves and related phenomena difficult to discern. In response, a reversed temperature gradient with $dT/dr < 0$ was employed. Utilising both the sloping lid and the reversed temperature gradient, constant Hide Number scans through the 'stationary-transition' region provided strong evidence for the existence of a Hopf bifurcation sequence, as shown in Figure 5.12. Hence, the regime was determined to be a near-resonant region, where nonlinear resonant instabilities caused a 23.3 to 41.5 'day' velocity amplitude oscillation to be set up within the dominant wavenumber-3 component and its harmonics, and with the maximum amplitude of the oscillation representing the point closest to the location of linear resonance, deduced to lie at 1.6 rads^{-1} for $\Theta_T = 0.14$. Some evidence for a possible period-doubling transition near the beginning of the oscillation and a route to chaos at its end were also observed. In this way, a clear example of topographic resonance in a differentially-heated annulus was uncovered.

- If topographic resonance is found, what is its mechanism for generation?

In terms of the mechanism of generation for the topographically resonant oscillation, the nonlinear instabilities were found to have terms in both wave-zonal flow and wave-wave interactions. The former manifest themselves in the antiphase relationship between the kinetic energy of the dominant wavenumber-3 component and the kinetic energy of the mean zonal flow over time, as illustrated by Figure 5.10. Over the oscillation period, energy is transferred back and forth between these two components. The wave-wave interactions are associated with the forced wave component losing energy to other modes via the creation of a resonant wave-triad comprised of the baroclinic and topographically-forced barotropic components of the dominant quasi-stationary wavenumber-3, and the baroclinic component of a quasi-stationary wavenumber-6. Figure 5.14 shows this impact as a strongly periodic phase-difference between the modes over time. Both the wave-triad and the antiphase kinetic energy relationship only appear within a relatively small region in parameter space, referred to as the 'stationary-transition' regime, where the flow enters a near-resonant state. Moving closer to the centre of the linear resonance causes these effects to strengthen and the oscillation to increase in amplitude, whilst moving further away weakens them, allowing the circulation to return to a non-resonating state.

- If topographic resonance is found under fully sinusoidal conditions, does it still occur with partially sinusoidal (i.e. isolated ridge) topography?

For the Partial Barriers study, whilst the isolated ridge used was not entirely wavenumber-1 in structure, it would be reasonable to assume that resonant interactions would occur mainly between the topography and a wavenumber-1 flow, if at all. However, despite a topographic-forced stationary wavenumber-1 component being noted at high Taylor Numbers, this component was never noted to dominate the flow structure, and neither the near-resonant 'stationary-transition' regime nor other evidence of topographic resonance were found in the experiments with the isolated ridge. Instead, two

new regimes were found. The first was an ‘interference’ region, found at low Taylor Numbers, wherein the stationary wavenumber-1 forced by the topography interacting with the dominant drifting wave and led to an interference effect, in the form of jet-shifting, as the waves crossed the peak of the base. The other regime was an ‘irregular’ region, found at High Taylor Numbers, where resonant wave-triads similar to that associated with a bifurcation sequence in the Resonance experiment were found to be associated with a transition toward erratic flow.

- Does blocking from partial barriers lead to the occurrence of multiple equilibria in the annulus?

The blocked bottom flow of the Partial Barriers experiment was found to be defined by a large persistent azimuthally-trapped wave upstream of the topographic peak, appearing as a stationary wavenumber-1, which extended further vertically than the topography and weakened as it crossed into the unblocked flow above. Within the ‘interference’ regime, this stationary wavenumber-1 interacted with the drifting dominant wavenumbers at mid-depth to form an oscillation between blocked and zonal states. As noted by Weeks et al (1997), the flows that resemble the blocked state exhibited reduced jet intensity but larger wave amplitude, along with a noticeable increase in the strength of anticyclonic eddies when compared to those that resembled the zonal state. However, these frequent transitions between states do not give evidence for the existence of multiple equilibria as, in the real atmosphere, both blocked and zonal flows are defined as discrete alternative states that the circulation ‘chooses’ to adopt based on initial conditions. On the other hand, within the small area of parameter space between the ‘interference’ and ‘irregular’ regimes, hysteresis was noted. In that area, which regime the flow structure ended up as did appear to be dependent on the initial conditions, namely whether the flow had been spun up from rest or from some other point in parameter space. As such, there is some evidence of multiple equilibria in this study of blocking from partial barriers, although it is not as widespread in location as was suggested by previous numerical studies, such as Risch (1999).

- Does bottom-located azimuthally-varying heating have a comparable effect on the large-scale flow to mechanical topography?

Employing flat heating elements, arranged in a similar shape to the Partial Barriers experiment's isolated ridge, in order to create azimuthally-varying heating in the annulus was indeed able to replicate mechanical topographic-like flows and dynamics, such as forced stationary baroclinic waves, resonant wave-triads and topographic interference. On the other hand, Jin and Ghil (1990) suggested that a thermally-forced study would not observe the wave-zonal flow interactions of a mechanical topographically-forced equivalent, due to the removal of form-drag effects, but would still see wave-wave interactions. Whilst the occurrence of resonant wave-triads do indeed give evidence of wave-wave interactions occurring under thermal topographic conditions, only limited correlation between the kinetic energies of the zonal mean flow and the dominant wave was noted. In this way nonlinear wave-zonal flow interactions were found to be reduced in importance to the flow structure compared to wave-wave interactions, but not to be entirely absent, especially within the higher Hide Number 'interference' regime. This appears to contradict the conclusions of Jin and Ghil's numerical model, perhaps due to its weakly nonlinear and barotropic framework lacking form-drag terms when mechanical topography is not present.

- If so, how similar are mechanical and thermal topography, over the same parameter space?

Over the same parameter space, the Thermal Topography experiment and the Partial Barriers experiment were found to have a great deal of similarities. Most notably, both experiments have a lack of dominant stationary activity, both show topographic interactions as the flow structure drifts over the peak / heating elements, creating flows similar to the blocked and zonal states, and both have the same general shape of regime diagram, separated into 'interference' and 'irregular' regions. However, the boundary between the 'interference' and 'irregular' regimes is significantly more gradual with thermal topography, leading to more transitions between a wider range of wavenumbers,

and stronger vacillation throughout. In contrast to the single wave-triad from the Resonant experiment's wavenumber-3 base, both the isolated ridge and the thermal topography produced a "butterfly" of Rossby-like waves made up of two nonlinear resonant wave-triads sharing a common mode: the first between the stationary wavenumber-1 component forced by the topography, and the drifting wavenumber-4 and wavenumber-5 components; and the second between the same stationary wavenumber-1 component forced by the topography, and the drifting wavenumber-5 and wavenumber-6 components. This would appear to indicate that the flows are dominated by nonlinear wave-wave interactions involving a stationary wave forced by the topography. In addition, this also shows that resonant wave-triads can still occur with thermal topographic forcing and are not dependant on mechanical topography, as was put forward by Jin and Ghil (1990). Furthermore, since the wave-triad interactions act in the same way as for the Partial Barriers experiment, and were associated with the occurrence of the 'irregular' regime in both studies, it is suggested that it is the general shape of the topography that determines whether the flow encounters a 'stationary-transition' regime and corresponding oscillation, or an 'irregular' regime.

8.2 Physical Implications of Results

In this section, the importance of the results gathered for understanding real planetary atmospheres and oceans is discussed. For convenience, the discussion is broken up into three topics: the Earth's Atmosphere, the Earth's Oceans, and Mars and Other Astronomical Objects.

8.2.1 Earth's Atmosphere

Low Frequency Variability

The results presented in this thesis suggest two separate mechanisms for generation of atmospheric LFV, due to the timescales of the interactions found. Both the 23.3 to 41.5 'day' topographically resonant oscillation period observed with a wavenumber-3 base and the 35.8 'day' topographic interaction cycle for the 'interference' regime with the isolated ridge and thermal topography are well within the 10-100 day timescale for atmospheric LFV. Both phenomena are therefore put forward as possible mechanisms for the occurrence of LFV, arising either due to the nonlinear interactions of the resonant wave-triad between the topography and the circulation in the resonating case, or in the form of interference effects between a stationary flow forced by topography and a drifting baroclinic wave in the non-resonating case. These impacts then form a parallel to the intraseasonal, topographic-forced waves and flows in the Northern Hemisphere.

Of the two, the more likely mechanism for generation is that of the topographic resonance case, as the evidence is more strongly backed up by the literature. Many nonlinear barotropic vorticity models, such as CDV and LG, suggest that there is a 30-60 day oscillation arising from an oscillating topographic instability associated with resonance between a linear wave and the topography, as described by Pedlosky (1981). The results of the Resonance experiments agree with the studies of Jin and Ghil (1990), Feigenbaum (1979) and Lin, Busse and Ghil (1989), in that vacillating stationary waves, Hopf bifurcations, period-doubling and a route to chaos are all found to occur in near-resonant locations of parameter space. In addition, the near-resonant region of the Resonance experiment was associated with the occurrence of resonant wave-triads, which have also been linked to LFV. Numerical models such as Luo (1994) have found notable wave-triads with oscillation periods of 30-60 days, although with varying component wavenumbers due to differences in the topography used.

Similarly, several other intraseasonal oscillations have been linked to topographic resonance, such as LG's 36-40 day extratropical oscillation – a topographically-locked zonal wavenumber-2 flow, as the Northern Hemisphere has essentially a wavenumber-2 topography, undergoing 'tilted-

trough vacillation'. The Resonance experiment found much the same flow in the topographically resonant 'stationary-transition' regime in the form of a 23.3 to 41.5 'day' oscillation, also undergoing transformation similar to 'tilted-trough vacillation' but with a wavenumber-3 dominant flow, due to the wavenumber-3 topographic base. Whilst tropical intraseasonal oscillations, like that noted by Lau and Chan (1985), have been also noted to occur in the atmosphere, Keppenne et al (2000) suggest that the extratropic oscillations are the most important in terms of determining the overall intraseasonal variability of the Northern Hemisphere, both due to their own effects and via interactions with the other major oscillations, such as the Madden-Julian Oscillation. As such, the proposed dominant aspects of LFV, the atmosphere's extratropic intraseasonal oscillations, have been strongly linked to topographic resonance instabilities, suggesting that the mechanism of generation for atmospheric LFV is indeed the circulation encountering a near-resonant forcing by the topography. As the current Resonance experiments only investigated a single monochromatic sinusoidal topography, and found the occurrence of only a single topographically resonant oscillation, it is possible that the multitude of intraseasonal oscillations found in the real atmosphere (at least in the extratropics) are each due to a separate topographic component and corresponding Hopf bifurcations. Future work using topography comprising of more than one dominant wavenumber would be needed to explore this further.

Atmospheric Flow Structure

The prevalence in the atmosphere for stationary waves that last for an entire season and occur consistently on an annual basis, in both hemispheres, was reviewed by James (1994). James presents arguments that these stationary waves must therefore arise from some permanent forcing, such as topography or thermal contrast, and focuses on baroclinic instability due to topography. Topographic resonance is discussed in a barotropic context, but it is suggested that "realistic" mountain ranges have too small a characteristic length to propagate resonant waves. On the other hand, in the current experiments, only under topographically near-resonant conditions (implying a fully sinusoidal topographic base) were stationary waves found to dominate the flow structure, even if the impact of

topographic resonance was small, as in the Extended-Regime experiments with the flat lid. In studies where topographic resonance was not observed, such as the Partial Barriers and Thermal Topography experiments, the flow was found to drift constantly throughout all of parameter space, interacting with the topography only via interference effects at high Hide Numbers and erratic multi-wavenumber flow at low Hide Numbers.

In addition, Reinhold and Pierrehumbert (1982) and James (1994) note that the atmospheric stationary waves were also commonly found to have westward phase shifts with height. This shows a strong poleward momentum and temperature flux, as well as vertically propagating waves, as derived in detail by Holton (1992) and Pedlosky (1987). James discusses that the amount of momentum and heat transport, and the group velocity of the waves, are proportional to the amount of the phase tilt observed. Unlike for stationary waves, in the current experiments phase shift with height was found to be almost universal for all fluid flows that showed baroclinic activity, and was not limited to near-resonant flows. Even in the Thermal Topography experiments, with no mechanical topography at all, a small phase shift was noted. These phase shifts with height were also always found to be tilting downstream, and thus changed direction between the Extended-Regime experiments and the other studies when the temperature gradient was reversed, as suggested by the laboratory experiments of Leach (1981), as well as atmospheric observations. To investigate the associated poleward momentum and temperature flux, as well as vertically propagating waves, it would be useful to conduct experiments in a numerical model of the annulus. This would also allow measurements of the above properties to be taken at any point throughout the fluid.

Multiple Equilibria

Throughout all the conducted experiments, only limited evidence of multiple equilibria in the annulus was observed, as was argued by Tung and Rosenthal (1985) and Cehelsky and Tung (1987). Locations of hysteresis or alternative states at the same point in parameter space were found to rarely occur, if at all. As such, the flow was therefore unable to ‘choose’ between these distinct states, based

on initial conditions. On the other hand, some evidence was found for the occurrence of the blocked and zonal states themselves. Firstly, in the Resonance experiments, within the oscillation region, the flow was found to be in a super-resonant state at the peaks, and dropped to a sub-resonant state as the jet dissipated during the troughs. For comparison, Tian et al (2001) found their zonal states to be super-resonant, and their blocked states to be sub-resonant, which suggests a link between bifurcations due to topographic resonance and multiple equilibria. Secondly, in the Partial Barriers and Thermal Topography experiments, within the 'interference' regime the flows that visually resembled the blocked state exhibited reduced jet intensity but larger wave amplitude, along with a noticeable increase in the strength of anticyclonic eddies when compared those that resembled the zonal state. This is exactly how the two states are defined in the real atmosphere, as noted by Weeks et al (1997), suggesting that the zonal and blocked states themselves come about from interactions between drifting waves and a stationary wave. However, in both cases, the two states were part of a regular oscillation with periodic transitions between them, and lacked the permanence required for multiple equilibria, unlike what was previously noted by Risch (1999).

Walker Circulation

The results of the Partial Barriers and Thermal Topography experiments were found to be extremely similar. In particular, only minor differences, such as the location and size of the area in parameter space wherein one regime transitions to the other, were found between the two studies, highlighting that mechanical and thermal topographies interact with the flow in very similar ways. This acts to verify the mathematical derivation carried out by Dickinson (1980), who showed evidence that planetary-scale waves should react to thermal topography in much the same way as to mechanical topography. Similarly, Kaspi and Schneider (2011) suggested that atmospheric cold anomalies observed on Eastern continental boundaries have associations with both topographic forcing and land-sea temperature differences, with each creating an impact similar in magnitude and effect.

Due to these similarities between the Thermal Topography and Partial Barriers experiments, the importance of the often overlooked Walker Circulation on the atmospheric circulation can be noted, with a land-sea temperature difference on the order of the polar-Equator temperature difference producing comparable flow patterns to that of a major mountain range. The Walker Circulation, in the case of the Thermal Topography study, was represented by jet-shifting interference effects. When the flow is not interacting with the thermal topography (i.e. the immediate temperature difference is lower) the zonal state with strong jet circulation occurs, and when the flow does interact with the thermal topography (i.e. the immediate temperature difference is higher) the blocked state with reduced jet circulation is found. This agrees well with the findings of Bjerknes (1969), wherein the strength of the Walker Circulation was found to be stronger when the corresponding sea-surface temperatures were lower, and weaker when they were higher. In addition, Julian and Chervin (1978) noted that the atmospheric impact of the land-sea temperature difference is felt westward (i.e. downstream) of the peak heat source. In the same way, the jet-shifting phenomenon of the Thermal Topography study was found to always occur downstream of the heating elements. This is therefore the first time the Walker Circulation has been so thoroughly replicated in a differentially-heated annulus.

Climate change

There are many recent publications that deal with atmospheric climate change, with a number suggesting that severe weather events are due to a rise in number and longevity of persistent blocked events and stationary waves. Of these, Petoukhov et al (2012) argue that the root cause of the blocked events is resonant wave-triads made of high wavenumbers in the atmosphere (wavenumber-6, wavenumber-7 and wavenumber-8 in that study). In the current experiments, both the Partial Barriers and Thermal Topography studies demonstrated high wavenumber resonant wave-triads, but this was associated more with the occurrence of the erratic ‘irregular’ regime, rather than persistent blocked events. Indeed, neither study found evidence of distinct, alternative blocked and zonal states, and

stationary waves were only observed with fully sinusoidal topography. On the other hand, Power and Smith (2007), Francis and Vavrus (2012) and Liu et al (2012) all put forward that the persistent blocked events are due to decreased atmospheric thermal topography, as a result of a reduction in sea-ice from climate change. The results of the Thermal Topography investigation appear to agree more with this proposal, as the impacts on the large-scale flow from azimuthally-varying heating were found to be comparable to that from mechanical topography, and a reduction in this forcing would be expected to lead to significant changes to atmospheric LFV and the global circulation, as discussed previously. Further experiments with varying amounts of heat input would be needed to investigate this further, however.

8.2.2 Earth's Oceans

Blocking

In the blocked sections of the ocean basin, Huthnance (1989) and Martínez and Allen (2004) note that trapped waves are a common and dynamically important aspect of the flow, with an impact on the ocean circulation on the order of wind forcing, according to the latter. The blocked bottom flow in the Partial Barriers study was found to be defined by a large persistent azimuthally-trapped wave upstream of the topographic peak, as well as smaller, irregularly-spaced downstream eddies. The azimuthally-trapped wave also extended further vertically than the topography, causing a stationary wavenumber-1 component to appear in the flow structures of higher levels, but weakened in magnitude as it crossed into the unblocked flow. This again bears similarity to the real oceanic flow found near coastal boundaries. On the other hand, these results are quite different to those of Wordsworth's (2008) fully blocked ocean basin experiments, which found a quasi-barotropic jet rather than trapped waves. This quasi-barotropic jet was suggested to be an equivalent to the western boundary currents of oceanic flows, similar to the observations discussed by Rayer, Johnson and Hide (1998). It is likely, therefore, that in the Partial Barriers experiment the existence of the unblocked

flow affected the structure of the blocked flow, as fluid could move vertically over the curved surface of the isolated ridge instead of generating a trapped jet structure. As such, further experiments replacing the curved ridge with a sheer barrier would be needed to investigate whether trapped jets, and thus evidence for western boundary currents in the annulus, can occur under partial barrier conditions.

Geothermal Activity

In the ocean circulation, thermal topography can arise from geothermal activity caused by volcanoes. In this case, the impact of geothermal heat flux at the ocean bottom is a reduction of stratification throughout the abyssal layer, resulting in a strengthening of the circulation, as observed by Mashayek et al (2013). In the Thermal Topography experiments, the heat influx from the heating elements created a similar impact to the mechanical topography of the Partial Barriers experiment, and thus could indeed be described as causing a strengthening of the circulation, in the form of baroclinic waves and interference effects. In contrast to the mechanical topographic study, however, the experiments with azimuthally-varying heating were found to be noticeably more uniform in the vertical direction, with the flow structure changing only slightly with height. As such, the results of the Thermal Topography experiments appear to replicate and verify all of Mashayek et al's proposed effects of geothermal heat flux on the oceanic flow. In addition, the observed similarity to mechanical topography also backs up the suggestion that geothermal heat flux is a vital component for inclusion into oceanic modelling.

8.2.3 Mars and Other Astronomical Objects

Martian Atmosphere

On Mars, the occurrence of quasi-stationary waves in the atmosphere is extremely important, being associated with the triggering of global dust storms by Hollingworth and Barnes (1996). This can be thought of as a parallel to Earth's persistent blocking states, as discussed earlier, and the severe weather events associated with them. From the Resonance experiments, it is known that topographic resonance, which was found to occur only under fully sinusoidal conditions, is associated with stationary and quasi-stationary flow structures, depending on how close the flow is to the location of linear resonance. As such, it is suggested that the Martian atmosphere should have some resonance with the topography, in order to form quasi-stationary waves. In turn, this may imply that the Martian atmosphere's interannual variability, as noted by Pankine and Ingersoll (2004), is due to the timescales of topographic resonant oscillations, as an equivalent to LFV in Earth's atmosphere. The Martian topographic resonance oscillation would have to be of a much longer period than that of the Resonance experiment, if this were the case.

Furthermore, the atmospheres of Mars and Earth have different linear stationary responses, with the former experiencing "global, low wavenumber responses", as noted in the numerical studies of Webster (1977) and Hollingsworth and Barnes (1995), and in observations, such as from Banfield et al. (1996). The Martian atmosphere is found to be dominated by low wavenumber disturbances, in turn linked to the formation of robust stationary eddies (and hence, global dust storms, as discussed earlier) in the Martian atmosphere, especially in the Northern Hemisphere. Hollingsworth and Barnes, amongst others, suggested that these disturbances are due to the Martian surface acting as both topographic and thermal forcing. In the Thermal Topography experiments, the regime diagram shows that lower wavenumbers were slightly more common than in the similar Partial Barriers experiments, especially at low Taylor Numbers and high Hide Numbers. In this way, it is possible that it is indeed the Martian thermal forcing that leads to low wavenumber flow structures, but this could only be fully

verified by further experiments using a combination of mechanical and thermal topography, such as by attaching flat heating elements to the topographic peaks.

Atmospheres of Venus and Titan

Other terrestrial planets and satellites in the Solar System also have notable large-scale topography, such as Venus and Titan. Both of these astronomical objects are different to Earth and Mars in that they have super-rotating atmospheres[20], however some Earth-like phenomena can still be found, such as polar vortexes and topographically-forced stationary waves on Venus, as observed by Taylor et al (1980) and Young et al (1987) respectively. In the annulus, replicating this super-rotation is challenging, largely due to the non-slip boundaries, and the issue is discussed in detail in Read (1986). With such a large zonal mean background flow, the current experiments would appear to suggest that the atmospheric flow structures evolved on these astronomical objects would most likely undergo strong vacillation, and favour the erratic 'irregular' regime over the 'interference' regime when encountering any isolated topographic peaks. As stationary waves are observed, topographic resonance may be possible as well, depending on the dominant wavenumber components of the topography and the circulation.

8.3 Further Work

The most obvious extensions to the work presented in this thesis would be to expand upon the amount of parameter space analysed in each of the previous studies. Further constant Hide Number scans could be conducted with the wavenumber-3 topographic base in order to more accurately determine the boundaries of the 'stationary-transition' regime and the precise location of linear resonance for that experimental arrangement. Changing the height of the topographic peaks and the

[20] The mechanism of generation and maintenance of this super-rotation is as yet unknown, though Gierasch (1975) notes that both zonal mean flow processes and eddy processes are necessary.

amount of heat input generated by the heating elements would also serve as a good initial development for all the studies, permitting investigation of how the scale of the topographic forcing affects near-resonant flow structures and interference phenomena. Across all the studies, these comparisons would give context to the results already gathered. These are merely simple additions to the current work, however, and the next sections will discuss more involved extensions.

8.3.1 Other Experimental Arrangements

As previously mentioned, the physical topography was designed to be as flexible as possible, allowing an enormous range of possible experiments. So great is the number of possible experiments that the studies conducted in this thesis were chosen by ordering the studies by virtue of time needed to implement them against their expected payoffs in results gathered. For example, using the method of interchangeable bases, a much greater number of topographies can be examined.

One notable extension is that of wavenumber superposition. Both Earth and Mars have topography that does not consist of a simple monochromatic sinusoid, unlike the Resonance experiments and most studies found in the literature. Hence, an investigation wherein the topographic forcing is made up of more than one wavenumber (that are not harmonically related to each other) should increase understanding of how more complex topography impacts upon the large-scale flow. In addition, this should also allow further investigation of the ties between topographic resonance of multiple wavenumbers and atmospheric LFV, as discussed previously.

As such, it was noted that in Hollingsworth and Barnes' (1996) Martian Fourier decomposition it appears that the topography in the Martian Southern Hemisphere appears to be mainly formed from both a wavenumber-1 and a wavenumber-3. This is illustrated in Figure 8.1.

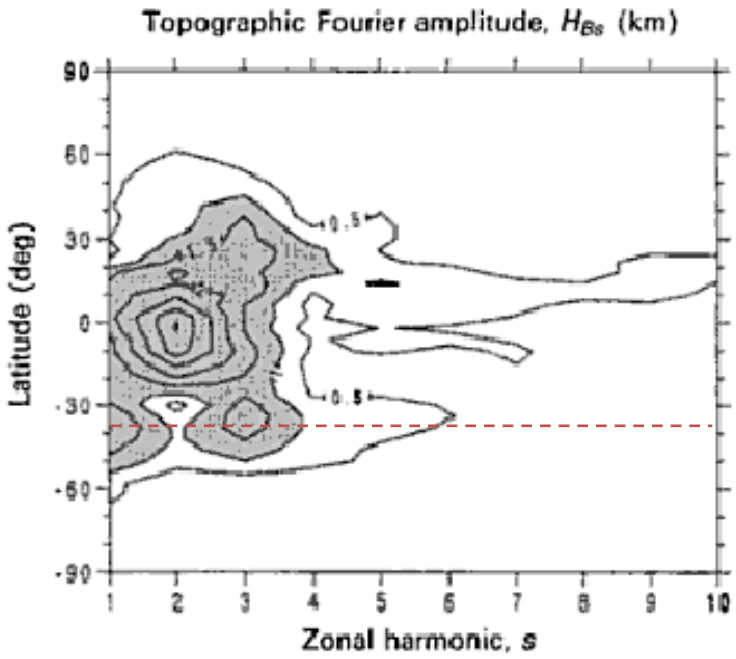

Figure 8.1: Fourier decomposition of Martian topography [from Read and Lewis (2004), created using a dataset by Hollingsworth and Barnes (1996)], with red dotted line indicating latitude of interest.

To verify this, a new Fourier analysis of the Martian topography was conducted (data taken from the LMD/UK Mars General Circulation Model LMD/UKMGCM), as shown in Figure 8.2. From this Figure it can be clearly observed that, at a certain latitude circle of about 40°S, wavenumber-1 and wavenumber-3 are dominant.

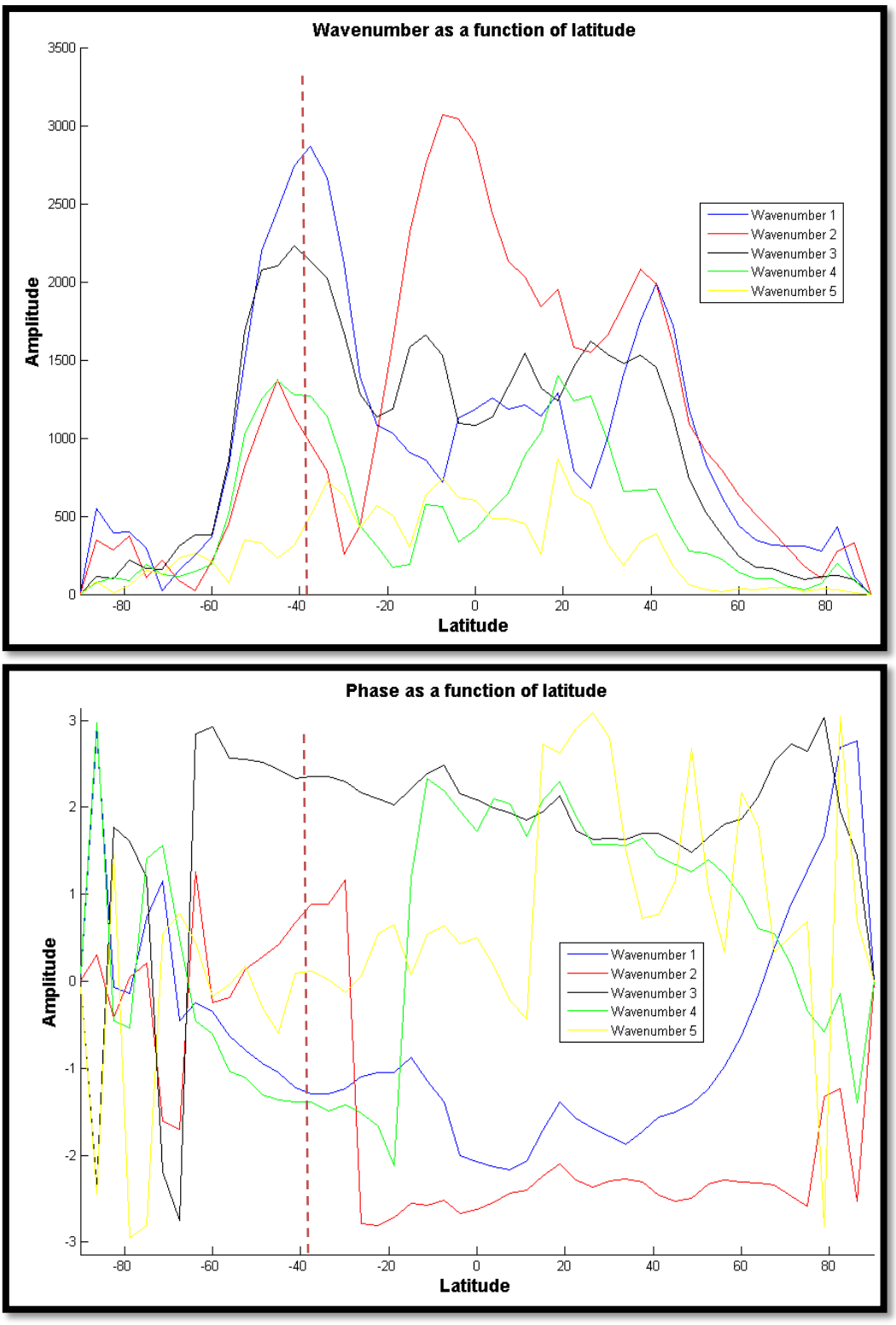

Figure 8.2: Fourier analysis of Martian topography, with red dotted line indicating latitude of interest.

Hence, ignoring lesser wavenumbers and utilising the amplitude and phase differences, a superposition of these wavenumbers was found - due to its relative amplitude and phase position, the impact of the wavenumber-1 component acts directly between two of the wavenumber-3 peaks. In this way, the superposition somewhat resembles a wavenumber-3 topography in which two of the peaks are roughly twice the height of the other. To simulate this, the bases can be arranged as in Figure 8.3, wherein two of the high-amplitude peaks and one of the low-amplitude peaks are combined to reflect the impact of the wavenumber-1 component. It is hoped that this arrangement will give a rough model for the topography of the Southern Hemisphere of Mars, for comparison with atmospheric observations, and thus should allow for the study of the effects of combining topographic wavenumbers in the annulus. The results could also be compared to this thesis' Resonance and Partial Barriers experiments, which show the individual impacts of the component wavenumber-3 and pseudo-wavenumber-1 bases, respectively, upon the flow structure.

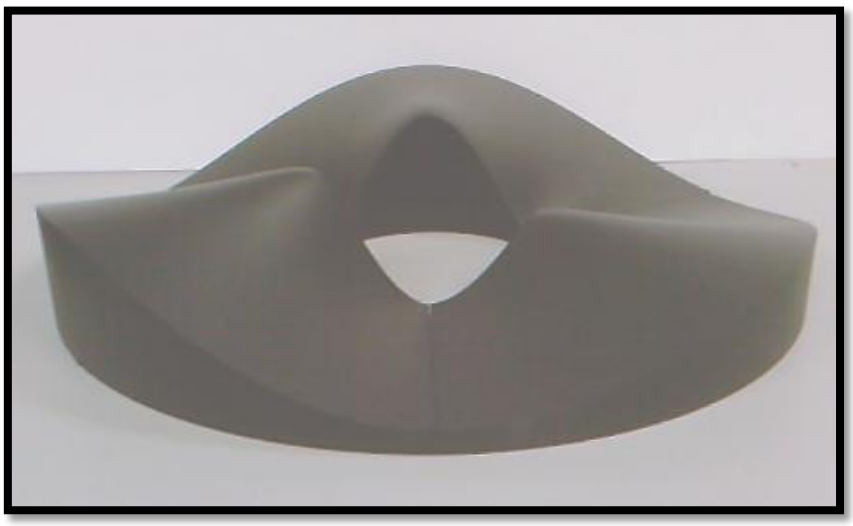

Figure 8.3: Bases arranged to produce superposition of wavenumber-1 and wavenumber-3.

As well as the response to multi-modal topography in the zonal direction, the annulus can be used to explore other radial modes. For example, Jin and Ghil's (1990) numerical model used a hemispherical curved peak in the middle of the channel, varying in both x and y, as shown in Figure 2.2. In this way, their topography was a partial barrier in both zonal and meridional directions. In the annulus, this could be achieved by the creation of interchangeable hemispherical blocks that could be

placed on the base in order to form either a single isolated peak, or several peaks in periodic locations. Addition of these blocks to the annulus would permit further comparison with the topographic resonance study of Jin and Ghil, as well as allowing observation of the differences in impact on the large-scale flow between radially-uniform and radially-varying topography.

Another possible investigation would be to study the occurrence of inertia-gravity waves in the baroclinic annulus. For example, Jacoby et al's (2011) numerical study using MORALS (discussed in the next section) found evidence of downward-propagating "roll-like instabilities" within the thermal boundary layer of the annulus' inner cylinder, suggested to be associated with inertia-gravity waves. These instabilities were proposed to be related to temperature anomalies found in both the laboratory (from Read (1992), in this case) and the numerical model at mid-radius. As this thesis' annulus is larger than that of Jacoby et al, it may be possible to more easily observe the effects of these inertia-gravity waves within the same region of parameter space, especially in terms of their interactions with the topographically-forced quasi-stationary waves found throughout the current experiments.

Thermal topography can also be combined with mechanical topography to create new experimental investigations. For example, using the elements with the isolated ridge arrangement would allow for further study of monsoon behaviour and Western boundary conditions. In addition, placing the elements on the ridges of the Martian superposition arrangement would give a parallel to the complete Martian topographic heating, as discussed earlier, whereby Martian mountains can act as heat sources (at the peaks) and sinks (at the troughs), as well as obstructions to the flow. Hence, heating elements placed on top of the topographic peaks should be able to simulate this effect, allowing study of both thermal and topographic forcings simultaneously, rather than one at a time. Once again, the results of this investigation could be compared to observed phenomena of the real Martian atmosphere, such as the previously noted low wavenumber global disturbances, though some differences between experimental results and observations would be expected due to the effects of the simplicity of the annulus' replication.

8.3.2 Numerical Study

As a final possible extension to this thesis, the experiments of each study could be repeated (and extended) utilising a numerical model. A numerical model set up to simulate a differentially-heated annulus could be employed for the same topographies as in this thesis, allowing comparison between the experimental and computational studies. The model would then be able to give measurements of pressure, temperature and velocity throughout the entire fluid, not just at set heights. Vertical velocity and flow activity within the boundary layers would be easier to observe as well, which would prove to be a great help for further investigation into blocking effects, for example. A numerical annulus model also bridges the gap between the current experiments and other numerical models from the literature, in particular channel models such as that of Jin and Ghil (1990). For example, Jin and Ghil's hemispherical isolated peak, discussed earlier, could also be recreated within an annulus model. In this way, the cause of any differing results can be determined to be due to differences between experimental and numerical models, or else due to differences between annular and channel arrangements.

The two most likely types of numerical models to be employed would be either a full Navier-Stokes Equation solution model or a more-simplified quasi-geostrophic model. An example of the former would be MORALS, standing for *Met Office/Oxford Rotating Annulus Laboratory Simulation* (see Farnell and Plumb (1975) for a full description), which has a quasi-geostrophic development in the form of QUAGMIRE, standing for *QUAsi-Geostrophic Model for Investigating Rotating fluids Experiments*. Both of these examples are distinct from those numerical models most commonly used in the literature (as mentioned in Chapter 2), as they are not employed to search for new atmospheric phenomena, but instead to increase the understanding of those already found, and attempt to achieve this by having geometry in the form of a rotating annulus like those used in the laboratory. This is an advantage since numerical simulations of laboratory flows are excellent for studying "fundamental dynamical phenomena", as noted by Williams, Read and Haine (2010), due to their simplicity and thus their ease of modelling. Navier-Stokes Equation solution models would be able to form

mechanical topography equivalent to the current experiments by deforming the bottom boundary layer and form thermal topography by including an additional heat source. On the other hand, quasi-geostrophic models would have to create both types of topography by including additional vertical velocity terms near the base. This, along with other simplifications, is offset by the increase in computational speed permitted by the quasi-geostrophic model. As such, the choice of which numerical model to utilise is dependent on what aspects of the topographic impact upon the flow structure are of interest in a particular future study. Available examples of both model types can also be multi-layer, allowing the vertical structure of the atmosphere to be investigated as rigorously or as roughly as required[21].

For a specific example, either type of numerical model (but preferably the quasi-geostrophic model for additional simplicity) could be employed to investigate the downstream phase shift with height observed in nearly all gathered results, as discussed previously. Measurements of the poleward heat and momentum transport, as well as vertical velocity, would be vital in quantitatively studying how the amount of shift with height impacts the large-scale flow. In addition, by comparing the results of a steady-state barotropic annulus with uniform zonal flow against the same arrangement but with a non-uniform zonal flow, it could be discovered whether the phase shift is due to a baroclinically-unstable flow being locked to the topography, whether it is just a feature of the zonally-symmetric flow or even whether there is a real distinction between the two. This would be of use for the real atmosphere as well, where the origin of phase shift with height of stationary waves is still uncertain.

[21] One- and two-layer models have already been discussed and, for example, Kondrashov, Ide and Ghil (2004) achieved a 'realistic' global simulation using a three-layer model.

References

Andrews, D.G., 2000. *An Introduction to Atmospheric Physics*. Cambridge: Cambridge University Press.

Banfield, D., Toigo, A.D., Ingersoll, A.P. & Paige, D.A., 1996. Martian Weather Correlation Length Scales. *Icarus,*119(1), pp.130-143.

Benzi, R., Malguzzi, P., Speranza, A. & Sutera, A., 1986. The Statistical Properties of General Atmospheric Circulation: Observational Evidence and a Minimal Theory of Bimodality. *Quart. J. R. Met. Soc.*, 112(473), pp.661-674.

Berggren, R., Bolin, B. & Rossby, C-G., 1949. An Aerological Study of Zonal Motion, its Perturbations and Break-down. *Tellus,* 1(2), pp.14-37.

Bjerknes, J., 1969. Atmospheric Teleconnections from the Equatorial Pacific. *Mon. Wea. Rev.,* 97(3), pp.163-172.

Boubnov, B.M., Golitsyn, G.S. & Senatorsky, A.O., 1991. Convection in a Rotating Cylindrical Annulus with Azimuthally Non-Uniform Heating. *Geophys. Astrophys. Fluid Dyn.,* 57(1), pp.1-18.

Boyer, D.L. & Chen. R., 1987. Laboratory Simulations of Mechanical Effects of Mountains on the General Circulation of the Northern Hemisphere: Uniform Shear Background Flow. *J. Atmos. Sci.*, 44(23), pp.3552-3575.

Bretherton, F.P., 1964. Resonant Interactions between Waves. The Case of Discrete Oscillations. *J. Fluid Mech.*, 20(3), pp.457-479.

Cehelsky, P. & Tung, K.K., 1987. Theories of Multiple Equilibria and Weather Regimes – A Critical Reexamination. Part II: Baroclinic Two-Layer Models. *J. Atmos. Sci.*, 44(21), pp.3282-3303.

Charney, J.G. & DeVore, J.G., 1979. Multiple Flow Equilibria in the Atmosphere and Blocking. *J. Atmos. Sci.*, 36(7), pp.1205-1216.

Charney, J.G. & Straus, D.M., 1980. Form-Drag Instability, Multiple Equilibria and Propagating Planetary Waves in Baroclinic, Orographically Forced, Planetary Wave Systems. *J. Atmos. Sci.*, 37(6), pp.1157-1176.

Charney, J.G., Shukla, J. & Mo, K.C., 1981. Comparison of a Barotropic Blocking Theory with Observation. *J. Atmos. Sci.*, 38(4), pp.762-779.

Cheng, N-S., 2008. Formula for the Viscosity of a Glycerol−Water Mixture. *Ind. Eng. Chem. Res.* 47(9), pp.3285-3288.

Cho, J.Y-K., Menou, K., Hansen, B.M.S. & Seager, S., 2008. Atmospheric Circulation of Close-In Extrasolar Giant Planets. 1. Global, Barotropic, Adiabatic Simulations. *The Astrophysical Journal*, 675(1), pp.817-845.

Dickey, J.O., Ghil, M. & Marcus, S.L., 1990. A 30–60 Day Oscillation in Length-of-Day and Atmospheric Angular Momentum: Extratropical Origin? In Boucher, C. & Wilkins, G.A., ed., *Earth Rotation and Coordinate Reference Frames.* New York: Springer US. **105**, pp.90-97.

Dickinson, R.E., 1980. Planetary Waves: Theory and Observation. In WMO, *Orographic Effects in Planetary Flows*, GARP Publ. Ser. No. 23, pp.51-84.

Donoso, G. & Ladera, C.L., 2012. Nonlinear Dynamics of a Magnetically Driven Duffing-Type Spring–Magnet Oscillator in the Static Magnetic Field of a Coil. *Eur. J. Phys.*, 33(6), pp.1473-1486.

Egger, J., 1978. Dynamics of Blocking Highs. *J. Atmos. Sci.*, 35(10), pp.1788-1801.

Esler, J.G., Polvani, L.M. & Scott, R.K., 2006. The Antarctic Stratospheric Sudden Warming of 2002: A Self-Tuned Resonance? *Geophysical Research Letters*, 33(12), L12804.

Farnell, L. & Plumb, R.A., 1975. Numerical Integration of Flow in a Rotating Annulus I: Axisymmetric Model. *Occasional Note Met O*, 21 75/3, [Unpublished Technical Report].

Feigenbaum, M.J. 1979. The Onset Spectrum of Turbulence. *Physics Letters A*, 74(6), pp.375-378.

Fincham, A.M. & Spedding, G.R., 1997. Low Cost, High Resolution DPIV for Measurement of Turbulent Fluid Flow. *Experiments in Fluids*, 23(6), pp.449-462.

Fowlis, W.W. & Hide, R., 1965. Thermal Convection in a Rotating Annulus of Liquid: Effect of Viscosity on the Transition between Axisymmetric and Non-Axisymmetric Flow Regimes. *J. Atmos. Sci.*, **22**, pp.541-558.

Francis, J.A. & Vavrus, S.J., 2012. Evidence Linking Arctic Amplification to Extreme Weather in Mid-Latitudes. *Geophysical Research Letters*, 39(6), L06801.

Früh, W-G., 1996. Low-Order Models of Wave Interactions in the Transition to Baroclinic Chaos. *Nonlinear Processes in Geophysics*, 3(3), pp.150-165.

Früh, W-G. & Read, P.L., 1997. Wave Interactions and the Transition to Chaos of Baroclinic Waves in a Thermally Driven Rotating Annulus. *Phil. Trans. Math. Phys. Eng. Sci.*, 355(1722), pp.101-153.

Ghil, M., 1987. Dyamnics, Statistics and Predictability of Planetary Flow Regimes. In Nicolis, C. & Nicolis, G., ed., *Irreversible Phenomena and Dynamical Systems Analysis in Geosciences C.* Dordrecht: D. Reidel Publishing Company. **192**, pp.241-283.

Ghil, M. & Mo, K., 1991. Intraseasonal Oscillations in the Global Atmosphere. Part I: Northern Hemisphere and Tropics. *J. Atmos. Sci.*, 48(5), pp.752–779.

Ghil, M., Kondrashov, D., Lott, F. & Robertson, A.W., 2003. Intraseasonal Oscillations in the Mid-Latitudes: Observations, Theory and GCM Results. In *Proc. ECMWF/CLIVAR Workshop on Simulation and Prediction of Intra-Seasonal Variability with Emphasis on the MJO*, pp.3-6.

Gierasch, P.J., 1975. Meridional Circulation and the Maintenance of the Venus Atmospheric Rotation. *J. Atmos. Sci.*, 32(6), pp.1038–1044.

Glycerine Producers' Association, 1963. *Physical Properties of Glycerine and Its Solutions*. New York: Glycerine Producers' Association.

Harlander, U., Wenzel, J., Alexandrov, K., Wang, Y. & Egbers, C., 2012. Simultaneous PIV and Thermography Measurements of Partially Blocked Flow in a Differentially Heated Rotating Annulus. *Exp. Fluids*, 52(4), pp.1077-1087.

Held, I.M., 1983. Stationary and Quasi-Stationary Eddies in the Extratropical Troposphere: Theory. In Hoskins, B.J. & Pearce, R.P., ed., *Large-Scale Dynamical Processes in the Atmosphere*. London: Academic Press Inc. (London) Ltd., Ch. 6.

Hide, R., 1953. Some Experiments on Thermal Convection in a Rotating Liquid. *Quart. J. R. Met. Soc.*, 79(339), pp.161, [Correspondence].

Hide, R., 1958. An Experimental Study of Thermal Convection in a Rotating Liquid. *Phil. Trans. R. Soc.Lon. A*, 250(983), pp.441-478.

Hide, R., Lewis, S.R. & Read, P.L., 1994. Sloping Convection: A Paradigm for Large-Scale Waves and Eddies in Planetary Atmospheres? *Chaos*, 4(2), pp.135-162.

Hide, R. & Mason, P.J., 1975. Sloping Convection in a Rotating Fluid. *Advances in Physics*, 24(1), pp.47-100.

Hignett, P., White, A.A., Carter, R.D., Jackson, W.D.N. & Small, R.M., 1985. A Comparison of Laboratory Measurements and Numerical Simulations of Baroclinic Wave Flows in a Rotating Cylindrical Annulus. *Quart. J. R. Met. Soc.*, 111(463), pp.131-154.

Hollingsworth, J.L. & Barnes, J.R., 1996. Forced Stationary Planetary Waves in Mars's Winter Atmosphere. *J. Atmos. Sci.*, 53(3), pp.428-448.

Holton, J.R., 1992. *An Introduction to Dynamic Meteorology.* 3rd ed. New York: Academic Press.

Hoskins, B.J. & Karoly, D.J., 1981. The Steady Linear Response of a Spherical Atmosphere to Thermal and Orographic Forcing. *J. Atmos. Sci.*, 38(6), pp.1179-1196.

Houghton, J., 2002. *The Physics of Atmospheres*. 3rd ed. Cambridge: Cambridge University Press.

Huthnance, J.M., 1989. Internal Tides and Waves near the Continental Shelf Edge. *Geophys. Astrophys. Fluid Dyn.*, 48(1-3), pp.81-106.

Jacoby, T.N.L., Read, P.L., Williams, P.D. & Young, R.M.B., 2011. Generation of Inertia–Gravity Waves in the Rotating Thermal Annulus by a Localised Boundary Layer Instability. *Geophys. Astrophys. Fluid Dyn.*, 105(2-3), pp.161-181.

James, I.N., 1988. Meteorology of a Flat Earth. *Nature*, **333**, pp.118.

James, I.N., 1994. *Introduction to Circulating Atmospheres*, Cambridge: Cambridge University Press.

Jin, F.F. & Ghil, M., 1990. Intraseasonal Oscillations in the Extratropics: Hopf Bifurcations and Topographic Instabilities. *J. Atmos. Sci.*, 47(24), pp.3007-3022.

Julian, P.R. & Chervin, R.M., 1978. A Study of the Southern Oscillation and Walker Circulation Phenomenon. *Mon. Wea. Rev.*, 106(10), pp.1433-1451.

Kartashova, E. & L'vov, V.S., 2007. Model of Intraseasonal Oscillations in Earth's Atmosphere. *Phys. Rev. Lett*. 98(19), 198501.

Kaspi, Y. & Schneider, T., 2011. Winter Cold of Eastern Continental Boundaries Induced by Warm Ocean Waters. *Nature*, **471**, pp.621–624.

Keppenne, C.L., Marcus, S.L., Kimoto, M. & Ghil, M., 2000. Intraseasonal Variability in a Two-Layer Model and Observations. *J. Atmos. Sci.*, 57(8), pp.1010–1028.

Kondrashov, D., Ide, K. & Ghil, M., 2004. Weather Regimes and Preferred Transition Paths in a Three-Layer Quasigeostrophic Model. *J. Atmos. Sci.*, 61(5), pp.568-587.

Koo, S. & Ghil, M., 2002. Successive Bifurcations in a Simple Model of Atmospheric Zonal-Flow Vacillation. *Chaos*, 12(2), pp.300-309.

Lau, K.M. & Chan, P.H., 1985. Aspects of the 40–50 Day Oscillation during the Northern Winter as Inferred from Outgoing Longwave Radiation. *Mon. Wea. Rev.*, 113(11), pp.1889–1909.

Leach, H., 1981. Thermal Convection in a Rotating Fluid: Effects due to Bottom Topography. *J. Fluid Mech.*, **109**, pp.75-87.

Legras, B. & Ghil, M., 1985. Persistent Anomalies, Blocking and Variations in Atmospheric Predictability. *J. Atmos. Sci.*, 42(5), pp.433-471.

Li, Q.G., Kung, R. & Pfeffer, R.L., 1986. An Experimental Study of Baroclinic Flows with and without Two-Wave Bottom Topography. *J. Atmos. Sci.*, 43(22), pp.2585-2599.

Li, Q.G., Kung, R. & Pfeffer, R.L., 1992. A Fluid Experiment of Large-Scale Topography Effect on Baroclinic Wave Flows. *Adv. Atmos. Sci.*, 9(1), pp.17-28.

Lin, R.Q., Busse, F. & Ghil, M., 1989. Transition to Two-Dimensional Turbulent Convection in a Rapidly-Rotating Annulus. *Geophys. Astrophys. Fluid Dyn.*, *45*(3-4), pp.131-157.

Liu, J., Curry, J.A., Wang, H., Song, M. & Horton, R.M., 2012. Impact of Declining Arctic Sea Ice on Winter Snowfall. *Proceedings of the National Academy of Sciences*, 109(11), pp.4074-4079.

Lu, H-L. & Miller, T.L., 1998. Characteristics of Annulus Baroclinic Flow Structure During Amplitude Vacillation. *Dyn. Atmos. Oceans*, 27(1-4), pp.485-503.

Luo, D., 1994. Quasi-resonant Interactions Among Barotropic Rossby Waves with Two-Wave Topography and Low Frequency Dynamics. *Geophys. Astrophys. Fluid Dyn.*, 76(1), pp.145-163.

Luo, D., 2005. A Barotropic Envelope Rossby Soliton Model for Block–Eddy Interaction, Part I: Effect of Topography. *J. Atmos. Sci.*, **62**, pp.5-21.

Madden, R.A. & Julian, P.R., 1971. Detection of a 40–50 Day Oscillation in the Zonal Wind in the Tropical Pacific. *J. Atmos. Sci.*, 28(5), pp.702-708.

Marcus, S.L., Ghil, M., Dickey, J.O. & Eubanks, T.M., 1990. Origin of the 30 - 60 Day Oscillation in the LOD and Atmospheric Angular Momentum: New Findings from the UCLA General Circulation Model. In *Earth Rotation and Coordinate Reference Frames*, pp.98-105. New York: Springer US.

Martínez, J.A. & Allen, J.S., 2004. A Modeling Study of Coastal-Trapped Wave Propagation in the Gulf of California. Part I: Response to Remote Forcing. *J. Phys. Oceanogr.*, 34(6), pp.1313-1331.

Martius, O., Polvani, L.M. & Davies, H.C., 2009. Blocking Precursors to Stratospheric Sudden Warming Events. *Geophysical Research Letters*, 36(14), L14806.

Mashayek, A., Ferrari, R., Vettoretti, G. & Peltier, W.R., 2013. The Role of the Geothermal Heat Flux in Driving the Abyssal Ocean Circulation. *Geophysical Research Letters*, 40(12), pp.3144-3149.

Mason, P.J., 1975. Baroclinic Waves in a Container with Sloping End Walls. *Phil. Trans. R. Soc. Lond. A*, 278(1284), pp.397-445.

Matsuno, T., 1971. A Dynamical Model of the Stratospheric Sudden Warming. *J. Atmos. Sci.*, 28(8), pp.1479-1494.

Meehl, G.A., 1994. Coupled Land-Ocean-Atmosphere Processes and South Asian Monsoon Variability. *Science*, 266(5183), pp.263-267.

Miller, T.L. & Butler, K.A., 1991. Hysteresis and the Transition between Axisymmetric Flow and Wave Flow in the Baroclinic Annulus. *J. Atmos. Sci.*, 48(6), pp.811-824

Molteni, F., 1996. On the Dynamics of Planetary Flow Regimes, Part II: Results from a Hierarchy of Orographically Forced Models. *J. Atmos. Sci.*, 53(14), pp.1972-1992.

Namias, J., 1950. The Index Cycle and Its Role in the General Circulation. *J. Meteor.*, 7(2), pp.130-139.

Nayvelt, L., Gierasch, P.J. & Cook, K.H., 1997. Modeling and Observations of Martian Stationary Waves. *J. Atmos. Sci.*, 54(8), pp.986-1013.

Pankine, A.A. & Ingersoll, A.P., 2004. Interannual Variability of Mars Global Dust Storms: An Example of Self-Organized Criticality? *Icarus*, *170*(2), pp.514-518.

Pedlosky, J., 1981. Resonant Topographic Waves in Barotropic and Baroclinic Flows. *J. Atmos. Sci.*, 38(12), pp.2626-2641.

Pedlosky, J., 1987. *Geophysical Fluid Dynamics*. 2nd ed. New York and Berlin: Springer-Verlag.

Petoukhov, V., Rahmstorf, S., Petri, S. & Schellnhuber, H.J., 2013. Quasiresonant Amplification of Planetary Waves and Recent Northern Hemisphere Weather Extremes. *Proceedings of the National Academy of Sciences*, 110(14), pp.5336-5341.

Pfeffer, R.L. & Chiang, Y., 1967. Two Kinds Of Vacillation In Rotating Laboratory Experiments. *Mon. Wea. Rev.*, 95(2), pp.75–82.

Philander, S.G.H., 1985. El Niño and La Niña. *J. Atmos. Sci.*, 42(23), pp.2652-2662.

Plumb, R.A., 1977. The Stability of Small Amplitude Rossby Waves in a Channel. J . Fluid Mech., 80(4), pp.705-720.

Power, S.B. & Smith, I.N., 2007. Weakening of the Walker Circulation and Apparent Dominance of El Niño Both Reach Record Levels, but has ENSO Really Changed? *Geophysical Research Letters*, 34(18), L18702.

Rayer, Q.G., Johnson, D.W. & Hide, R., 1998. Thermal Convection in a Rotating Fluid Annulus Blocked by a Radial Barrier. *Geophys. Astrophys. Fluid Dyn.*, 87(3), pp.215-252.

Read, P.L., 1986. Super-Rotation and Diffusion of Axial Angular Momentum: I. 'Speed Limits' for Axisymmetric Flow in a Rotating Cylindrical Fluid Annulus. *Quart. J. R. Met. Soc.*, 112(471), pp.231-251.

Read, P.L., 1992. Applications of Singular Systems Analysis to "Baroclinic Chaos". *Physica D*, 58(1), pp.455-468.

Read, P.L. & Lewis, S.R., 2004. *The Martian Atmosphere Revisited: Atmosphere and Environment of a Desert Planet*. Chichester: Praxis Publishing Ltd.

Read, P.L., Maubert, P., Randriamampianina, A. & Früh W-G., 2004. DNS of Transitions towards Structural Vacillation in an Air-Filled, Rotating Baroclinic Annulus. *J. Fluid Mech.*, [Submitted].

Read, P.L. & Risch, S.H., 2011. A Laboratory Study of Global-Scale Wave Interactions in Baroclinic Flow with Topography, Part I: Multiple Flow Regimes. *Geophys. Astrophys. Fluid Dyn.*, 105(2-3), pp.128-160.

Reinhold, B.B. & Pierrehumbert, R.T., 1982. Dynamics of Weather Regimes: Quasi-Stationary Waves and Blocking. *Mon. Wea. Rev.*, 110(9), pp.1105-1145.

Rhines, P.B., 1975. Waves and Turbulence on a Beta-Plane. *J. Fluid Mech.*, 69(3), pp.417-443.

Risch, S.H., 1999. *Large-Scale Wave Interactions in Baroclinic Flow with Topography*. DPhil. University of Oxford.

Risch, S.H. & Read, P.L., 2014. A Laboratory Study of Global-Scale Wave Interactions in Baroclinic Flow with Topography, Part II: Vacillations and Low-Frequency Variability. *Geophys. Astrophys. Fluid Dyn.*, [Submitted].

Shulmeister, J., 1999. Australasian Evidence for Mid-Holocene Climate Change Implies Precessional Control of Walker Circulation in the Pacific. *Quat. Int.*, **57/58**, pp.81-91.

Simmons, A.J., Wallace, J.M. & Branstator, G.W., 1983. Barotropic Wave Propagation and Instability, and Atmospheric Teleconnection Patterns. *J. Atmos. Sci.*, 40(6), pp.1363–1392.

Smith, AK., 1989. An Investigation of Resonant Waves in a Numerical Model of an Observed Sudden Stratospheric Warming. *J. Atmos. Sci.*, 46(19), pp.3038-3054.

Sommeria, J., 2003. *Correlation Imaging Velocimetry at the Coriolis Facility*. [online] Laboratoire des Ecoulements Géophysiques et Industriels. Available at: <http://servforge.legi.grenoble-inp.fr/projects/soft-uvmat/attachment/wiki/WikiStart/CIV_doc_lim.pdf> [Accessed 23 September 2013].

Taylor, F.W., Beer, R., Chahine, M.T., Diner, D.J., Elson, L.S., Haskins, R.D., McCleese, D.J., Martonchik, J.V., Reichley, P.E., Bradley, S.P., Delderfield, J., Schofield, J.T., Farmer, C.B., Froidevaux, L., Leung, J., Coffey, M.T. & Gille, J.C., 1980. Structure and Meteorology of the Middle Atmosphere of Venus: Infrared Remote Sensing from the Pioneer Orbiter. *Journal of Geophysical Research: Space Physics (1978–2012)*, 85(A13), pp.7963-8006.

Taylor, G.I., 1923. Experiments on the Motion of Solid Bodies in Rotating Fluids. *Proc. R. Soc. Lon. A*, **104**, pp.213-218.

Tian, Y., Weeks, E.R., Ide, K., Urbach, J.S., Baroud, C.N., Ghil, M. & Swinney, H.L., 2001. Experimental and Numerical Studies of an Eastward Jet over Topography. *J. Fluid Mech.*, **438**, pp.129-157.

Tribbia, J. & Ghil, M. 1990. Forced Zonal Flow over Topography and the 30–60 Day Oscillation in Atmospheric Angular Momentum. *NCAR Ms*, 501/89-5, National Center for Atmospheric Research, Boulder, CO.

Tung, K.K. & Lindzen, R.S., 1979. A Theory of Stationary Long Waves. Part I: A Simple Theory of Blocking. *Mon. Wea. Rev.*, 107(6), pp.714-734.

Tung, K.K. & Rosenthal, A.J., 1985. Theories of Multiple Equilibria and Weather Regimes – A Critical Reexamination. Part I: Barotropic Models. *J. Atmos. Sci.*, 42(24), pp.2804-2819.

Vettin, F., 1857. Ueber den aufsteigenden Luftstrom, die Entstehung des Hagels und der Wirbel-Stuerme. *Annalen der Physik*, 178(10), pp.246-255.

Völker, C., 1999. Momentum Balance in Zonal Flows and Resonance of Baroclinic Rossby Waves. *J. Phys. Oceanogr.*, 29(8), pp.1666-1681.

Wallace, J.M., 1983. The Climatological Mean Stationary Waves: Observational Evidence. In Hoskins, B.J. & Pearce, R.P., ed., *Large-Scale Dynamical Processes in the Atmosphere*. London: Academic Press Inc. (London) Ltd. Ch. 2.

Wang, B. & Redekopp, L.G., 2001. Long Internal Waves in Shear Flows: Topographic Resonance and Wave-Induced Global Instability. *Dyn. Atmos. Oceans*, 33(4), pp.263-302.

Webster, P.J., 1977. The Low-Latitude Circulation of Mars. *Icarus*, 30(4), pp.626-649.

Weeks, E.R., Tian, Y., Urbach, J.S., Ide, K., Swinney, H.L. & Ghil, M., 1997. Transitions Between Blocked And Zonal Flows In A Rotating Annulus With Topography. *Science*, 278(5343), pp.1598-1601.

Williams, G.P., 1967. Thermal Convection in a Rotating Fluid Annulus: Part 2 - Classes of Axisymmetric Flow. *J. Atmos. Sci.*, 24(2), pp.162-174.

Williams, P.D., Read, P.L. & Haine, T.W.N., 2010. Testing the Limits of Quasi-Geostrophic Theory: Application to Observed Laboratory Flows Outside of the Quasi-Geostrophic Regime. *J. Fluid Mech.*, **649**, pp.187-203.

Woollings, T., 2013. Dynamical Influences on European Climate: An Uncertain Future. *Phil. Trans. R. Soc. Lon. A*, 368(1924), pp.3733-3756.

Wordsworth, R.D., 2008. *Theoretical and Experimental Investigations of Turbulent Jet Formation in Planetary Fluid Dynamics.* DPhil. University of Oxford.

Yang, S., Reinhold, B. & Källén, E., 1997. Multiple Weather Regimes and Baroclinically Forced Spherical Resonance. *J. Atmos. Sci.*, 54(11), pp.1397-1409.

Young, R.E., Walterscheid, R.L., Schubert, G., Seiff, A., Linkin, V.M. & Lipatov, A.N., 1987. Characteristics of Gravity Waves Generated by Surface Topography on Venus: Comparison with the VEGA Balloon Results. *J. Atmos. Sci.*, 44(18), pp.2628–2639.